Osman Gültekin, MSc

Computational Inelasticity of Fibrous Biological Tissues with a Focus on Viscoelasticity, Damage and Rupture

DOCTORAL THESIS

to achieve the university degree of

Doktor der technischen Wissenschaften

submitted to

Graz University of Technology

Supervisor

Univ.-Prof. Dipl-Ing. Dr. techn. Gerhard A. Holzapfel

Institute of Biomechanics

Graz, September 2018

AFFIDAVIT

I declare that I have authored this thesis independently, that I have not used other than the declared sources/resources, and that I have explicitly indicated all material which has been quoted either literally or by content from the sources used. The text document uploaded to TUGRAZonline is identical to the present doctoral thesis.

Date

Signature

Preface

This dissertation is the final outcome of four and a half years of a challenging research study performed between 2014 and 2018, during my employment as a research assistant at the Institute of Biomechanics at Graz University of Technology.

First and foremost, I would like to express my deep gratitude to my supervisor, Prof. Gerhard A. Holzapfel, for giving me the opportunity to do my doctoral study at the institute and for his constructive criticisms, encouragements and fruitful discussions in academic matters which played a significant role in the achievement of this thesis. My sincere thanks are extended to Prof. Peter Wriggers for his acceptance to become the co–examiner of my doctoral thesis.

I would like to also express my gratitude to Dr. Hüsnü Dal for being a great mentor and friend since my master study at the international master degree program COMMAS at University of Stuttgart. The publications we have co–authored attest to our fruitful collaboration for a long time.

I always feel indebted to Dr. Serdar Göktepe as he was the first scholar to familiarize me with the realm of continuum and computational mechanics during the joyful years of my bachelor study at Middle East Technical University in Ankara.

Next, I would like to thank the current and former colleagues from the institute, in particular Bettina Strametz, Daniel Haspinger, Gerhard Sommer, Anju Babu and Candice Towler for valuable helps, fruitful discussions, and the entertaining after–work activities throughout the years I have spent in Graz. I would like to say a hearty thank you to my friend Faik Barış Can Cansız for his support and friendship.

I would like to mention my beloved family to whom this thesis is dedicated: Nihat Gültekin, Sahuriye Gültekin and Tayfun Gültekin. Without their love, patience and encouragement this work could not have been accomplished. Last but not least, I am thankful to my little niece, Nehir Gültekin for being a source of joy during this period.

Abstract

Practical and ethical limitations generally impede the purely experimental characterization of the relations between the mechanical loads acting on cells, tissues, organs and the nonlinear inelastic phenomena, such as damage and fracture, thereby favoring the use of numerical modeling and simulations. The subsequent chapters deliver a dissemination of the extensive efforts to model the inelastic mechanical response occurring in human cardiovascular tissue, such as viscoelasticity, damage and rupture associated with the human myocardial and arterial wall under hemodynamic loads.

Anisotropic fracture of arterial walls are evident from the intrinsic structure of the wall conferred by the collagen fibers embedded in an otherwise isotropic, thick–walled solid. The first two contributions aim at developing a computational framework capable of handling the anisotropic fracture. To this end, the crack phase–field approach is blended with a novel energy–based anisotropic criterion, in other words, the crack driving source term based on the distinction of the isotropic and anisotropic failure process. In addition, an anisotropic crack surface density function is introduced within the context of fibrous tissue modeling which orients the crack propagation parallel to the direction of fibers. The crack phase–field approach is, in principle, hinged on the gradient damage models with the inherent ingredients of fracture mechanics, e.g., the critical energy release rate.

The third study investigates the interesting case of aortic dissection from a numerical viewpoint. A simplistic model of a human aorta with a prescribed initial tear is presented where the incipient propagation of the aortic dissection around the initial tear tracks the mean orientation of a single family of fibers when subjected to a supra–physiological loading, thereby manifesting a helical growth in the wall which is in line with clinical observations. The results also imply the significance of systematic experimental analyses of the aortic tissue, enabling the constituent (elastin, collagen) and layer (intima, media, adventitia) specific rupture properties of the wall.

Further, an orthotropic viscoelastic model for the human passive myocardium is presented which captures the strong hystereses and stress relaxation behavior observed upon the biaxial extension and triaxial shear experiments on human test specimens. Of equal importance is the accuracy of the computational models mimicking the quasi–incompressible behavior of soft biological tissues under mechanical loading which is covered in a systematic way in the final study.

Zusammenfassung

Praktische und ethische Einschränkungen erschweren die experimentelle Charakterisierung von Beziehungen zwischen mechanischen Belastungen, die auf Zellen, Geweben und Organe wirkt, und den nichtlinearen inelastischen Phänomenen, wie dem Materialbruch. Aufgrund dieser experimentellen Limitationen finden numerische Modellierung und Simulationen eine bevorzugte Anwendung. Die folgenden Kapitel erklären die Bemühungen, inelastische mechanische Reaktionen, wie Viskoelastizität, Schädigung und Ruptur, welche im menschlichen kardiovaskulären Geweben unter hämodynamischen Belastungen auftreten können, zu modellieren.

Die ersten beiden Beiträge präsentieren ein neuartiges computerunterstütztes Modell, welches in der Lage ist den anisotropen Materialbruch in biologischen Geweben zu behandeln. Zu diesem Zweck wurde die Phasenfeldmethode für den Rissfortschritt, kurz Riss-Phasenfeldmethode, mit einem neuartigen energiebasierenden anisotropen Kriterium gekoppelt. Dabei basiert der Quellterm des Rissfortschritts auf die Unterscheidung zwischen isotropen und anisotropen Versagensprozess. Zusätzlich wird im Rahmen der Modellierung von fibrösen Geweben eine anisotrope Dichtefunktion der Riss-Oberfläche eingeführt, die das Risswachstum parallel zur Faserrichtung orientiert. Die Riss-Phasenfeldmethode beruht im Prinzip auf Gradienten-Schädigungsmodelle mit inhärenten Bestandteilen der Bruchmechanik, z.B. der kritischen Energieabgabe-Rate.

Die dritte Studie untersucht den interessanten Fall einer Aortendissektion Mithilfe numerischer Methoden. In dieser Studie wird ein vereinfachtes menschliches Aortenmodell unter supra-physiologischen Belastung mit einem vorgegebenen Anfangsriss angenommen. Die beginnende Rissausbreitung der Aortendissektion verfolgt dabei die Hauptausrichtung einer Faserfamilie, sodass sich das Risswachstum helixförmig in der Wand ausbreitet, das den klinischen Beobachtungen entspricht. Die Ergebnisse weisen auf die Wichtigkeit von systematischen experimentellen Untersuchungen des Aortengewebes hin, wobei sich komponentenabhängige (Elastin, Kollagen) und schichtenspezifische Ruptureigenschaften der Aortenwand als essentiell erscheinen.

Außerdem wird ein orthotropes viskoelastisches Modell für das menschliche passive Myokard vorgestellt, welches die ausgeprägte Hysterese und das deutliche Spannungsrelaxationsverhalten unter biaxialen Zug- und triaxialen Scherbelastungen des menschlichen Myokards wiedergeben kann. In der letzten Studie dieser Doktorarbeit wird die Bedeutung der Genauigkeit von Computermodellen, die das quasi-inkompressible Verhalten von weichen biologischen Geweben unter mechanischer Belastung imitiert, systematisch behandelt.

Contents

1 INTRODUCTION

Biomechanics, in simple terms, is the development, extension (e.g. modeling of growth in biological tissues) and application of mechanics to address the related biophysical phenomena featuring organ, tissue, cellular, and molecular levels (Humphrey [97]). As the name implies, biomechanics encompasses several subjects and concepts derived in the realm of classical mechanics, e.g., from heat transfer to tissue deformation and from Mullins–type (Mullins [148]) damage to fracture, to name but a few.

Biomechanics is mainly concerned with the better understanding of the physiology and patho–physiology of living systems by applying the principles of mechanics. This understanding employs the two-pronged approach of empiricism and theoretical analysis. It needs to be emphasized that the two prongs inextricably intertwine with each other. Theoretician is the one leading the experimenter through his explicit questions brought up as sharp as possible. The latter, by his experiments, tries to bring out relevant answers to these questions. Thus, it is the job of the theoretician to guide the experimenter through the performance, interpretation of the experiments and the synthesis of their results. The work of the experimenter, however, also entails theory by means of constrained variables inherent to the nature of problems; therefore, theory governs the experimental process from the initial stages up to the finishing touches, see Popper [166] and Humphrey [97]. By analogy, computer models and their analyses can be viewed as experiments of numerical kinds required due to geometric and material nonlinearities associated with, e.g., biological tissues. The achievements taken place for the last three decades in biomedical measurement, imaging technologies and numerical analyses are impressive, clearly demonstrating that computational modeling have become the third prong besides theory and experiment.

According to fact sheets provided by World Health Organization (WHO) [159], cardiovascular diseases (CVDs) with 17.7 million cases represent 31% of all global deaths happened in 2015. There is a pressing need for predicting the inelastic effects associated with aneurysms, atherosclerosis, aortic dissections and viscoelasticity where a salient relation exists between the histological structure and mechanical response of the arterial/aortic wall and the myocardium. Hence, computational models with their rapid development may provide a virtual environment which can represent human cardiovascular tissue and its structure. New insights of the underlying mechanics of soft biological tissues can be grasped in health and disease. This may eventually lead to improvements in medical monitoring, planning of surgical interventions and risk assessment of CVDs which will accommodate the essential impetus for *in silico medicine*. In the thesis, focus is placed upon the numerical modeling of the inelastic phenomena, e.g., progressive damage, rupture and viscoelasticity, occurring in the cardiovascular tissues in health and disease.

1.1 Extracellular Matrix

Occupying the intercellular space, the complex network of extracellular matrix (ECM) provides shape and resilience to the tissue apart from serving as a scaffold. ECM also influences extracellular communication through signaling, diffusion and chemical reactivity. It consists of fibers such as collagen and elastin, and the ground substance composed of proteoglycans (e.g., aggrecan, syndecan), multi-adhesive gylcoproteins (e.g., fibronection, laminin), and glycosaminoglycans (e.g., dermatan sulfate) (Ross & Pawlina [177]).

1.1.1 Collagen

Being the most abundant structural protein of the connective tissue, the flexible collagen fibers constitute about 30–40% of all body proteins in most mammals according to Verzár [227]. Representing the main load carrying element under tension, collagen fibers appear undulated in the absence of load, whilst they first straighten and then are recriuted to contribute to the mechanical response of the tissue during loading, see Yang et al. [237].

Collagen fibers appear to be composed of bundles of threadlike subunits called collagen fibrils. Fibrils are traversed along their length by banding patterns called d–spacing that repeats consistently every 67 [nm] as seen in the atomic force microscopic image in Fig. 1.1(a). This banding pattern displays the subunit structure of the fibril, i.e. the arrangement of the collagen molecules assembled into the fibril through intermolecular cross–links (mainly covalent bonds) with d–spacing comprised of a hole and overlap zones, see Fig. 1.1(b). It has been observed by Schmid et al. [183] that the stretch occurring in the cross-links is one order of magnitude smaller than the macroscopic stretch during the uniaxial extension of adventitial strips. Collagen molecules, in their turn, are formed by three polypeptides (α–chains) intertwined in a right–handed helical path creating a triple helix via intramolecular cross–links (hydrogen bonds). Each polypeptide consists of regularly arranged amino acids; glycine, proline and hydroxyproline as illustrated in Fig. 1.1(b) (Sherman et al. [193]).

Collagen fibers are formed in 28 different types. However, type I, III–VI and VIII are the most common forms that exist in the cardiovascular system. Among them, type I and type III are fibrillar collagens providing resistance to tension and supportive scaffolding for arterial walls, respectively. They present almost all other connective tissues from skin to ligaments. The interested reader is referred to Ross & Pawlina [177] for a more elaborate account.

The synthesis of collagen fibrils involves series of highly intricate intra–cellular (within the fibroblasts) and extra–cellular events which are stimulated by transforming growth factor β (TGF–β). Like all proteins in the body, collagen fibers are continually degraded and resynthesized which enables the tissue to grow and remodel itself in response to changes in the mechanical environment. They can be degraded either by a proteolytic or phagocytotic ways. The proteolytic degradation takes place outside the cells and is caused by the enzymes, namely matrix metalloproteinases (MMPs). MMPs include the collagenases

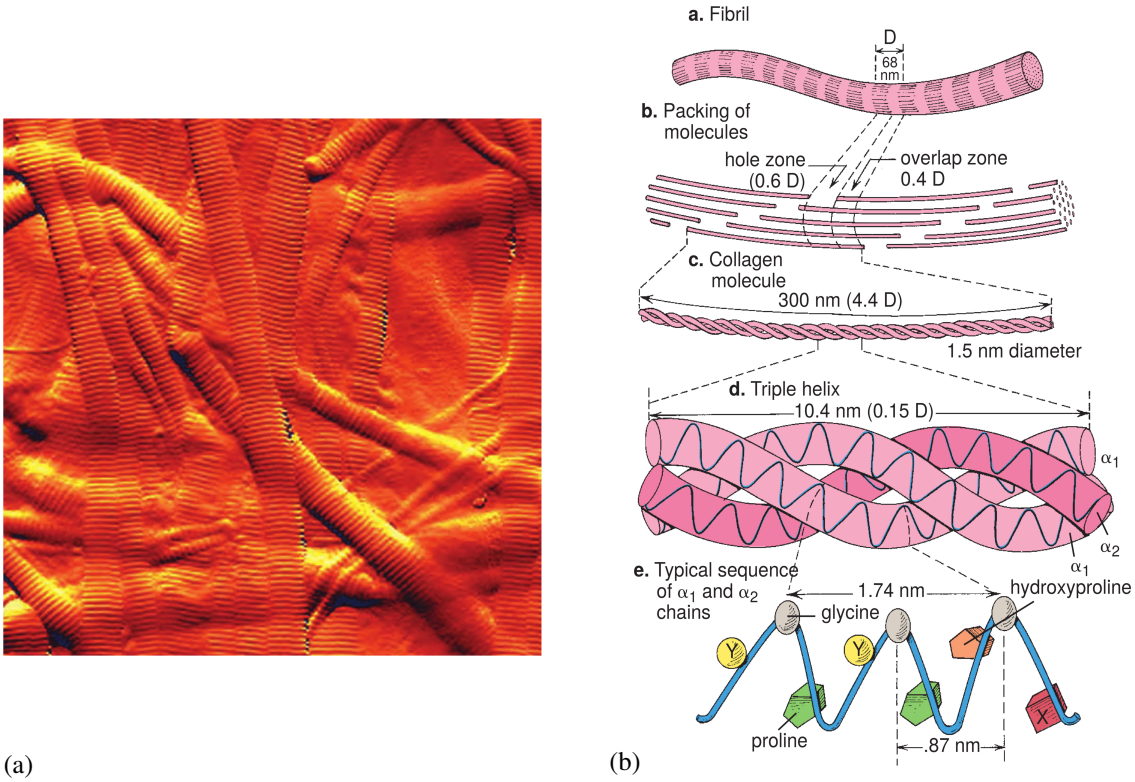

(a) (b)

Figure 1.1 (a) Atomic force microscopic image of type I collagen fibrils in the connective tissues with the banding patterns on the surface; (b) single collagen fibril reflecting the banding patterns with d–spacing (67 [nm]). Each fibril is assembled by collagen molecules featuring a triple helix. The triple helix, measuring about 300 [nm] in length and 1.5 [nm] in thickness, is made up of α–chains with every third amino acid of the chain being a glycine. The positions X and Y are predominantly proline and hydroxyproline, respectively; adopted from Ross & Pawlina [177].

that degrade type I–III, and X collagens; the gelatinases responsible for degrading the fibronectin and elastin; the stromelysins removing proteoglycans and fibronectin, and finally the matrilysins digesting type IV collagen and proteoglycans. Phagocytotic degradation, however, occurs intracellularly through the activity of macrophages that removes the components of the ECM (Ross & Pawlina [177]).

1.1.2 Elastin

Typically thinner than collagen, the elastin protein constitute a rubber–like three dimensional network and in contrast to collagen they do not manifest a pronounced hierarchical structure, see Fig. 1.2(a). Together with the fibrillin microfibrils, elastin molecules form elastic fibers as the backbone elastin is surrounded by a network of fibrillin microfibrils, e.g., fibrillin–1 (Holzapfel et al. [83]). Elastin consists of polypeptides, mostly the glycine.

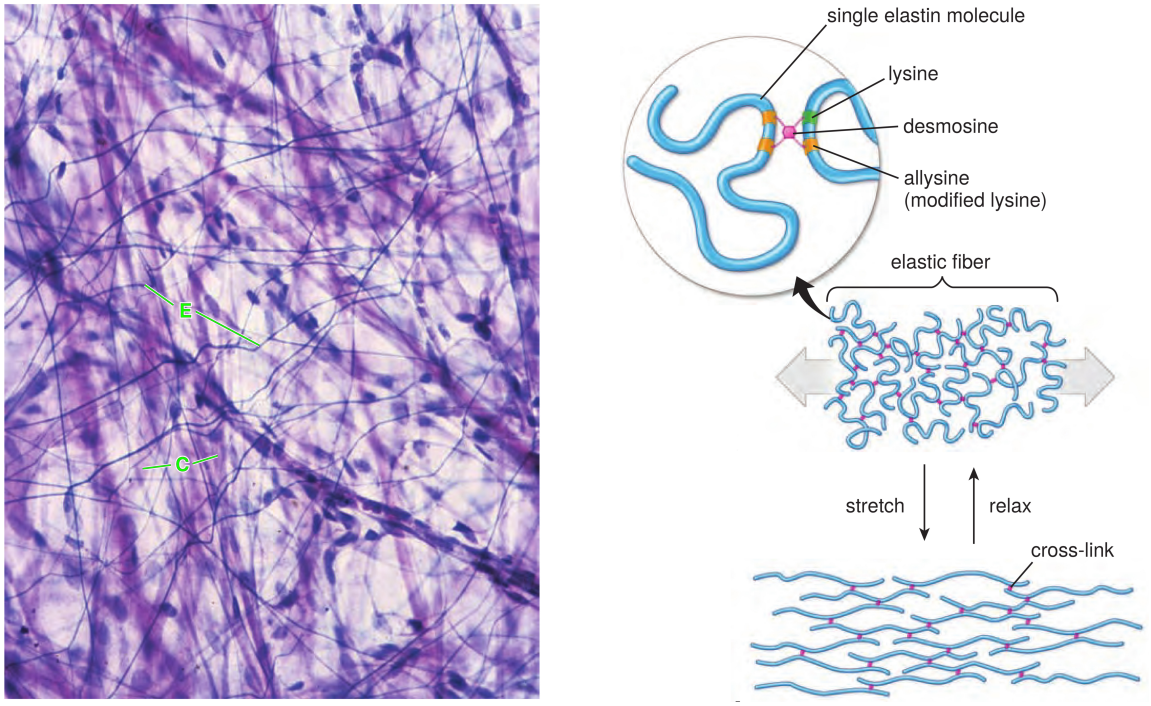

(a) (b)

Figure 1.2 (a) Photomicrograph of a stained mesentery with threadlike branching strands corresponding to elastin (E) and much thicker unbranced threads being the collagen fibers (C); (b) desmosine and isodesmosine linking elastin molecules thereby forming a cross–linked network. In the mean time, the elasticity of the elastin network is shown with a stretched and relaxed configuration; adopted from Ross & Pawlina [177]).

In fact, compared with collagen, the contents of proline and hydroxyproline are much lower in elastin network. The loose, unstructured elastin molecules are bound together via covalent cross–links mainly formed by desmosine and isodesmosine as depicted in Fig. 1.2(b) (Ross & Pawlina [177]). From a mechanical standpoint, the long elastin molecules are much more complaint than collagen and can be stretched 2.5 times their initial length during loading while the network reverts to its original unstretched state when the load is withdrawn, see Fig. 1.2(b). An inflation test performed by Roach & Burton [173] on a human external iliac artery upon the enzymatic removal of the collagen and elastin through formic acid and trypsin, respectively, attests to the characteristic mechanical role of elastin and collagen as shown in Fig. 1.3. At relatively low pressures, the stiffness of the untreated artery (control curve) is conferred by the elastin, see the collagen–digested curve, whereas the tension–length behavior in higher pressures is chiefly determined by the collagen, see the elastin–digested curve, as the undulated collagen fibrils are gradually recruited.

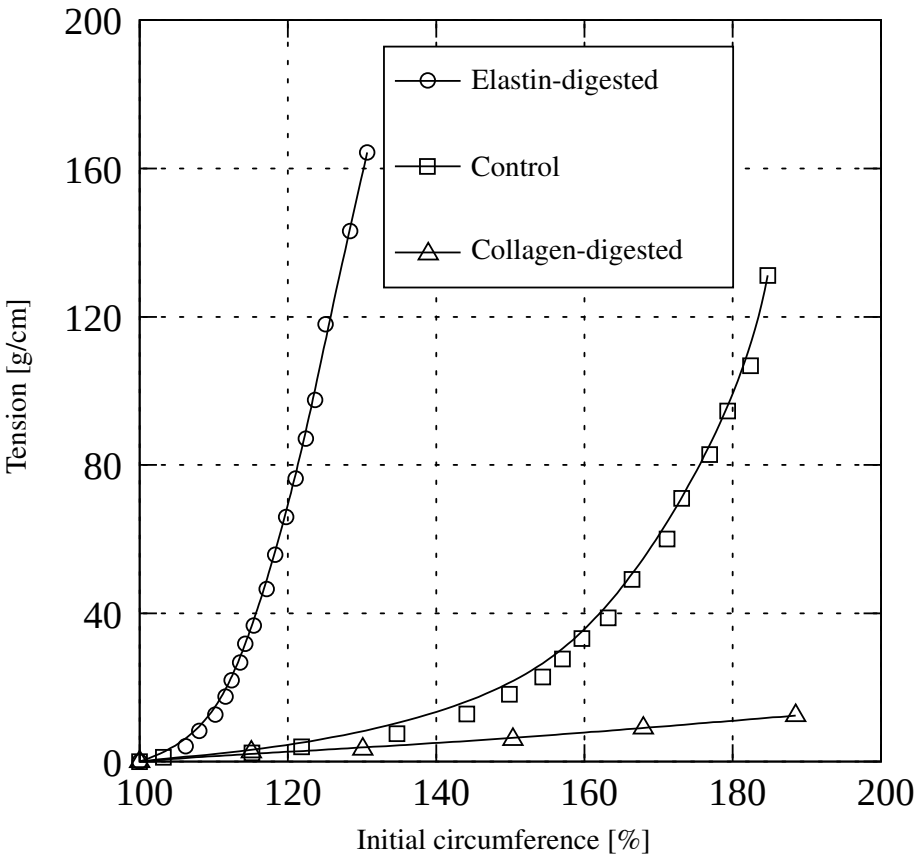

Figure 1.3 Tension–length curves of a human external iliac artery subjected to pressure for the elastin–digested (via trypsin), the collagen–digested (via formic acid), and the control (untreated artery) specimens. The elastin–digested (empty circles) and the collagen–digested (empty triangles) curves represent the mechanical response of the collagen and elastin, respectively, whilst the control (empty squares) curve attests to the typical J–shaped mechanical behavior of the artery; reconstructed from Roach & Burton [173].

1.1.3 Other mechanically relevant constituents

That the proteoglycans (PGs) may directly or indirectly contribute to the mechanical response as decorins link the adjoining collagen fibers together, thereby guaranteeing the mechanical coupling of microfibrils, is demonstrated by e.g., Lewis et al. [120] for bovine cornea, which might be also the case for elastic arteries albeit without ample evidences as of yet.

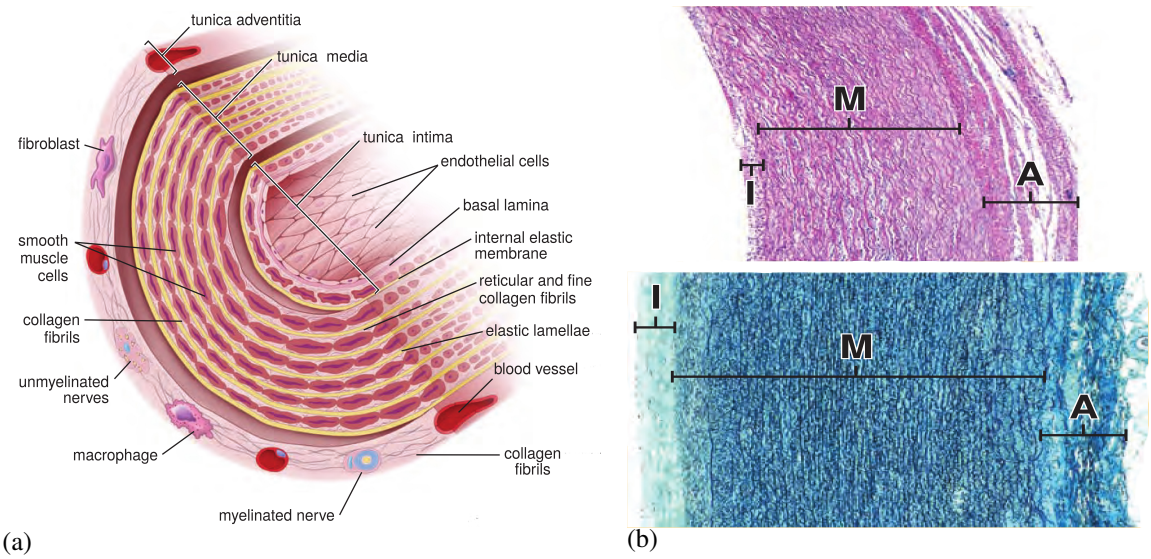

(a) (b)

Figure 1.4 (a) Schematic diagram of a typical elastic artery with cellular and extracellular components. The *tunica* media is manifested by several alternating layers of elastic lamellae and smooth–muscle cells. Embedded are the collagen fibers, adhesion molecules, GAGs and PGs. (b) Micrographs show the stained human aorta from a child (upper) and an adult (lower) with distinct layers; *tunica* intima (I), *tunica* media (M) and *tunica* adventitia (A); reconstructed from Ross & Pawlina [177].

1.2 Elastic Arteries

Serving primarily as conduction tubes the elastic arteries include the aorta, pulmonary, common carotid, subclavian and common iliac arteries which are distended during systole, whereas the recoiling from the distended state occurs during diastole, which preserves the arterial blood pressure. They consist of three distinct layers, namely the *tunica* intima, the *tunica* media and the *tunica* adventitia as indicated in Fig. 1.4(a). The medial layer of elastic arteries is made up of several sub–layers of elastic fibers and smooth muscle cells which allows the artery to resist the pressure fluctuations caused by the rhythmic contraction of the heart. The number of elastic lamellae in the wall tends to increase with age, see Fig. 1.4(b).

1.2.1 *Tunica* intima

The *tunica* intima comprises endothelium, basal lamina, subendothelial layer composed chiefly of collagen, elastic fibers and occasionally smooth muscle cells, and internal elastic lamella separating the the intima and media as depicted in Fig. 1.4(a). The endothelium is a single layer in young and healthy individuals and assume a spindle–shape when subjected to shear stress due to blood flow. The mechanical stimuli afterwards is conveyed to the smooth-muscle cells in the media which regulates the diameter of the artery (Alberts et al.

[2]). The endothelial layer may thicken and stiffen with age, a condition called arteriosclerosis (Holzapfel et al. [83]). According to the findings of Schriefl et al. [188], there may be up to four peculiar families of collagen fibers in the intima of the aorta.

1.2.2 *Tunica* media

The middle layer the *tunica* media is composed of as many as 70 fenestrated medial lamellar unit holding two adjacent elastic lamellae which are interposed by collagen fibers, smooth muscle cells, GAGs, PGs, etc., see Fig. 1.4(a). The extracellular constitutents in the media are proliferated by smooth muscle cells. In the experimental study of Schriefl et al. [188], two families of collagen fibers were observed in the media of aorta, whereas there exists only one preferred (mean) direction in the media of the common iliac artery. It should be also emphasized that two families of fibers sequentially appear in the aorta in a repetitive manner with each medial lamellar unit having single fiber family. Therefore, the *tunica* media operates as the main load–bearing layer under physiological conditions.

1.2.3 *Tunica* adventitia

The outermost adventitial layer mainly consists of collagen and some elastin fibers organized in a loose network and help the wall resist the supra–physiological loadings and prevent the artery from rupture. Schriefl et al. [188] observed two mean collagen fiber alignment in the human aorta and common iliac artery. Apart from that, the *tunica* adventitia also hosts fibroblasts, macrophages, *vasa vasorum* supplying blood to the vascular walls in large arteries, and *nervi vascularis* regulating the contraction of the smooth muscle cells, as shown in Fig. 1.4(a).

1.3 Related Diseases

Herein general overviews of some cardiovascular diseases, such as aortic dissection, atherosclerosis and aneurysms are given which eventually cause severe damage and even rupture of the tissue.

1.3.1 Aortic dissection

Aortic dissection mostly presents itself with an initial tear in the intimal layer, common locations of which are near the aortic root and the isthmus of the descending aorta beyond the origin of the left subclavian artery (Cherry & Dake [27]). Such a radial onset of the aortic dissection across the layers of the aorta is followed by a helical propagation, i.e. the tear advances further on the tangential plane by mostly tracking the orientation of single family of fibers in a medial lamellar unit which elicits the formation of the false lumen next to the true one. Consequently, substantial amount of blood flows through the false lumen, reducing the supply of nutrients and oxygen to the body parts. The blood accumulated in the false lumen may flow back to the true lumen if there happens an exit (reentry) tear,

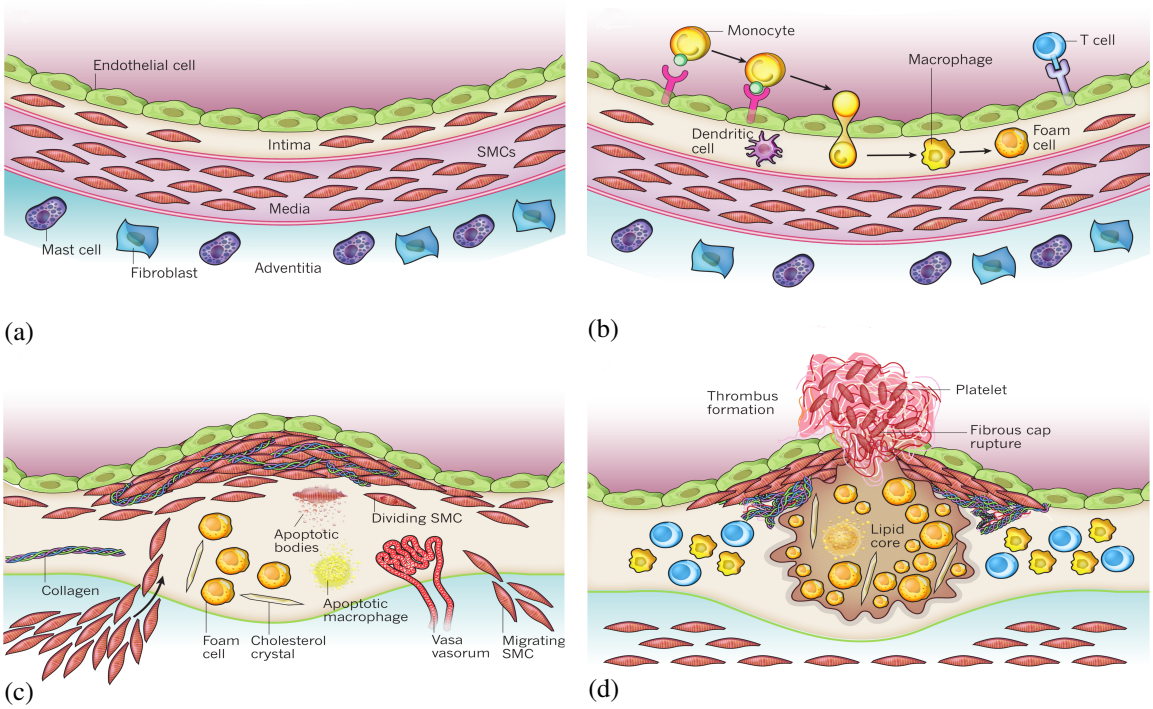

Figure 1.5 Schematic views of (a) the three–layered normal artery with the corresponding components, see Sec. 1.2; (b) the initial stage of the atherosclerosis with the formation of foam cells; (c) the well–developed stage of the atherosclerosis with SMCs migrating to the intima to secrete collagen fibers forming a fibrous cap; (d) the thrombus formation upon the rupture of the fibrous cap; adopted from Libby et al. [122].

or else the remaining intact part of the wall gradually weakens and become susceptible for dilatation and rupture. The main factors associated with the aortic dissection are the hypertension, cystic medial necrosis, connective tissue disorders, e.g., Marfan syndrome and Ehlers–Danlos syndrome, aneurysms, trauma, e.g., car accidents, cardiac catherization, male sex, and old individuals aged 60 to 70 years, see Criado [35], Dunning et al. [43], Rajagopal et al. [169] and Tsamis et al. [223], for more details.

1.3.2 Atherosclerosis

The development of atherosclerosis emanates from degenerative changes in the mono-layered endothelial cells, see Fig. 1.5(a), which influences the permeability of the endothelium and promotes the access of the low–density lipoprotein (LDL) particles inside the wall. In the meantime, normally deattached leukocytes start to adhere to the endothelium via adhesion molecules, predominantly the monocytes, see Fig. 1.5(b). Once trapped in the wall, monocytes transform into macrophages, envelop the LDL particles and turn into foam cells that features the incipient atheroma formation. Meanwhile, SMCs residing in

the *tunica* media migrate into the *tunica* intima where their phenotype alters whereby proliferate mainly collagen fibers and create a fibrous cap overlying the newly formed plaque, see Fig. 1.5(c). Some of the lipid–rich foam cells die due to apoptosis (programmed cell death) in the course of time which causes the lipid to be released, forming a lipid pool known as the necrotic core of the plaque. Further growth of the atherosclerotic plaque leads to the stenoses reducing the area of the lumen. When untreated, a rupture of the fibrous cap elicits thrombus triggered by the coagulant material exposed to the blood, see Fig. 1.5(d). The risk factors for atherosclerosis involves hypertension, smoking, diabetes and the male gender. For a more comprehensive view, the reader is among others referred to Libby et al. [122] and Holzapfel et al. [92].

1.3.3 Aneurysm

Aneurysms, a disease in the cardiovascular system, can be generally described as a local dilation of the aorta thereby manifesting a balloon–like bulge in the wall of the aorta. During the formation of aneurysms, the wall experiences significant changes in terms of histology and material properties while the stress exerted by the blood pressure on the localized part enormously increases, an alarming stage beyond which the rupture may follow if the wall cannot withstand the applied hemodynamic loads. Aneurysms mainly occur in the thoracic and abdominal aortas; however, they may also be diagnosed in the cerebral arteries situated at the base of the brain. The primary risk factors that trigger the vascular disease are known to be aging, smoking, hypertension, atherosclerosis and genetic disorders (Kroon & Holzapfel [116], Humphrey & Holzapfel [99] and Kim et al. [115]).

1.4 Human Heart

Heart, the major organ of the cardiovascular system, is a natural pump made up of helical network of muscle fibers organized in laminar sheets. The heart includes four chambers, namely the right and left atria and right and left ventricles, with four valves: tricuspid, pulmonary, aortic and mitral valves controlling the blood flow in the heart. The interatrial and interventricular septum segregating the right and left sides of the heart. Two circuits: the pulmonary circulation, where the blood is conveyed from the heart to the lungs, and the systemic circulation, where the blood is conveyed from the heart to the rest of the body, distribute the blood in which the heart plays the central role. The wall of human heart is comprised of three layers: epicardium, myocardium and endocardium.

1.4.1 Epicardium

The outermost layer epicardium consists of a single layer of mesothelial cells underlying connective and adipose tissue. Hosting blood vessels and nerves that supply the heart, the epicardium cushions the wall in the pericardial cavity filled with pericardial fluid, see Fig. 1.6. Elastin and the epimysial collagen are the most abundant structural components in the epicardium (Humphrey [97] and Ross & Pawlina [177]).

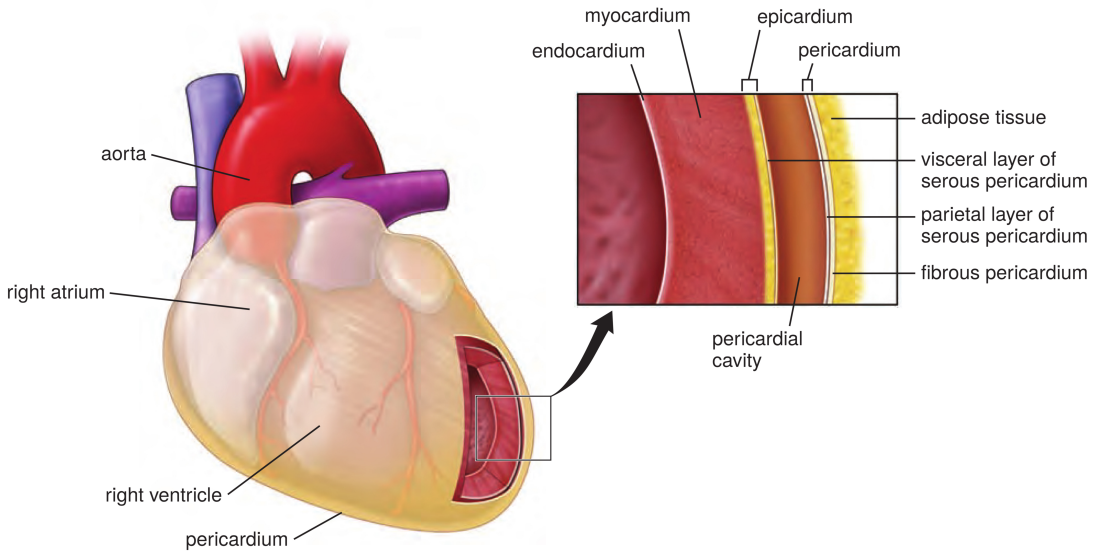

Figure 1.6 Schematic views of the layers of the heart and pericardium surrounded by adipose tissue. The pericardium comprises two layers, namely the fibrous and parietal layer. The pericardial cavity fills the space between the visceral and the parietal layers. Beneath the epicardium lies the myocardium consisting of cardiac muscle, while the inner layer endocardium overlies the myocardium; adopted from Ross & Pawlina [177].

1.4.2 Myocardium

Being the thickest layer in the heart, the myocardium consists of endomysial and perimysial collagen which characterizes the orthotropic local structure of the tissue. In addition, the cardiac muscle fibers called myocytes lie in this layer as well, which are, together with collagen fibers, organized in laminae of sheets enclosing 3–4 cell thickness. Rohmer et al. [176] reported on how fiber and sheet orientations alter not only transmurally but also from apex to base. The interested reader is also referred to Sands et al. [180, 181].

1.4.3 Endocardium

Composed of primarily the endothelium, subendothelial connective tissue and smooth muscle cells the endocardium also contains structural extracellular proteins like elastin and epimysial collagen fibers, though similar to the epicardium it is not considered as a structural layer resisting the blood pressure during cardiac cycles (Humphrey [97] and Ross & Pawlina [177]).

1.5 Nonlinear Continuum Mechanics

The aim of this section is the coherent exploitation of the notions of continuum mechanics, i.e. the basic relations of motion in a body, geometric mapping, kinematics, stress measures and the local and global forms of balance laws. The topics treated in this section are based on the seminal books by Gurtin et al. [70], Holzapfel [80], Marsden & Hughes [128], Ogden [156], Truesdell and Noll [220], the lecture notes by Miehe [137] and the PhD thesis of Göktepe [61].

1.5.1 Basic geometric maps and fundamental deformation measures

Let the solid body at time $t_0 \in \mathcal{T} \subset \mathbb{R}_+$ be referred to as the reference configuration in the three–dimensional Euclidean space $\mathcal{B} \subset \mathbb{R}^3$. Similarly, the configuration of the body at current time $t \in \mathcal{T} \subset \mathbb{R}_+$ is referred to as the spatial configuration $\mathcal{S} \subset \mathbb{R}^3$. The material point $\boldsymbol{X} \in \mathcal{B}$ is mapped through the bijective deformation map $\boldsymbol{\varphi}_t(\boldsymbol{X})$ onto the spatial point $\boldsymbol{x} \in \mathcal{S}$, i.e.

$$\boldsymbol{\varphi}_t(\boldsymbol{X}) : \left\{ \begin{array}{ll} \mathcal{B} \times \mathcal{T} \to & \mathcal{S}, \\ (\boldsymbol{X}, t) \mapsto & \boldsymbol{x} = \boldsymbol{\varphi}(\boldsymbol{X}, t), \end{array} \right. \tag{1.1}$$

which characterizes the motion in the solid body, see Fig. 1.7. Subsequently, we introduce the material velocity and the acceleration

$$\boldsymbol{V}_t(\boldsymbol{X}) := \partial_t \boldsymbol{\varphi}(\boldsymbol{X}, t) = \frac{\mathrm{d}}{\mathrm{d}t} \boldsymbol{\varphi}_{\boldsymbol{X}}(t), \qquad \boldsymbol{A}_t(\boldsymbol{X}) := \partial_t \boldsymbol{V}(\boldsymbol{X}, t) = \frac{\mathrm{d}}{\mathrm{d}t} \boldsymbol{V}_{\boldsymbol{X}}(t) \tag{1.2}$$

in conjunction with the the spatial velocity and the acceleration

$$\boldsymbol{v}_t(\boldsymbol{x}, t) := \boldsymbol{V}_t(\boldsymbol{X}) \circ \boldsymbol{\varphi}_t^{-1}(\boldsymbol{x}), \qquad \boldsymbol{a}_t(\boldsymbol{x}, t) := \boldsymbol{A}_t(\boldsymbol{X}) \circ \boldsymbol{\varphi}_t^{-1}(\boldsymbol{x}) = \partial_t \boldsymbol{v} + \nabla_{\boldsymbol{x}} \boldsymbol{v} \cdot \boldsymbol{v}. \tag{1.3}$$

The reference $\mathcal{B}$ and spatial $\mathcal{S}$ configurations are continuous three–dimensional manifolds parametrized locally in the neighborhoods $\mathcal{N}_X \subset \mathcal{B}$ and $\mathcal{N}_x \subset \mathcal{S}$ by overlapping coordinate charts $\{X^A\}_{A=1,2,3}$ and $\{x^a\}_{a=1,2,3}$, respectively. Probably the most fundamental deformation measure used in continuum mechanics is the deformation gradient $\boldsymbol{F}$ defined as

$$\boldsymbol{F} := \nabla_X \boldsymbol{\varphi}_t(\boldsymbol{X}) \qquad \text{with} \qquad F_A^a = \frac{\partial x^a}{\partial X^A}, \tag{1.4}$$

which maps tangents $\boldsymbol{T} \in T_X\mathcal{B}$ of material curves onto tangents $\boldsymbol{t} \in T_x\mathcal{S}$ of spatial curves, as shown in Fig. 1.7. This can be expressed by

$$\boldsymbol{F} : \left\{ \begin{array}{ll} T_X\mathcal{B} \to & T_x\mathcal{S}, \\ \boldsymbol{T} \mapsto & \boldsymbol{t} = \boldsymbol{F}\boldsymbol{T}, \end{array} \right. \qquad \text{with} \qquad t^a = F_A^a T^A. \tag{1.5}$$

In what follows the basic mapping relationships resulting from the deformation gradient are given between the reference infinitesimal line, area and volume elements $\mathrm{d}\boldsymbol{X}$, $\mathrm{d}\boldsymbol{A}$, $\mathrm{d}V \in \mathcal{B}$ and their spatial counterparts $\mathrm{d}\boldsymbol{x}$, $\mathrm{d}\boldsymbol{a}$, $\mathrm{d}v \in \mathcal{S}$ such that

$$\mathrm{d}\boldsymbol{x} = \boldsymbol{F}\mathrm{d}\boldsymbol{X}, \qquad \mathrm{d}\boldsymbol{a} = \operatorname{cof} \boldsymbol{F}\mathrm{d}\boldsymbol{A}, \qquad \mathrm{d}v = J\mathrm{d}V. \tag{1.6}$$

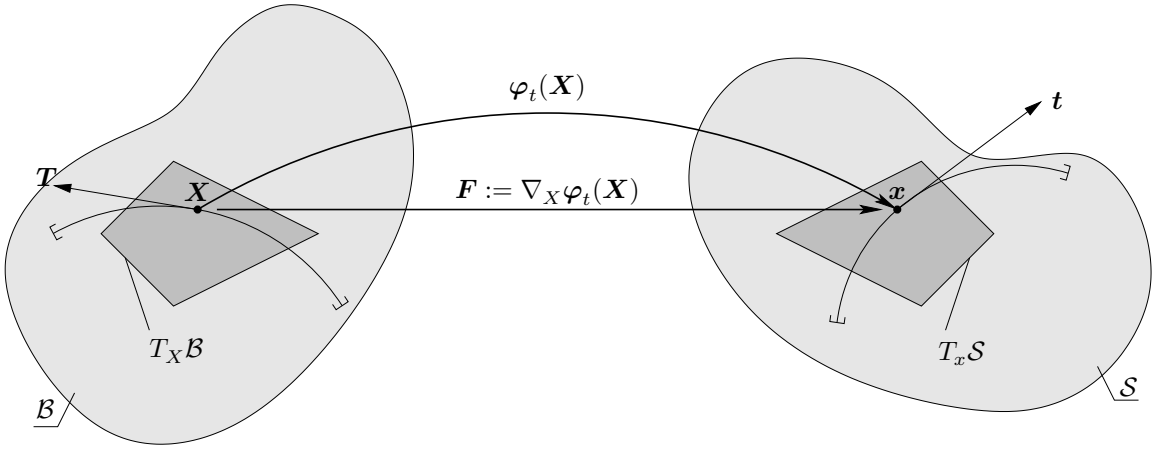

Figure 1.7 The deformation gradient $\boldsymbol{F}$ is defined as a tangent map, linearly transforming the material tangent vector $\boldsymbol{T} \in T_X\mathcal{B}$ at $\boldsymbol{X}$ onto the spatial tangent vector $\boldsymbol{t} \in T_x\mathcal{S}$ at $\boldsymbol{x}$.

In (1.6), we introduce the determinant of the deformation gradient $J := \det\boldsymbol{F} > 0$ which is restricted to positive real numbers ensuring the impenetrability of the solid material considered. In addition, the cofactor of the deformation gradient is defined, i.e. $\operatorname{cof}\boldsymbol{F} := \partial_{\boldsymbol{F}}\det\boldsymbol{F} = \det\boldsymbol{F}\boldsymbol{F}^{-\mathrm{T}} = J\boldsymbol{F}^{-\mathrm{T}}$. The physical interpretation of the cofactor is elucidated upon the expansion on $(1.6)_2$ yielding Nanson's formulas, i.e.

$$\boldsymbol{n}\mathrm{d}a = \operatorname{cof}\boldsymbol{F}\boldsymbol{N}\mathrm{d}A = J\boldsymbol{F}^{-\mathrm{T}}\boldsymbol{N}\mathrm{d}A, \tag{1.7}$$

where $\boldsymbol{F}^{-\mathrm{T}}$ appears as the normal map since it transforms the co-vectors $\boldsymbol{N}$ of the reference co-tangent space $T_X^*\mathcal{B}$ onto the co-vectors $\boldsymbol{n}$ of the spatial co-tangent space $T_x^*\mathcal{S}$ through

$$\boldsymbol{F}^{-\mathrm{T}} : \begin{cases} T_X^*\mathcal{B} \to & T_x^*\mathcal{S}, \\ \boldsymbol{N} \mapsto \boldsymbol{n} & = \boldsymbol{F}^{-\mathrm{T}}\boldsymbol{N}. \end{cases} \tag{1.8}$$

With the tangent and the co-tangent spaces at hand, the manifolds $\mathcal{B}$ and $\mathcal{S}$ are now locally equipped with the symmetric and positive definite covariant reference $\boldsymbol{G}$ and spatial $\boldsymbol{g}$ metric tensors. The introduction of the metric tensors, as we shall see in the subsequent sections, establishes a canonical form for the pull-back and push-forward relations between the reference and spatial configurations, leading to somehow easier derivations of the Eulerian rate and the elasticity tensor, independent of the particular choice of the coordinate system. In fact, their use provides a generic framework which applies to all coordinate systems. The metric tensors simplify to the Kronecker deltas, i.e. $G_{AB} = \delta_{AB}$ and $g_{ab} = \delta_{ab}$, in the Cartesian coordinate system. The metrics $\boldsymbol{G}$ and $\boldsymbol{g}$ link the tangent and co–tangent spaces

$$\boldsymbol{G} : \begin{cases} T_X\mathcal{B} \to T_X^*\mathcal{B}, \\ \boldsymbol{T} \mapsto \boldsymbol{N} = \boldsymbol{G}\boldsymbol{T}, \end{cases} \qquad \boldsymbol{g} : \begin{cases} T_X\mathcal{S} \to T_X^*\mathcal{S}, \\ \boldsymbol{t} \mapsto \boldsymbol{n} = \boldsymbol{g}\boldsymbol{t}, \end{cases} \tag{1.9}$$

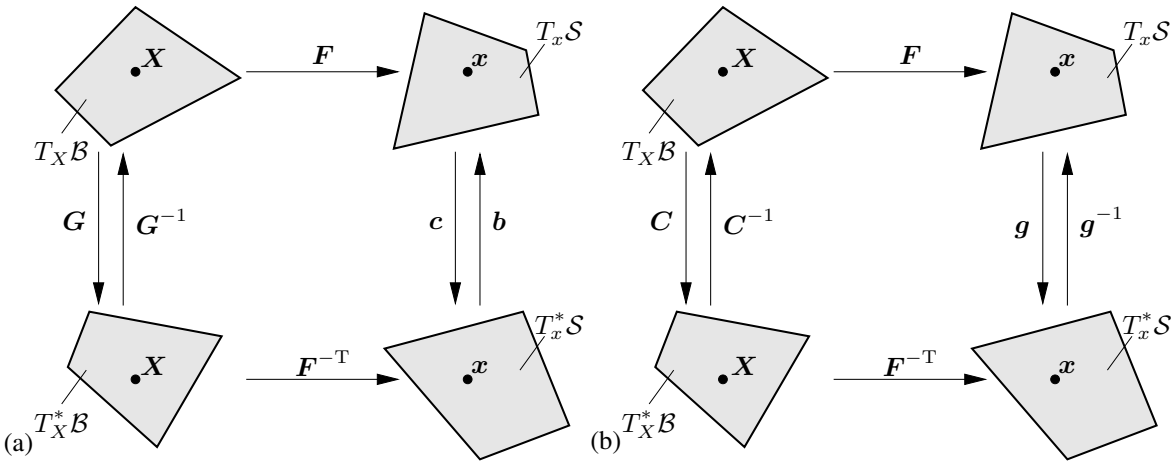

Figure 1.8 (a) and (b) show the push-forward and pull-back operations on $\boldsymbol{G}$ and $\boldsymbol{g}$ and their contravariant inverse metrics $\boldsymbol{G}^{-1}$ and $\boldsymbol{g}^{-1}$, respectively.

through index lowering operations, i.e.

$$\begin{aligned} \boldsymbol{T}^\flat &= \boldsymbol{G}\boldsymbol{T}, & T_A &= G_{AB}T^B, \\ \boldsymbol{t}^\flat &= \boldsymbol{g}\boldsymbol{t}, & t_a &= g_{ab}t^b, \end{aligned} \tag{1.10}$$

and the index raising operations, respectively, i.e.

$$\begin{aligned} \boldsymbol{T} &= \boldsymbol{G}^{-1}\boldsymbol{T}^\flat, & T^A &= G^{AB}T_B, \\ \boldsymbol{t} &= \boldsymbol{g}^{-1}\boldsymbol{t}^\flat, & t^a &= g^{ab}t_b. \end{aligned} \tag{1.11}$$

Figure 1.8(a) illustrates the push–forward $\boldsymbol{\varphi}_*(\bullet)$ operations on the covariant metric $\boldsymbol{G}$ and the contravariant inverse metric $\boldsymbol{G}^{-1}$ engendering the left Cauchy–Green tensor $\boldsymbol{b}$ along with its inverse $\boldsymbol{b}^{-1} = \boldsymbol{c}$,

$$\begin{aligned} \boldsymbol{b} := \boldsymbol{\varphi}_*(\boldsymbol{G}^{-1}) &= \boldsymbol{F}\boldsymbol{G}^{-1}\boldsymbol{F}^{\mathrm{T}}, & b^{ab} &= F^a_A G^{AB} F^b_B, \\ \boldsymbol{c} = \boldsymbol{b}^{-1} := \boldsymbol{\varphi}_*(\boldsymbol{G}) &= \boldsymbol{F}^{-\mathrm{T}}\boldsymbol{G}\boldsymbol{F}^{-1}, & c_{ab} &= (F^{-1})^A_a G_{AB} (F^{-1})^B_b. \end{aligned} \tag{1.12}$$

In an analogous way, Fig. 1.8(b) indicates the pull–back $\boldsymbol{\varphi}^*(\bullet)$ operations on the co–variant metric $\boldsymbol{g}$ and the contra-variant inverse metric $\boldsymbol{g}^{-1}$ leading to the right Cauchy–Green tensor $\boldsymbol{C}$ along with its inverse $\boldsymbol{C}^{-1}$,

$$\begin{aligned} \boldsymbol{C} := \boldsymbol{\varphi}^*(\boldsymbol{g}) &= \boldsymbol{F}^{\mathrm{T}}\boldsymbol{g}\boldsymbol{F}, & C_{AB} &= F^a_A g_{ab} F^b_B, \\ \boldsymbol{C}^{-1} := \boldsymbol{\varphi}^*(\boldsymbol{g}^{-1}) &= \boldsymbol{F}^{-1}\boldsymbol{g}^{-1}\boldsymbol{F}^{-\mathrm{T}}, & (C^{-1})^{AB} &= (F^{-1})^A_a g^{ab} (F^{-1})^B_b, \end{aligned} \tag{1.13}$$

1.5.2 Cauchy theorem and fundamental stress measures

In Sec. 1.5.1, the notation $\boldsymbol{T} \in T_X\mathcal{B}$ and $\boldsymbol{t} \in T_x\mathcal{S}$ has been used to indicate Lagrangian and Eulerian tangents. However, the definition here completely changes such that they

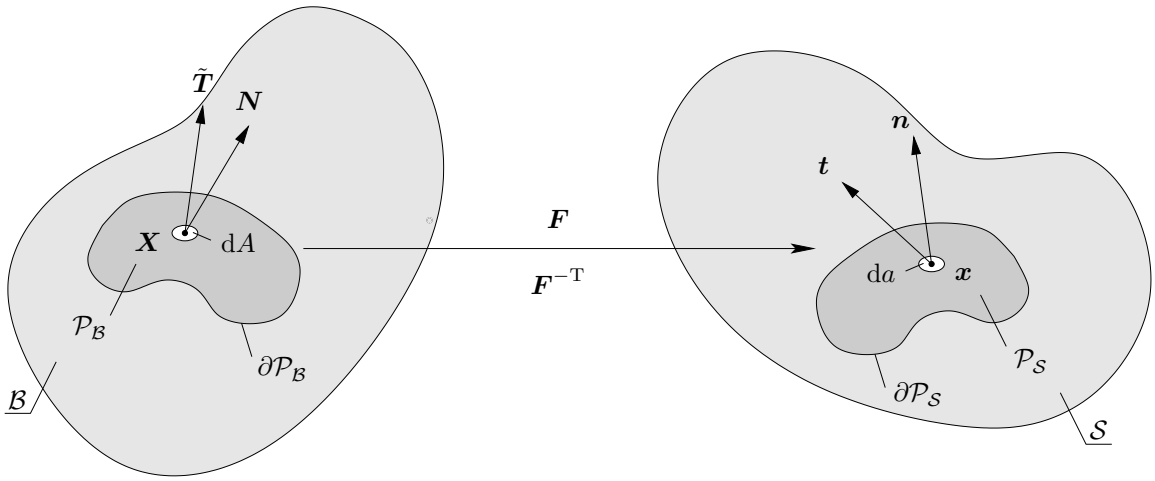

Figure 1.9 The material $\tilde{\boldsymbol{T}}(\boldsymbol{X}, t; \boldsymbol{N}) \in T_X\mathcal{B}$ and spatial $\boldsymbol{t}(\boldsymbol{x}, t; \boldsymbol{n}) \in T_x\mathcal{S}$ traction (stress) vectors representing the force exerted on the surfaces of the cut parts $\partial\mathcal{P}_\mathcal{B}$ and $\partial\mathcal{P}_\mathcal{S}$, by the rest of the body in the neighborhood, respectively.

now characterize the traction vectors as physical objects. Focusing on purely mechanical problems, let us now consider an extracted part of the body $\mathcal{P}_\mathcal{B} \subset \mathcal{B}$ and $\mathcal{P}_\mathcal{S} \subset \mathcal{S}$ with the inner boundaries $\partial\mathcal{P}_\mathcal{B}$ and $\partial\mathcal{P}_\mathcal{S}$, respectively, see Fig. 1.9. The vector $\boldsymbol{t} \in T_x\mathcal{S}$ is defined to be the true traction vector acting on the deformed surface $\mathrm{d}a$ of $\partial\mathcal{P}_\mathcal{S}$ which represents the force exerted on the cut out part $\partial\mathcal{P}_\mathcal{S}$ by the rest of the body in the neighborhood $\mathcal{P}_\mathcal{S}\backslash\mathcal{S}$. The Cauchy stress theorem postulates

$$\boldsymbol{t}(\boldsymbol{x}, t; \boldsymbol{n}) := \boldsymbol{\sigma}(\boldsymbol{x}, t)\boldsymbol{n} \quad \text{with} \quad t^a = \sigma^{ab} n_b, \tag{1.14}$$

where the spatial traction vector $\boldsymbol{t} \in T_x\mathcal{S}$ and the spatial normal vector $\boldsymbol{n} \in T_x^*\mathcal{S}$ of the surface $\partial\mathcal{P}_\mathcal{S}$ are related through the Cauchy (true) stress tensor $\boldsymbol{\sigma}$ that can be readily proven by a static equilibrium of tractions acting on four planes of a tetrahedron. The Cauchy stress tensor relates the actual force to the actual deformed area. Upon weighting $\boldsymbol{\sigma}$ by the Jacobian J, we obtain the so-called Kirchhoff stress tensor, i.e.

$$\boldsymbol{\tau} := J\boldsymbol{\sigma}, \tag{1.15}$$

which preserves the geometrical properties of the Cauchy stress tensor $\boldsymbol{\sigma}$. Let us now define another spatial traction vector $\boldsymbol{T} \in T_x\mathcal{S}$ coaxial with the $\boldsymbol{t} \in T_x\mathcal{S}$ that relates the current force to the reference area through the force equality,

$$\boldsymbol{T}\mathrm{d}A = \boldsymbol{t}\mathrm{d}a. \tag{1.16}$$

Next, we introduce the first Piola-Kirchhoff stress tensor with the property

$$\boldsymbol{T}(\boldsymbol{X}, t; \boldsymbol{N}) := \boldsymbol{P}(\boldsymbol{X}, t)\boldsymbol{N}, \quad T^a = P^{aB} N_B. \tag{1.17}$$

By inserting (1.7), (1.14) and (1.17) into (1.16), we arrive at the following relation

$$\boldsymbol{P} = J\boldsymbol{\sigma}\boldsymbol{F}^{-\mathrm{T}} = \boldsymbol{\tau}\boldsymbol{F}^{-\mathrm{T}}, \tag{1.18}$$

where the Piola transformation, i.e. $(\blacksquare) = J(\bullet)\boldsymbol{F}^{-\mathrm{T}}$ is exploited. Such a transformation results in the Piola identity

$$J\mathrm{div}(\bullet) = \mathrm{DIV}(\blacksquare) = \mathrm{DIV}(J(\bullet)\boldsymbol{F}^{-\mathrm{T}}), \tag{1.19}$$

implying $\mathrm{DIV}(J\boldsymbol{F}^{-\mathrm{T}}) = \boldsymbol{0}$ and $\mathrm{div}(J\boldsymbol{F}^{\mathrm{T}}) = \boldsymbol{0}$, as well. The identities can be readily obtained by applying the Gauss integral theorem on the spatial surface integral of the traction $\boldsymbol{t}$ using the area map in (1.7). The pull-back operation on the spatial traction vectors $\boldsymbol{T} \in T_x\mathcal{S}$ yields material traction vectors $\tilde{\boldsymbol{T}} \in T_X\mathcal{B}$ such that

$$\tilde{\boldsymbol{T}} = \boldsymbol{\varphi}^*(\boldsymbol{T}) = \boldsymbol{F}^{-1}\boldsymbol{T}, \quad \tilde{T}^A = (F^{-1})^A_a T^a. \tag{1.20}$$

The relation between material traction vector $\tilde{\boldsymbol{T}}$ and material normal vector $\boldsymbol{N}$ is established by the second Piola-Kirchhoff stress tensor $\boldsymbol{S}$ that reads

$$\tilde{\boldsymbol{T}}(\boldsymbol{X}, t; \boldsymbol{N}) = \boldsymbol{S}(\boldsymbol{X}, t)\boldsymbol{N}. \tag{1.21}$$

Now, the different measures of stress with the help of their mapping properties can be related to one another, as summarized in Fig. 1.10, from which the pull-back relations are identified as follows

$$\begin{aligned} \boldsymbol{S} &:= \boldsymbol{F}^{-1}\boldsymbol{P}, & S^{AB} &= (F^{-1})^A_a P^{aB}, \\ \boldsymbol{S} &:= \boldsymbol{F}^{-1}\boldsymbol{\tau}\boldsymbol{F}^{-\mathrm{T}}, & S^{AB} &= (F^{-1})^A_a \tau^{ab} (F^{-1})^B_b, \end{aligned} \tag{1.22}$$

which is followed by the push-forward relations, i.e.

$$\begin{aligned} \boldsymbol{\tau} &:= \boldsymbol{P}\boldsymbol{F}^{\mathrm{T}}, & \tau^{ab} &= P^{aB}(F^{\mathrm{T}})^b_B, \\ \boldsymbol{\tau} &:= \boldsymbol{F}\boldsymbol{S}\boldsymbol{F}^{\mathrm{T}}, & \tau^{ab} &= F^a_A S^{AB} F^b_B. \end{aligned} \tag{1.23}$$

1.5.3 Stress power and dual variables

With the deformation and stress definitions at hand, we now proceed to the descriptions of the stress power per unit volume $\mathcal{P}$. Beginning with the most fundamental definition we first state that

$$\mathcal{P} := (\boldsymbol{g}\boldsymbol{P}) : \dot{\boldsymbol{F}} \quad \text{with} \quad \mathcal{P} = g_{ab} P^{bA} \dot{F}^a_A, \tag{1.24}$$

which is characterized by the two-point setting of the constitutive equation based on the dual variables $\boldsymbol{P}$ and $\boldsymbol{F}$. Alternatively, the representation of stress power can be expressed in terms of a fully Lagrangian (reference) setting, i.e.

$$\mathcal{P} := \boldsymbol{S} : \frac{1}{2}\dot{\boldsymbol{C}} = \boldsymbol{S} : \dot{\boldsymbol{E}} \quad \text{with} \quad \mathcal{P} = S^{AB}\dot{E}_{AB}, \tag{1.25}$$

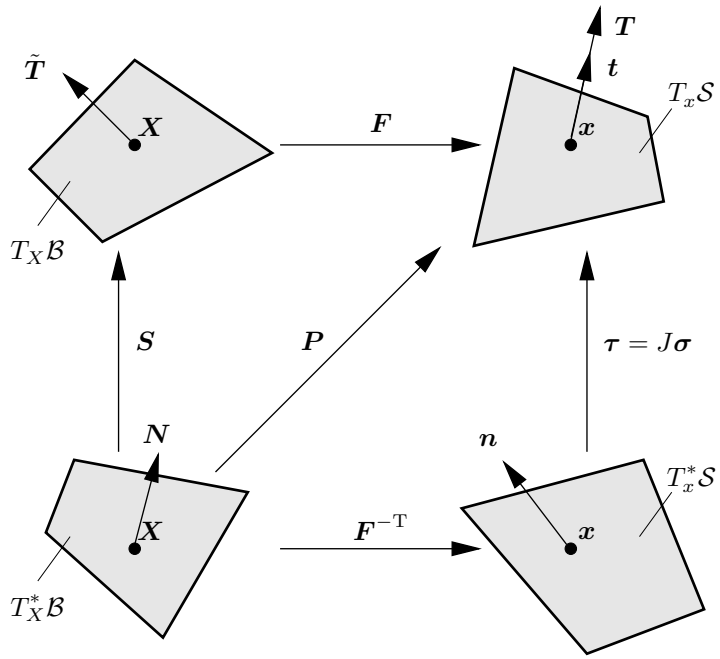

Figure 1.10 The push-forward and pull-back operations on stress measures corresponding to their covariant and contravariant representations.

where the second Piola-Kirchhoff tensor $\boldsymbol{S}$ and the right Cauchy Green tensor $\boldsymbol{C}$ are said to be dual objects. The rate of $\boldsymbol{C}$ can also be formulated in terms of the Green strain rate tensor $\dot{\boldsymbol{E}}$. The push-forward of (1.25) results in the Eulerian (spatial) setting,

$$\mathcal{P} := \boldsymbol{\tau} : \boldsymbol{\pounds}_{\boldsymbol{v}}\boldsymbol{e} = \boldsymbol{\tau} : \frac{1}{2}\boldsymbol{\pounds}_{\boldsymbol{v}}\boldsymbol{g} = \boldsymbol{\tau} : \boldsymbol{d} \quad \text{with} \quad \mathcal{P} = \tau^{ab} d_{ab} \tag{1.26}$$

describing the Kirchhoff stress tensor $\boldsymbol{\tau}$ as a dual quantity to Eulerian metric $\boldsymbol{g}$. Furthermore, we may introduce the Green and Almansian strain tensors by

$$\begin{aligned} \boldsymbol{E} &:= \frac{1}{2}(\boldsymbol{C} - \boldsymbol{G}), \qquad & E_{AB} &= \frac{1}{2}(C_{AB} - G_{AB}), \\ \boldsymbol{e} &:= \frac{1}{2}(\boldsymbol{g} - \boldsymbol{c}), & e_{ab} &= \frac{1}{2}(g_{ab} - c_{ab}). \end{aligned} \tag{1.27}$$

In (1.26) the introduced Lie-derivative $\boldsymbol{\pounds}_{\boldsymbol{v}}$ defines the objective (Oldroyd–type) rates of the Eulerian tensor fields in three steps, i.e.

$$\boldsymbol{\pounds}_{\boldsymbol{v}}(\bullet) := \boldsymbol{\varphi}_*[\frac{\mathrm{d}}{\mathrm{d}t}\boldsymbol{\varphi}^*(\bullet)]. \tag{1.28}$$

In the first step, the Eulerian object is brought to the time–invariant Lagrangian setting via a pull-back operation. Then, the material time derivative is computed over the Lagrangian object. Finally, the resulting quantity is pushed forward to the Eulerian configuration. As

an example, the application of the Lie-derivative to the current metric $\boldsymbol{g}$ yields the rate of deformation tensor $\boldsymbol{d}$ as follows

$$\boldsymbol{\pounds}_{\boldsymbol{v}}\boldsymbol{g} := \boldsymbol{F}^{-\mathrm{T}}\frac{\mathrm{d}}{\mathrm{d}t}(\boldsymbol{F}^{\mathrm{T}}\boldsymbol{g}\boldsymbol{F})\boldsymbol{F}^{-1} = \boldsymbol{g}\boldsymbol{l} + \boldsymbol{l}^{\mathrm{T}}\boldsymbol{g} = 2\,\mathrm{sym}(\boldsymbol{g}\boldsymbol{l}) = 2\boldsymbol{d}, \tag{1.29}$$

where $\boldsymbol{l}$ denotes the spatial velocity gradient with the definition $\boldsymbol{l} := \nabla_x \boldsymbol{v} = \dot{\boldsymbol{F}}\boldsymbol{F}^{-1}$. Finally, the equality of the three different description of the stress power $\mathcal{P}$ can be shown as follows,

$$\begin{aligned}
\mathcal{P} &:= \boldsymbol{\tau} : \boldsymbol{d} = \boldsymbol{\tau} : \mathrm{sym}(\boldsymbol{g}\boldsymbol{l}) = \boldsymbol{P}\boldsymbol{F}^{\mathrm{T}} : \boldsymbol{g}\dot{\boldsymbol{F}}\boldsymbol{F}^{-1} = \boldsymbol{g}\boldsymbol{P} : \dot{\boldsymbol{F}}, \\
\mathcal{P} &:= \boldsymbol{\tau} : \boldsymbol{d} = \boldsymbol{\tau} : \frac{1}{2}\boldsymbol{\pounds}_{\boldsymbol{v}}(\boldsymbol{g}) = \boldsymbol{F}\boldsymbol{S}\boldsymbol{F}^{\mathrm{T}} : \frac{1}{2}\boldsymbol{F}^{-\mathrm{T}}\dot{\boldsymbol{C}}\boldsymbol{F}^{-1} = \boldsymbol{S} : \frac{1}{2}\dot{\boldsymbol{C}}.
\end{aligned} \tag{1.30}$$

1.5.4 Balance laws

The fundamental balance laws listed as the balance of mass, momentum and angular momentum along with the first and second law of thermodynamics are the basic axioms of thermomechanics for the primary field variables which are valid for all continuous bodies independent of the material response, i.e. constitutive laws. Let a certain special volume $\mathcal{P}_{\mathcal{S}}$ be enclosed by a smooth boundary $\partial\mathcal{P}_{\mathcal{S}}$, as shown in Fig. 1.9, for which the balance relations are established via the volumetric source and the surface flux terms yielding a temporal change of the quantity under consideration.

1.5.4.1 Reynold's transport theorem

Let us assume a continuously differentiable spatial scalar field $\phi(\boldsymbol{x}, t)$ in the part of the body $\mathcal{P}_{\mathcal{S}}$. The Reynolds' transport theorem is obtained through total time derivative of a volume integral of ϕ as

$$\begin{aligned}
\frac{\mathrm{d}}{\mathrm{d}t}\int\limits_{\mathcal{P}_{\mathcal{S}}} \phi(\boldsymbol{x}, t)\mathrm{d}v &= \int\limits_{\mathcal{P}_{\mathcal{B}}} \left[\frac{\mathrm{d}\phi(\boldsymbol{x}, t)}{\mathrm{d}t}J + \phi(\boldsymbol{x}, t)\frac{\mathrm{d}J}{\mathrm{d}t}\right]\mathrm{d}V \\
&= \int\limits_{\mathcal{P}_{\mathcal{S}}} \left[\dot{\phi} + \phi(\boldsymbol{x}, t)\,\mathrm{div}\,\boldsymbol{v}\right]\mathrm{d}v
\end{aligned} \tag{1.31}$$

with the identity, i.e. $\dot{J} := \mathrm{d}J/\mathrm{d}t = \mathrm{cof}\,\boldsymbol{F} : \dot{\boldsymbol{F}} = J\,\mathrm{tr}\,\boldsymbol{l} = J\,\mathrm{div}\,\boldsymbol{v}$. Then, the material time derivative of $\phi(\boldsymbol{x}, t)$ akin to $(1.3)_2$ recasts (1.31) into

$$\begin{aligned}
\frac{\mathrm{d}}{\mathrm{d}t}\int\limits_{\mathcal{P}_{\mathcal{S}}} \phi(\boldsymbol{x}, t)\mathrm{d}v &= \int\limits_{\mathcal{P}_{\mathcal{S}}} \left[\partial_t\phi + \nabla_{\boldsymbol{x}}\phi \cdot \boldsymbol{v} + \phi\,\mathrm{div}\,\boldsymbol{v}\right]\mathrm{d}v \\
&= \int\limits_{\mathcal{P}_{\mathcal{S}}} \left[\partial_t\phi + \mathrm{div}(\phi\boldsymbol{v})\right]\mathrm{d}v.
\end{aligned} \tag{1.32}$$

The Reynolds' transport theorem can further be elaborated upon the Gauss integral theorem applied on the right–hand side of (1.32) as follows

$$\frac{\mathrm{d}}{\mathrm{d}t}\int\limits_{\mathcal{P}_\mathcal{S}} \phi(\boldsymbol{x},t)\mathrm{d}v = \int\limits_{\mathcal{P}_\mathcal{S}} \partial_t\phi \mathrm{d}v + \int\limits_{\partial\mathcal{P}_\mathcal{S}} \phi\boldsymbol{v}\cdot\boldsymbol{n}\mathrm{d}a. \tag{1.33}$$

The first term on the right–hand side of (1.33) describes the temporal evolution of the scalar field ϕ in $\mathcal{P}_\mathcal{S}$, while the second term characterizes the surface flux of $\phi\boldsymbol{v}$ with the unit outward normal vector $\boldsymbol{n}$ across the boundary $\partial\mathcal{P}_\mathcal{S}$.

1.5.4.2 Balance of mass

The total mass of the part of the solid $\mathcal{P}_\mathcal{S}$ remains constant, i.e. the mass can be neither produced nor destroyed inside $\mathcal{P}_\mathcal{S}$. In addition, the mass flux transferring the mass over the surface $\partial\mathcal{P}_\mathcal{S}$ is not permitted. With the introduction of the spatial mass density $\rho(\boldsymbol{x},t)$ and its material counterpart, i.e. the reference mass density $\rho_0(\boldsymbol{X})$, the conservation of mass requires

$$\frac{\mathrm{d}}{\mathrm{d}t}\mathcal{M} := \frac{\mathrm{d}}{\mathrm{d}t}\int\limits_{\mathcal{P}_\mathcal{S}} \rho(\boldsymbol{x},t)\,\mathrm{d}v = \frac{\mathrm{d}}{\mathrm{d}t}\int\limits_{\mathcal{P}_\mathcal{B}} J\rho(\boldsymbol{x},t)\,\mathrm{d}V = \frac{\mathrm{d}}{\mathrm{d}t}\int\limits_{\mathcal{P}_\mathcal{B}} \rho_0(\boldsymbol{X},t)\,\mathrm{d}V = 0. \tag{1.34}$$

The integrand must also fulfill the equality for an infinitesimal part, where $\lim \mathcal{P}_\mathcal{S} \to \mathrm{d}v$, which states the local mass balance equations

$$\dot{\rho} + \rho\,\mathrm{div}\,\boldsymbol{v} = 0 \quad \text{and} \quad J\rho(\boldsymbol{x},t) = \rho_0(\boldsymbol{X},t), \tag{1.35}$$

where we make use of the Reynolds' transport theorem (1.31) and substitute $\rho(\boldsymbol{x},t)$ for $\phi(\boldsymbol{x},t)$.

1.5.4.3 Balance of linear momentum

The time evolution of the linear momentum $\mathcal{I}$ of the part $\mathcal{P}_\mathcal{S}$ is equal to the sum of all the forces acting on the body which are the actions from a distance in $\mathcal{P}_\mathcal{S}$ and at the vicinity on $\partial\mathcal{P}_\mathcal{S}$ accounted by the mass specific body force $\boldsymbol{\gamma}(\boldsymbol{x},t)$ and surface traction vector $\boldsymbol{t}$, respectively, i.e.

$$\frac{\mathrm{d}}{\mathrm{d}t}\mathcal{I} := \frac{\mathrm{d}}{\mathrm{d}t}\int\limits_{\mathcal{P}_\mathcal{S}} \rho\boldsymbol{v}(\boldsymbol{x},t)\,\mathrm{d}v = \int\limits_{\mathcal{P}_\mathcal{S}} \rho\boldsymbol{\gamma}(\boldsymbol{x},t)\,\mathrm{d}v + \int\limits_{\partial\mathcal{P}_\mathcal{S}} \boldsymbol{t}(\boldsymbol{x},t;\boldsymbol{n})\,\mathrm{d}a. \tag{1.36}$$

Inserting the mass balance $(1.35)_1$ into (1.36), the Cauchy stress theorem and Gaussian integral theorem on the surface term yield the local form of the spatial linear momentum balance

$$\rho\dot{\boldsymbol{v}} = \rho\boldsymbol{\gamma} + \mathrm{div}\,\boldsymbol{\sigma}. \tag{1.37}$$

The material form of the local linear momentum balance reads

$$\rho_0\dot{\boldsymbol{V}} = \rho_0\boldsymbol{\gamma}_0 + \mathrm{Div}\,\boldsymbol{P}, \tag{1.38}$$

where $\boldsymbol{\gamma}_0(\boldsymbol{X},t) := \boldsymbol{\gamma}(\boldsymbol{x},t)\circ\boldsymbol{\varphi}_t(\boldsymbol{X})$ denotes the material body force given per unit mass.

1.5.4.4 Balance of angular momentum

The resultant moment acting on the part of the body $\mathcal{P}_\mathcal{S}$ must be equal to the temporal change of the angular momentum which can be formulated as

$$\frac{\mathrm{d}}{\mathrm{d}t}\int\limits_{\partial\mathcal{P}_\mathcal{S}} \boldsymbol{x}\times\rho\boldsymbol{v}\,\mathrm{d}v = \int\limits_{\partial\mathcal{P}_\mathcal{S}} \boldsymbol{x}\times\rho\boldsymbol{\gamma}\,\mathrm{d}v + \int\limits_{\partial\mathcal{P}_\mathcal{S}} \boldsymbol{x}\times\boldsymbol{t}\,\mathrm{d}a. \tag{1.39}$$

The insertion of mass balance (1.35) in conjunction with the Cauchy stress and Gaussian integral theorem leads to

$$\int\limits_{\partial\mathcal{P}_\mathcal{S}} \boldsymbol{x}\times(\rho\dot{\boldsymbol{v}} - \rho\boldsymbol{\gamma} - \operatorname{div}\boldsymbol{\sigma})\,\mathrm{d}v = \boldsymbol{0}. \tag{1.40}$$

The above equality can only be satisfied for the Cauchy stress tensor to be symmetric. Thus, the balance of angular momentum results in

$$\boldsymbol{\sigma} = \boldsymbol{\sigma}^{\mathrm{T}} \quad . \tag{1.41}$$

Observing the other stress measures, e.g., $\boldsymbol{\tau}$ and $\boldsymbol{S}$, since they are obtained through push-forward and pull-back relations, these measures also need to satisfy the symmetry relation except the first Piola-Kirchhoff stress $\boldsymbol{P}$ being generally a non-symmetric tensor, i.e.

$$\boldsymbol{\tau} = \boldsymbol{\tau}^{\mathrm{T}}, \qquad \boldsymbol{P}\boldsymbol{F}^{\mathrm{T}} = \boldsymbol{F}\boldsymbol{P}^{\mathrm{T}}, \qquad \boldsymbol{S} = \boldsymbol{S}^{\mathrm{T}}. \tag{1.42}$$

1.5.4.5 First law of thermodynamics

The first law of thermodynamics postulates the change of total energy in the body with respect to time is equal to the sum of the mechanical and thermal power, i.e.

$$\frac{\mathrm{d}}{\mathrm{d}t}(\mathcal{K}+E) = \mathcal{P}+\mathcal{Q}, \tag{1.43}$$

where the sum of the time evolution of the kinetic energy

$$\mathcal{K} := \int\limits_{\mathcal{P}_\mathcal{S}} \frac{1}{2}\,\rho\boldsymbol{v}\cdot\boldsymbol{v}^\flat\,\mathrm{d}v \tag{1.44}$$

and the internal energy

$$E := \int\limits_{\mathcal{P}_\mathcal{S}} \rho e\,\mathrm{d}v \tag{1.45}$$

is in equilibrium with that of the mechanical power

$$\mathcal{P} := \int\limits_{\mathcal{P}_\mathcal{S}} \rho\boldsymbol{\gamma}\cdot\boldsymbol{v}^\flat\,\mathrm{d}v + \int\limits_{\partial\mathcal{P}_\mathcal{S}} \boldsymbol{t}\cdot\boldsymbol{v}^\flat\,\mathrm{d}a, \tag{1.46}$$

and the thermal power defined as follows

$$\mathcal{Q} := \int_{\mathcal{P}_\mathcal{S}} \rho r \, \mathrm{d}v - \int_{\partial\mathcal{P}_\mathcal{S}} \boldsymbol{q} \cdot \boldsymbol{n} \, \mathrm{d}a. \tag{1.47}$$

The above–stated equations (1.44)–(1.47) contain the spatial velocity covector $\boldsymbol{v}^\flat = \boldsymbol{g}\boldsymbol{v}$, the internal energy per unit mass $e(\boldsymbol{x}, t)$, the mass specific heat source $r(\boldsymbol{x}, t)$ and the surface heat flux vector $\boldsymbol{q}(\boldsymbol{x}, t)$ together with the unit outward normal $\boldsymbol{n}$. Utilizing the previous relations, namely the balance of mass (1.35) and the linear momentum (1.37), in conjunction with the Cauchy stress and Gaussian integral theorem, the spatial local form is obtained, i.e.

$$\rho\dot{e} = \boldsymbol{\sigma} : (\boldsymbol{g}\boldsymbol{l}) + \rho r + \operatorname{div} \boldsymbol{q}. \tag{1.48}$$

The material local form of (1.48) is derived through the introduction of the reference heat flux vector $\boldsymbol{Q}$ fulfilling the equality $\boldsymbol{q} \cdot \boldsymbol{n}\mathrm{d}a = \boldsymbol{Q} \cdot \boldsymbol{N}\mathrm{d}A$ with the aid of the area map $\boldsymbol{Q} := J\boldsymbol{q}\boldsymbol{F}^{-\mathrm{T}}$. Therefore, the equality $J \operatorname{div} \boldsymbol{q} = \operatorname{Div}(\boldsymbol{Q})$ is identically met for the material local form which reads

$$\rho_0\dot{e} = \boldsymbol{S} : \frac{1}{2}\dot{\boldsymbol{C}} + \rho_0 R - \operatorname{Div}(\boldsymbol{Q}), \tag{1.49}$$

where we define $R(\boldsymbol{X}, t) = r(\boldsymbol{x}, t) \circ \boldsymbol{\varphi}_t(\boldsymbol{X})$.

1.5.4.6 Second law of thermodynamics

The second law of thermodynamics is an inequality which serves as an essential mathematical restriction on the constitutive relations governing the heat conduction and the evolution of internal variables that describe a dissipative mechanism in the body. Power expenditures represent a macroscopic energy transfer as they are understood as the velocity of material points. As an addition, heat represents another way of energy transfer due to the fluctuations in atoms and/or molecules leading to disorder in the system. Entropy is none other than a measure of this disorder. For the part of the body $\mathcal{P}_\mathcal{S}$ concerned, we define the total entropy $\boldsymbol{\mathcal{H}}$ by integrating the specific entropy $\eta(\boldsymbol{x}, t)$ over the volume, i.e.

$$\boldsymbol{\mathcal{H}} := \int_{\mathcal{P}_\mathcal{S}} \rho\eta \mathrm{d}v. \tag{1.50}$$

The temporal change of the entropy can be reversible or irreversible. External sources cause the reversible change of the entropy while the irreversible changes arise from the dissipative processes such as plastic deformation, damage, etc. The basic premise of the second law is that systems tend to increase their degree of disorder which generates a net entropy production that is always non-negative for which we define a mass specific form $\gamma(\boldsymbol{x}, t)$. The integration of $\gamma(\boldsymbol{x}, t)$ over the volume yields the total entropy production

$$\boldsymbol{\Gamma} := \int_{\mathcal{P}_\mathcal{S}} \rho\gamma \mathrm{d}v \geq 0. \tag{1.51}$$

Furthermore, we suppose that similar to the heat flow, the entropy also flows at a rate given by

$$\boldsymbol{\mathcal{S}} := \int\limits_{\mathcal{P}_\mathcal{S}} \frac{\rho r}{\theta} \mathrm{d}v - \int\limits_{\partial\mathcal{P}_\mathcal{S}} \frac{\boldsymbol{q}\cdot\boldsymbol{n}}{\theta} \mathrm{d}a. \tag{1.52}$$

With the definitions (1.50)–(1.52), we write the entropy imbalance as

$$\boldsymbol{\Gamma} := \frac{\mathrm{d}}{\mathrm{d}t}\boldsymbol{\mathcal{H}} - \boldsymbol{\mathcal{S}} \geq 0, \tag{1.53}$$

which can be elaborated as

$$\int\limits_{\mathcal{P}_\mathcal{S}} \rho\gamma \mathrm{d}v := \frac{\mathrm{d}}{\mathrm{d}t}\int\limits_{\mathcal{P}_\mathcal{S}} \rho\eta \mathrm{d}v - \int\limits_{\mathcal{P}_\mathcal{S}} \frac{\rho r}{\theta}\mathrm{d}v + \int\limits_{\partial\mathcal{P}_\mathcal{S}} \frac{\boldsymbol{q}\cdot\boldsymbol{n}}{\theta}\mathrm{d}a \geq 0, \tag{1.54}$$

where θ stands for the absolute temperature, i.e. $\theta > 0$. From (1.54) we arrive at the spatial local form of the entropy imbalance, i.e.

$$\rho\gamma = \rho\dot{\eta} - \rho\frac{r}{\theta} + \operatorname{div}\left(\frac{\boldsymbol{q}}{\theta}\right) = \rho\dot{\eta} - \rho\frac{r}{\theta} + \frac{1}{\theta}\operatorname{div}\boldsymbol{q} - \frac{1}{\theta^2}\boldsymbol{q}\cdot\nabla_{\boldsymbol{x}}\theta \ \geq 0 \tag{1.55}$$

by making use of the conventional steps. The above inequality can also be rewritten in the form of Clausius-Duhem inequality

$$\rho\dot{\eta} \geq \rho\frac{r}{\theta} - \frac{1}{\theta}\operatorname{div}\boldsymbol{q} + \frac{1}{\theta^2}\boldsymbol{q}\cdot\nabla_{\boldsymbol{x}}\theta, \tag{1.56}$$

for which the material local form reads

$$\rho_0\dot{\eta} \geq \rho_0\frac{R}{\theta} - \frac{1}{\theta}\operatorname{Div}\boldsymbol{Q} + \frac{1}{\theta^2}\boldsymbol{Q}\cdot\nabla_X\theta. \tag{1.57}$$

1.5.4.7 Dissipation and thermomechanics

The entropy production in (1.55) with the absolute temperature θ results in the spatial dissipation

$$\mathcal{D} := \rho\gamma\theta \geq 0, \tag{1.58}$$

composed of two separate contributions, namely local and conductive parts, i.e. $\mathcal{D} = \mathcal{D}_{\mathrm{loc}} + \mathcal{D}_{\mathrm{con}}$. Next, we introduce the Clausius-Planck inequality

$$\mathcal{D}_{\mathrm{loc}} := \rho\dot{\eta}\theta - (\rho r - \operatorname{div}\boldsymbol{q}) \ \geq 0, \tag{1.59}$$

and the heat conduction inequality

$$\mathcal{D}_{\mathrm{con}} := -\frac{1}{\theta}\boldsymbol{q}\cdot\nabla_{\boldsymbol{x}}\theta = -\frac{1}{\theta}\boldsymbol{Q}\cdot\nabla_{\boldsymbol{X}}\theta \ \geq 0, \tag{1.60}$$

which stipulates the non-negativeness in a more strict sense as compared with (1.55). The local part of the Clausius–Planck inequality (1.59) along with the spatial energy balance (1.48) leads to

$$\mathcal{D}_{\text{loc}} := \rho\dot{\eta}\theta - \rho\dot{e} + \boldsymbol{\sigma} : (\boldsymbol{gl}) \ \geq 0. \tag{1.61}$$

The material description of the above expression is obtained after multiplying (1.61) with the Jacobian J and redefining the quantities $\theta\eta \leftarrow \rho_0\theta\eta$ and $e \leftarrow \rho_0 e$, i.e.

$$J\mathcal{D}_{\text{loc}} := \dot{\eta}\theta + \dot{e} + \boldsymbol{gP} : \dot{\boldsymbol{F}}. \tag{1.62}$$

The thermomechanical potentials encountered in thermomechanics are generally dependent on a set of variables in terms of stress, strain, entropy and absolute temperature. In the case of inelastic materials, however, internal variables which are extensively used in the constitutive formulation of dissipative materials need to be incorporated into this set. Internal variables might be observable whereas cannot be externally controlled. The thermodynamical forces $\{\boldsymbol{\mathcal{F}}\}$ conjugate to internal variables set $\{\boldsymbol{\mathcal{I}}\}$ generally do not explicitly appear until we formulate the energy balance equation.

Let us now briefly touch upon the four basic thermomechanical potentials: the first one is the internal energy e which depends on the deformation gradient $\boldsymbol{F}$ and the entropy η such that $e = \hat{e}(\boldsymbol{F}, \eta, ...)$; the second is the Helmholtz free energy $\Psi = \hat{\Psi}(\boldsymbol{F}, \theta, ...) := e - \theta\eta$; the third is the Gibbs free energy $g = \hat{g}(\boldsymbol{gP}, \theta, ...) := \Psi - \boldsymbol{gP} : \boldsymbol{F}$, and finally the enthalpy $h = \hat{h}(\boldsymbol{gP}, \eta, ...) := e - \boldsymbol{gP} : \boldsymbol{F}$. Following the common practice in solid mechanics, we stick to the Helmholtz free energy. Inserting $\Psi := e - \theta\eta$ into equation (1.62) we end up with

$$J\mathcal{D}_{\text{loc}} := \boldsymbol{gP} : \dot{\boldsymbol{F}} - \dot{\Psi} - \eta\dot{\theta} \geq 0. \tag{1.63}$$

Focusing on a local dissipative theory of the grade–1, where only first gradients are considered, the problem of thermoinelasicity for a homogeneous material is contingent on the internal variables. Referring to the principle of equipresence the free energy Ψ depends upon the same set of field variables as, e.g., the stress tensor, heat flux vector, internal energy and the entropy, i.e.

$$\Psi = \hat{\Psi}(\boldsymbol{g}; \boldsymbol{F}, \theta, \mathcal{G}, \boldsymbol{\mathcal{I}}), \tag{1.64}$$

where $\mathcal{G} := \nabla_X \theta$ is the temperature gradient as being a vector variable. By inserting the time derivative of the free energy $\dot{\Psi} = \partial_{\boldsymbol{F}}\Psi : \dot{\boldsymbol{F}} + \partial_\theta\Psi : \dot{\theta} + \partial_{\mathcal{G}}\Psi \cdot \dot{\mathcal{G}} + \partial_{\boldsymbol{\mathcal{I}}}\Psi : \dot{\boldsymbol{\mathcal{I}}}$ in the Clausius-Planck inequality, we rewrite (1.63) as

$$J\mathcal{D}_{\text{loc}} := (\boldsymbol{gP} - \partial_{\boldsymbol{F}}\Psi) : \dot{\boldsymbol{F}} - (\eta + \partial_\theta\Psi) : \dot{\theta} - \partial_{\mathcal{G}}\Psi \cdot \dot{\mathcal{G}} - \partial_{\boldsymbol{\mathcal{I}}}\Psi : \dot{\boldsymbol{\mathcal{I}}} \ \geq 0. \tag{1.65}$$

Coleman's method contends that the above thermodynamic restriction should be fulfilled for an arbitrary rate of deformation gradient, temperature and temperature gradient; therefore

$$\boldsymbol{gP} := \partial_{\boldsymbol{F}}\Psi, \quad \eta := -\partial_\theta\Psi \quad \text{and} \quad \partial_{\mathcal{G}}\Psi = \boldsymbol{0}. \tag{1.66}$$

The equation (1.66) states that free energy does not depend on the temperature gradient $\mathcal{G}$, i.e. $\Psi = \hat{\Psi}(\boldsymbol{g}; \boldsymbol{F}, \theta, \boldsymbol{\mathcal{I}})$, and postulates the constitutive relations for stresses and entropy.

Subsequently, the reduced form of the Clausius Planck inequality reads

$$J\mathcal{D}_{\text{loc}} := \boldsymbol{\mathcal{F}} : \dot{\boldsymbol{\mathcal{I}}} \geq 0 \quad \text{with} \quad \boldsymbol{\mathcal{F}} := -\partial_{\boldsymbol{\mathcal{I}}}\Psi. \tag{1.67}$$

In the remainder of the investigation, we pursue an entirely thermoelastic formulation with vanishing local dissipations. The free energy must satisfy the principle of material objectivity, saying that the free energy must be invariant for rigid body rotations superimposed on the current configuration. Therefore, we locally require $\Psi(\boldsymbol{g}; \boldsymbol{F}, \theta) = \Psi(\tilde{\boldsymbol{g}}; \tilde{\boldsymbol{F}}, \theta)$, where $\tilde{\boldsymbol{F}} := \boldsymbol{Q}_*(\boldsymbol{F}) := \boldsymbol{Q}\boldsymbol{F}$ and $\tilde{\boldsymbol{g}} := \boldsymbol{Q}_*(\boldsymbol{g}) := \boldsymbol{Q}^{-\mathrm{T}}\boldsymbol{g}\boldsymbol{Q}^{-1}$ for all $\boldsymbol{Q} \in \mathcal{O}(3)$, the proper orthogonal group. The right Cauchy-Green tensor $\boldsymbol{C}$ *a priori* satisfies the condition

$$\boldsymbol{C} := \boldsymbol{F}^T\boldsymbol{g}\boldsymbol{F} = \tilde{\boldsymbol{F}}^{\mathrm{T}}\tilde{\boldsymbol{g}}\tilde{\boldsymbol{F}}. \tag{1.68}$$

Therefore, the free–energy function assumes a reduced form

$$\hat{\Psi}(\boldsymbol{C}, \theta) = \Psi(\boldsymbol{F}^{\mathrm{T}}\boldsymbol{g}\boldsymbol{F}, \theta). \tag{1.69}$$

Accordingly, one can rewrite the term $(\boldsymbol{g}\boldsymbol{P} - \partial_{\boldsymbol{F}}\Psi) : \dot{\boldsymbol{F}}$ in $(1.66)_1$ as $(\boldsymbol{S} - 2\partial_{\boldsymbol{C}}\hat{\Psi}) : \frac{1}{2}\dot{\boldsymbol{C}}$ and express the functional definition of the second Piola-Kirchhoff stress tensor in the following form

$$\boldsymbol{S} = 2\partial_{\boldsymbol{C}}\hat{\Psi}(\boldsymbol{C}, \theta). \tag{1.70}$$

By using equalities stated in (1.23) and (1.30), we further obtain

$$(\boldsymbol{S} - 2\partial_{\boldsymbol{C}}\hat{\Psi}) : \frac{1}{2}\dot{\boldsymbol{C}} = \boldsymbol{\tau} : \frac{1}{2}\boldsymbol{\pounds}_{\boldsymbol{v}}\boldsymbol{g} - 2\partial_{\boldsymbol{C}}\Psi : \frac{1}{2}\boldsymbol{F}^{\mathrm{T}}\boldsymbol{\pounds}_{\boldsymbol{v}}\boldsymbol{g}\boldsymbol{F} = (\boldsymbol{\tau} - 2\boldsymbol{F}\partial_{\boldsymbol{C}}\Psi\boldsymbol{F}^{\mathrm{T}}) : \frac{1}{2}\boldsymbol{\pounds}_{\boldsymbol{v}}\boldsymbol{g}. \tag{1.71}$$

Such an equality further leads us to the Doyle & Ericksen [42] formula

$$\boldsymbol{\tau} = 2\partial_{\boldsymbol{g}}\Psi(\boldsymbol{g}; \boldsymbol{F}, \theta), \tag{1.72}$$

where the equality $2\boldsymbol{F}\partial_{\boldsymbol{C}}\Psi\boldsymbol{F}^{\mathrm{T}} = 2\partial_{\boldsymbol{g}}\Psi(\boldsymbol{g}; \boldsymbol{F}, \theta)$ can be proven by a chain rule, see Marsden & Hughes [128]. Finally, the Eulerian form of the elasticity tensor is given as

$$\mathbb{c} = 4\partial^2_{\boldsymbol{g}\boldsymbol{g}}\Psi(\boldsymbol{g}; \boldsymbol{F}, \theta). \tag{1.73}$$

1.6 Fracture Mechanics

Fracture mechanics deals with not only the failure of engineering materials, such as metals, concrete, polymers, etc., but it is also pertinent to the rupture of biological tissues, e.g., bones, tendons, arterial walls, etc. In contrast to the approach of material strength, the determinant material properties in fracture mechanics are flaw size and the fracture toughness. From an atomic viewpoint, the fracture takes place when the applied stress is sufficient to break the bonds, i.e. the attractive forces that hold the atoms together. The theoretical foundations of the classical theory of fracture in solids date back to the works of

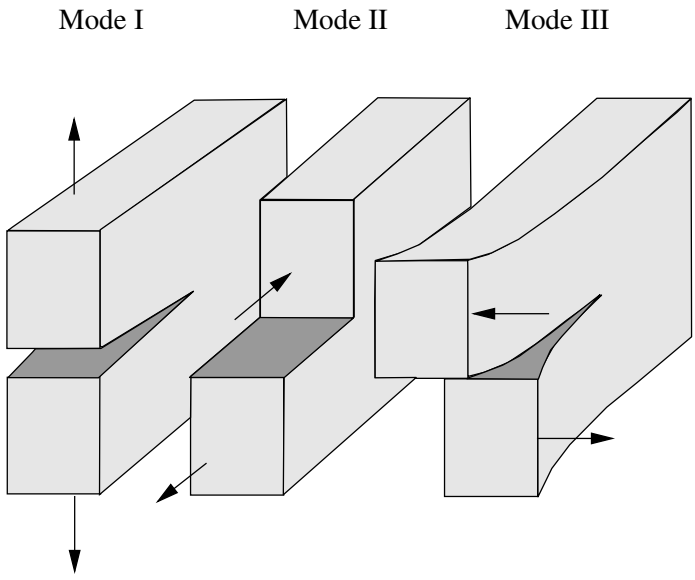

Figure 1.11 Fracture modes that can be applied on a crack.

Inglis [105], Griffith [63], Westergaard [233] and Irwin [106]. Fig. 1.11 illustrates fracture modes of loading, namely mode–I (opening) where load is applied perpendicular to the crack plane, mode–II (in–plane shear) where the load acts parallel to the crack plane but perpendicular to the crack front edge, and finally in mode–III (out–of–plane shear) the load acts parallel to both the crack plane and the crack front edge. A solid domain can also be loaded in a combination of two or three modes. There are basically two alternative approaches in fracture mechanics, namely the energy criterion and the stress intensity, which are on par with each other under certain circumstances. More deep and highly erudite discussions can be found among others in Anderson [5] and Tada et al. [211].

1.6.1 The Griffith energy balance

The work of Inglis [105] focused on the problem of stress concentrations around elliptical holes in glassy materials. However, in the case of a sharp crack where $a \gg b$, see in Fig. 1.12, the solution thereof posed an issue that the calculated stresses approach infinity at the crack tip, i.e.

$$\sigma_{\text{crack tip}} = 2\sigma \left(\frac{a}{\rho}\right)^{1/2}, \quad \text{with} \quad \rho = \frac{b^2}{a}, \tag{1.74}$$

which renders the solution non–physical as even very small loads applied would engender infinite stresses near the crack tip. Griffith [63] conceived of a global perspective in fracture mechanics and employed a balance of energy in the entire solid body. The energy approach states that a unit extension of the crack occurs if the available potential energy prevails the resistance of the material, e.g., surface energy, plastic work etc. To better illustrate the energy concept, let us consider a plate of thickness B and width $w \gg 2a$ which involves

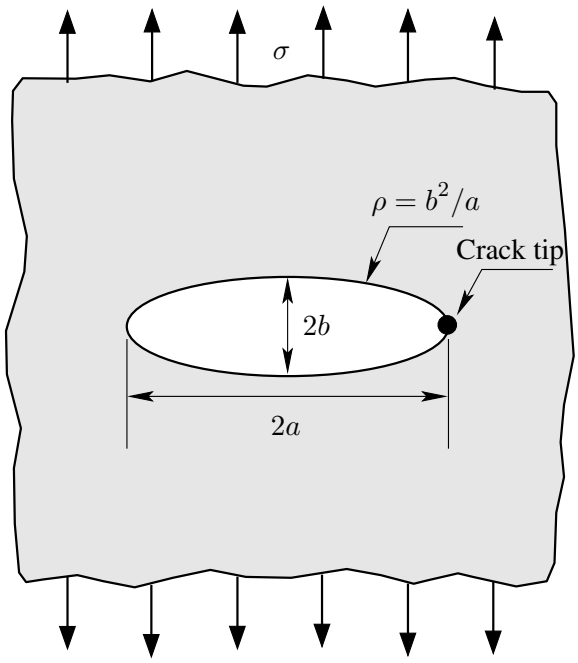

Figure 1.12 Elliptical flaw with a length $2a$ and width $2b$ in a flat plate creating stress concentrations when the stress σ is applied perpendicular to the major axis of the ellipse having a radius of curvature ρ; reconstructed from Anderson [5].

a crack of length $2a$, see Fig. 1.13. The plate is subjected to a constant stress σ. The plane stress conditions can be applied in the context of linear small strain elasticity. The Griffith energy balance for an infinitesimal increase in the crack area $\mathrm{d}A$ postulates under equilibrium conditions the following differential form

$$\frac{\mathrm{d}\Pi}{\mathrm{d}A} = \frac{\mathrm{d}U}{\mathrm{d}A} + \frac{\mathrm{d}W_\mathrm{s}}{\mathrm{d}A} = 0, \tag{1.75}$$

where Π stands for the total potential energy in the system, U denotes the potential energy provided by the internal elastic energy E and the external work P such that $U = E - P$. The work needed to create unit infinitesimal cracked area $\mathrm{d}A$ is indicated by W_s which can in the physical sense be regarded as the dissipated energy D, where $W_\mathrm{s} = D$. The equation (1.75) can further be written as

$$-\frac{\mathrm{d}U}{\mathrm{d}A} = \frac{\mathrm{d}W_\mathrm{s}}{\mathrm{d}A}. \tag{1.76}$$

Later, Griffith used the Inglis solution for calculating the fracture stress σ_f. To this end, he assumed two triangles at the top and the bottom of the crack flanks of a width $2a$ and height βa, corresponding to an unloaded state due to the existing crack, see Fig. 1.13. Exploiting the symmetry with respect to the center line and having a recourse to the Inglis solution, the parameter turns out to be $\beta = \pi$ for plane stress loading, yielding an unloaded volume

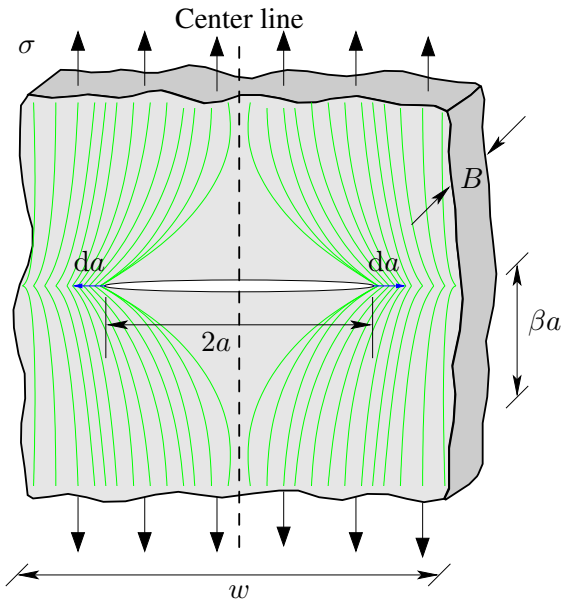

Figure 1.13 Sharp crack of length $2a$ in an infinite sheet of thickness B with stress trajectories denoted by the green color. A crack extension of $\mathrm{d}a$ at both ends leads to a formation of new cracked surface with an area $\mathrm{d}A = B\mathrm{d}a$; reconstructed from Anderson [5].

$V_{\text{unload}} = \pi a^2 B$. Griffith afterwards calculated the potential energy for one–half of the infinite plate subject to a decrease due to the crack formation, i.e.

$$U = \frac{\sigma^2 V}{2E} - \frac{\sigma^2 \pi a^2 B}{2E}, \tag{1.77}$$

where V, σ and E denote the constant volume of the entire domain, the remote stress and the Young's modulus, respectively. Next, we determine the energy input required to break the atomic bonds and grow the crack, i.e. to create a cracked surface of lenght a,

$$W_{\text{s}} = 2\gamma_{\text{s}} a B, \tag{1.78}$$

where γ_{s} denotes the energy required to break atomic bonds per unit surface area created by the crack in [joule/m^2]. The question of interest is whether the existing crack will grow by $\mathrm{d}A = B\mathrm{d}a$. Using the equilibrium (1.76), i.e.

$$\frac{\mathrm{d}U}{\mathrm{d}A} = -\frac{\sigma^2 \pi a}{E} \qquad \text{and} \qquad \frac{\mathrm{d}W_{\text{s}}}{\mathrm{d}A} = 2\gamma_{\text{s}}, \tag{1.79}$$

we obtain the fracture stress as follows

$$\sigma_{\text{f}} = \left(\frac{2\gamma_{\text{s}} E}{\pi a} \right)^{1/2}. \tag{1.80}$$

The above equation only holds for ideally brittle solids. For materials exhibiting plastic flow before fracture such as metals, Irwin [106] modified (1.80) such that

$$\sigma_{\mathrm{f}} = \left(\frac{2(\gamma_{\mathrm{s}} + \gamma_{\mathrm{p}})E}{\pi a} \right)^{1/2}, \tag{1.81}$$

where γ_{p} accounts for the additional energy required to be liberated due to dislocation motion in the vicinity of the crack tip.

1.6.2 The concept of energy release rate

In view of the Griffith's theory, Irwin [107] proposed an energy release rate G as a measure of the available energy for unit crack extension, i.e.

$$G = -\frac{\mathrm{d}U}{\mathrm{d}A}, \tag{1.82}$$

which can be also viewed as the crack extension force or the crack driving force. Note that "rate" refers here to the change with respect to the area, not time. Next, we define the energy absorption rate R such that

$$R = \frac{\mathrm{d}W_{\mathrm{s}}}{\mathrm{d}A}, \tag{1.83}$$

which describes the resistance of the material against the crack formation. At the critical value of the energy release rate, namely G_{c} where $G = G_{\mathrm{c}}$, the crack starts to grow as expressed by the following equilibrium

$$G_{\mathrm{c}} = R, \tag{1.84}$$

which is also the condition for a stable crack growth along with

$$\frac{\mathrm{d}G}{\mathrm{d}A} \leq \frac{\mathrm{d}R}{\mathrm{d}A}. \tag{1.85}$$

It is worth mentioning that G_{c} is a measure of the fracture toughness of the material. The unstable crack growth occurs when

$$\frac{\mathrm{d}G}{\mathrm{d}A} > \frac{\mathrm{d}R}{\mathrm{d}A}. \tag{1.86}$$

The resistance R tends to remain constant over the entire crack extension, a general case for ideally brittle materials, for which the critical energy release rate G_{c} can be unambiguously determined. However, ductile materials due to the plastic zone at the tip of the crack experiences a rising R as the crack grows, therefore, the driving force G must also increase in order to maintain the crack propagation. Falling resistance R can be attributed to the metals failing by cleavage undergoes very high strain rate near the crack tip, suppressing the plastic deformation. As a result, the resistance to cleavage crack becomes less than

that at the onset of the fracture. The intriguing case of crack propagation during aortic dissection, see Sec. 1.3.1, seems to fall into the category of falling crack resistance R. That is, it can be speculated that the dissection advances more easily upon the incipient crack propagation that renders less hemodynamic forces to cause the separation of the unit area in the wall during the dissection progression.

1.6.3 The stress intensity factor

Focusing on the isotropic linear elastic material behavior, certain crack configurations allow us to obtain closed–form stress expressions in the solid. Stress intensity factor K [Pa m$^{1/2}$] appears as an useful measure which assumes distinct values with regard to the fracture modes, such as K_{I}, K_{II} and K_{III}. Assuming the plain strain conditions, the stress fields ahead of a crack tip for mode–I, for instance, can be written as

$$\begin{aligned}
\sigma_{xx} &= \frac{K_{\mathrm{I}}}{\sqrt{2\pi r}}\cos\left(\frac{\theta}{2}\right)\left[1-\sin\left(\frac{\theta}{2}\right)\sin\left(\frac{3\theta}{2}\right)\right],\\
\sigma_{yy} &= \frac{K_{\mathrm{I}}}{\sqrt{2\pi r}}\cos\left(\frac{\theta}{2}\right)\left[1+\sin\left(\frac{\theta}{2}\right)\sin\left(\frac{3\theta}{2}\right)\right],\\
\sigma_{xy} &= \frac{K_{\mathrm{I}}}{\sqrt{2\pi r}}\cos\left(\frac{\theta}{2}\right)\sin\left(\frac{\theta}{2}\right)\cos\left(\frac{3\theta}{2}\right),\\
\sigma_{zz} &= \nu(\sigma_{xx}+\sigma_{yy}),\\
\sigma_{xz} &= 0,\\
\sigma_{yz} &= 0,
\end{aligned} \tag{1.87}$$

where r is the distance between the crack tip and the point near the tip where the stresses are calculated, whereas θ is the angle measured between the point of interest and the axis of the crack alignment. The relationships between the crack tip stresses and K for other modes can be found in, e.g., Anderson [5]. Stresses away from the crack tip are governed by the remote stress (stress generated well beyond the crack tip), the size of the crack and the specimen. Closed–form solutions exist for a number of simple configurations, such as center cracked, single–edge notch, disc–shaped compact test specimens which are listed in Tada et al. [211]. As an example, the relationship between K_{I} and the global behavior can be shown as a function of the remote stress and the crack size, i.e.

$$K_{\mathrm{I}} = F(\sigma, a). \tag{1.88}$$

The solution for the problem described in Fig. 1.13, e.g., yields

$$K_{\mathrm{I}} = \sigma\sqrt{\pi a}. \tag{1.89}$$

The relationship between the stress intensity factor K_{I} for mode–I and the energy release rate G can be given as

$$G = \frac{K_{\mathrm{I}}^2}{E'}, \tag{1.90}$$

where $E' = E$ for plane stress condition, whilst $E' = E/(1-\nu^2)$ for plain stress case with ν denoting the Poisson's ratio.

1.7 Crack Phase-field Modeling

The above–stated Griffith approach inherits certain shortcomings as well. In fact, the Griffith approach falls short of describing curvilinear crack paths, crack kinking and branching angles. Francfort & Marigo [54] proposed a variational approach to Griffith's energy approach that alleviate the problems thereof through energy minimization. For an elaborate historical account, the reader is referred to the forthcoming chapters. The hallmark of the crack phase–field approach can be motivated through an 1-D case of an infinitely long bar $L = [-\infty, +\infty]$ aligned in x-axis with a crack at $x = 0$. In fact, the sharp crack topology Γ described by an auxiliary scalar field variable $d(x) \in [0, 1]$, i.e.

$$d(x) : \begin{cases} 1 & \text{for} \quad x = 0 \\ 0 & \text{otherwise.} \end{cases} \tag{1.91}$$

The equation (1.91) characterizes a discontinuous function where $d = 1$ corresponds to a fractured material, while $d = 0$ indicates the totally intact state. The variable $d(x)$ is hereinafter termed the crack phase–field accounting for the homogenized micro–cracks and micro–voids evolving in the solid body. A characteristic length–scale parameter l interpolates between the intact and the fully broken states, allow the 2-D sharp crack surface Γ to smear out in 3-D domain. The phase–field $d(x)$ can be approximated via the following functions,

$$\begin{aligned} d(x) &= \exp\left(\frac{-|x|}{l}\right), \\ d(x) &= \begin{cases} \left(1 - \frac{|x|}{\sqrt{2}l}\right)^2, & |x| < \sqrt{2}l \\ 0, & \text{otherwise} \end{cases} \\ d(x) &= \left(1 + \frac{|x|}{l}\right) \exp\left(\frac{-|x|}{l}\right). \end{aligned} \tag{1.92}$$

The first function $(1.92)_1$ is originally proposed by Miehe et al. [143], while the second one $(1.92)_2$ can be found in Pham et al. [164]. The final exponential form $(1.92)_3$ is suggested by Borden et al. [15] for fourth–order phase–field models. Figure 1.14 indicates the dependence of the diffusion of the phase–field $d(x)$ on the different choices for a given l.

1.7.1 Governing equations at small strains

Let $\Omega \in \mathbb{R}^\delta$ and $\mathcal{T}$ be a continuous solid body and the process time interval, respectively, where $\delta \in \{1, 2, 3\}$ sets the dimension. The surface of the solid body is denoted by $\partial\Omega \in$

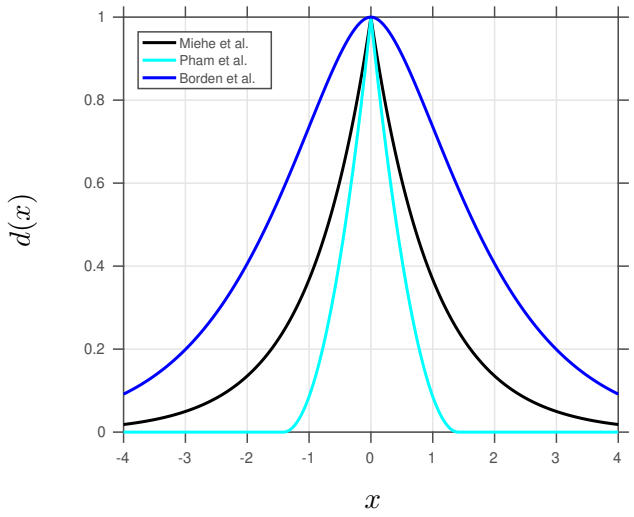

Figure 1.14 Phase–field approximations to cracking along an infinite bar at $x = 0$ by using various functions.

$\mathbb{R}^{\delta-1}$. The primary field variables of the fracturing elastic solid, within the small strain context, are the displacement field $\boldsymbol{u}(\boldsymbol{x}, t)$ and the phase–field $d(\boldsymbol{x}, t)$, i.e.

$$\boldsymbol{u} : \begin{cases} \Omega \times \mathcal{T} & \rightarrow & \mathbb{R}^{\delta}, \\ (\boldsymbol{x}, t) & \mapsto & \boldsymbol{u}(\boldsymbol{x}, t), \end{cases} \qquad d : \begin{cases} \Omega \times \mathcal{T} & \rightarrow & [0, 1], \\ (\boldsymbol{x}, t) & \mapsto & d(\boldsymbol{x}, t), \end{cases} \tag{1.93}$$

defined at a material point $\boldsymbol{x}$ at time $t \in \mathcal{T}$. The symmetric part of the gradient of the displacement vector $\boldsymbol{u}$ defines the standard strain tensor in the following way:

$$\boldsymbol{\varepsilon}(\boldsymbol{u}) := \nabla_{\mathrm{s}} \boldsymbol{u} = \frac{1}{2}(\nabla \boldsymbol{u} + \nabla^{\mathrm{T}} \boldsymbol{u}). \tag{1.94}$$

Now let us derive the governing strong forms of the elastic–fracture problem describing mechanical deformation and phase–field evolution. To this end, we introduce the energy storage functional E in a linear elastic body Ω,

$$E = \int_{\Omega} \psi(\boldsymbol{\varepsilon}, d) \mathrm{d}\Omega, \tag{1.95}$$

in which the Helmholtz free–energy function per unit volume $\psi(\boldsymbol{\varepsilon}, d)$ is composed of a monotonically degrading function $g(d)$ and an effective free energy term $\psi_0(\boldsymbol{\varepsilon})$ such that

$$\psi(\boldsymbol{\varepsilon}, d) = [g(d) + k]\psi_0(\boldsymbol{\varepsilon}). \tag{1.96}$$

In (1.96), k represents an artificial elastic rest energy via $k\psi_0(\boldsymbol{\varepsilon}) > 0$, which prevents the full degradation of the energy, thereby ensuring a well-posed problem for partly broken

solid. Next, we introduce the crack energy functional D in a linear elastic body Ω, i.e.

$$D = g_{\mathrm{c}} \int_{\Omega} \gamma(d, \nabla d) \mathrm{d}\Omega, \tag{1.97}$$

where g_{c} stands for the critical fracture energy, while $\gamma(d, \nabla d)$ denotes the crack surface density function given as

$$\gamma(d, \nabla d) = \frac{1}{2l}(d^2 + l^2 \nabla d \cdot \nabla d). \tag{1.98}$$

Finally, the external work functional P states

$$P = \int_{\Omega} \boldsymbol{\gamma} \cdot \boldsymbol{u} \mathrm{d}\Omega + \int_{\partial\Omega^t} \boldsymbol{t} \cdot \boldsymbol{u} \mathrm{d}\partial\Omega, \tag{1.99}$$

where the quantity $\boldsymbol{\gamma}$ and $\boldsymbol{t}$ represents the body force and the prescribed tractions acting on the Neumann boundary, respectively. The total potential energy in the sense of (1.75) can then be written as

$$\Pi = E + D - P. \tag{1.100}$$

By imposing the stationary potential energy on Π, we obtain a variational problem of the type

$$\{\boldsymbol{u}, d\} = \mathrm{Arg} \left\{ \inf_{\boldsymbol{u} \in \mathcal{W}_u} \inf_{d \in \mathcal{W}_d} \Pi(\boldsymbol{u}, d) \right\}, \tag{1.101}$$

with the admissible domains for the state variables

$$\begin{aligned} \mathcal{W}_u &:= \{\boldsymbol{u} \mid \ \boldsymbol{u} = \boldsymbol{0} \quad \text{on} \quad \partial\Omega_u\}, \\ \mathcal{W}_d &:= \{d \mid d = 0 \quad \text{on} \quad \partial\Omega_d\}. \end{aligned} \tag{1.102}$$

The variation of the total potential energy Π can be expressed as

$$\begin{aligned} \delta\Pi = &\int_{\Omega} g(d) \partial_{\boldsymbol{\varepsilon}} \psi_0 : \delta\boldsymbol{\varepsilon} \mathrm{d}\Omega - \int_{\Omega} \boldsymbol{\gamma} \cdot \delta\boldsymbol{u} \, \mathrm{d}\Omega - \int_{\partial\Omega^t} \boldsymbol{t} \cdot \delta\boldsymbol{u} \, \mathrm{d}\partial\Omega \\ &+ \int_{\Omega} g'(d) \psi_0 \delta d \, \mathrm{d}\Omega + \frac{g_{\mathrm{c}}}{l} \int_{\Omega} \left(d\delta d + l^2 \nabla d \cdot \nabla \delta d \right) \mathrm{d}\Omega = 0, \end{aligned} \tag{1.103}$$

where the derivative of the degradation function with respect to the phase–field is denoted by $g'(d) = \partial_d g(d)$. Application of the Gauss integral and Cauchy stress theorems yield

$$\begin{aligned} \delta\Pi = &- \int_{\Omega} \{\mathrm{Div}[g(d)\boldsymbol{\sigma}_0] + \boldsymbol{\gamma}\} \cdot \delta\boldsymbol{u} \, \mathrm{d}\Omega + \int_{\partial\Omega^t} [g(d)\boldsymbol{\sigma}_0 \cdot \boldsymbol{n} - \boldsymbol{t}] \cdot \delta\boldsymbol{u} \, \mathrm{d}\partial\Omega \\ &+ \int_{\Omega} \left[g'(d)\psi_0 + \frac{g_{\mathrm{c}}}{l} \left(d - l^2 \Delta d \right) \right] \delta d \, \mathrm{d}\Omega + \int_{\partial\Omega^t} \nabla d \cdot \boldsymbol{n} \delta d \, \mathrm{d}\partial\Omega = 0, \end{aligned} \tag{1.104}$$

in which the constitutive relation $\boldsymbol{\sigma}_0 = \partial_{\boldsymbol{\varepsilon}}\psi_0$ is incorporated. The equality (1.104) must hold for arbitrary values of $\delta\boldsymbol{u}$ and δd from which we obtain the coupled balance equations

$$\begin{aligned} &1:\ \mathrm{Div}[g(d)\boldsymbol{\sigma}_0] + \boldsymbol{\gamma} = \boldsymbol{0} \qquad \text{on } \Omega, \\ &2:\ \frac{g_{\mathrm{c}}}{l}\left(d - l^2\Delta d\right) = -g'(d)\psi_0 \qquad \text{on } \Omega, \end{aligned} \tag{1.105}$$

along with the Neumann-type boundary conditions

$$g(d)\boldsymbol{\sigma}_0 \cdot \boldsymbol{n} = \boldsymbol{t} \quad \text{on } \partial\Omega^t, \qquad \nabla d \cdot \boldsymbol{n} = 0 \quad \text{on } \partial\Omega^t. \tag{1.106}$$

It is worth emphasizing that (1.103) constitutes the weak form of the governing equations stated in (1.105) together with the boundary conditions in (1.106). Motivated by the local damage outlined by the discontinuous damage mechanics, Miehe et al. [140] introduced a crack driving source term $\mathcal{H}$ stored as a local history field in the deformation history s, i.e.

$$\mathcal{H}(\boldsymbol{x}, t) = \max_{s\in[0,t]} \psi_0(\boldsymbol{\varepsilon}, s), \tag{1.107}$$

which also imposes irreversibility of the crack growth, i.e. $d_{t+\Delta t} \geq d_t, \forall \boldsymbol{x} \in \Omega$. Note that various fracture criteria as to effective free energy, stress and stretch can be incorporated into the crack driving source term $\mathcal{H}$, see, e.g., Gültekin et al. [67].

1.7.2 Computational framework at small strains

The continuous solid body Ω is subdivided into $\mathrm{n_{el}}$ finite elements (interchangeably denote both the number of volume and surface elements), i.e.

$$\Omega \approx \mathop{\mathsf{A}}_{e=1}^{\mathrm{n_{el}}} \Omega^e, \tag{1.108}$$

where Ω^e represents the configuration of a single sub–domain. In a typical finite element implementation, the use of matrix (Voigt) notation instead of tensorial notation confers efficiency in storage and computations. Restricting ourselves to 2-D setting, the primary variables $\boldsymbol{u}$, d as well as the test functions $\delta\boldsymbol{u}$, δd are approximated by $\mathcal{C}^0$ continuous shape functions between the physically meaningful free parameters, i.e. nodal values of displacement $\boldsymbol{d}_I^u$ and the phase–field $\boldsymbol{d}_I^d$

$$\begin{aligned} \boldsymbol{u} &= \sum_{I=1}^{\mathrm{n}} \boldsymbol{N}_I^u \boldsymbol{d}_I^u, \qquad & d &= \sum_{I=1}^{\mathrm{n}} \boldsymbol{N}_I^d \boldsymbol{d}_I^d, \\ \delta\boldsymbol{u} &= \sum_{I=1}^{\mathrm{n}} \boldsymbol{N}_I^u \delta\boldsymbol{d}_I^u, \qquad & \delta d &= \sum_{I=1}^{\mathrm{n}} \boldsymbol{N}_I^d \delta\boldsymbol{d}_I^d, \end{aligned} \tag{1.109}$$

with n indicating the number of nodes per volume element as well as the surface element. The shape functions $\boldsymbol{N}_I^u$ and $\boldsymbol{N}_I^d$ can be given as

$$\boldsymbol{N}_I^u = \begin{bmatrix} N_I & 0 \\ 0 & N_I \end{bmatrix}, \qquad \boldsymbol{N}_I^d = \begin{bmatrix} N_I \end{bmatrix}. \tag{1.110}$$

Note that N_I and d_I are none but the shape function and the phase–field in relation to node I. In (1.109), the discrete nodal displacement $\boldsymbol{d}_I^u$ and the phase–field $\boldsymbol{d}_I^d$ arrays are defined as follows

$$\boldsymbol{d}_I^u = \begin{bmatrix} u_{x_I} \\ u_{y_I} \end{bmatrix}, \qquad \boldsymbol{d}_I^d = \begin{bmatrix} d_I \end{bmatrix}. \tag{1.111}$$

The derivatives of the primary field variables $\boldsymbol{\varepsilon}$, $\nabla\delta d$ and the respective test functions $\delta\boldsymbol{\varepsilon}$, $\delta\nabla\delta d$ are interpolated in a similar fashion by

$$\begin{aligned} \boldsymbol{\varepsilon} &= \sum_{I=1}^{\mathrm{n}} \boldsymbol{B}_I^u \boldsymbol{d}_I^u, & \nabla d &= \sum_{I=1}^{\mathrm{n}} \boldsymbol{B}_I^d \boldsymbol{d}_I^d, \\ \delta\boldsymbol{\varepsilon} &= \sum_{I=1}^{\mathrm{n}} \boldsymbol{B}_I^u \delta\boldsymbol{d}_I^u, & \nabla\delta d &= \sum_{I=1}^{\mathrm{n}} \boldsymbol{B}_I^d \delta\boldsymbol{d}_I^d, \end{aligned} \tag{1.112}$$

where the strain displacement and phase-field gradient matrices are defined by

$$\boldsymbol{B}_I^u = \begin{bmatrix} N_{I,x} & 0 \\ 0 & N_{I,y} \\ N_{I,y} & N_{I,x} \end{bmatrix}, \qquad \boldsymbol{B}_I^d = \begin{bmatrix} N_{I,x} \\ N_{I,y} \end{bmatrix}. \tag{1.113}$$

Insertion of the results in (1.109) and (1.112) into the weak form (1.103) leads to nodal residual arrays at each node

$$\begin{aligned} \boldsymbol{r}_I^u &= \int_{\Omega^e} g(d) \boldsymbol{B}_I^{u^{\mathrm{T}}} \partial_{\boldsymbol{\varepsilon}} \psi_0 \,\mathrm{d}\Omega - \int_{\Omega^e} \boldsymbol{N}_I^{u^{\mathrm{T}}} \boldsymbol{\gamma} \,\mathrm{d}\Omega - \int_{\partial\Omega^{t,e}} \boldsymbol{N}_I^{u^{\mathrm{T}}} \boldsymbol{t} \,\mathrm{d}\,\partial\Omega = \boldsymbol{0}, \\ \boldsymbol{r}_I^d &= \int_{\Omega^e} g'(d) \boldsymbol{N}_I^d \psi_0 \,\mathrm{d}\Omega + \frac{g_{\mathrm{c}}}{l} \int_{\Omega^e} \left(\boldsymbol{N}_I^d d + l^2 \boldsymbol{B}_I^{d^{\mathrm{T}}} \nabla d \right) \mathrm{d}\Omega = 0, \end{aligned} \tag{1.114}$$

which are required to vanish for arbitrary displacements $\delta\boldsymbol{d}_I^u$ and phase–fields $\delta\boldsymbol{d}_I^d$. The nodal residual array $\boldsymbol{r}_I^u$ associated with the mechanical deformation generally features a nonlinear characteristics, although $\boldsymbol{r}_I^d$ is linear. Therefore, we linearize the residual expressions in (1.114) and obtain the nodal tangent arrays

$$\begin{aligned} \boldsymbol{K}_{IJ}^{uu} &= \int_{\Omega^e} g(d) \boldsymbol{B}_I^{u^{\mathrm{T}}} \partial^2_{\boldsymbol{\varepsilon}\boldsymbol{\varepsilon}} \psi_0 \boldsymbol{B}_J^u \,\mathrm{d}\Omega, \\ \boldsymbol{K}_{IJ}^{ud} &= \int_{\Omega^e} g'(d) \boldsymbol{B}_I^{u^{\mathrm{T}}} \partial_{\boldsymbol{\varepsilon}} \psi_0 \boldsymbol{N}_J^d \,\mathrm{d}\Omega, \\ \boldsymbol{K}_{IJ}^{du} &= \int_{\Omega^e} g'(d) \boldsymbol{N}_I^d \partial_{\boldsymbol{\varepsilon}} \psi_0 \boldsymbol{B}_J^u \,\mathrm{d}\Omega, \\ \boldsymbol{K}_{IJ}^{dd} &= \int_{\Omega^e} g''(d) \boldsymbol{N}_I^d \psi_0 \boldsymbol{N}_J^d \,\mathrm{d}\Omega + \frac{g_{\mathrm{c}}}{l} \int_{\Omega^e} \left(\boldsymbol{N}_I^d \boldsymbol{N}_J^d + l^2 \boldsymbol{B}_I^{d^{\mathrm{T}}} \boldsymbol{B}_J^d \right) \mathrm{d}\Omega, \end{aligned} \tag{1.115}$$

associated with nodes I and J, where the second derivative of the degradation function with respect to the phase–field parameter d is represented by $g''(d) = \partial_{dd} g(d)$. As a solution procedure, we employ the incremental–iterative solution strategy based on a Newton–type scheme. To this end, the global residual vectors and tangent matrices are computed through an assembly process of the element residual and tangent arrays, i.e.

$$\begin{aligned} \boldsymbol{r}^u &= \bigwedge_{e=1}^{\mathrm{n_{el}}} \boldsymbol{r}_e^u, & \boldsymbol{r}^d &= \bigwedge_{e=1}^{\mathrm{n_{el}}} \boldsymbol{r}_e^d, \\ \boldsymbol{K}^{uu} &= \bigwedge_{e=1}^{\mathrm{n_{el}}} \boldsymbol{K}_e^{uu}, & \boldsymbol{K}^{ud} &= \bigwedge_{e=1}^{\mathrm{n_{el}}} \boldsymbol{K}_e^{ud}, \\ \boldsymbol{K}^{du} &= \bigwedge_{e=1}^{\mathrm{n_{el}}} \boldsymbol{K}_e^{du}, & \boldsymbol{K}^{dd} &= \bigwedge_{e=1}^{\mathrm{n_{el}}} \boldsymbol{K}_e^{dd}, \end{aligned} \tag{1.116}$$

which are the sum of nodal residual (1.114) and tangent arrays (1.115), respectively. Thus,

$$\begin{aligned} \boldsymbol{r}_e^u &= \sum_{I=1}^{\mathrm{n}} \boldsymbol{r}_I^u, & \boldsymbol{r}_e^d &= \sum_{I=1}^{\mathrm{n}} \boldsymbol{r}_I^d, \\ \boldsymbol{K}_e^{uu} &= \sum_{I=1}^{\mathrm{n}} \sum_{J=1}^{\mathrm{n}} \boldsymbol{K}_{IJ}^{uu}, & \boldsymbol{K}_e^{ud} &= \sum_{I=1}^{\mathrm{n}} \sum_{J=1}^{\mathrm{n}} \boldsymbol{K}_{IJ}^{ud}, \\ \boldsymbol{K}_e^{du} &= \sum_{I=1}^{\mathrm{n}} \sum_{J=1}^{\mathrm{n}} \boldsymbol{K}_{IJ}^{du}, & \boldsymbol{K}_e^{dd} &= \sum_{I=1}^{\mathrm{n}} \sum_{J=1}^{\mathrm{n}} \boldsymbol{K}_{IJ}^{dd}. \end{aligned} \tag{1.117}$$

Considering a typical time increment $\Delta t = t_{\mathrm{n}+1} - t_{\mathrm{n}}$, where $t_{\mathrm{n}+1}$ and t_{n} represent the current and the previous time steps, the below global linear algebraic system of equations are solved

$$\begin{bmatrix} \boldsymbol{d}^u \\ \boldsymbol{d}^d \end{bmatrix}_{t_{n+1}}^{i+1} = \begin{bmatrix} \boldsymbol{d}^u \\ \boldsymbol{d}^d \end{bmatrix}_{t_{n+1}}^{i} - \begin{bmatrix} \boldsymbol{K}^{uu} & \boldsymbol{K}^{ud} \\ \boldsymbol{K}^{du} & \boldsymbol{K}^{dd} \end{bmatrix}_{t_{n+1}}^{i^{-1}} \begin{bmatrix} \boldsymbol{r}^u \\ \boldsymbol{r}^d \end{bmatrix}_{t_{n+1}}^{i}, \tag{1.118}$$

for the $(i+1)^{\mathrm{th}}$ Newton iteration at the current time $t_{\mathrm{n}+1}$ which continues until $||\boldsymbol{r}^u||^{i+1} < \mathrm{tol}$ is satisfied. It needs to be highlighted that symmetry of the global system can not be guaranteed when the crack driving source term $\mathcal{H}$ in (1.107) is incorporated into $\boldsymbol{r}_I^d$ in (1.114) and $\boldsymbol{K}_{IJ}^{du}$ in (1.115). A more robust solution scheme would be the one–pass operator splitting algorithm based on the sequential updates of the displacement field and the crack phase–field which partitions the system thereby requiring only the diagonal terms, i.e. $\boldsymbol{K}^{uu}$ and $\boldsymbol{K}^{dd}$ in the global tangent matrix, see, e.g., Miehe et al. [140], for which the first sub–system reads

$$\left[\boldsymbol{d}^u\right]_{t_{n+1}}^{i+1} = \left[\boldsymbol{d}^u\right]_{t_{n+1}}^{i} - \left[\boldsymbol{K}^{uu}\right]_{t_{n+1}}^{i^{-1}} \left[\boldsymbol{r}^u\right]_{t_{n+1}}^{i}, \tag{1.119}$$

which is followed by

$$\left[\boldsymbol{d}^d\right]_{t_{n+1}} = \left[\boldsymbol{K}^{dd}\right]_{t_{n+1}}^{-1} \left[\boldsymbol{r}^d\right]_{t_{n+1}}. \tag{1.120}$$

The relation (1.120) can be solved directly as being a linear system of algebraic equations.

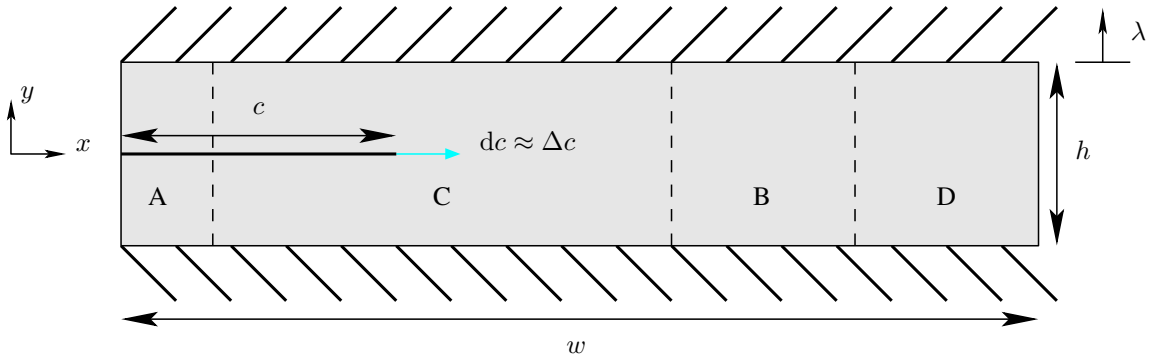

Figure 1.15 Pure shear specimen with an initial crack of length c, manifesting four different strain states: A, B, C, D upon a uniform stretch λ along the y-direction, leading to a unit crack extension $\mathrm{d}c \approx \Delta c$; reconstructed from Rivlin & Thomas [172].

1.7.3 Relation between Griffith energy release rate G_c and the critical fracture energy g_c

In order to show the relation between the Griffith energy release rate G_c and the critical fracture energy g_c used in the crack phase–field modeling, let us consider a test specimen clamped at the bottom and the top in the y–direction whose width w is sufficiently greater than the height h. The length of the initial sharp crack c is also sufficiently greater than h, as shown in Fig. 1.15. When the specimen is deformed by a stretch value of λ upon separating the clamps along y–direction, the state of the deformation in the domain presents four different regions; region A is substantially undeformed, region B, however, is in a state of pure shear, region C characterizes a rather complicated state of strain, and region D deviates from being in the state of pure shear due to the free–force edge at the right-end of the specimen. Assuming that the stretch λ is uniform in the region B, an infinitesimal crack extension $\mathrm{d}c$ at the tip of the crack c does not change the region C, however, the region A will grow at the expense of the region B, see the seminal article by Rivlin & Thomas [172] for details. In fact, this infinitesimal crack creates a surface area $t\mathrm{d}c$ with t being the thickness, and converts a volume of $ht\mathrm{d}c$ from the state of pure shear B into the undeformed state A. Using the concept of critical energy release rate introduced in (1.82), we write in the absence of external work P that

$$G_\mathrm{c} = -\frac{\mathrm{d}U}{\mathrm{d}A} = -\frac{\mathrm{d}E}{\mathrm{d}A} \approx -\frac{\Delta E}{\Delta A}, \tag{1.121}$$

where the increment of the internal elastic energy ΔE follows from the difference between the volume integral of the free energies at A, $\Psi_A = 0$ and at B, $\Psi_B = \Psi(\lambda)$, i.e.

$$\Delta E = 0 - \int_{\mathcal{B}} \Psi(\lambda)\mathrm{d}V \approx -\Psi(\lambda)ht\Delta c. \tag{1.122}$$

Then, the newly formed cracked surface area assumes

$$\Delta A = t\Delta c. \tag{1.123}$$

Plugging (1.122) and (1.123) into (1.121), we derive the expression for the critical energy release rate

$$G_{\mathrm{c}} = -\frac{\Delta E}{t\Delta c} = h\Psi(\lambda). \tag{1.124}$$

Now, let us turn our attention into the phase–field modeling. Elaborating on (1.76), we write

$$-\frac{\mathrm{d}E}{\mathrm{d}A} = \frac{\mathrm{d}W_{\mathrm{s}}}{\mathrm{d}A} = \frac{\mathrm{d}D}{\mathrm{d}A} \approx \frac{\Delta D}{\Delta A}, \tag{1.125}$$

where the incremental crack energy functional ΔD reads

$$\Delta D = \frac{g_{\mathrm{c}}}{2l}\int\limits_{\mathcal{B}} (d^2 + l^2 \nabla d \cdot \nabla d)\mathrm{d}V. \tag{1.126}$$

The gradient term in (1.126) can be simplified to 1–D due to the specimen geometry, i.e.

$$\nabla d = \frac{\partial d}{\partial y} = d' \quad \text{since} \quad \frac{\partial d}{\partial x} = \frac{\partial d}{\partial z} = 0. \tag{1.127}$$

The integral along y–axis yields

$$\Delta D = \frac{g_{\mathrm{c}} t\Delta c}{2l}\int\limits_{-h/2}^{h/2} (d^2 + l^2 d'^2)\mathrm{d}y. \tag{1.128}$$

The use of the exponential function in $(1.92)_1$ and its derivative, i.e.

$$d'(y) = -\frac{1}{l}\exp\left(-\frac{|y|}{l}\right) \quad \text{for} \quad y > 0, \tag{1.129}$$

recasts the integral expression in (1.128) as follows

$$\Delta D = \frac{g_{\mathrm{c}} t\Delta c}{l}\int\limits_{-h/2}^{h/2}\left[\exp\left(-\frac{2y}{l}\right)\right]\mathrm{d}y = \frac{2g_{\mathrm{c}} t\Delta c}{l}\int\limits_{0}^{h/2}\left[\exp\left(-\frac{2y}{l}\right)\right]\mathrm{d}y. \tag{1.130}$$

Assuming $h/2 \gg l \rightarrow h/2 \approx \infty$, we obtain

$$\Delta D = -g_{\mathrm{c}} t\Delta c\left[\exp\left(-\frac{2y}{l}\right)\right]_0^{\infty} = g_{\mathrm{c}} t\Delta c. \tag{1.131}$$

Therefore, the following relation holds

$$\frac{\Delta D}{\Delta A} = g_{\mathrm{c}}. \tag{1.132}$$

Finally, we reveal that the Griffith energy release rate G_{c} is equivalent to the critical fracture energy g_{c} according to

$$G_{\mathrm{c}} = -\frac{\Delta E}{\Delta A} = \frac{\Delta D}{\Delta A} = g_{\mathrm{c}}. \tag{1.133}$$

The above–stated formalism readily links the the critical fracture energy to the Griffith energy release rate for an isotropic continuum. Before closing the discussion, it is worth mentioning the treatment of anisotropic continua, which renders a much more complex problem to handle as substantiated by Gültekin et al. [66–68], Li et al. [121], and Teichtmeister et al. [216] among others. In can be inferred that the Griffith energy release rate as well as the critical fracture energy are likely to be described in tensorial form instead of a scalar G_{c} or g_{c} in order to pinpoint the differences in the rupture behavior of the materials tested which feature preferred orientations.

1.8 Organization of the Thesis

The thesis is a compilation of five scientific papers, which are concerned with the computational modeling of soft biological tissues with an emphasis on the inelastic mechanical response occurring in the aortic wall and the myocardium. The research contributions presented in the following chapters are:

1. *A phase-field approach to model fracture of arterial walls: Theory and finite element analysis*, **O. Gültekin, H. Dal, G. A. Holzapfel**, Computer Methods in Applied Mechanics and Engineering, $312(2016)542$–566.

   This study presents a thermodynamically consistent crack phase–field approach to model the fracture of anisotropic solids at finite strains with a reference to arterial walls. A variational formulation of the multi–field problem of deformation and phase–field accounting for the elastic mechanical response and the damage accumulation in the tissue imparts the strong forms of the governing equations which are none but the macroscopic balance of linear momentum and the microscopic crack evolution equation, respectively. In addition, a novel energy–based failure criterion is proposed that features distinct failure processes as to isotropic matrix and anisotropic collagenous part by means of an isotropic and an anisotropic energetic crack driving force and critical fracture energy. In the end, the numerical performance of the proposed model is demonstrated via fits against experimental data obtained from human specimens.

2. *Numerical aspects of anisotropic failure in soft biological tissues favor energy–based criteria: A rate–dependent anisotropic crack phase–field model*, **O. Gültekin, H. Dal, G. A. Holzapfel**, Computer Methods in Applied Mechanics and Engineering, $331(2018)23$–52.

   This article focuses on the incorporation of the anisotropic crack surface together with various anisotropic stress-based failure criteria into the previously presented

modeling framework. In particular, an anisotropic structure tensor appearing in the crack surface density function aligns the crack parallel to the fiber orientation via penalty parameters with an associated sensitivity. Following that, the Tsai–Wu, Hill and the principal stress criteria are compared with the energy–based criterion suggested in the previous contribution where the respective predictions in regard to the crack initiation and propagation are investigated. The results favor the energy-based criterion as a better candidate as being more compatible with the variational formulation.

3. *Computational modeling of progressive damage and rupture in fibrous biological tissues: Application to aortic dissection*, **O. Gültekin, S. P. Hager, H. Dal, G. A. Holzapfel**, Biomechanics and Modeling in Mechanobiology, submitted.

   This contribution handles a pathological condition of aortic dissection, which may elicit a sudden mortality, from a purely computational standpoint based on the modeling concepts introduced in the two previous articles. In order to communicate certain physical aspects of the disease, an idealized hollow cylindrical segment composed of several sub–layers involving a degenerated medial layer together with healthy medial and adventitial layers is modeled, which represent the human thoracic aorta. The geometry is further tailored with the incorporation of initial tears with varying sizes spanning several sub-layers across the thickness of the wall. The nascent crack propagation of the aortic dissection under supra-physiological cyclic loading follows the alignment of the single family of fibers in a medial lamellar unit, thereby portraying a helical crack growth which substantiates the clinical findings.

4. *An orthotropic viscoelastic model for the passive myocardium: Continuum basis and numerical treatment*, **O. Gültekin, G. Sommer, G. A. Holzapfel**, Computer Methods in Biomechanics and Biomedical Engineering, $19(2016)1647$–1664.

   This study draws the attention on the need to model the human myocardium as a viscoelastic, thick-walled, orthotropic and nonlinear material based on the experimental analyses attesting a strong hysteresis and stress relaxation phenomena upon biaxial extension and triaxial shear tests performed on human specimens. The model features a three–dimensional analogy of a generalized one dimensional Maxwell model which is linked to rate equations of the viscous overstresses originating from the orthotropic mechanical response of the tissue. The fitting capability of the proposed model is assessed through *in silico* examples mimicking the experiments.

5. *On the quasi-incompressible finite element analysis of anisotropic hyperelastic materials*, **O. Gültekin, H. Dal, G. A. Holzapfel**, Computational Mechanics, in press.

   Entirely hyperelastic though the constitutive response is, this contribution refers to the systematic *in silico* comparisons of the performances of several finite element formulations under the assumption of quasi–incompressibility which is of great interest to inelastic models as well since the finite elasticity essentially constitutes a

basis for the inelastic models. In view of this reasoning, the classical treatment of the $Q1P0$ finite element and its coalescence with the augmented Lagrangian method are compared with a recently suggested modality, i.e. the use of unsplit deformation gradient for the anisotropic response of the material. The numerical examples corroborates the new modality in terms of the numerical efficiency and the physical assessment of the fiber stretches enabled by the use of the anisotropic invariants *per se*, and not their unimodular forms.

A chapter of a book and two conference proceedings are also part of the manuscript:

- *A brief review on computational modeling of rupture in soft biological tissues*, **O. Gültekin, G. A. Holzapfel**. In: E. Oñate, D. Peric, E. de Souza Neto, M. Chiumenti (eds.) Advances in Computational Plasticity. A Book in Honour of D. Roger J. Owen. Springer, Berlin, (2018), vol 46, pp 113–144.

- *Phase-field models for the failure of anisotropic continua*, **H. Dal, O. Gültekin, F. A. Denli, G. A. Holzapfel**, Proceedings in Applied Mathematics and Mechanics, 17(2017)91–94.

- *Crack phase-field modeling of anisotropic rupture in fibrous soft tissues*, **O. Gültekin, H. Dal, G. A. Holzapfel**. In E. Oñate, D.R.J. Owen, D. Peric, E. de Souza Neto, and M. Chiumenti (eds.). Proceedings of the XIV International Conference on Computational Plasticity–Fundamentals and Applications COMPLAS XIV, (2017)139–150.

Together with the accepted abstracts:

- **O. Gültekin, H. Dal, G. A. Holzapfel** [2018]: *Numerical Modeling of Rupture in Human Arterial Walls*, WCB 2018 8th World Congress of Biomechanics, July 8–12, 2018, Dublin, Ireland.

- **O. Gültekin, H. Dal, G. A. Holzapfel** [2018]: *A Phase-field Approach to Model Aortic Dissections*, ESMC 2018 10th European Solid Mechanics Conference, July 2–6, 2018, Bologna, Italy.

- **O. Gültekin, H. Dal, G. A. Holzapfel** [2017]: *Phase-field Modeling of Rupture in Soft Biological Tissues*, COMPLAS 2017 14th International Conference on Computational Plasticity – Fundamentals and Applications, September 5–7, 2017, Barcelona, Spain.

- **O. Gültekin, H. Dal, G. A. Holzapfel** [2016]: *A Phase-field Approach to Model Fracture of Arterial Walls*, ECCOMAS 2016 7th European Congress on Computational Methods in Applied Sciences and Engineering, June 5–10, 2016, Crete, Greece.

- **O. Gültekin, G. Sommer, G. A. Holzapfel** [2015]: *An Orthotropic Viscoelastic Formulation for the Passive Myocardium: Continuum Basis and Numerical Treatment*, ESMC 2015 9th European Solid Mechanics Conference, July 6–10, 2015, Madrid, Spain.

2 A PHASE-FIELD APPROACH TO MODEL FRACTURE OF ARTERIAL WALLS: THEORY AND FINITE ELEMENT ANALYSIS

Abstract This study uses a recently developed phase-field approach to model fracture of arterial walls with an emphasis on aortic tissues. We start by deriving the regularized crack surface to overcome complexities inherent in sharp crack discontinuities, thereby relaxing the acute crack surface topology into a diffusive one. In fact, the regularized crack surface possesses the property of Gamma-Convergence, i.e. the sharp crack topology is restored with a vanishing length-scale parameter. Next, we deal with the continuous formulation of the variational principle for the multi-field problem manifested through the deformation map and the crack phase-field at finite strains which leads to the Euler-Lagrange equations of the coupled problem. In particular, the coupled balance equations derived render the evolution of the crack phase-field and the balance of linear momentum. As an important aspect of the continuum formulation we consider an invariant–based anisotropic constitutive model which is additively decomposed into an isotropic part for the ground matrix and an exponential anisotropic part for the two families of collagen fibers embedded in the ground matrix. In addition we propose a novel energy-based anisotropic failure criterion which regulates the evolution of the crack phase–field. The coupled problem is solved using a one–pass operator–splitting algorithm composed of a mechanical predictor step (solved for the frozen crack phase-field parameter) and a crack evolution step (solved for the frozen deformation map); a history field governed by the failure criterion is successively updated. Subsequently, a conventional Galerkin procedure leads to the weak forms of the governing differential equations for the physical problem. Accordingly, we provide the discrete residual vectors and a corresponding linearization yields the element matrices for the two sub-problems. Finally, we demonstrate the numerical performance of the crack phase-field model by simulating uniaxial extension and simple shear fracture tests performed on specimens obtained from a human aneurysmatic thoracic aorta. Model parameters are obtained by fitting the set of novel experimental data to the predicted model response; the finite element results agree favorably with the experimental findings.

2.1 Introduction

Over the last decades the physiological and pathological aspects of arterial tissues have become a prominent research topic in continuum and computational mechanics in regard to constitutive modeling, damage and fracture mechanics since there exists a salient relation between the histological architecture and the mechanical behavior of arteries in response to loading. As such, ever increasing number of studies have been a fashion to allow the latest

advances in the complex structural composition of the arterial wall to be embodied into models which can mimic the mechanical behavior of the tissue in a computer environment.

2.1.1 Histology and mechanical behavior of arterial walls, related diseases

The arterial wall consists of three distinct layers: the intima (tunica intima), the media (tunica media) and the adventitia (tunica externa). In healthy young individuals the innermost layer, the intima, is composed of a single layer of endothelial cells, and hence has a negligible contribution to the mechanical behavior of the arterial wall. However, due to the development of the sub-endothelial layer with age it thickens and stiffens (arteriosclerosis) so that the mechanical contribution may become significant. The middle layer, the media, involves smooth muscle cells, elastin and collagen fibers arranged in several sub-laminae operating as the main load bearing layer under physiological conditions. The outermost layer, the adventitia, comprises fibroblasts, fibrocytes, and bundles of collagen fibers. Fibroblasts are the cells responsible for secreting elastin and collagen. The adventitia is the main functioning layer under supra-physiological loading conditions to prevent the artery from rupture [83].

Subsequently, we cast a closer look into the structural, mechanical and functional characteristics of the constituents that emanate from their composition and orientation in the arterial wall. The endothelial cells, e.g., assume a spindle shape when subjected to shear stress as a result of blood flow and convey this mechanical stimuli to smooth muscle cells which regulate the diameter of the artery [2]. The long molecules of elastin compose a rubber-like network having cross-links with each other. They can be stretched about 2.5 times their initial length and keep the original size of the artery upon a stretch or contraction [97]. The structural protein collagen, however, emerges as the main load carrying constituent among all. Collagen molecules, called tropocollagens, organize themselves into collagen fibrils through intermolecular cross-links. These fibrils assemble into collagen fibers by proteoglycans (PGs). The orientation of the collagen fibers in both the media and the adventitia renders a helical structure [83]. To give an overall idea in regard to the mechanical contribution of cross-links to the tissue, it is observed that the fibrillar stretch is about one order of magnitude smaller than the macroscopic stretch [183]. Type I and III are the most common types of collagen in arterial walls [58]. In the absence of load, collagen fibers appear wavy and in a crimped form. When the load is present they gradually straighten and further elongate as the load increases. In fact, they exhibit a J-like stress-strain behavior [237]. Furthermore, similar to ropes, they cannot withstand compressive forces.

With regard to constitutive models to characterize the mechanical behavior of the arterial wall, the model considerations have followed a propensity from being isotropic thin-walled to anisotropic thick-walled at finite deformation, as can be found in, e.g., [38, 40, 56] among others. Their applicability is limited due to the lack of either convexity or anisotropy. Besides, [56] can only recover special types of deformation as being two-dimensional. All of those aforecited models with their variants are essentially purely phenomenological. Another constitutive approach, blended with anisotropy and polycon-

vexity, was suggested in [83]. It was developed on the basis of a thick-walled tube which assumes an incompressible solid. The micro-structural information was partly imparted by this model. It was later modified to take account of an axisymmetric model of collagen fiber dispersion [58] and a non-symmetric collagen fiber dispersion [85]. Aside from the aforementioned set of models, it is noteworthy to refer to a different (debatable) model approach namely to use worm-like chains to capture the mechanical response of biological tissues, i.e. [1] and [13]; for a review concerned with the mathematical modeling of the mechanical properties of soft biological tissues that constitute arterial walls, see [87].

Considering diseases that trigger a cascade of mechanically degenerative processes we hereby address some general aspects of aneurysm, atherosclerosis and aortic dissection which eventually may result in the fracture of the wall. Aneurysms can be viewed as a local dilation of the aorta forming a balloon-like bulge on the localized part of the wall upon the onset of aneurysm. The stress acting on this localized part increases while the wall strength experiences degradation. The fracture happens if the dilated aortic wall can not carry the wall tension due to hemodynamic loads which may bring fatal consequences. The primary factors causing aneurysms are known to be aging, smoking, hypertension, atherosclerosis and genetic disorders [99, 115]. The fact that atherosclerosis have turned out to be a prevailing cause of casualties draws the attention of modern medical science. The formation of atherosclerotic plaques is attributed to the low wall (laminar) shear stress associated with the disrupted laminar blood flow which forms a breeding ground for the fibroinflammatory lipid plaque. This plaque gradually grows and narrows the lumen of the artery; causes also adverse changes in the mechanical properties i.e. fibrotic media loses its elasticity considerably and rupture can be induced by the increase of blood pressure in case of an excessive atherosclerotic plaque [25, 36, 92]. Aortic dissections commence with an initial tear in the intima which advances further in the radial direction towards the media. The dissection propagates later in the axial direction owing to blood flow while it retains to be located on the sub–adventitial plane (between the sub-layers of media or media and adventitia) which creates a false lumen that can entirely close off the lumen of the aorta [35].

2.1.2 Damage and fracture models in arterial walls

To the best of our knowledge, there are only a few endeavors to model failure of arterial walls. The study [57] implemented the XFEM (Extended Finite Element Method), a technique to model crack growth without re-meshing, on the basis of PUFEM (Partition of Unity Finite Element Method) which allows the local enrichment functions, i.e. Heaviside functions, associated with additional degrees of freedom to be integrated into a finite element approximation [11, 145, 146]. In [57] the authors showed a numerical analysis of a peeling experiment (mode-I) on a dissected aortic medial strip in the form of delamination. Later on, the study [50] documented the simulation of the fracture of an atherosclerotic arterial wall in three-dimension by using an anisotropic extension of the irreversible isotropic cohesive element model, as proposed in [160]. The surface-like cohesive elements are inserted between two solid elements where the crack is expected to

grow and the opening displacements are resisted by cohesive tractions. Next, the study [51] performed the identical numerical test as in [57] and compared the results with various mesh sizes. A recently developed phase-field model for fracture, on which we will give a detailed background information in the forthcoming section, applied to the arterial wall, is documented in [168]. However, the compressive stiffness attributed to collagen fibers in the free-energy function utilized in [168] was not physically justified, inasmuch as it is a well accepted practice within the biomechanics community that collagen fibers are not regarded as compression-resistant elements. Subsequently, they employed this model on two-dimensional numerical examples. A visual comparison of the overall crack growth between the simulation results (Fig. 12(a)) and the typical experimental test results (Fig. 5 in [92]) suggests a conspicuous discrepancy. In addition to the abovementioned continuum models there are some multi-scale approaches available, [71, 240], to model the failure of biological tissues by connecting the micro-scale failure of individual collagen fibers with the macro-scale material response.

Apart from the fracture phenomenon, [8] modeled stress-softening behavior evident in cyclic tension tests of arterial walls by applying continuum damage mechanics (CDM), see [110], with $(1 - d)$ inserted only in the anisotropic part of the hyperelastic function i.e. damage solely occurs in fibers. [186] extended the approach by postulating a stochastic method to account for the sliding of the PG bridges that connect collagen fibrils, and speculated that they are responsible for the damage evolution in arterial walls. A recent study by [185] introduced a three-dimensional relaxed incremental variational damage model, thereby convexifying the energy in case of a loss of convexity with a convex hull due to [9].

2.1.3 Crack phase-field approach to fracture

Fracture, in general, is accompanied by a series of irreversible inhomogeneous micromechanisms where a number of imperfections initiated at micro level, i.e. voids and cracks, grow in a particular way in the course of time to form macro-voids and macro-cracks which gives rise to the accumulation of damage in advance of the fracture. This can be realized as a material deterioration by means of stress softening [202].

The authors of [63] and [108] laid the foundations of the classical theory of brittle fracture with well-known shortcomings to determine curvilinear crack paths, crack kinking and branching angles. These problems regarding the Griffith theory can be eliminated through variational principles due to energy minimization, as introduced in a phase-field model for a quasi-static brittle fracture in [54], and with the numerical implementation in [17] that approximates the Mumford-Shah functional [149] with a framework rendered by the Γ-convergence theory. This theory tracks the behavior of global minimum of problems (minimum values and minimizers) by 'integrating out' the local minimizers in the limit [19]. For a comprehensive overview we refer to [18]. The hallmark of all the aforementioned considerations is to provide a diffusive crack topology, healing the sharp crack surface, which approximates between intact and cracked states of the material by means of a scalar assisting variable. Aside from that, the study documented in [72] independently

applied a phase-field approach to the brittle fracture based on the Ginzburg-Landau type of evolution equation.

All the above stated approaches suffer from being either unrealistic in the sense that a crack is driven both in tension and compression or they are thermodynamically inconsistent. An alternative quasi-static small strain phase-field model (second-order phase-field theory) of fracture has been presented in [143] with the property of being thermodynamically consistent and allowing crack growth only in tension. Accordingly, this proposed approach handles an incremental variational setup for a two-field problem of gradient-type dissipative solids with a characteristic length scale. From the modeling point of view, this model is conceptually in accordance with CDM. A finite strain extension of this model, as discussed in Sec. 2.1.2, can be found in [65] and [168]. There are also studies dealing with higher order phase-field models (fourth-order phase-field theory) of the strongly anisotropic fracture which resorts to the extended Cahn-Hilliard framework [121].

If we reveal a noticeable advantage of the crack phase-field approach to those approaches outlined in Sec. 2.1.2, we can state that crack phase-field models avoid the modeling of discontinuities, whereas the models listed in Sec. 2.1.2 try to model discontinuities by means of nodal enrichment techniques using PUFEM or re-meshing strategies which make them a costly task to handle, especially, three-dimensional domains.

In our present contribution, we basically follow the quasi-static brittle fracture model documented in [140, 143] where a robust operator-splitting algorithm is implemented. Nevertheless, instead of an incremental formulation we present a continuous formulation of the variational principle for the multi-field problem manifested through the deformation map and the crack phase-field at finite deformations. Besides, we consider the crack growth being driven by a novel energy-based anisotropic failure criterion in accordance with the mechanics of arterial tissues. Furthermore, unlike [168], the represented numerical simulations are carried out in the three-dimensional domain. As a matter of fact, we simulate the fracture of an aortic aneurysmatic tissue specimen undergoing both uniaxial extension and simple shear loads and compare the results with a novel experimental study recently conducted in [205].

To provide a motivation of the present study in a nutshell, Fig. 2.1(a) displays a medial strip of a human aneurysmatic thoracic aorta sample prepared for a uniaxial extension test, while Fig. 2.1(b) shows the segment of the thoracic aorta from which the strip was cut out. Figure 2.1(c) displays the ruptured strip after the extension test whereby the constitutive and computational modeling of tissue failure is requested.

2.1.4 Organization of the work

The article is organized as follows. In Sec. 2.2 we introduce the field variables governing the coupled problem with corresponding finite strain kinematics. Additionally, the Ginzburg-Landau type phase-field model is motivated both in one and three dimension s. In Sec. 2.3 we outline the continuous formulation of the variational framework for the coupled two-field problem by obtaining the strong form of balance equations, also called Euler-Lagrange equations, based on power balance. Section 2.4 is concerned with the in-

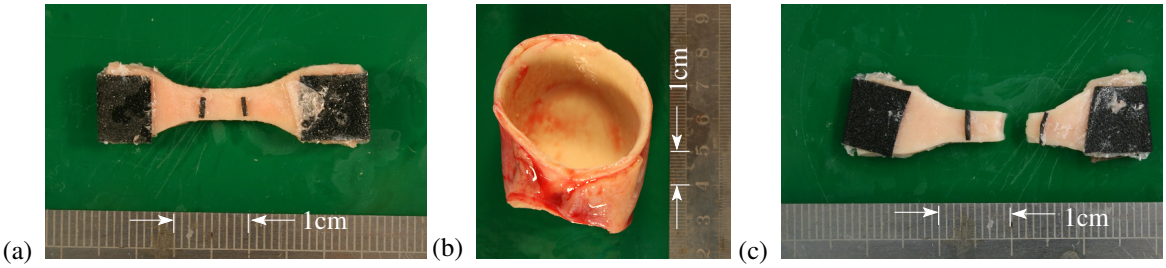

Figure 2.1 (a) Intact strip of the media prepared for a uniaxial extension test; (b) segment of a human aneurysmatic thoracic aorta from which the strip was cut out; (c) ruptured strip after the test.

corporation of an anisotropic hyperelastic constitutive model to delineate the mechanical behavior of the wall in the Eulerian framework. In the sequel, we propose an energy-based anisotropic failure criterion where a critical fracture energy scaled by the length-scale parameter, i.e. the width required to have a smooth approximation of the crack, controls the evolution of the crack phase-field with respect to the isotropic and the anisotropic part of the effective free-energy function. With this setup at hand in Sec. 2.5 we perform a staggered solution update that partitions the monolithic solution scheme into two sub-problems which contain minimizers for each partial problem. Subsequently, we obtain the weak form of the balance equations by means of a standard Galerkin procedure and we continue with the linearization of the nonlinear weighted-residual expressions. Later, we develop the algebraic counterparts of the weighted-residual expressions and their linearized terms. Finally, in Sec. 2.6, we perform representative numerical examples that fit a set of novel experimental data obtained from both uniaxial extension and simple shear tests in a quasi-static manner.

2.2 Multi-field Problem for Failure in an Anisotropic Continuum

In this section, we focus on the primary field variables, namely the crack phase-field d and the deformation map $\boldsymbol{\varphi}$ governed by the Euler-Lagrange equations which determine the diffusive crack topology and the balance of linear momentum. We introduce the finite elasticity in anisotropic solids paying attention to the structure of the tissue. Next we briefly motivate the crack phase-field in a one-dimensional setting and continue with the modeling of failure in three-dimensional continua which resorts to [140, 143].

2.2.1 The primary field variables of the multi-field problem

Let us assume a material body at time $t_0 \in \mathcal{T} \subset \mathbb{R}$, which we refer to as the reference configuration in the three-dimensional space designated by $\mathcal{B} \subset \mathbb{R}^3$ with the material point $\boldsymbol{X} \in \mathcal{B}$. In the same manner the placement of the deformed body at current time $t \in \mathcal{T} \subset \mathbb{R}$ we refer to as the spatial configuration denoted by $\mathcal{S} \subset \mathbb{R}^3$ with the spatial point $\boldsymbol{x} \in \mathcal{S}$ mapped through the deformation map $\boldsymbol{\varphi}$, see Fig. 2.2. As long as $t \subset \mathbb{R}$ is fixed, one can

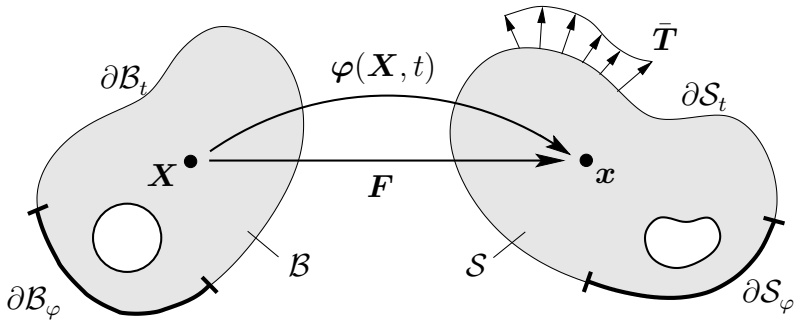

Figure 2.2 Nonlinear deformation of a solid. The reference configuration $\mathcal{B} \in \mathbb{R}^3$ and the spatial configuration $\mathcal{S} \in \mathbb{R}^3$. $\boldsymbol{\varphi} : \mathcal{B} \times \mathbb{R} \mapsto \mathbb{R}^3$ is the nonlinear deformation map which maps at time $t \in \mathbb{R}_t$ material point position $\boldsymbol{X} \in \mathcal{B}$ onto spatial position $\boldsymbol{x} = \boldsymbol{\varphi}(\boldsymbol{X}, t) \in \mathcal{S}$. The deformation gradient $\boldsymbol{F}$ maps a Lagrangian line element $\mathrm{d}\boldsymbol{X}$ onto its Eulerian counterpart $\mathrm{d}\boldsymbol{x} = \boldsymbol{F}\mathrm{d}\boldsymbol{X}$.

also write $\boldsymbol{\varphi}_t(\boldsymbol{X})$ [128]. Its definition renders

$$\boldsymbol{\varphi}_t(\boldsymbol{X}) : \begin{cases} \mathcal{B} \times \mathcal{T} & \rightarrow & \mathcal{S}, \\ (\boldsymbol{X}, t) & \mapsto & \boldsymbol{x} = \boldsymbol{\varphi}(\boldsymbol{X}, t). \end{cases} \tag{2.1}$$

Additionally let us introduce the surface $\partial\mathcal{B} \subset \mathbb{R}^2$ of the reference configuration $\mathcal{B} \subset \mathbb{R}^3$. Alongside with the deformation map $\boldsymbol{\varphi}$ in (2.1) we now elucidate the basic geometric mapping for the crack phase-field d. The time-dependent auxiliary crack phase-field parameter is

$$d : \begin{cases} \mathcal{B} \times \mathcal{T} & \rightarrow & [0, 1], \\ (\boldsymbol{X}, t) & \mapsto & d(\boldsymbol{X}, t), \end{cases} \tag{2.2}$$

which interpolates between the intact ($d = 0$) and the ruptured ($d = 1$) state of the material.

2.2.1.1 Kinematics

The material gradient of the deformation map $\boldsymbol{\varphi}$ leads to the deformation gradient

$$\boldsymbol{F} = \nabla\boldsymbol{\varphi}, \tag{2.3}$$

which maps the unit Lagrangian line element $\mathrm{d}\boldsymbol{X}$ onto its Eulerian counterpart $\mathrm{d}\boldsymbol{x} = \boldsymbol{F}\mathrm{d}\boldsymbol{X}$. The gradient operators $\nabla[\bullet]$ and $\nabla_x[\bullet]$ denote the gradient operator with respect to the reference $\boldsymbol{X}$ and the spatial $\boldsymbol{x}$ coordinates, respectively. Moreover, the Jacobian $J := \det\boldsymbol{F} > 0$ characterizes the volume map of infinitesimal reference volume elements onto associated spatial volume elements. Furthermore, we equip the two manifolds $\mathcal{B}$ and $\mathcal{S}$ with the covariant reference metric tensor $\boldsymbol{G}$ and spatial metric tensor $\boldsymbol{g}$. They

are required for mapping between the co- and contravariant objects in the Lagrangian and Eulerian manifolds [128]. Then, the right and left Cauchy–Green tensors read

$$\boldsymbol{C} = \boldsymbol{F}^T \boldsymbol{g} \boldsymbol{F}, \qquad \boldsymbol{b} = \boldsymbol{F} \boldsymbol{G}^{-1} \boldsymbol{F}^T, \tag{2.4}$$

which measure the deformation in the Lagrangian and Eulerian configurations, respectively. The energy stored in a hyperelastic isotropic material is characterized by the invariants

$$I_1 = \mathrm{tr}\boldsymbol{C}, \qquad I_2 = \frac{1}{2}\left[I_1^2 - \mathrm{tr}(\boldsymbol{C}^2)\right], \qquad I_3 = \det \boldsymbol{C}. \tag{2.5}$$

The anisotropic response of biological tissues requires the description of additional invariants. To this end, we introduce two reference unit vectors $\boldsymbol{M}$ and $\boldsymbol{M}'$ for the fiber orientations and their spatial counterparts

$$\boldsymbol{m} = \boldsymbol{F}\boldsymbol{M}, \qquad \boldsymbol{m}' = \boldsymbol{F}\boldsymbol{M}', \tag{2.6}$$

which idealize the micro-structure of the arterial wall. We can express the related Eulerian form of the structure tensors $\boldsymbol{A}_{\boldsymbol{m}}$ and $\boldsymbol{A}_{\boldsymbol{m}'}$ as follows

$$\boldsymbol{A}_{\boldsymbol{m}} = \boldsymbol{m} \otimes \boldsymbol{m}, \qquad \boldsymbol{A}_{\boldsymbol{m}'} = \boldsymbol{m}' \otimes \boldsymbol{m}'. \tag{2.7}$$

Upon simplifications elucidated through a particular material response provided by experiments and the incompressibility condition, i.e. $I_3 = 1$, the only isotropic invariant remains to render the isotropic mechanical response of the tissue is I_1 which takes the following form in the spatial configuration

$$I_1 = \boldsymbol{g} : \boldsymbol{b}. \tag{2.8}$$

Besides, the physically meaningful additional invariants

$$I_4 = \boldsymbol{m} \cdot \boldsymbol{g}\boldsymbol{m}, \qquad I_6 = \boldsymbol{m}' \cdot \boldsymbol{g}\boldsymbol{m}', \tag{2.9}$$

are sufficient to capture the anisotropic response of the thoracic aortic tissue.

2.2.1.2 Finite elasticity of an anisotropic solid

Finite elasticity of biological tissues is governed by the balance equation derived from the principle of minimum potential energy, i.e.

$$\boldsymbol{\varphi} = \mathrm{Arg}\left\{\inf_{\boldsymbol{\varphi} \in \mathcal{W}_{\boldsymbol{\varphi}}} E(\boldsymbol{\varphi}) - P(\boldsymbol{\varphi})\right\}, \tag{2.10}$$

with the energy storage functional E and the external work functional P according to

$$E(\boldsymbol{\varphi}) = \int_{\mathcal{B}} \Psi(\boldsymbol{F}, \boldsymbol{A}_{\boldsymbol{m}}, \boldsymbol{A}_{\boldsymbol{m}'}) \mathrm{d}V, \qquad P(\boldsymbol{\varphi}) = \int_{\mathcal{B}} \rho_0 \bar{\boldsymbol{\gamma}} \cdot \boldsymbol{\varphi} \mathrm{d}V + \int_{\partial \mathcal{B}_t} \bar{\boldsymbol{T}} \cdot \boldsymbol{\varphi} \mathrm{d}A, \tag{2.11}$$

respectively. Therein ρ_0, $\bar{\boldsymbol{\gamma}}$ and $\bar{\boldsymbol{T}}$ are the density, the prescribed body force and the surface traction in the reference configuration, respectively, while Ψ denotes the free-energy function per unit reference volume; the specific form for the constitutive behavior of arterial walls is introduced in Sec. 2.4.1. The minimization problem (2.10) is subjected to Dirichlet-type boundary conditions, i.e.

$$\mathcal{W}_{\varphi} := \{\boldsymbol{\varphi} \mid \boldsymbol{\varphi} \in H^1(\mathcal{B}),\ \boldsymbol{\varphi} = \bar{\boldsymbol{\varphi}} \quad \text{where} \quad \bar{\boldsymbol{\varphi}} \in \partial\mathcal{B}_{\varphi}\}. \tag{2.12}$$

According to the minimization principle, the deformation map $\boldsymbol{\varphi}$ delineated by a respective field minimizes the functional (2.10) which leads to the balance equation

$$\operatorname{Div} \boldsymbol{P} + \rho_0 \bar{\boldsymbol{\gamma}} = \boldsymbol{0} \tag{2.13}$$

for a quasi-static deformation in the domain $\mathcal{B}$ along with the Neumann-type boundary condition

$$\boldsymbol{P} \cdot \boldsymbol{N} = \bar{\boldsymbol{T}} \qquad \text{on} \qquad \partial\mathcal{B}_t. \tag{2.14}$$

The balance equation (2.13) is the Euler-Lagrange equation of the minimization problem (2.10). Herein, $\boldsymbol{P}$ is the first Piola–Kirchhoff stress tensor and $\boldsymbol{N}$ is the Lagrangian unit surface normal vector.

2.2.2 Ginzburg-Landau type phase-field model for diffusive crack

In this section, the Ginzburg-Landau type phase-field approach for brittle fracture of isotropic solids will be briefly summarized, as outlined in [140, 143]. The extension of the brittle fracture to the anisotropic solid will be provided in Sec. 2.3.

2.2.2.1 Field equation for crack phase-field in one-dimensional setting

In order to motivate the phase-field approximation to cracking phenomenon, an infinite one-dimensional bar $L = [-\infty, +\infty]$ with a crack that initiates at the origin $x = 0$ can be contemplated. The domain is then defined to be $\mathcal{B} = \Gamma \times L$ with a constant cross-section Γ on $x \in L$. The assisting crack phase-field variable $d(x) \in [0, 1]$ characterizes the acute crack topology with

$$d(x) := \delta(x) : \begin{cases} 1 & \text{for} \quad x = 0, \\ 0 & \text{otherwise}, \end{cases} \tag{2.15}$$

described by the Kronecker delta function $\delta(x)$ as the discrete version of the Dirac delta function, where $d = 0$ and $d = 1$ mark the intact and the cracked (ruptured) state of the considered material, respectively , as depicted in Fig. 2.3(a). The auxiliary scalar field variable d represents the homogenized growth of micro-cracks and micro-voids within the material, as described in CDM. Next, this sharp crack topology is approximated to a diffusive crack topology via the exponential function

$$d(x) = e^{-|x|/l}, \tag{2.16}$$

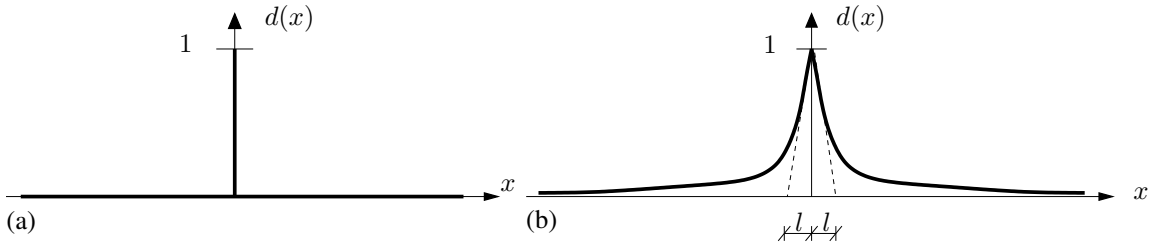

Figure 2.3 (a) Sharp crack topology described by the Kronecker delta function $d(x) = \delta(x)$ for vanishing length-scale parameter $l \to 0$; (b) diffusive crack topology $d(x) = e^{-|x|/l}$ with a length-scale parameter equal to l. Adopted from [143].

which makes the crack spread over the axial domain L, with the length-scale parameter l regularizing the sharp crack topology, see Fig. 2.3(b). Note that equation (2.16) is the solution of the homogeneous ordinary differential equation

$$d(x) - l^2 d''(x) = 0 \tag{2.17}$$

subjected to the Dirichlet-type boundary conditions

$$d(0) = 1, \qquad d(\pm\infty) = 0. \tag{2.18}$$

From a purely mathematical standpoint the differential equation (2.17) can be regarded as the Euler-Lagrange equation of the variational principle

$$d = \text{Arg}\left\{ \inf_{d \in \mathcal{W}_d} I(d) \right\}, \tag{2.19}$$

with the space of admissible solutions $\mathcal{W}_d := \{d | d(0) = 1,\ d(\pm\infty) = 0\}$. The equivalent functional form delineating a potential for the one-dimensional problem is given as

$$I(d) = \frac{1}{2} \int_{\mathcal{B}} (d^2 + l^2 d'^2) \mathrm{d}x. \tag{2.20}$$

An integration of the Galerkin-type weak form of the differential equation (2.17) provides this functional.

2.2.2.2 Field equation for crack phase-field in three-dimensional setting

The multi-dimensional formulation of the cracking in solid structures can be achieved akin to the aforementioned one-dimensional motivation in Sec. 2.2.2.1. The respective deformation field is displayed in Fig. 2.4(a). For a non-deformable domain, the gradient operator can simply be taken as $\nabla_x[\bullet] = \nabla[\bullet]$. Provided that an acute crack surface topology at time t is given as $\Gamma(t) \subset \mathbb{R}^2$ in the solid $\mathcal{B}$, the regularized crack surface $\Gamma_l(d)$, see Fig. 2.4(b), adopts the following multi-dimensional form

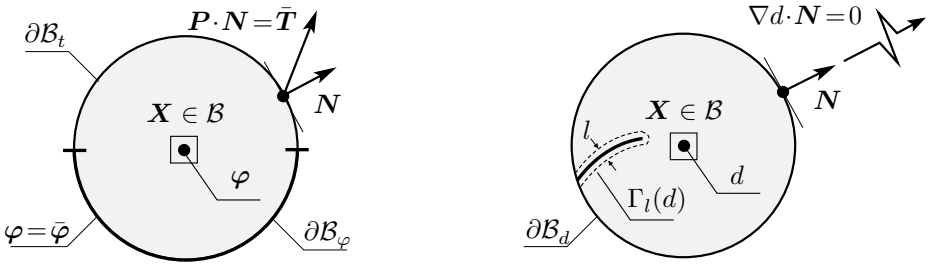

(a) Deformation field (b) Crack phase-field

Figure 2.4 The multi-field problem: (a) mechanical problem of deformation; (b) evolution of the crack phase-field problem.

$$\Gamma_l(d) = \int_{\mathcal{B}} \gamma(d, \nabla d)\mathrm{d}V, \tag{2.21}$$

where the volume-specific crack surface density reads

$$\gamma(d, \nabla d) = \frac{1}{2l}(d^2 + l^2|\nabla d|^2). \tag{2.22}$$

Following the steps employed in the one-dimensional problem, we can now state the minimization principle

$$d(\boldsymbol{X}, t) = \mathrm{Arg}\left\{\inf_{d\in\mathcal{W}_{\Gamma(t)}} \Gamma_l(d)\right\}, \tag{2.23}$$

along with the Dirichlet-type boundary constraint

$$\mathcal{W}_{\Gamma(t)} = \{d|d(\boldsymbol{X}, t) = 1 \quad \text{at} \quad \boldsymbol{X} \in \Gamma(t)\}. \tag{2.24}$$

Upon the minimization of the regularized crack surface functional we derive the Euler-Lagrange equations of the above stated variational principle, i.e.

$$d - l^2\Delta d = 0 \quad \text{in } \mathcal{B} \qquad \text{and} \qquad \nabla d \cdot \boldsymbol{N} = 0 \quad \text{on } \partial\mathcal{B}, \tag{2.25}$$

where Δd signifies the Laplacian of the crack phase-field which interpolates between the intact and the ruptured state of the material proportional to the length-scale parameter l, as depicted in Fig. 2.4(b), and $\boldsymbol{N}$ is the unit surface normal oriented outward in the reference configuration. The Euler-Lagrange equations (2.25) are derived in Appendix, see also [65].

2.3 Governing Equations of the Multi-field Problem

Now we are focusing on the minimization principle of the global power balance that governs the multi-field problem, which yields the coupled balance equations for the evolution of the crack phase-field and the balance of linear momentum.

2.3.1 Energy storage functional in an anisotropic solid

As a point of departure, we redefine the energy storage functional $(2.11)_1$ for the hyperelasticity of an anisotropic solid as

$$E(\boldsymbol{\varphi}, d) := \int_{\mathcal{B}} \Psi(\boldsymbol{F}, \boldsymbol{A}_{\boldsymbol{m}}, \boldsymbol{A}_{\boldsymbol{m}'}; d) \mathrm{d}V \tag{2.26}$$

in terms of the free-energy function Ψ for a degrading continuum, with

$$\Psi(\boldsymbol{F}, \boldsymbol{A}_{\boldsymbol{m}}, \boldsymbol{A}_{\boldsymbol{m}'}; d) := g(d)\Psi_0(\boldsymbol{F}, \boldsymbol{A}_{\boldsymbol{m}}, \boldsymbol{A}_{\boldsymbol{m}'}), \tag{2.27}$$

where Ψ_0 is the effective free-energy function of the hypothetical intact solid. A monotonically decreasing quadratic degradation function, i.e.

$$g(d) := (1-d)^2, \tag{2.28}$$

describes the degradation of the solid with the evolving crack phase-field parameter d, with the following growth conditions:

$$g'(d) \leq 0 \qquad \text{with} \qquad g(0) = 1, \qquad g(1) = 0, \qquad g'(1) = 0. \tag{2.29}$$

The first condition ensures degradation, while the second and third condition set the limits for the intact and the ruptured state, and the final condition ensures the saturation at $d \to 1$.

2.3.2 Rate of energy storage functional and external power functional

Time derivative of (2.26) gives the rate of energy storage functional

$$\mathcal{E}(\dot{\boldsymbol{\varphi}}, \dot{d}; \boldsymbol{\varphi}, d) := \int_{\mathcal{B}} (\boldsymbol{P} : \dot{\boldsymbol{F}} - f\dot{d}) \mathrm{d}V. \tag{2.30}$$

Herein,

$$\boldsymbol{P} = \partial_{\boldsymbol{F}} \Psi(\boldsymbol{F}, \boldsymbol{A}_{\boldsymbol{m}}, \boldsymbol{A}_{\boldsymbol{m}'}; d), \qquad f := -\partial_d \Psi(\boldsymbol{F}, \boldsymbol{A}_{\boldsymbol{m}}, \boldsymbol{A}_{\boldsymbol{m}'}; d) \tag{2.31}$$

are the first Piola–Kirchhoff stress tensor $\boldsymbol{P}$ and the energetic force f which is work conjugate to the crack phase-field d, respectively. The external power functional can be described as

$$\mathcal{P}(\dot{\boldsymbol{\varphi}}) = \int_{\mathcal{B}} \rho_0 \bar{\boldsymbol{\gamma}} \cdot \dot{\boldsymbol{\varphi}} \mathrm{d}V + \int_{\partial \mathcal{B}_t} \bar{\boldsymbol{T}} \cdot \dot{\boldsymbol{\varphi}} \mathrm{d}A. \tag{2.32}$$

2.3.3 Crack energy functional and crack dissipation functional

The crack energy functional D_{c} can be defined with the help of the volume-specific crack surface density (2.22) according to

$$D_{\mathrm{c}}(d) = \int_{\mathcal{B}} g_{\mathrm{c}} \gamma(d, \nabla d) \mathrm{d}V, \tag{2.33}$$

where g_{c} denotes the critical fracture energy required to convert an un-cracked matter into a cracked matter. The evolution of (2.33) yields the crack dissipation functional $\mathcal{D}$, i.e.

$$\mathcal{D}(\dot{d}) = \int_{\mathcal{B}} g_{\mathrm{c}} [\delta_d \gamma(d, \nabla d)] \dot{d} \, \mathrm{d}V, \tag{2.34}$$

where $\delta_d \gamma$ denotes the variational derivative of the crack surface density γ, [143], with the explicit form

$$\delta_d \gamma = \frac{1}{l}(d - l^2 \Delta d), \tag{2.35}$$

which can be shown in an analogous manner to that given in Appendix. The second law of thermodynamics requires that the dissipation functional has to be non-negative for all admissible deformation processes, i.e. $\mathcal{D} \geq 0$.

2.3.4 Variational formulation based on power balance

The above stated functionals (2.30), (2.32) and (2.34) yield the power balance for the multi-field problem

$$\Pi(\dot{\boldsymbol{\varphi}}, \dot{d}) = \mathcal{E}(\dot{\boldsymbol{\varphi}}, \dot{d}) + \mathcal{D}(\dot{d}) - \mathcal{P}(\dot{\boldsymbol{\varphi}}) = 0. \tag{2.36}$$

On the basis of (2.36), a rate-type mixed variational principle can be constructed via a minimization principle for the quasi-static process, i.e.

$$\{\dot{\boldsymbol{\varphi}}, \dot{d}\} = \mathrm{Arg} \left\{ \inf_{\dot{\boldsymbol{\varphi}} \in \mathcal{W}_{\dot{\varphi}}} \inf_{\dot{d} \in \mathcal{W}_{\dot{d}}} \Pi(\dot{\boldsymbol{\varphi}}, \dot{d}) \right\}, \tag{2.37}$$

with the admissible domains for the state variables

$$\begin{aligned} \mathcal{W}_{\dot{\varphi}} &:= \{\dot{\boldsymbol{\varphi}} \mid \dot{\boldsymbol{\varphi}} = \mathbf{0} \quad \text{on} \quad \partial\mathcal{B}_{\varphi}\}, \\ \mathcal{W}_{\dot{d}} &:= \{\dot{d} \mid \dot{d} = 0 \quad \text{on} \quad \partial\mathcal{B}_{d}\}. \end{aligned} \tag{2.38}$$

The variation of the functional leads to the Euler-Lagrange equations which describe the multi-field problem for the brittle fracture of an anisotropic hyperelastic solid, i.e.

$$\begin{aligned} &1\text{:}\ \ \mathrm{Div}\, \boldsymbol{P} + \rho_0 \bar{\boldsymbol{\gamma}} = \mathbf{0}, \\ &2\text{:}\ \ (f - g_{\mathrm{c}} \delta_d \gamma) \dot{d} = 0, \end{aligned} \tag{2.39}$$

along with the loading-unloading conditions ensuring the principal of maximum dissipation in case of an evolution of the crack phase-field parameter d, i.e.

$$\dot{d} \geq 0, \qquad f - g_c \delta_d \gamma \leq 0, \qquad (f - g_c \delta_d \gamma)\dot{d} = 0. \tag{2.40}$$

The first condition ensures the irreversibility of the evolution of the crack phase-field parameter. The second condition is an equality for an evolving crack, and it is negative for a stable crack. The third condition is the balance law for the evolution of the crack phase-field subjected to the former conditions. The balance of static equilibrium $(2.39)_1$ can be recast, by making use of the Piola identity, into the following form

$$J \operatorname{div}(J^{-1}\boldsymbol{\tau}) + \rho_0 \bar{\boldsymbol{\gamma}} = \mathbf{0}, \tag{2.41}$$

where $\boldsymbol{\tau}$ denotes the Kirchhoff stress tensor.

2.4 Constitutive Equations of the Multi-field Problem

In this section, we shed light on (i) the constitutive equations that capture the nonlinear anisotropic response of arterial tissues, and (ii) the associated energy-based anisotropic failure criterion that portrays the state of the material at which the cracking starts and propagates.

2.4.1 Constitutive equations

To characterize the local anisotropic mechanical response of an intact aortic tissue we specify the free-energy function Ψ_0 in (2.27) and adopt the polyconvex, invariant-based anisotropic free-energy function

$$\Psi_0(\boldsymbol{F}, \boldsymbol{A}_{\boldsymbol{m}}, \boldsymbol{A}_{\boldsymbol{m}'}) := \Psi_0^{\mathrm{iso}}(J, I_1) + \Psi_0^{\mathrm{ani}}(I_4, I_6), \tag{2.42}$$

which additively decomposes into an isotropic neo-Hookean part responsible for the mechanical behavior of the ground matrix, i.e.

$$\Psi_0^{\mathrm{iso}}(J, I_1) := \kappa(J - \ln J - 1) + \frac{\mu}{2}(I_1 - 2\ln J - 3), \tag{2.43}$$

and an exponential anisotropic free-energy function taking into account the contributions of the collagen fibers, i.e. [83]

$$\Psi_0^{\mathrm{ani}}(I_4, I_6) := \frac{k_1}{2k_2} \sum_{i=4,6} \{\exp[k_2(I_i - 1)^2] - 1\}, \tag{2.44}$$

idealized by two distinct families of collagen fibers. Therein, κ denotes the penalty parameter whereas μ is the shear modulus. In the anisotropic term k_1 and k_2 stand for a stress-like material parameter and a dimensionless parameter, respectively. In the free-energy function (2.42) the anisotropic terms in (2.44) only contribute when the fibers are extended,

that is when $I_4 > 1$ or $I_6 > 1$. If one or more of these conditions is not satisfied then the relevant part of the anisotropic function is omitted from (2.44). If, e.g., I_4 and I_6 are less than or equal to 1, then the function Ψ_0 is purely isotropic.

At this point we briefly touch upon some aspects regarding the computational treatment of the incompressible material behavior. The studies [6, 155] discuss the non-physical volumetric deformation of an anisotropic material for the case that the hyperelastic model stated in (2.42) is mistakenly used in the compressible domain; e.g., a sphere reinforced with one family of fibers would be deformed into a sphere with a larger size upon inflation instead of an ellipsoidal shape. Another study [75] mentions that the volumetric-deviatoric split gives rise to a non-physical reduction in the stress along the fiber direction lowered through the lateral expansion which leads to an increase in the volume ratio. A careful treatment of incompressible materials is necessary since very large values of the penalty parameter κ may lead to ill-conditioning of the global tangent arrays, known as locking. This can be circumvented by mixed finite element methods due to a three-field Hu-Washizu variational principle along with the augmented Lagrangian method to enforce incompressibility. For more details, we refer to, e.g., [80, 133, 200]. Another strategy is based on the use of higher-order elements which can eliminate the parasitic stresses, see [74]. The use of mixed element formulations, however, requires special attention, particularly in phase-field problems of fracture since the degradation of the uniform volumetric response within an element domain cannot be arbitrarily chosen, i.e. the phase-field d calculated at each Gauss point does not match with the volumetric response described on the element level. In the view of the aforementioned information and our main focus on modeling fracture we have tried to avoid such computational complexities at this stage and have chosen the penalty parameter κ to be $\approx 10^3\,\mu$ which allows the analysis of a nearly incompressible material (compressibility effects are small).

Exploiting the Coleman–Noll procedure on the Clausius–Planck inequality , and using the form of the free-energy function Ψ as introduced in (2.27), we may retrieve the Kirchhoff stress tensor $\boldsymbol{\tau}$ as follows

$$\boldsymbol{\tau} := 2\partial_{\boldsymbol{g}}\Psi = g(d)\boldsymbol{\tau}_0, \qquad \boldsymbol{\tau}_0 = 2\partial_{\boldsymbol{g}}\Psi_0, \tag{2.45}$$

where $g(d)$ is the monotonically decreasing quadratic degradation function as provided in (2.28). Insertion of (2.42) along with (2.43) and (2.44) into the definition $(2.45)_2$ leads to the stress expression for the intact material

$$\boldsymbol{\tau}_0 = \hat{p}\boldsymbol{g}^{-1} + \mu(\boldsymbol{b} - \boldsymbol{g}^{-1}) + 2\psi_4 \boldsymbol{m}\otimes\boldsymbol{m} + 2\psi_6(\boldsymbol{m}'\otimes\boldsymbol{m}' + \boldsymbol{m}'\otimes\boldsymbol{m}'), \tag{2.46}$$

where $\hat{p} := \kappa(J-1)$, and the deformation-dependent scalar coefficients ψ_4 and ψ_6 are defined as

$$\begin{aligned} \psi_4 &:= \partial_{I_4}\Psi_0 = k_1(I_4 - 1)\exp[k_2(I_4-1)^2], \\ \psi_6 &:= \partial_{I_6}\Psi_0 = k_1(I_6 - 1)\exp[k_2(I_4-1)^2]. \end{aligned} \tag{2.47}$$

Furthermore we need to derive the Kirchhoff stress tensor $\boldsymbol{\tau}$ with respect to the Eulerian metric $\boldsymbol{g}$ to obtain the following Eulerian elasticity tensors

$$\mathbb{c} := 4\partial^2_{\boldsymbol{gg}}\Psi = g(d)\mathbb{c}_0, \qquad \mathbb{c}_0 = 4\partial^2_{\boldsymbol{gg}}\Psi_0. \tag{2.48}$$

Insertion of (2.46) and (2.47) into the definition $(2.48)_2$ gives the Eulerian elasticity tensor $\mathbb{c}_0$ for the intact material

$$\mathbb{c}_0 = (\hat{p} + \kappa)\boldsymbol{g}^{-1} \otimes \boldsymbol{g}^{-1} - 2\hat{p}\mathbb{I}_{\boldsymbol{g}^{-1}} + 2\mu\mathbb{I}_{\boldsymbol{g}^{-1}} + 4\psi_{44}\mathbb{M} + 4\psi_{66}\mathbb{M}', \tag{2.49}$$

where the symmetric fourth-order identity tensor $\mathbb{I}_{\boldsymbol{g}^{-1}}$ has the following index representation: $\mathbb{I}^{ijkl} = (g^{ik}g^{jl} + g^{il}g^{jk})/2$ which is with respect to the metric $\boldsymbol{g}^{-1}$. In addition, the scalar coefficients ψ_{44} and ψ_{66} can be given as

$$\begin{aligned} \psi_{44} &:= \partial_{I_4}\psi_4 = k_1[1 + 2k_2(I_4 - 1)^2]\exp[k_2(I_4 - 1)^2], \\ \psi_{66} &:= \partial_{I_6}\psi_6 = k_1[1 + 2k_2(I_6 - 1)^2]\exp[k_2(I_6 - 1)^2], \end{aligned} \tag{2.50}$$

and the fourth-order structure tensors take on the following form

$$\mathbb{M} := \boldsymbol{m} \otimes \boldsymbol{m} \otimes \boldsymbol{m} \otimes \boldsymbol{m}, \qquad \mathbb{M}' := \boldsymbol{m}' \otimes \boldsymbol{m}' \otimes \boldsymbol{m}' \otimes \boldsymbol{m}'. \tag{2.51}$$

2.4.2 Energy-based anisotropic failure criterion

According to experimental data of aortic tissues the related failure mechanism is anisotropic, see, e.g., [203] and [205]. In order to describe the anisotropic failure, we further elaborate on the equation for the evolution of the crack phase-field and substitute the equations $(2.31)_2$, (2.35) in $(2.39)_2$ for $\dot{d} \geq 0$ and then (2.27), (2.28) in $(2.31)_2$ to obtain the following

$$f - \frac{g_{\mathrm{c}}}{l}(d - l^2\Delta d) = 0, \qquad f = 2(1 - d)\Psi_0. \tag{2.52}$$

We now assume distinct failure processes for the ground matrix and the fibers. Accordingly, the energetic force f can be additively decomposed into an isotropic part f_{iso} and an anisotropic part f_{ani} according to

$$f = f_{\mathrm{iso}} + f_{\mathrm{ani}} \begin{cases} f_{\mathrm{iso}} = 2(1 - d)\Psi_0^{\mathrm{iso}}, \\ f_{\mathrm{ani}} = 2(1 - d)\Psi_0^{\mathrm{ani}}. \end{cases} \tag{2.53}$$

Next, we introduce the distinct critical fracture energies over length scale $g_{\mathrm{c}}^{\mathrm{iso}}/l$ for the ground matrix and $g_{\mathrm{c}}^{\mathrm{ani}}/l$ for the fibers which are dual to the free-energy functions for the isotropic and the anisotropic parts, respectively, see (2.42). Consequently, (2.52) can be modified to account for the distinct failure assumption. After some simple algebraic manipulations, we obtain

$$2(1 - d)\frac{\Psi_0^{\mathrm{iso}}}{g_{\mathrm{c}}^{\mathrm{iso}}/l} = d - l^2\Delta d, \qquad 2(1 - d)\frac{\Psi_0^{\mathrm{ani}}}{g_{\mathrm{c}}^{\mathrm{ani}}/l} = d - l^2\Delta d. \tag{2.54}$$

In the subsequent treatment we define dimensionless crack driving functions for the isotropic ($\bar{\mathcal{H}}^{\mathrm{iso}}$) and anisotropic ($\bar{\mathcal{H}}^{\mathrm{ani}}$) parts in (2.54), i.e.

$$\bar{\mathcal{H}}^{\mathrm{iso}} = \frac{\Psi_0^{\mathrm{iso}}}{g_{\mathrm{c}}^{\mathrm{iso}}/l}, \qquad \bar{\mathcal{H}}^{\mathrm{ani}} = \frac{\Psi_0^{\mathrm{ani}}}{g_{\mathrm{c}}^{\mathrm{ani}}/l}. \tag{2.55}$$

By superposing the isotropic and anisotropic failure processes (2.54), we obtain with the use of (2.55)

$$d - l^2 \Delta d = (1-d)\bar{\mathcal{H}}, \qquad \text{where} \qquad \bar{\mathcal{H}} = \bar{\mathcal{H}}^{\text{iso}} + \bar{\mathcal{H}}^{\text{ani}}. \tag{2.56}$$

The left-hand side of $(2.56)_1$ is the geometric resistance to crack growth whereas the right-hand side is the local source term for crack growth [168]. In order to enforce the irreversibility condition and prevent the healing effects, the dimensionless source term $(2.56)_2$ is modified, i.e.

$$\mathcal{H}(t) = \max_{s\in[0,t]} \left[\langle\, \bar{\mathcal{H}}(s) - 1 \,\rangle \right]. \tag{2.57}$$

In the above, the Macaulay brackets $\langle\,(\bullet)\,\rangle = [\,(\bullet) + |(\bullet)|\,]/2$ filter out the positive values for $\bar{\mathcal{H}}(s)$ and keeps the anisotropic solid intact below a threshold energy density, i.e. until the failure surface is reached. Hence, the crack phase-field does not evolve for a dimensionless crack source term $\bar{\mathcal{H}}(s) < 1$. The specific choice for $\mathcal{H}(t)$ ensures in (2.57) the irreversibility of the crack evolution and a positive energetic force f. The failure Ansatz (2.57) can be used for transversely isotropic as well as anisotropic biological tissues with two or more fiber families including dispersion. In Sec. 2.6.1 we investigate some aspects of the proposed failure criterion for a simple homogeneous case.

2.5 Finite Element Formulation

In this section, we present a staggered set of algebraic equations derived from the strong forms of the coupled set of equations through a Galerkin type finite element formulation. At the first stage, we consider two decoupled sub-problems by the virtue of operator-splitting. In the sequel, we construct the weak forms of the equations (2.41), $(2.39)_2$ and consistently linearize them along the field variables, namely the deformation map $\boldsymbol{\varphi}(\boldsymbol{X}, t)$, the crack phase-field $d(\boldsymbol{X}, t)$. An identical temporal as well as spatial discretization scheme is employed for the deformation map and the crack phase-field. The field variables are appropriately discretized with isoparametric shape functions to transform the continuous integral equations of the nonlinear weighted-residuals and their linearizations to a set of coupled, discrete algebraic equations. Finally, this set of algebraic equations are solved by a one-pass operator-splitting algorithm in a Newton-type iterative solver for the nodal degrees of freedom.

2.5.1 One-pass operator-splitting algorithm

We consider a discrete time increment $\tau = t_{n+1} - t_n$ where t_{n+1} and t_n stand for the current and previous time steps, respectively. The operator-splitting algorithm is composed of two sub-algorithms, i.e.

$$\texttt{ALGO}_{\text{CM}} = \texttt{ALGO}_{\text{C}} \circ \texttt{ALGO}_{\text{M}}. \tag{2.58}$$

Here, such an algorithm yields a decoupling within the time interval and results in partitioned symmetric structures for the mechanical and crack-growth sub-problems. In fact,

the operator-splitting algorithm converts the non-convex coupled problem into two convex and symmetric sub-problems which are computationally more feasible than the monolithic scheme. Within this context, the algorithm of each sub-problem is obtained as follows

$$(M): \begin{cases} J\,\mathrm{div}(J^{-1}\boldsymbol{\tau}) + \rho_0\bar{\gamma} = \mathbf{0}, \\ \\ \dot{d} = 0, \end{cases} \quad \text{and} \quad (C): \begin{cases} \dot{\boldsymbol{\varphi}} = \mathbf{0}, \\ \\ d - l^2\Delta d - (1-d)\mathcal{H} = 0. \end{cases} \tag{2.59}$$

The (first) algorithm (M) is the mechanical predictor step which is solved for the frozen crack phase-field parameter $d = d_n$, while the algorithm (C) is the crack evolution step for the frozen deformation map $\boldsymbol{\varphi} = \boldsymbol{\varphi}_n$.

2.5.2 Galerkin-type weak formulation

This section is devoted to the transformation of the coupled balance equations into their weak forms through a conventional Galerkin procedure. To this end, we introduce two test function fields $\delta\boldsymbol{\varphi}$ and δd, which satisfy the essential boundary conditions, according to

$$\begin{aligned} \delta\boldsymbol{\varphi} \in \mathcal{W}_{\delta\varphi} &:= \{\delta\boldsymbol{\varphi} \mid \delta\boldsymbol{\varphi} = \mathbf{0} \quad \text{on} \quad \bar{\boldsymbol{\varphi}} \in \partial\mathcal{B}_{\varphi}\}, \\ \delta d \in \mathcal{W}_{\delta d} &:= \{\delta d \mid \delta d = 0 \quad \text{on} \quad \boldsymbol{X} \in \Gamma(d)\}. \end{aligned} \tag{2.60}$$

The strong form of the equations (2.59) are multiplied with the admissible test functions (2.60) and integrated over the domain $\mathcal{B}$ leading to the weak form for the static force balance and the evolution of the crack phase-field. Following the Galerkin procedure, the Gaussian integral and the Cauchy theorems lead to the subsequent weighted-residual expressions of the field variables for the static force balance, i.e.

$$G^{\varphi} = G^{\varphi}_{\text{int}}(\delta\boldsymbol{\varphi}, \boldsymbol{\varphi}, d) - G^{\varphi}_{\text{ext}}(\delta\boldsymbol{\varphi}) = 0 \begin{cases} G^{\varphi}_{\text{int}} = \displaystyle\int_{\mathcal{B}} \mathrm{sym}[\nabla_x(\delta\boldsymbol{\varphi})] : \boldsymbol{\tau}\,\mathrm{d}V, \\ \\ G^{\varphi}_{\text{ext}} = \displaystyle\int_{\mathcal{B}} \delta\boldsymbol{\varphi}\cdot\rho_0\bar{\gamma}\,\mathrm{d}V + \int_{\partial\mathcal{B}} \delta\boldsymbol{\varphi}\cdot\bar{\boldsymbol{T}}\,\mathrm{d}A, \end{cases} \tag{2.61}$$

where the body force $\bar{\gamma}$ and the surface traction $\bar{\boldsymbol{T}}$ are assumed to be prescribed. Using similar arguments, the weak forms of the phase-field problem can be elaborated as

$$G^{d} = G^{d}_{\text{int}}(\delta d, \boldsymbol{\varphi}, d) - G^{d}_{\text{ext}}(\delta d) = 0 \begin{cases} G^{d}_{\text{int}} = \displaystyle\int_{\mathcal{B}} \delta d[d - (1-d)\mathcal{H}]\mathrm{d}V + \int_{\mathcal{B}} \nabla(\delta d)\cdot l^2\nabla d\,\mathrm{d}V, \\ \\ G^{d}_{\text{ext}} = 0. \end{cases} \tag{2.62}$$

The geometric and the constitutive terms endow the weighted-residual expressions in (2.61) and (2.62) with nonlinearity; hence, a reliable and efficient solution of these equations

entails a consistent linearization with regard to all quantities, i.e. $\boldsymbol{\varphi}$ and d associated with the nonlinear problem about $\boldsymbol{\varphi} = \tilde{\boldsymbol{\varphi}}$ and $d = \tilde{d}$:

$$\begin{aligned} \mathrm{Lin} G^{\varphi}|_{\tilde{\boldsymbol{\varphi}}} &= G^{\varphi}(\delta\boldsymbol{\varphi}, \tilde{\boldsymbol{\varphi}}, d) + \Delta G^{\varphi}(\delta\boldsymbol{\varphi}, \tilde{\boldsymbol{\varphi}}, d; \Delta\boldsymbol{\varphi}) = 0, \\ \mathrm{Lin} G^{d}\Big|_{\tilde{d}} &= G^{d}(\delta d, \boldsymbol{\varphi}, \tilde{d}) + \Delta G^{d}(\delta d, \boldsymbol{\varphi}, \tilde{d}; \Delta d) = 0. \end{aligned} \tag{2.63}$$

The above expressions are fashioned by Taylor's expansion through the Gâteaux derivative that yields the linear incremental terms ΔG^{φ} and ΔG^{d}, which are decomposed in the following way

$$\Delta G^{\varphi} = \Delta G^{\varphi}_{\mathrm{int}} - \Delta G^{\varphi}_{\mathrm{ext}}, \qquad \Delta G^{d} = \Delta G^{d}_{\mathrm{int}} - \Delta G^{d}_{\mathrm{ext}}. \tag{2.64}$$

Since we have prescribed values for the body force $\bar{\gamma}$ and the surface traction $\bar{\boldsymbol{T}}$, the external increment vanishes, i.e. $\Delta G^{\varphi}_{\mathrm{ext}} = 0$. Besides, we conclude that the external term $\Delta G^{d}_{\mathrm{ext}}$ disappears as well. Accordingly, we first operate on $\Delta G^{\varphi}_{\mathrm{int}}$ which takes on the following form

$$\Delta G^{\varphi}_{\mathrm{int}} = \int_{\mathcal{B}} \{\mathrm{sym}[\nabla_x(\delta\boldsymbol{\varphi})] : \mathbb{C} : \mathrm{sym}[\nabla_x(\Delta\boldsymbol{\varphi})] + \nabla_x(\delta\boldsymbol{\varphi}) : \nabla_x(\Delta\boldsymbol{\varphi})\boldsymbol{\tau}\}\mathrm{d}V. \tag{2.65}$$

Maintaining the same formalism, we can now expand on the internal increment $\Delta G^{d}_{\mathrm{int}}$ describing the linearization of the crack phase-field around $\tilde{d}$ at an incremental time step τ, i.e.

$$\Delta G^{d}_{\mathrm{int}} = \int_{\mathcal{B}} \delta d(1 + \mathcal{H})\Delta d \,\mathrm{d}V + \int_{\mathcal{B}} \nabla(\delta d) \cdot l^2 \nabla(\Delta d) \,\mathrm{d}V. \tag{2.66}$$

2.5.3 Spatial discretization

We perform a spatial discretization of the field variables and construct residual vectors together with the element matrices. Here we briefly present an overview of the underlying theoretical aspects of the finite element discretization but mainly focus on the algebraic counterparts of the residual expressions. For an in-depth treatment of the discretization methods we refer to, e.g., [95, 235]. Accordingly, we discretize the reference domain $\mathcal{B}$ into element sub-domains $\mathcal{B}^h_e$ within the body and the Neumann surface $\partial\mathcal{B}$ into $\partial\mathcal{B}^h_e$. Thus, we write

$$\mathcal{B} \approx \bigcup_{e=1}^{\mathrm{n_{el}}} \mathcal{B}^h_e, \qquad \partial\mathcal{B} \approx \bigcup_{e=1}^{\mathrm{n^t_{el}}} \partial\mathcal{B}^h_e, \tag{2.67}$$

where $\mathrm{n_{el}}$ is the number of finite elements while $\mathrm{n^t_{el}}$ stands for the number of surface finite elements. Then, the field variables $\boldsymbol{\varphi}$, d, the weighting functions $\delta\boldsymbol{\varphi}$, δd and the related increments $\Delta\boldsymbol{\varphi}$, Δd are interpolated by the Ansatz functions (shape functions) $\mathcal{N}$ in between physically meaningful free parameters, i.e. the values of the displacement and phase-field at the nodes. In fact, we discretize the field variables, the corresponding

weighting functions and increments by means of the same $\mathcal{C}^0$ continuous shape functions (Bubnov-Galerkin method). These shape functions are then multiplied by the nodal values $\hat{\boldsymbol{x}}$, $\delta\hat{\boldsymbol{x}}$, and $\Delta\hat{\boldsymbol{x}}$ for the deformation field on each element. In an analogous manner, for each element the nodal values $\hat{d}$, $\delta\hat{d}$, and $\Delta\hat{d}$ of the crack phase-field are multiplied by the shape functions. In addition, we need the gradient of the weighting functions ($\nabla_x(\delta\boldsymbol{\varphi})$, $\nabla(\delta d)$) and the incremental fields ($\nabla_x(\Delta\boldsymbol{\varphi})$, $\nabla(\Delta d)$) to be obtained from the partial derivatives of the shape functions ($\nabla_x\mathcal{N}$, $\nabla\mathcal{N}$).

In the next step, we insert the equation (2.67) and the aforestated expressions into (2.61) and (2.62), as formulated in Sec. 2.5.2, in order to obtain the discrete residual vectors

$$\begin{aligned}
\mathbb{R}^{\varphi} &= \mathop{\mathsf{A}}_{e=1}^{\mathrm{n_{el}}} \sum_{i=1}^{\mathrm{n_{en}}} \delta\hat{\boldsymbol{x}}^{\mathrm{T}^i} \int_{\mathcal{B}_e^h} (\boldsymbol{B}^{\mathrm{T}^i}\boldsymbol{\tau}_e - \mathcal{N}^i\rho_{0e}\bar{\boldsymbol{\gamma}}_e)\mathrm{d}V - \mathop{\mathsf{A}}_{e=1}^{\mathrm{n_{el}^t}} \sum_{i=1}^{\mathrm{n_{sf}}} \delta\hat{\boldsymbol{x}}^{\mathrm{T}^i} \int_{\partial\mathcal{B}_e^h} \mathcal{N}^i\bar{\boldsymbol{T}}_e\mathrm{d}A = \boldsymbol{0}, \\
\mathbb{R}^{d} &= \mathop{\mathsf{A}}_{e=1}^{\mathrm{n_{el}}} \sum_{i=1}^{\mathrm{n_{en}}} \delta\hat{d}^i \int_{\mathcal{B}_e^h} \{\mathcal{N}^i[d_e - (1-d_e)\mathcal{H}_e] + \nabla^{\mathrm{T}}\mathcal{N}^i\, l_e^2\nabla d_e\}\mathrm{d}V = 0,
\end{aligned} \tag{2.68}$$

where $(\bullet)_e$ denotes the matrix form of the associated quantities, e.g., $\boldsymbol{\tau}_e$ is the 6×1 Kirchhoff stress matrix, on a typical element, and $\mathrm{n_{en}}$ and $\mathrm{n_{sf}}$ denote the number of nodes per volume and surface element, respectively. In (2.68) we have also introduced the 6×3 matrix $\boldsymbol{B}^i$, associated with node i, which consists of the partial derivatives of the shape functions with respect to the spatial coordinates x_j. In the sequel, we identify the discrete forms of the linearized terms in analogy to the residual vectors by substituting the necessary arguments for the continuous representations in (2.65) and (2.66). The linearization process then reads

$$\mathrm{Lin}\mathbb{R} = \mathbb{R} + \frac{\partial\mathbb{R}}{\partial\mathbb{U}}\Delta\mathbb{U}, \qquad \mathbb{R} = \begin{bmatrix}\mathbb{R}^{\varphi}\\ \mathbb{R}^{d}\end{bmatrix}, \qquad \mathbb{U} = \begin{bmatrix}\boldsymbol{\varphi}^h\\ d^h\end{bmatrix}. \tag{2.69}$$

The insertion of the discrete forms of the field variables yield the coupled element matrix. Thus,

$$\mathbb{K} = \frac{\partial\mathbb{R}}{\partial\mathbb{U}} = \begin{bmatrix}\mathbb{K}^{\varphi\varphi} & \boldsymbol{0}\\ \boldsymbol{0} & \mathbb{K}^{dd}\end{bmatrix}, \tag{2.70}$$

and the element matrices of each sub-problem take on the following forms

$$\begin{aligned}
\mathbb{K}^M := \mathbb{K}^{\varphi\varphi} &= \mathop{\mathsf{A}}_{e=1}^{\mathrm{n_{el}}} \sum_{i=1}^{\mathrm{n_{en}}}\sum_{j=1}^{\mathrm{n_{en}}} \delta\hat{\boldsymbol{x}}^{\mathrm{T}^i}\boldsymbol{K}^{ij}_{\varphi\varphi,e}\Delta\hat{\boldsymbol{x}}^j, \\
\mathbb{K}^C := \mathbb{K}^{dd} &= \mathop{\mathsf{A}}_{e=1}^{\mathrm{n_{el}}} \sum_{i=1}^{\mathrm{n_{en}}}\sum_{j=1}^{\mathrm{n_{en}}} \delta\hat{d}^i\boldsymbol{K}^{ij}_{dd,e}\Delta\hat{d}^j,
\end{aligned} \tag{2.71}$$

where $\mathbb{K}^M$ is the stiffness matrix related to the mechanical predictor, while $\mathbb{K}^C$ is the stiffness matrix describing the crack evolution. The components of the tangent matrices

$\boldsymbol{K}^{ij}_{\varphi\varphi,e}$ and $\boldsymbol{K}^{ij}_{dd,e}$ for one element related to the nodes i, j can be given as

$$\begin{aligned}\boldsymbol{K}^{ij}_{\varphi\varphi,e} &= \int_{\mathcal{B}^h_e} (\boldsymbol{B}^{\mathrm{T}^i} \boldsymbol{D}_e \boldsymbol{B}^j + \nabla_x^{\mathrm{T}} \mathcal{N}^i \boldsymbol{\tau}_e \nabla_x \mathcal{N}^j) \mathrm{d}V, \\ \boldsymbol{K}^{ij}_{dd,e} &= \int_{\mathcal{B}^h_e} [\mathcal{N}^i (1+\mathcal{H}_e) \mathcal{N}^j + \nabla^{\mathrm{T}} \mathcal{N}^i l_e^2 \nabla \mathcal{N}^j] \mathrm{d}V,\end{aligned} \tag{2.72}$$

where $\boldsymbol{D}_e$ designates the matrix form of the elasticity tensor $\mathbb{C}$ for a typical element. Table 2.1 summarizes the operator-splitting algorithm which forms the basis for the implementation of the numerical scheme; the phase-field d is driven by the local history field $\mathcal{H}(t_{n+1})$.

Table 2.1 Operator-splitting algorithm for the multi-field problem in $[t_n, t_{n+1}]$.

1. *Initialization*	–	At time t_n given: deformation map, phase-field, history field $\boldsymbol{\varphi}_n$, d_n, $\mathcal{H}_n$
2. *Update*	–	Update the prescribed loads $\bar{\boldsymbol{\gamma}}$, $\bar{\boldsymbol{\varphi}}$ and $\bar{\boldsymbol{T}}$ at current time t_{n+1}
3. *Compute* $\boldsymbol{\varphi}_{n+1}$	–	Determine $\boldsymbol{\varphi}_{n+1}$ from the minimization problem of elasticity
ALGO$_M$	•	$G^{\varphi} = \int_{\mathcal{B}} \mathrm{sym}[\nabla_x(\delta\boldsymbol{\varphi})] : \boldsymbol{\tau} \mathrm{d}V - \int_{\mathcal{B}} \delta\boldsymbol{\varphi} \cdot \rho_0 \bar{\boldsymbol{\gamma}} \mathrm{d}V - \int_{\partial\mathcal{B}} \delta\boldsymbol{\varphi} \cdot \bar{\boldsymbol{T}} \mathrm{d}A = 0$
4. *Compute history*	–	Check crack initiation/propagation condition, update history
	•	$\mathcal{H}(t_{n+1}) \leftarrow \begin{cases} \mathcal{H}(t_n) & \text{if} \quad \mathcal{H}(t_{n+1}) < \mathcal{H}(t_n) \\ \mathcal{H}(t_{n+1}) & \text{else} \end{cases}$
5. *Compute* d_{n+1}	–	Determine d_{n+1} from the minimization problem of crack topology
ALGO$_C$	•	$G^d = \int_{\mathcal{B}} \delta d[d - (1-d)\mathcal{H}] \mathrm{d}V + \int_{\mathcal{B}} \nabla(\delta d) \cdot l^2 \nabla d \, \mathrm{d}V = 0$

2.6 Representative Numerical Examples

In this section, we illustrate the performance of the proposed crack phase-field model applied to aortic fracture through numerical simulations to capture the experimental data. The failure criterion with the related failure envelope is analyzed in Sec. 2.6.1 for a simple geometry and loading condition (homogeneous problem), while Sections 2.6.2 and

2.6.3 show numerical simulations for uniaxial extension and simple shear tests with the anisotropic failure criterion (2.57).

The experiments are conducted on aneurysmatic specimens extracted from the media of a human thoracic aorta possessing two families of collagen fibers. The performed numerical simulations are based on the experimental data of the specimens which were obtained through different deformation modes (uniaxial extension and simple shear in the circumferential and longitudinal directions); for more details see the recent study [205], specimen *AVIII* therein.

2.6.1 Numerical investigation of the failure criterion for a homogeneous problem

Although the initiation and propagation of a crack in a tissue can become a highly inhomogeneous phenomenon in terms of stress es and strains, driven by an intricate combination of deformation modes, a homogeneous problem with simple loading conditions can provide further insight to the energy-based anisotropic failure criterion used in the present model. Therefore, we consider a unit cube discretized by one hexahedral element which resolves the analytical solution for the deformation and stress, and discards all non-local effects due to the gradient of the crack phase-field ∇d and the length-scale parameter l ($= 1\,\text{mm}$), see Fig. 2.5(a). In this case, the tissue is regarded to be transversely isotropic with one family of fibers oriented along the x-direction. The elastic parameters required for the constitutive law are chosen to be $\mu = 10\,\text{kPa}$, $k_1 = 20\,\text{kPa}$ and $k_2 = 1$. As for the crack phase-field, the critical fracture energies are selected as $g_\text{c}^\text{iso} = 5\,\text{kPa}\,\text{mm}$ and $g_\text{c}^\text{ani} = 15\,\text{kPa}\,\text{mm}$. We investigate several loading conditions. First, we perform uniaxial extension tests along the x and the y-direction with a stretch ratio $\lambda_x = 2$ and $\lambda_y = 2$, respectively. Subsequently, the tissue undergoes biaxial deformations with the stretch ratios $\lambda_x : \lambda_y = 2 : 1.1, 2 : 1.25, 2 : 1.5, 2 : 1.75, 2 : 2, 1.75 : 2, 1.5 : 2, 1.25 : 2$, and $1.1 : 2$.

Figure 2.5(a) demonstrates the obtained failure envelope at which the failure criterion is satisfied, leading to $d > 0$. The corresponding isotropic and anisotropic energy states of the tissue are shown in Fig. 2.5(b). Therein the uniaxial extension in the x-direction up to a stretch of 2 leads to a stress and energy state denoted by A, whereas C pinpoints the uniaxial extension in the y-direction up to a stretch of 2. The stress and energy states due to the equibiaxial stretch $2 : 2$ are indicated by B. This study clearly addresses the anisotropy of the failure criterion. In fact, the plane-stress failure envelope exhibits an elliptic curve for the investigated stretch ratios, while the failure energy interpolates linearly between the anisotropic and isotropic free-energies for the transversely isotropic tissue.

2.6.2 Uniaxial extension tests of thoracic aorta with anisotropic failure

In the experimental investigations, excised aneurysmatic medial strips from a human thoracic aorta are tested along the circumferential (θ) and longitudinal (z) directions by means of uniaxial extension in accordance with the testing protocol documented in [205]. These aforecited tests are numerically reproduced *in silico* with a monotonic load pattern (stretch λ) exerted on the strips with an incision, as depicted in Fig. 2.6(a). The finite

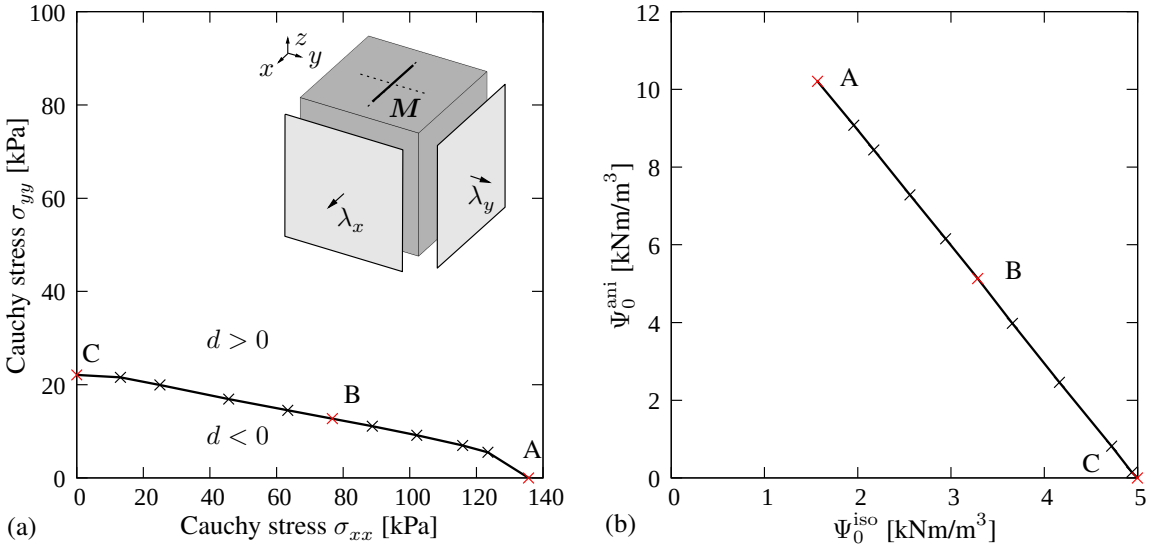

Figure 2.5 (a) Unit cube with a transversely isotropic tissue consisting of one family of fibers with orientation $\boldsymbol{M}$ parallel to the x-direction – failure envelope in regard to the Cauchy stresses σ_{xx} and σ_{yy} at which the failure criterion is satisfied, leading to $d > 0$; (b) corresponding isotropic and anisotropic energy states of the tissue (Ψ_0^{iso}, Ψ_0^{ani}).

element mesh of the strip is generated with $3\,880$ eight-node hexahedral elements with a length-scale parameter $l = 0.4\,\mathrm{mm}$. The generated mesh is refined in the regions between the incision and the opposite edge for which l satisfies $l \geq 2h$ for the crack zone to be resolved properly [143], where h denotes the minimum element size, see Fig. 2.6(b). The displacements are constraint at the $\theta = 0$, $r = 0$, and $z = 0$ planes along the θ-, r-, and z- directions, respectively. The geometry and the related finite element mesh of the incised strip is the analogue of Fig. 2.6.

While the elastic material parameters are estimated via nonlinear least-squares analysis by utilizing *lsqnonlin* on MATLAB® at a material point, the critical fracture energies $g_{\mathrm{c}}^{\mathrm{iso}}$ and $g_{\mathrm{c}}^{\mathrm{ani}}$ according to (2.55) are identified for each test through a quantitative comparison of the stress-stretch curves of the simulation results with those of the corresponding experimental data. It should be noted that in the nonlinear least-squares analysis we used the stress-stretch data until the ultimate stress which leads to the aforementioned elastic material parameters. The elastic and the crack phase-field parameters are summarized in Table 2.2. For a comparison of uniaxial extension test data with the finite element results in terms of Cauchy stress versus stretch for strips in the circumferential and longitudinal directions see Fig. 2.7(a),(b). Note that the curves provided via finite element analysis are obtained by considering the average of all nodal stresses at the planes $\theta = 12\,\mathrm{mm}$ and $z = 12\,\mathrm{mm}$ in the circumferential and longitudinal directions, respectively. The results agree favorably with the anisotropic response of the tissue obtained from the experiments. The crack initiates from the tip of the incised region where the stress concentration and, therefore, the energy of the intact tissue takes on larger values than the other regions, and hence satisfies

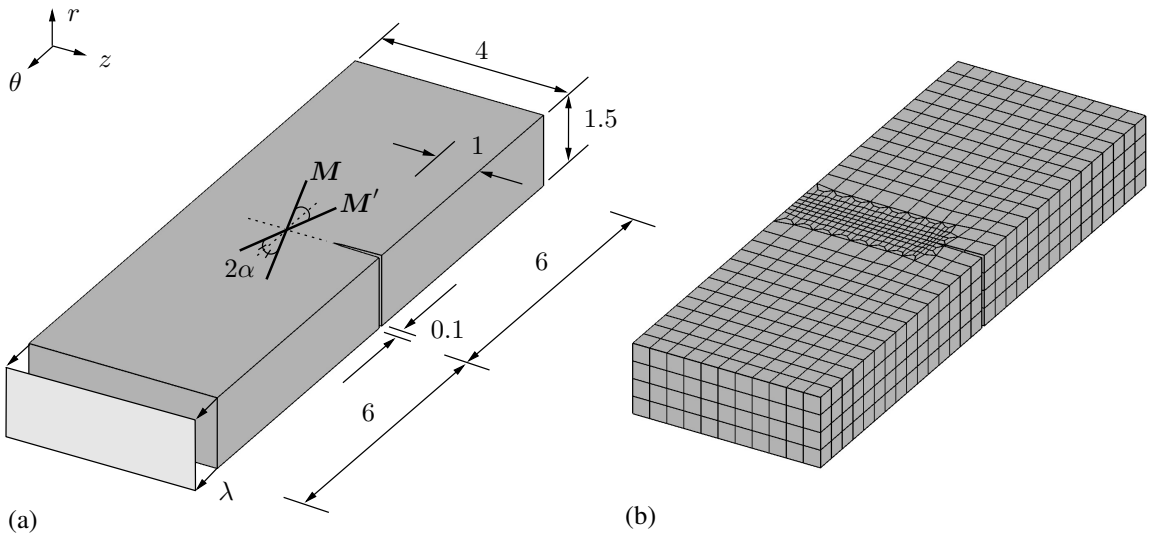

Figure 2.6 (a) Geometry of the specimen oriented in the circumferential θ-direction, uniaxially loaded by stretch λ. The structure of the media is characterized by two families of fibers, oriented in the directions $\boldsymbol{M}$ and $\boldsymbol{M}'$ in the reference configuration, corresponding to the collagenous component of the material, and they are symmetrically arranged with respect to the cylinder axis – α is the angle between the fibers and the circumferential direction; (b) finite element mesh of the corresponding geometry with refinement around the incision. Dimensions are provided in millimeters.

Table 2.2 Elastic and crack phase-field parameters for anisotropic failure of aneurysmatic circumferential and longitudinal medial strips of an aorta under uniaxial extension.

Elastic	μ	$= 16.95\,\text{kPa}$
	k_1	$= 243.57\,\text{kPa}$
	k_2	$= 2.57$
	α	$= 44.5^\circ$
Crack phase-field	g_c^iso	$= 32\,\text{kPa mm}$ along the θ-direction
	g_c^ani	$= 112\,\text{kPa mm}$ along the θ-direction
	g_c^iso	$= 32\,\text{kPa mm}$ along the z-direction
	g_c^ani	$= 35\,\text{kPa mm}$ along the z-direction

the failure condition. What follows is a nearly straight pattern as the phase-field grows toward s the opposite edge at which the failure occurs. This is realized by a sudden loss of the load-bearing capacity , as illustrated in the corresponding stress-stretch curves of Fig. 2.7. Figure 2.8 shows the distributions of the crack phase-field d and the circumferential Cauchy stress $\sigma_{\theta\theta}$ at the particular stress-stretch locations A, B, C and D, as indicated

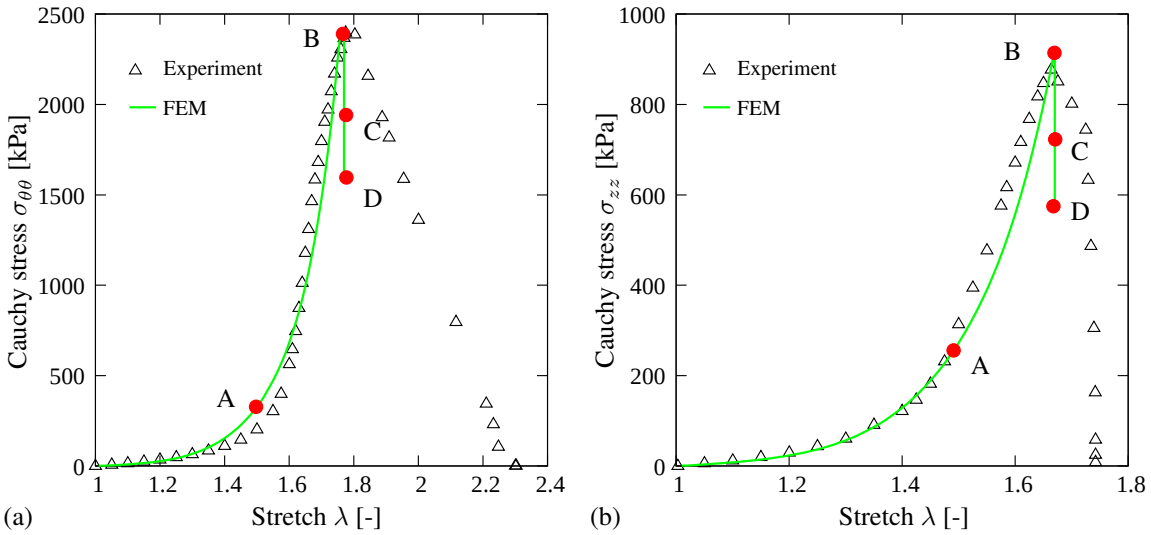

Figure 2.7 Uniaxial extension test data (triangles) and corresponding finite element results (solid curves): Cauchy stress versus stretch for a strip in (a) the circumferential θ-direction and (b) the longitudinal z-direction.

in Fig. 2.7(a), while the related crack phase-field d and the longitudinal Cauchy stress σ_{zz} at the four states indicated in Fig. 2.7(b) are shown in Fig. 2.9.

2.6.3 Simple shear tests of thoracic aorta with anisotropic failure

Concerning the simple shear tests, the medial specimens are subjected to shear along the θ- and z-directions, referred to as $z\theta$ mode and θz mode (the first index refers to the plane while the second to the direction), respectively. Incisions are made to induce failure on a certain plane, see [205]. Such experiments are replicated computationally with respect to a monotonic shear load applied to the specimens with symmetric incisions; for the related geometries see Fig. 2.10(a),(c). In the sequel, the geometry of the specimen, which is sheared along the θ-direction ($z\theta$ mode), is discretized with $23\,525$ four-node tetrahedral elements with a length-scale parameter $l = 0.167$ mm, see Fig. 2.10(b), while for the other geometry (θz mode) $22\,657$ finite elements are used with $l = 0.25$ mm, see Fig. 2.10(d). Note that l is chosen to satisfy $l > 2h$ in order to resolve the crack surface properly, see [143]. The meshes are refined in the areas where the crack is expected to propagate in order to resolve the crack zone. With respect to the Dirichlet-boundary conditions the nodes on the $z = 0$ plane are constraint in three directions for the $z\theta$ mode, while those located on the $\theta = 0$ plane are constraint in three directions for the θz mode. The elastic material parameters are estimated via nonlinear least-squares analysis by utilizing *lsqnonlin* on MATLAB®. The critical fracture energies $g_{\mathrm{c}}^{\mathrm{iso}}$ and $g_{\mathrm{c}}^{\mathrm{ani}}$ are predicted for each mode through a quantitative comparison of the Cauchy stress versus the amount of shear curves of the simulation results with those of the corresponding experiments. The elastic and the crack-field parameters for simple shear are summarized in Table 2.3. Here the mechanical

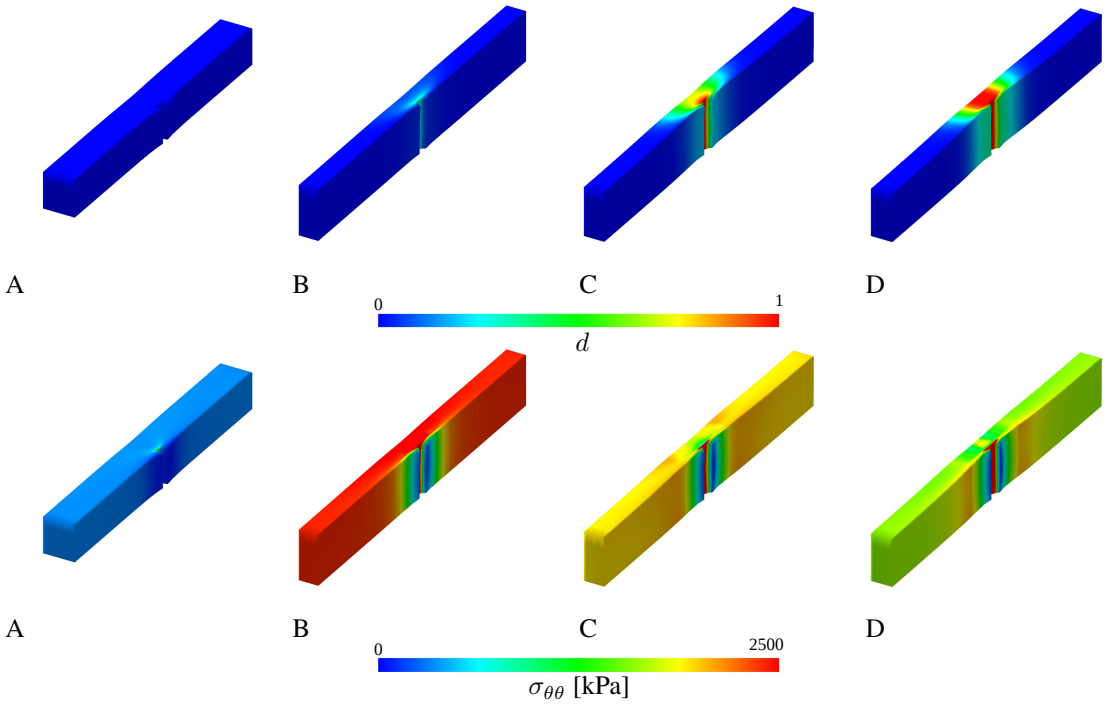

Figure 2.8 Numerical results of uniaxial extension in the circumferential θ-direction with anisotropic failure at the stress-stretch locations A, B, C and D indicated in Fig. 2.7(a): (above) distribution of crack phase-field d; (below) corresponding circumferential Cauchy stress $\sigma_{\theta\theta}$.

response of the tissue is also assumed to be elastic up to the ultimate stress yielding the aforestated elastic material parameters.

Figure 2.11 shows the finite element results in terms of the Cauchy stress ($\sigma_{z\theta}$ and $\sigma_{\theta z}$) versus the amount of shear (γ) and they agree well with the anisotropic experimental response. It needs to be underlined that the numerical results provided in Fig. 2.11 are obtained by considering the average of all nodal stresses at the edge $z = \theta = 3\,\text{mm}$ for the $z\theta$ mode, and at the edge $\theta = 3$, $z = 5\,\text{mm}$ for the θz mode. The onset of the cracks is observed at the two tips of the symmetrically incised region where the stress concentration, and therefore, the energy of the intact tissue satisfies the failure condition. The two distinct crack patterns meet in the middle of the refined region at which the complete failure phenomenon manifests itself. This is accompanied by the sudden loss of the load-bearing capacity as depicted in the corresponding curves of the Cauchy shear stress versus the amount of shear, see Fig. 2.11. Figure 2.12 illustrates the distributions of the crack phase-field d and the Cauchy shear stress $\sigma_{z\theta}$ at the locations A, B, C and D (indicated in Fig. 2.11(a)), while the crack phase-field d and the shear stress $\sigma_{\theta z}$ at the four states (according to Fig. 2.11(b)) are displayed in the Fig. 2.13.

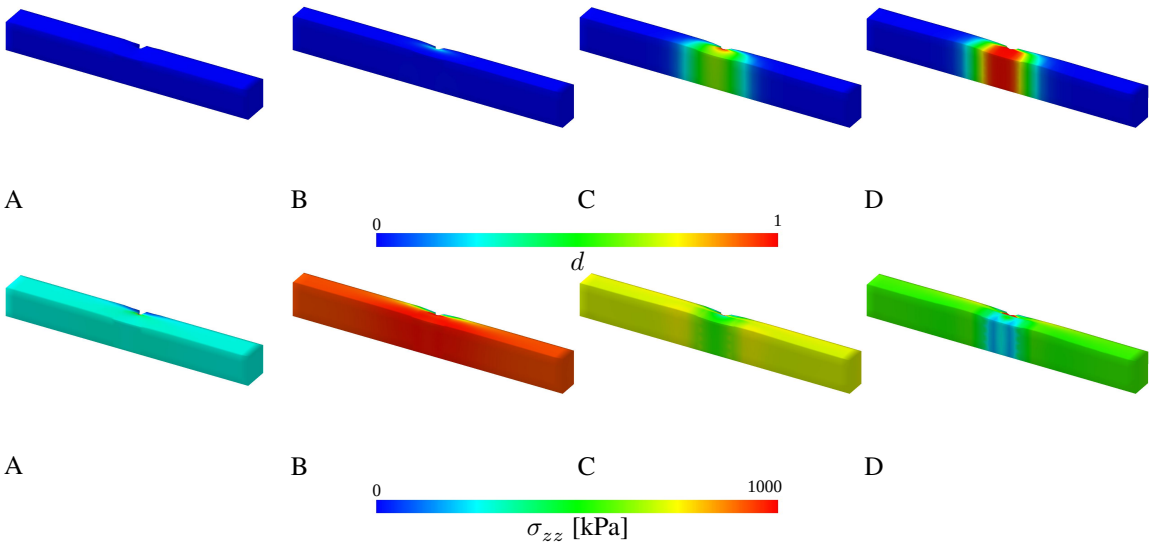

Figure 2.9 Numerical results of uniaxial extension in the longitudinal z-direction with anisotropic failure at the stress-stretch locations A, B, C and D indicated in Fig. 2.7(b): (above) distribution of crack phase-field d; (below) corresponding longitudinal Cauchy stress σ_{zz}.

2.7 Discussion

In this study we have proposed a new anisotropic crack phase-field approach to model failure of aortic tissues undergoing finite deformation. An anisotropic invariant-based hyperelastic model along with the phase-field model of fracture describe the elastic mechanical behavior of the tissue and the associated crack growth, respectively. The evolution of the crack phase-field was constructed on the basis of two critical fracture energies, one for the ground matrix and the other one for the collagen fibers. On the theoretical side, the multi-field problem was established on a rate-type variational principle, while on the numerical side the time-discrete incremental counterpart of the rate-type variational principle was replaced by a Galerkin-type weak formulation where the staggered finite element formulation was employed for a quasi-static process.

On the constitutive part, the aortic tissue (in this study it is the media) is treated as a fiber-reinforced material with the fibers corresponding to the collagenous component of the material and symmetrically disposed with respect to the cylinder axis; the used constitutive law is nonlinear and anisotropic. The evolution of the crack phase-field is dictated by an energy-based anisotropic failure criterion using critical fracture energies which relate to the ground matrix and the collagen fibers, as emphasized in Sec. 2.4.2. In addition, we also focused on the numerical implementation of the model and, finally, present quantitative comparisons of simulation results with experimental data that substantiate our modeling endeavors.

Aortic tissues are structurally comparable to fiber-reinforced composites. The mechanical behavior of the tissue before and after the onset of a crack is strongly dependent on

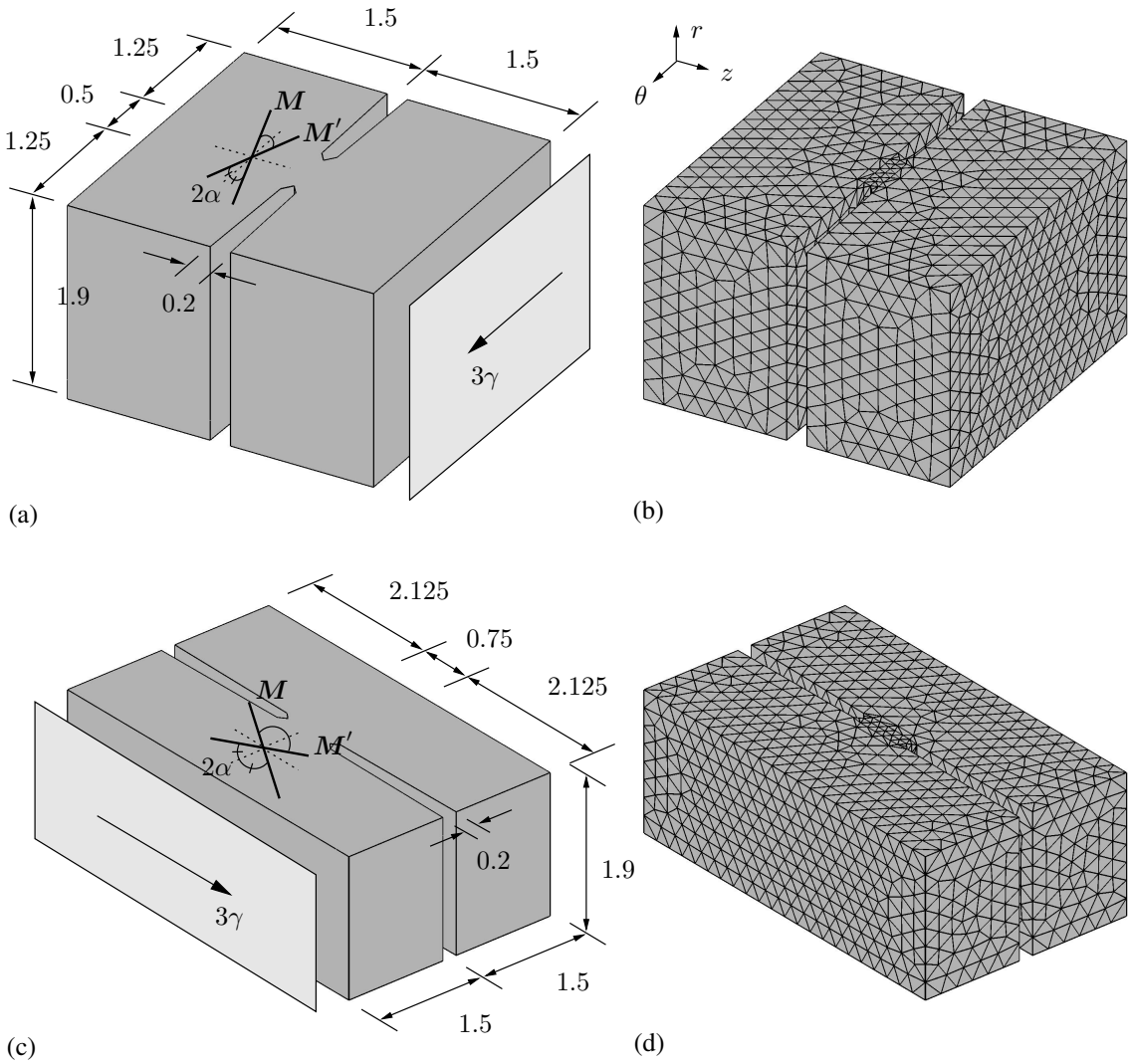

Figure 2.10 (a),(c) Geometries of the specimens sheared in the circumferential θ-direction ($z\theta$ mode) and in the longitudinal z-direction (θz mode) by the displacement 3γ (thickness times amount of shear). The structure of the media is characterized by two families of fibers, oriented in the directions $\boldsymbol{M}$ and $\boldsymbol{M}'$ in the reference configuration, corresponding to the collagenous component of the material, and they are symmetrically arranged with respect to the cylinder axis – α is the angle between the fibers and the circumferential direction; (b),(d) related finite element meshes of the corresponding geometries with refinements around the incisions. Dimensions are provided in millimeters.

the heterogeneties of the material, i.e. regional variations of tissue components such as collagen and elastin, existence of micro-defects, micro-calcification, etc. [71, 101, 102]. Accordingly, the hyperelastic constitutive model and the failure criterion presented here

Table 2.3 Elastic and crack phase-field parameters for anisotropic failure of aneurysmatic aortic specimens under simple shear along the circumferential (θ) and longitudinal (z) directions.

Elastic	μ	$= 80.74\,\text{kPa}$
	k_1	$= 62.04\,\text{kPa}$
	k_2	$= 0.23$
	α	$= 53.68^\circ$
Crack phase-field	g_c^iso	$= 80\,\text{kPa mm}$ along the θ-direction
	g_c^ani	$= 105\,\text{kPa mm}$ along the θ-direction
	g_c^iso	$= 120\,\text{kPa mm}$ along the z-direction
	g_c^ani	$= 240\,\text{kPa mm}$ along the z-direction

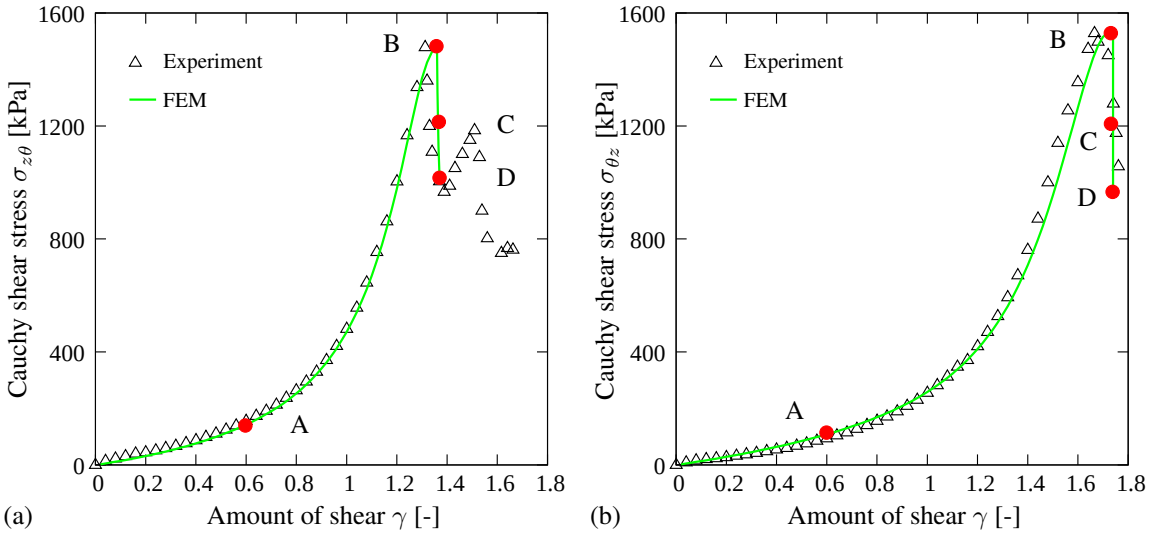

Figure 2.11 Simple shear test data (triangles) and corresponding finite element results (solid curves): (a) Cauchy shear stress $\sigma_{z\theta}$ versus amount of shear γ for the $z\theta$ mode; (b) Cauchy shear stress $\sigma_{\theta z}$ versus γ for the θz mode.

can be modified in order to consider the tissue micro-structure, e.g., histologically related parameters such as the density and dispersion of collagen fibers. In particular, the dispersion of collagen fibers both in-plane and out-of-plane, see [85] for more details, may considerably affect the failure mechanism. In addition, in order to shape the overall mechanical response of the tissue the role of collagen cross-links and proteoglycans should not be overlooked.

Tissue failure often occurs within different loading steps, i.e. in a typical stress-stretch curve two, sometimes more peaks can be observed until complete rupture. Thereby, the

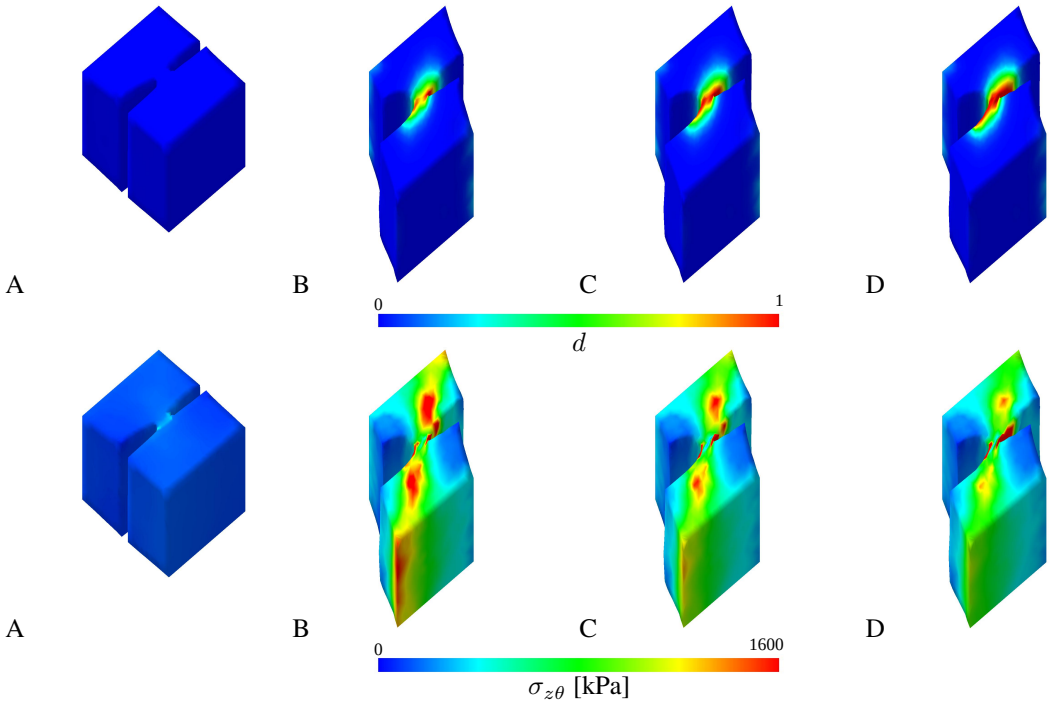

Figure 2.12 Distributions of the finite element results of simple shear in the circumferential θ-direction ($z\theta$ mode) with anisotropic failure at the locations A, B, C and D according to Fig. 2.11(a): (above) distribution of crack phase-field d; (below) corresponding Cauchy shear stress $\sigma_{z\theta}$.

rupture of one fiber bundle is followed by the other; see, e.g., the experimental shear data ($z\theta$ mode) illustrated in Fig. 2.11(a). In a sense, this evokes a distinct evolution of the crack phase-field in regard to each fiber family, as suggested in [65]. The experimental tissue data of the post-cracking behavior, i.e. the mechanical response of the tissue beyond reaching the ultimate stress until complete rupture, show also a considerable variability, see, e.g., Fig. 2.11. An alternative modeling approach which may increase the numerical accuracy is the use of a higher-order phase-field model, see, e.g., [121]. That allows to capture the fracture of highly anisotropic solids at finite strains.

One of the criticisms of the presented model may be the choice of the elastic material parameters that render two different parameter sets, compare with Tables 2.2 and 2.3. We hereby point out that the fusion of the uniaxial extension and shear test data, at least for the experimental data set we use, was not satisfactory, albeit we tried to minimize one objective function involving the sum of squares of both uniaxial and shear responses. In other words we were not able to find one set of elastic parameters which was able to mimic both tests. The same unsatisfactory results were observed by trying to use one set of $g_{\mathrm{c}}^{\mathrm{iso}}$ and $g_{\mathrm{c}}^{\mathrm{ani}}$ throughout the finite element simulations.

We note that in the presented study we focused on the mechanical response of the medial tissue, treated as a solid, and we entirely neglect the intricate feed-back mecha-

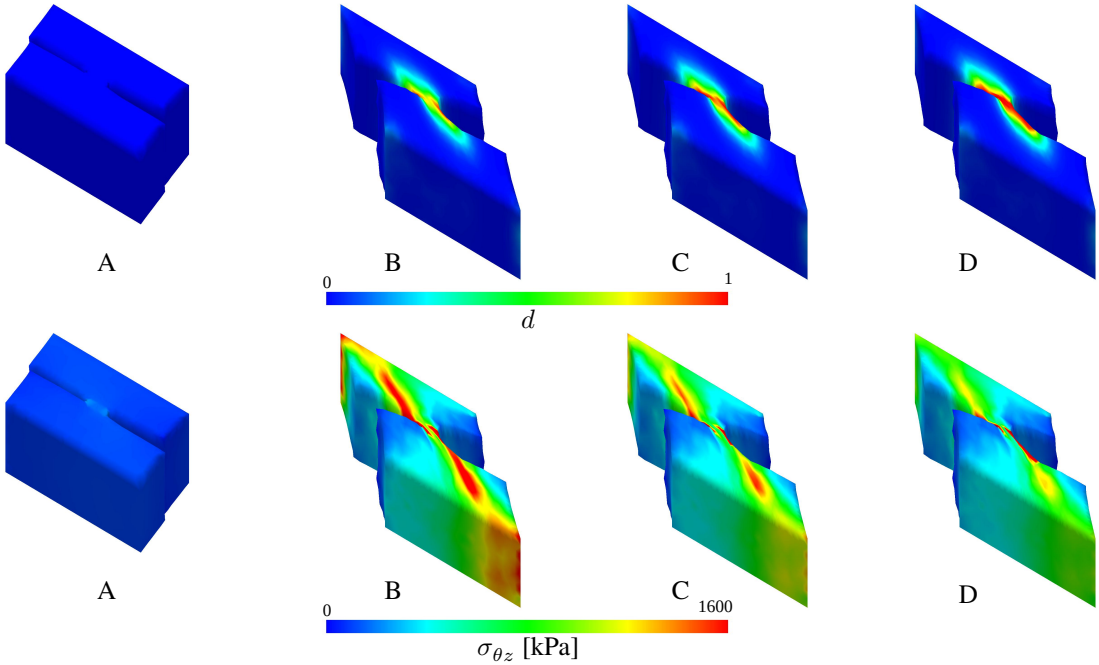

Figure 2.13 Distributions of the numerical results of simple shear in the longitudinal z-direction (θz mode) with anisotropic failure at the locations A, B, C and D according to Fig. 2.11(b): (above) distribution of crack phase-field d; (below) corresponding Cauchy shear stress $\sigma_{\theta z}$.

nism between the mechanical and the biochemical environment of the tissue known as *mechanotrandsduction*. Nevertheless, the presented approach with the aforementioned phenomenological and structurally motivated enhancements provides the basis to model fracture of soft biological tissues, in particular of aortic tissues, which may occur in pathologies such as aneurysms and atherosclerotic plaques but also in healthy tissues due to impact loads that may occur during an accident.

Acknowledgments

H.D. gratefully acknowledges financial support from TUBITAK (BIDEB 2232, Project # 114C073), while O.G. acknowledges financial support from the National Institutes of Health (research grant no. NIH 7R01HL117063-03). Discussion and the provision of Fig. 1 by Selda Sherifova and Dr. Gerhard Sommer are acknowledged.

2.8 Appendix

2.8.1 Derivation of the Euler-Lagrange equations (2.25)

The minimization principle (2.23) can be interpreted as the first variation of the regularized crack surface $\delta\Gamma_l(d)$ to be equal to zero. With the use of (2.21) and (2.22) we

obtain

$$\begin{aligned}\delta\Gamma_l(d) &= \partial_d \Gamma_l(d)\,\delta d + \partial_{\nabla d}\Gamma_l(d)\nabla\delta d \\ &= \frac{1}{l}\int_{\mathcal{B}} (d\,\delta d + l^2\nabla d\cdot\nabla\delta d)\mathrm{d}V = 0. \end{aligned} \tag{2.73}$$

Let us now focus on the second term in $(2.73)_2$. The exploitation of the product rule gives

$$\int_{\mathcal{B}} l^2\nabla d\cdot\nabla\delta d\mathrm{d}V = l^2\int_{\mathcal{B}} \mathrm{Div}(\nabla d\,\delta d)\mathrm{d}V - l^2\int_{\mathcal{B}} \Delta d\,\delta d\mathrm{d}V, \tag{2.74}$$

and the Gaussian integral theorem provides

$$\int_{\mathcal{B}} l^2\nabla d\cdot\nabla\delta d\,\mathrm{d}V = l^2\int_{\partial\mathcal{B}} \nabla d\cdot\boldsymbol{N}\delta d\mathrm{d}A - l^2\int_{\mathcal{B}} \Delta d\,\delta d\,\mathrm{d}V \tag{2.75}$$

so that from $(2.73)_2$ we obtain

$$\delta\Gamma_l(d) = \frac{1}{l}\int_{\mathcal{B}} (d - l^2\Delta d)\delta d\mathrm{d}V + l\int_{\partial\mathcal{B}} \nabla d\cdot\boldsymbol{N}\delta d\,\mathrm{d}A = 0. \tag{2.76}$$

For any δd this relation is zero when $d - l^2\Delta d = 0$ in $\mathcal{B}$ and $\nabla d\cdot\boldsymbol{N} = 0$ on $\partial\mathcal{B}$, which is the requested result (2.25).

3 NUMERICAL ASPECTS OF ANISOTROPIC FAILURE IN SOFT BIOLOGICAL TISSUES FAVOR ENERGY–BASED CRITERIA: A RATE–DEPENDENT ANISOTROPIC CRACK PHASE–FIELD MODEL

Abstract A deeper understanding to predict fracture in soft biological tissues is of crucial importance to better guide and improve medical monitoring, planning of surgical interventions and risk assessment of diseases such as aortic dissection, aneurysms, atherosclerosis and tears in tendons and ligaments. In our previous contribution (Gültekin, et al., CMAME, 312:542-566, 2016) we have addressed the rupture of aortic tissue by applying a holistic geometrical approach to fracture, namely the crack phase-field approach emanating from variational fracture mechanics and gradient damage theories. In the present study, the crack phase-field model is extended to capture anisotropic fracture using an anisotropic volume-specific crack surface function. In addition, the model is equipped with a rate-dependent formulation of the phase-field evolution. The continuum framework captures anisotropy, is thermodynamically consistent and based on finite strains. The resulting Euler-Lagrange equations are solved by an operator-splitting algorithm on the temporal side which is ensued by a Galerkin-type weak formulation on the spatial side. On the constitutive level, an invariant-based anisotropic material model accommodates the nonlinear elastic response of both the ground matrix and the collagenous components. Subsequently, the basis of extant anisotropic failure criteria are presented with an emphasis on energy-based, Tsai-Wu, Hill, and principal stress criteria. The predictions of the various failure criteria on the crack initiation, and the related crack propagation are studied using representative numerical examples, i.e. a homogeneous problem subjected to uniaxial and planar biaxial deformations is established to demonstrate the corresponding failure surfaces whereas uniaxial extension and peel tests of an anisotropic (hypothetical) tissue deal with the crack propagation with reference to the mentioned failure criteria. Results favor the energy-based criterion as a better candidate to reflect a stable and physically meaningful crack growth, particularly in complex three-dimensional geometries with a highly anisotropic texture at finite strains.

3.1 Introduction

The estimation of failure mechanisms in soft biological tissues is of fundamental importance for medical monitoring and preoperative planning of diseases ranging not only from aneurysms (Humphrey and Holzapfel [99] and Kim et al. [115]) to atherosclerosis (Chatzizisis et al. [25] and Holzapfel et al. [92]), but it also pertains to aortic dissection (Criado [35] and Roccabianca et al. [175]) and tears in ligaments and tendons (Lee

et al. [117], Weiss and Gardiner [231] and Sharma and Maffulli [192]). However, the tangled structural composition of soft biological tissues and the gap in our knowledge on the biochemomechanical processes occurring in the tissue at different scales still pose a number of challenges on the modeling endeavors. Besides, the intricate *in vivo* loading conditions impose conspicuous limits on computational models to characterize physically relevant failure. In our previous contribution (Gültekin et al. [66]) we have addressed these issues by establishing a continuum framework within the context of the crack phase-field approach and proposed a novel energy-based anisotropic failure criterion, the linchpin of any fracture model. To date, several contributions have been made with respect to failure criteria, however, to the best of the authors' knowledge, none of them has touched upon the numerical comparisons of failure criteria by embedding them into a finite element formulation at finite strains. In addition, the variety of failure criteria in terms of arguments treated therein (e.g., free-energy functions, stress or strain tensors) makes it necessary to investigate them thoroughly, expose their strengths and weaknesses in terms of their capability to describe an admissible failure surface and a crack propagation which in the end leads to rupture.

Fracture of many materials is preceded and influenced by the progressive occurrence and the interaction of various micro and macro-cracks. Therein included are soft biological tissues which behave anisotropically, a feature originating from the complex collagenous texture embedded in a rather soft isotropic matrix. To elucidate the phenomena of fracture, the strength of materials traditionally provides analytic relations for the failure under combined stresses. Another approach called fracture mechanics regards the failure as a progressive process where the material is assumed to contain flaws for which the size, shape and location determine fracture (Tsai and Hahn [221] and Talreja and Singh [213]). Hill [77] proposed a failure criterion along the lines of von Mises and Huber to account for anisotropic materials, a modification of which was presented by Azzi and Tsai [7], commonly referred to as the Tsai-Hill criterion. The criterion by Tsai and Wu [222] takes different classes of materials into account, thereby conferring a much wider spectrum which ranges from triclinic to isotropic materials. In addition, we refer to two intriguing anisotropic failure criteria proposed mainly for composite laminates, namely the stress-invariant based criterion by Hashin [73] and the strain-energy based criterion by Wolfe and Butalia [234], applied to small strains.

Computational modeling of fracture traditionally deals with the numerical treatment of complex crack topologies, i.e. surface discontinuities. In this regard, numerous contributions have been proposed to date, see, e.g., cohesive element formulations (Ortiz and Pandolfi [160] and Ferrara and Pandolfi [50, 51]), element enrichment techniques (Simo et al. [198] and Linder and Armero [123]), nodal enrichment techniques (Belytschko and Black [11], Moës et al. [146] and Gasser and Holzapfel [57]), and energy limiter approaches (Dal and Kaliske [37]), to name but a few. In contrast, the crack phase-field model of fracture avoids the realization of discontinuities and surmounts the well-known shortcomings of the classical theory of brittle fracture by Griffith [63] and Irwin [108], e.g., the determination of curvilinear crack paths and branching angles, as introduced by Francfort and

Marigo [54] in the context of a variational principle due to an energy minimization. The numerical implementation of this variational principle conducted by Bourdin et al. [17] approximates the Mumford-Shah functional (Mumford and Shah [149]) with a framework based on the Γ-convergence theory, see Ambrosio and Tortorelli [4]. The key aspect of all these contributions is to provide a diffusive crack topology by smearing out the sharp crack surface over a solid domain regularized by a length-scale parameter l. Recent contributions documented by Miehe and coworkers [140, 143] provide a thermodynamically consistent and canonical algorithmic framework for the phase-field formulation for brittle fracture. Extension of these models to dynamic brittle fracture are presented in the studies of Borden et al. [16] and Hofacker and Miehe [78]. The phase-field approach to fracture has hitherto been successfully applied to several coupled multi-physics problems ranging from thermoelastic-plastic to chemomechanical fracture, see, e.g., Miehe et al. [138, 139, 142]. Albeit their resemblance of gradient damage theories, crack phase-field models contain the essential ingredients of fracture mechanics such as the critical fracture energy g_{c} (Griffith-type critical energy release rate), see Griffith [63]. In the meantime, they act as a mediator between the aforementioned approaches, i.e. the strength of materials and the fracture mechanics by bringing them on the same platform.

Based on the extended Cahn-Hilliard model (Cahn and Hilliard [21]), the orientation-dependent crack phase-field evolution has been considered recently by, e.g., Li et al. [121] and Teichtmeister et al. [216] to account for the anisotropic surface energy emanating from the preferred directions in materials. Moreover, Clayton and Knap [28] and Nguyen et al. [152] proposed anisotropic phase-field models for polycrystals. In several materials such as soft biological tissues the anisotropic fracture is not only a geometrical phenomenon but also a mechanical event arisen from the fibrous structure embedded in an otherwise isotropic matrix material which undoubtedly entails the use of an anisotropic crack driving force. Within this context, crack phase-field applications in biomechanics can be found in Gültekin [65], later in Gültekin et al. [66] and Raina and Miehe [168].

The paper is organized as follows. The investigation starts in Sec. 3.2 with a brief review of the underlying geometry, kinematics and the constitutive model characterizing an anisotropic elastic response subject to degradation. Subsequently, we pursue a variational principle for the multi-field problem of fracture and obtain the Euler-Lagrange equations based on a power balance. The framework particularly features a viscous extended dissipation functional to account for the rate-dependent evolution of the crack phase-field. Section 3.3 is then concerned with the theoretical synopsis of the anisotropic failure criteria:

- Energy-based failure criterion
- Tsai-Wu failure criterion
- Hill failure criterion
- Principal stress failure criterion

In Sec. 3.4, we employ a staggered solution-update scheme partitioning the monolithic solution into two sub-problems followed by a Galerkin-type weak formulation. Sec. 3.5

demonstrates the performance of the proposed model by comparing failure surfaces and crack propagations associated with the above-stated anisotropic failure criteria for simple yet representative boundary-value problems and loading conditions using the finite element analysis. Sec. 3.6–3.7 provide a discussion of the results obtained and a conclusion of the article, respectively.

3.2 Multi-field Problem for Failure in Anisotropic Continuum

We devote this section to phase-field modeling of fracture phenomena. To this end, the primary field variables, namely the crack phase-field d and the deformation map $\boldsymbol{\varphi}$, are introduced in relation to the evolution of the crack and the balance of linear momentum, respectively. Subsequently, an account on constitutive modeling of anisotropic hyperelastic arterial walls consisting of two families of collagen fibers is provided. Afterwards, we report on the saddle point principle of the global power balance due to a quasi-static process of loading, and obtain the Euler-Lagrange equations of the multi-field problem. The numerical edifice, unlike Gültekin [65] and Gültekin et al. [66], also embodies the rate-dependent dissipation functional provided by a Perzyna-type (Perzyna [163]) viscous extension. For the relevant nonlinear continuum mechanics used in the present paper see, e.g., the books and monographs by Eringen [49], Truesdell and Noll [220], Spencer [206], Marsden and Hughes [128], Miehe [135], Holzapfel [80], and Gurtin et al. [70].

3.2.1 Primary field variables of the multi-field problem

To describe the motion of a solid, we consider a material body at time $t_0 \in \mathcal{T} \subset \mathbb{R}^+$ whose reference configuration possesses an undeformed stress-free state, and is henceforth denoted by $\mathcal{B} \subset \mathbb{R}^3$, with the material point $\boldsymbol{X} \in \mathcal{B}$, while $\partial\mathcal{B} \subset \mathbb{R}^2$ denotes the surface of the reference configuration $\mathcal{B} \subset \mathbb{R}^3$. The deformed body at current time $t \in \mathcal{T} \subset \mathbb{R}^+$ is then referred to as the spatial configuration designated by $\mathcal{S} \subset \mathbb{R}^3$ with the spatial point $\boldsymbol{x} \in \mathcal{S}$. The surface of the spatial configuration $\mathcal{S} \subset \mathbb{R}^3$ is expressed by $\partial\mathcal{S} \subset \mathbb{R}^2$. Accordingly, we introduce the bijective deformation map $\boldsymbol{\varphi}(\boldsymbol{X}, t)$, i.e.

$$\boldsymbol{\varphi}_t(\boldsymbol{X}) : \begin{cases} \mathcal{B} \times \mathcal{T} & \to \quad \mathcal{S}, \\ (\boldsymbol{X}, t) & \mapsto \quad \boldsymbol{x} = \boldsymbol{\varphi}(\boldsymbol{X}, t), \end{cases} \tag{3.1}$$

which maps a material point $\boldsymbol{X}$ onto a spatial point $\boldsymbol{x}$, see Fig. 3.1. Note that one can also write $\boldsymbol{\varphi}_t(\boldsymbol{X})$ as long as $t \subset \mathbb{R}^+$ is fixed (Marsden and Hughes [128]). Having characterized the fundamental geometric map for deformations, we can now proceed to the essential geometrical entities of the phase-field modeling. The basic geometric mapping for the time-dependent auxiliary crack phase-field d reads

$$d : \begin{cases} \mathcal{B} \times \mathcal{T} & \to \quad [0, 1], \\ (\boldsymbol{X}, t) & \mapsto \quad d(\boldsymbol{X}, t), \end{cases} \tag{3.2}$$

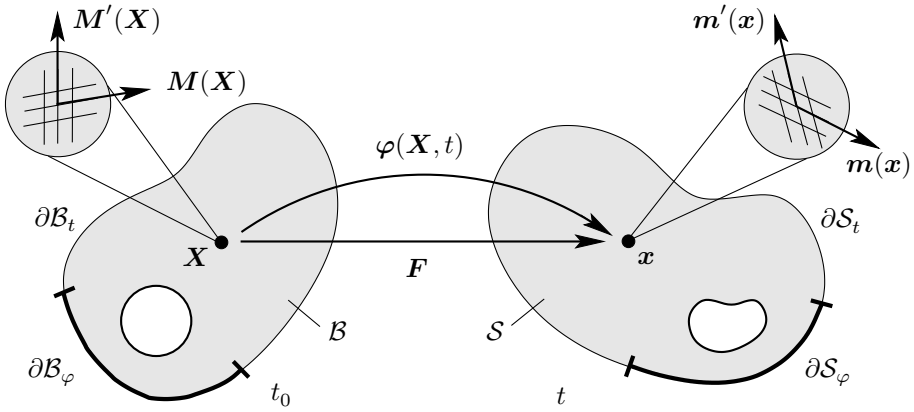

Figure 3.1 Nonlinear deformation of an anisotropic solid with the reference configuration $\mathcal{B} \in \mathbb{R}^3$ and the spatial configuration $\mathcal{S} \in \mathbb{R}^3$. The nonlinear deformation map is $\boldsymbol{\varphi} : \mathcal{B} \times \mathcal{T} \rightarrow \mathcal{S}$, which transforms a material point $\boldsymbol{X} \in \mathcal{B}$ onto a spatial point $\boldsymbol{x} = \boldsymbol{\varphi}(\boldsymbol{X}, t) \in \mathcal{S}$ at time t. The anisotropic micro-structure of the material point $\boldsymbol{X}$ is rendered by two families of fibers with unit vectors $\boldsymbol{M}$ and $\boldsymbol{M}'$. Likewise, the anisotropic micro-structure of the spatial point $\boldsymbol{x}$ is described by $\boldsymbol{m}$ and $\boldsymbol{m}'$, as the spatial counterparts of $\boldsymbol{M}$ and $\boldsymbol{M}'$, respectively.

which interpolates between the intact ($d = 0$) and the ruptured ($d = 1$) state of the material. The multi-dimensional problem of fracture is basically composed of a deformable mechanical domain and a non-deformable domain of the phase-field, as depicted in the Fig. 3.2(a) and (b), respectively.

3.2.2 Kinematics

Consider the deformation map $\boldsymbol{\varphi}$ at a fixed time t, then the deformation gradient reads

$$\boldsymbol{F} = \nabla\boldsymbol{\varphi}, \tag{3.3}$$

which maps the unit tangent of a reference point onto its counterpart in the spatial configuration. The gradient operators $\nabla(\bullet)$ and $\nabla_x(\bullet)$ denote the gradients with respect to the reference and the spatial coordinates $\boldsymbol{X}$ and $\boldsymbol{x}$, respectively. The deformation gradient $\boldsymbol{F}$, its cofactor $\mathrm{cof}\boldsymbol{F} = J\boldsymbol{F}^{-\mathrm{T}}$, and its Jacobian $J = \mathrm{det}\boldsymbol{F}$ relate the deformation of the infinitesimal line ($\mathrm{d}\boldsymbol{X}$ and $\mathrm{d}\boldsymbol{x}$), the area ($\mathrm{d}\boldsymbol{A}$ and $\mathrm{d}\boldsymbol{a}$), and the volume ($\mathrm{d}V$ and $\mathrm{d}v$) elements, i.e.

$$\mathrm{d}\boldsymbol{x} = \boldsymbol{F}\mathrm{d}\boldsymbol{X}, \qquad \mathrm{d}\boldsymbol{a} = \mathrm{cof}\boldsymbol{F}\mathrm{d}\boldsymbol{A}, \qquad \mathrm{d}v = J\mathrm{d}V. \tag{3.4}$$

The deformations are non-penetrable for $J > 0$. Accordingly, we denote the symmetric right and left Cauchy-Green tensors as

$$\boldsymbol{C} = \boldsymbol{F}^{\mathrm{T}}\boldsymbol{g}\boldsymbol{F}, \qquad \boldsymbol{b} = \boldsymbol{F}\boldsymbol{g}^{-1}\boldsymbol{F}^{\mathrm{T}}, \tag{3.5}$$

utilized as deformation measures in the reference and spatial configurations, respectively. Additionally, the continuous three-dimensional manifolds, i.e. the reference configuration

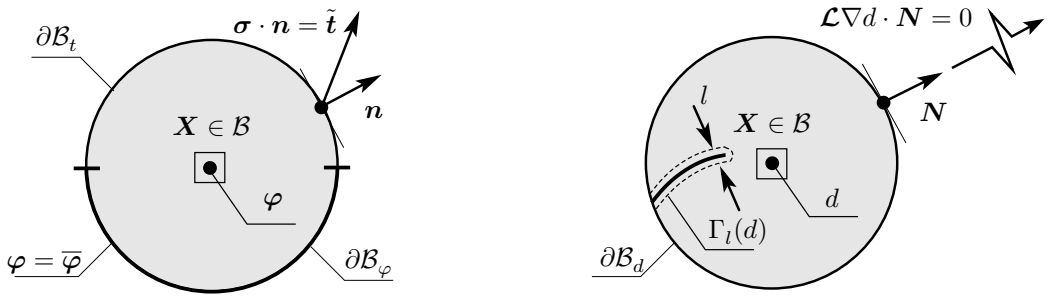

(a) Deformation field (b) Crack phase-field

Figure 3.2 Multi-field problem: (a) mechanical problem of deformation along with Dirichlet and Neumann-type boundary conditions actualized by $\varphi = \overline{\varphi}$ and the Cauchy theorem $\boldsymbol{\sigma}\cdot\boldsymbol{n}=\tilde{\boldsymbol{t}}$, respectively; (b) evolution of the crack phase-field problem with the Neumann-type boundary condition $\mathcal{L}\nabla d\cdot\boldsymbol{N}=0$.

$\mathcal{B}$ and the spatial configuration $\mathcal{S}$, are locally equipped with the covariant reference and spatial metric tensors $\boldsymbol{g}=\delta_{IJ}\boldsymbol{E}^I\otimes\boldsymbol{E}^J$ and $\boldsymbol{g}=\delta_{ij}\boldsymbol{e}^i\otimes\boldsymbol{e}^j$, respectively, where δ_{IJ} and δ_{ij} are simply evaluated as the Kronecker deltas. Moreover, the following three invariants

$$I_1=\boldsymbol{g}:\boldsymbol{b},\qquad I_2=\frac{1}{2}\left[I_1^2-\operatorname{tr}(\boldsymbol{b}^2)\right],\qquad I_3=\det\boldsymbol{b}. \tag{3.6}$$

account for an isotropic hyperelastic response of a solid in the spatial configuration. The anisotropic mechanical response of the arterial tissue requires the use of additional invariants. To this end, we introduce the Eulerian form of the structure tensors $\boldsymbol{A}_{\boldsymbol{m}}$ and $\boldsymbol{A}_{\boldsymbol{m}'}$ as

$$\boldsymbol{A}_{\boldsymbol{m}}=\boldsymbol{m}\otimes\boldsymbol{m},\qquad \boldsymbol{A}_{\boldsymbol{m}'}=\boldsymbol{m}'\otimes\boldsymbol{m}', \tag{3.7}$$

where the micro-structure of the tissue is idealized by $\boldsymbol{m}$ and $\boldsymbol{m}'$ as the spatial counterparts of the reference unit vectors $\boldsymbol{M}$ and $\boldsymbol{M}'$, as shown in Fig. 3.1. Thus,

$$\boldsymbol{m}=\boldsymbol{F}\boldsymbol{M},\qquad \boldsymbol{m}'=\boldsymbol{F}\boldsymbol{M}', \tag{3.8}$$

describe two families of fibers embedded in the isotropic ground matrix. Accordingly, we introduce the (physically meaningful) fourth and sixth invariants

$$I_4=\boldsymbol{m}\cdot\boldsymbol{g}\boldsymbol{m},\qquad I_6=\boldsymbol{m}'\cdot\boldsymbol{g}\boldsymbol{m}' \tag{3.9}$$

in order to capture the anisotropic response of the tissue.

3.2.3 Anisotropic crack phase-field model

For a non-deformable domain, the gradient operator can simply be taken as $\nabla_x[\bullet]=\nabla[\bullet]$. Provided that an acute crack surface topology at time t is defined by $\Gamma(t)\subset\mathbb{R}^2$ in the solid $\mathcal{B}$ through a surface integral $\Gamma(d)=\int_\Gamma \mathrm{d}A$, the regularized crack surface $\Gamma_l(d)$ approximated by a volume integral adopts the following three-dimensional form

$$\Gamma_l(d)=\int_{\mathcal{B}}\gamma(d,\nabla d)\mathrm{d}V,\quad \text{where}\quad \gamma(d,\nabla d)=\frac{1}{2l}(d^2+l^2\nabla d\cdot\nabla d) \tag{3.10}$$

designates the *isotropic* volume-specific crack surface (crack density) function, which satisfies the condition $\gamma(d, \boldsymbol{Q} \star \nabla d) = \gamma(d, \nabla d), \forall \boldsymbol{Q} \in \mathcal{O}(3)$. The tensor variable $\boldsymbol{Q}$ denotes the rotations in the orthogonal group $\mathcal{O}(3)$, which contains rotations and reflections, and $\star$ stands for the Rayleigh product. The length-scale parameter l controls the breadth of the crack. This approximation can be extended to a class of anisotropic materials such that

$$\Gamma_l(d) = \int_{\mathcal{B}} \gamma(d, \nabla d; \boldsymbol{\mathcal{L}}) \mathrm{d}V, \quad \text{where} \quad \gamma(d, \nabla d; \boldsymbol{\mathcal{L}}) = \frac{1}{2l}(d^2 + \nabla d \cdot \boldsymbol{\mathcal{L}} \nabla d) \tag{3.11}$$

is the *anisotropic* volume-specific crack surface (crack density) function, which satisfies the condition $\gamma(d, \boldsymbol{Q} \star \nabla d) = \gamma(d, \nabla d), \forall \boldsymbol{Q} \in \mathcal{G} \subset \mathcal{O}(3)$, where $\mathcal{G}$ designates a symmetry group as a subset of $\mathcal{O}(3)$. The second-order anisotropic structure tensor $\boldsymbol{\mathcal{L}}$ is given as

$$\boldsymbol{\mathcal{L}} = l^2[\boldsymbol{I} + \omega_{\mathrm{M}}(\boldsymbol{M} \otimes \boldsymbol{M}) + \omega_{\mathrm{M}'}(\boldsymbol{M}' \otimes \boldsymbol{M}')], \tag{3.12}$$

which aligns the evolution of the crack according to the orientation of fibers in the continuum, see Fig. 3.3. Therein, the anisotropy parameters ω_{M} and $\omega_{\mathrm{M}'}$ regulate the transition from weak to strong anisotropy for two families of fibers. For isotropic solids, the parameters $\omega_{\mathrm{M}} = \omega_{\mathrm{M}'}$ are zero, whereas for a general anisotropic continuum with several family of fibers, they must lie in an open range, i.e. $-1 < \omega_i < \infty$ where $i \in \{\mathrm{M}, \mathrm{M}', \ldots\}$ in order to satisfy the ellipticity condition for $\Gamma_l(d)$. Following this, we can state the minimization principle

$$d(\boldsymbol{X}, t) = \mathrm{Arg} \left\{ \inf_{d \in \mathcal{W}_{\Gamma(t)}} \Gamma_l(d) \right\}, \tag{3.13}$$

along with the Dirichlet-type boundary constraint

$$\mathcal{W}_{\Gamma(t)} = \{d | d(\boldsymbol{X}, t) = 1 \quad \text{at} \quad \boldsymbol{X} \in \Gamma(t)\}. \tag{3.14}$$

Upon the minimization of the regularized crack surface functional we derive the Euler-Lagrange equations according to

$$\frac{1}{l}[d - \nabla \cdot (\boldsymbol{\mathcal{L}} \nabla d)] = 0 \quad \text{in } \mathcal{B}, \qquad \text{and} \qquad \boldsymbol{\mathcal{L}} \nabla d \cdot \boldsymbol{N} = 0 \quad \text{on } \partial\mathcal{B}, \tag{3.15}$$

where the divergence term interpolates d between the intact and the ruptured state of the material. In $(3.15)_2$ $\boldsymbol{N}$ denotes the unit surface normal oriented outward in the reference configuration.

3.2.3.1 The concept of effective length scale

The anisotropic structure tensor $\boldsymbol{\mathcal{L}}$ defined in (3.12) motivates the concept of *effective* length scale parameter which can be represented by polar plots (Teichtmeister et al. [216]) in the sense of the surface energy $g_c \Gamma_l(d)$ and its reciprocal (Li et al. [121] and Nguyen et al. [152]), where g_c is referred to as the critical fracture energy (Griffith-type critical energy release rate). To this end, imagine the sharp crack $\Gamma \in \mathcal{B}$ to be the parametric curve

$\boldsymbol{X}_\Gamma(\zeta)$ traced out by the parameter ζ, i.e. $\zeta \to \boldsymbol{X}_\Gamma(\zeta)$ so that the position of $\forall \boldsymbol{X} \in \mathcal{B}$ can be uniquely determined by

$$\boldsymbol{X}(\zeta, \nu) = \boldsymbol{X}_\Gamma(\zeta) + \nu \boldsymbol{e}_\nu. \tag{3.16}$$

The base vectors $\boldsymbol{e}_\zeta$ and $\boldsymbol{e}_\nu$ denote the respective unit tangent and the normal at point $\boldsymbol{X}_\Gamma(\zeta)$, and establish the local coordinate system (ζ, ν) alongside the global Cartesian system (x, y), see Fig. 3.4(a). Now, let the angle between the x-axis and the tangent of the crack at position $\boldsymbol{X}_\Gamma(\zeta)$ be $\phi = \angle(\boldsymbol{e}_x, \boldsymbol{e}_\zeta)$, while the angle between the orientation $\boldsymbol{M}$ of a family of fibers and the x-axis is denoted by $\alpha = \angle(\boldsymbol{e}_x, \boldsymbol{M})$. Then, by assuming the *effective* length scale parameter l_{e} to be sufficiently small compared with the length of the sharp crack $|\Gamma|$ we arrive at

$$l_{\mathrm{e}}(\phi, \alpha) = l^2[1 + \omega_{\mathrm{M}} \cos^2(\phi - \alpha) + \omega_{\mathrm{M}'} \sin^2(\phi - \alpha)] \tag{3.17}$$

for an orthotropic case, where the second family of fibers $\boldsymbol{M}'$ is aligned perpendicular to the first fiber family $\boldsymbol{M}$, see Fig. 3.4(a).

Figure 3.4(b)–(d) depict the polar plots of the effective length scale parameter $l_{\mathrm{e}}(\phi, \alpha)$, as introduced in (3.17), for specific choices of ω_{M} and $\omega_{\mathrm{M}'}$. Specifically, the plot denoted by $(*)$ in Fig. 3.4(c) recovers the transversely isotropic distribution of the effective length scale parameter for $\omega_{\mathrm{M}'} = 0.5$ and vanishing ω_{M}. Another feature of the model is discernable by the plot $(**)$ in Fig. 3.4(d), where the effective length scale parameter l_{e} renders isotropy with a wider range ($l_{\mathrm{e}} = 1.5l$) for $\omega_{\mathrm{M}} = \omega_{\mathrm{M}'} \equiv 0.5$. This feature is the natural consequence of the second-order phase-field models providing a two-fold symmetry unlike the fourth-order phase-field models conferring a four-fold symmetry, a more detailed discussion can be found in Remark 1.

Remark 1. A fourth-order crack phase-field approach to fracture has been recently proposed by Borden et al. [15] for isotropic solids. Anisotropic extensions of this fourth-order model are suggested by, e.g., Li et al. [121] and Teichtmeister et al. [216]. In such a case, the anisotropic crack density function in $(3.11)_2$ can be recast into a more general form, i.e.

$$\gamma(d, \nabla d, \nabla^2 d; \boldsymbol{\mathcal{L}}, \mathbb{L}) = \frac{1}{2l} d^2 + \frac{l}{4} \nabla d \cdot \boldsymbol{\mathcal{L}} \nabla d + \frac{l^3}{32} \nabla^2 d : \mathbb{L} : \nabla^2 d, \tag{R1.1}$$

where $\nabla^2 d$ and $\mathbb{L}$ stand for the second gradient of the phase-field and a fourth-order anisotropic structure tensor, respectively. Insertion of (R1.1) into $(3.11)_1$ together with the minimization principle (3.13) yields

$$d - \frac{l^2}{2} \nabla \cdot (\boldsymbol{\mathcal{L}} \nabla d) + \frac{l^4}{16} \nabla \cdot [\nabla \cdot (\mathbb{L} : \nabla^2 d)] = 0, \tag{R1.2}$$

along with the Neumann-type boundary constraints

$$[\boldsymbol{\mathcal{L}} \nabla d + \frac{l^2}{8} \nabla \cdot (\mathbb{L} : \nabla^2 d)] \cdot \boldsymbol{N} = 0 \quad \text{on } \partial\mathcal{B}, \qquad \text{and} \qquad \mathbb{L} : \nabla^2 d \cdot \boldsymbol{N} = \boldsymbol{0} \quad \text{on } \partial\mathcal{B}. \tag{R1.3}$$

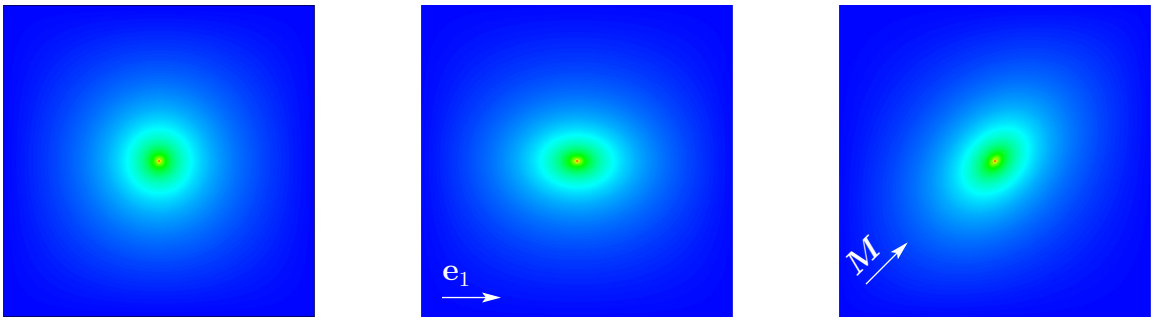

(a) $\boldsymbol{\mathcal{L}} = l^2\boldsymbol{I}$ (b) $\boldsymbol{\mathcal{L}} = l^2(\boldsymbol{I} + \mathbf{e}_1 \otimes \mathbf{e}_1)$ (c) $\boldsymbol{\mathcal{L}} = l^2(\boldsymbol{I} + \boldsymbol{M} \otimes \boldsymbol{M})$

Figure 3.3 (a) Isotropic damage field; (b) anisotropic damage field with fiber angle $\alpha = 0°$; (c) anisotropic damage field with $\alpha = 45°$.

The numerical implementation of the above-stated fourth-order approach requires C^1-continuous shape functions for a conforming approximation, an arduous task for 3-dimensional analyses. An account on the alternative treatment circumventing the C^1-continuity requirement is provided by Teichtmeister et al. [216]. Higher-order approaches become particularly relevant for strongly anisotropic materials for which energetically preferable zig-zag crack patterns are observable. However, its relevance to soft biological tissues is dubious as they seem to exhibit weak anisotropy. This is justified by a phenomenon called aortic dissection where the nascent crack in the medial layer of an aorta propagates either axially or helically following the orientation of one fiber family regardless of the existence of other fiber families. Therefore, our modeling endeavors are confined to use a second-order anisotropic crack phase-field approach.

3.2.4 Constitutive modeling of artery walls

In order to reflect the local anisotropic mechanical behavior of the hypothetically intact arterial wall, we postulate a specific form of the effective Helmholtz free-energy function split into the effective isotropic Ψ_0^{iso} and the anisotropic Ψ_0^{ani} parts,

$$\Psi_0(\boldsymbol{g}, \boldsymbol{F}, \boldsymbol{A}_{\boldsymbol{m}}, \boldsymbol{A}_{\boldsymbol{m}'}) = \Psi_0^{\text{iso}}(\boldsymbol{g}, \boldsymbol{F}, J) + \Psi_0^{\text{ani}}(\boldsymbol{g}, \boldsymbol{F}, \boldsymbol{A}_{\boldsymbol{m}}, \boldsymbol{A}_{\boldsymbol{m}'}). \tag{3.18}$$

The effective isotropic part Ψ_0^{iso} and the anisotropic part Ψ_0^{ani} are functions of the invariants such that

$$\Psi_0^{\text{iso}}(\boldsymbol{g}, \boldsymbol{F}, J) = \hat{\Psi}_0^{\text{iso}}(J, I_1), \qquad \Psi_0^{\text{ani}}(\boldsymbol{g}, \boldsymbol{F}, \boldsymbol{A}_{\boldsymbol{m}}, \boldsymbol{A}_{\boldsymbol{m}'}) = \hat{\Psi}_0^{\text{ani}}(I_4, I_6), \tag{3.19}$$

for which the following neo-Hookean form

$$\hat{\Psi}_0^{\text{iso}}(J, I_1) = \kappa(J - \ln J - 1) + \frac{\mu}{2}(I_1 - 2\ln J - 3) \tag{3.20}$$

represents the mechanical response of the ground matrix, whereas the exponential form

$$\hat{\Psi}_0^{\text{ani}}(I_4, I_6) = \frac{k_1}{2k_2} \sum_{i=4,6} \{\exp[k_2(I_i - 1)^2] - 1\} \tag{3.21}$$

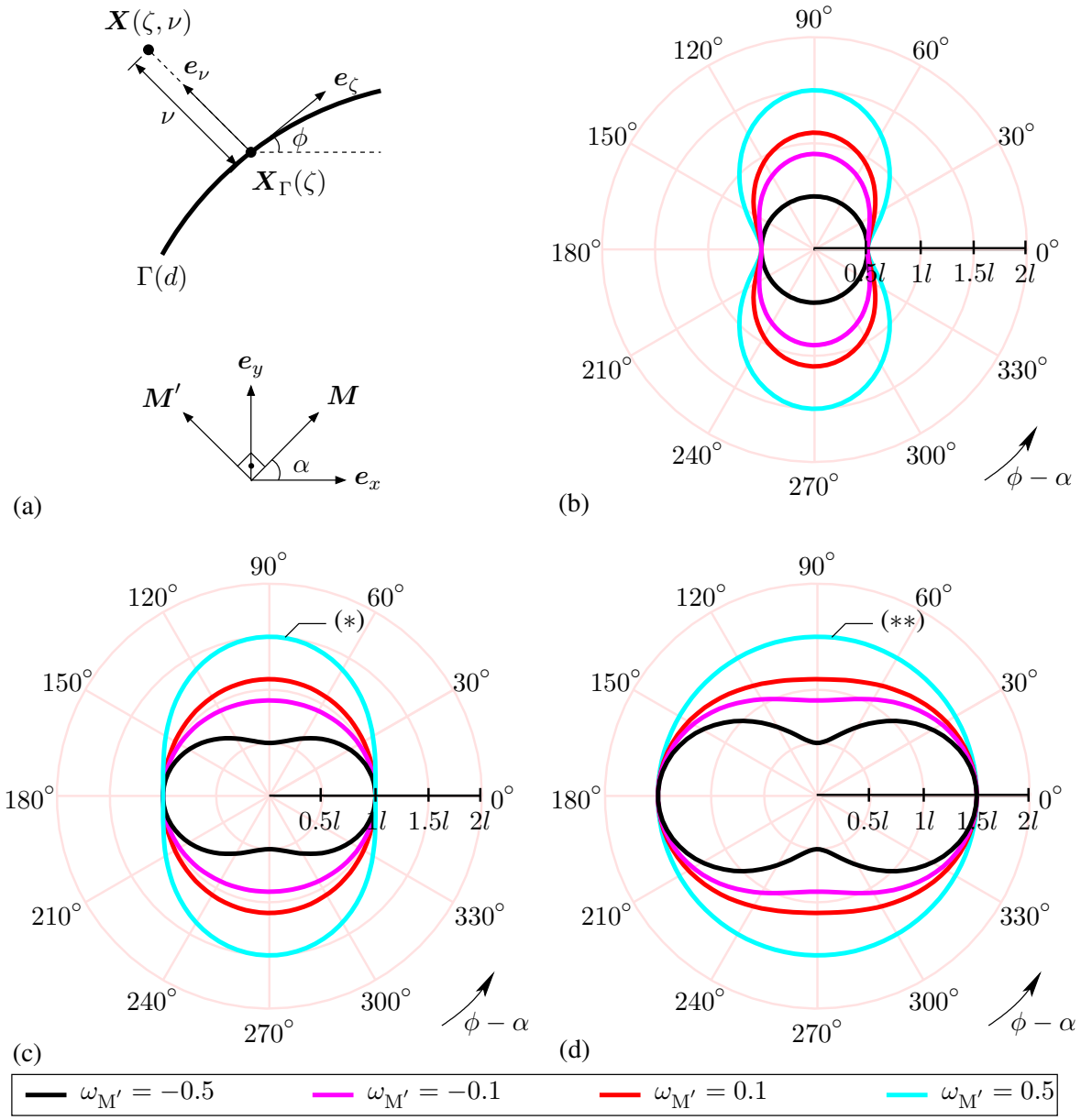

Figure 3.4 (a) Geometric profile of the sharp crack $\Gamma \in \mathcal{B}$ at point $\boldsymbol{X}_\Gamma(\zeta)$ together with the global and local coordinates systems (x, y) and (ζ, ν), respectively. Polar plots of the effective length scale parameter $l_{\mathrm{e}}(\phi, \alpha)$ shown for an orthotropic case ($\boldsymbol{M} \perp \boldsymbol{M}'$) in (3.17), with the anisotropy parameter (b) $\omega_{\mathrm{M}} = -0.5$; (c) $\omega_{\mathrm{M}} = 0.0$; (d) $\omega_{\mathrm{M}} = 0.5$. The values assumed by the other anisotropy parameter $\omega_{\mathrm{M}'}$ are shown in color (see the legend).

represents the elastic response of the two distinct families of collagen fibers (Holzapfel et al. [83]). In (3.20) κ and μ denote the bulk modulus and the shear modulus, respectively, whereas the anisotropic term (3.21) involves k_1 and k_2 representing a stress-like material

parameter and a dimensionless parameter, respectively. Note that (3.21) contributes to the mechanical response provided that the concerning family of fibers is under extension, i.e. when $I_4 > 1$ or $I_6 > 1$. To implement the constitutive model in a typical implicit finite element program, we require the stress tensor and its sensitivity with respect to the associated deformation measure. Exploiting the Coleman–Noll procedure on the Clausius–Planck inequality, and using the decoupled form of the effective free energy Ψ_0 in (3.18), the effective Kirchhoff stress tensor $\boldsymbol{\tau}_0$ is obtained as

$$\boldsymbol{\tau}_0 = 2\partial_{\boldsymbol{g}}\Psi_0 = \boldsymbol{\tau}_0^{\mathrm{iso}} + \boldsymbol{\tau}_0^{\mathrm{ani}}. \tag{3.22}$$

The effective Kirchhoff stress $\boldsymbol{\tau}_0$ due to the isotropic and anisotropic contributions, i.e. $\boldsymbol{\tau}_0^{\mathrm{iso}}$ and $\boldsymbol{\tau}_0^{\mathrm{ani}}$, defined in (3.22), are

$$\boldsymbol{\tau}_0^{\mathrm{iso}} = 2\partial_{\boldsymbol{g}}\Psi_0^{\mathrm{iso}} = \hat{p}\boldsymbol{g}^{-1} + \mu(\boldsymbol{b} - \boldsymbol{g}^{-1}), \quad \boldsymbol{\tau}_0^{\mathrm{ani}} = 2\partial_{\boldsymbol{g}}\Psi_0^{\mathrm{ani}} = 2\psi_4 \boldsymbol{m}\otimes\boldsymbol{m} + 2\psi_6 \boldsymbol{m}'\otimes\boldsymbol{m}', \tag{3.23}$$

where the penalty term reads $\hat{p} = \kappa(J-1)$. The deformation-dependent scalar coefficients ψ_4 and ψ_6 are defined as

$$\psi_4 = \partial_{I_4}\Psi_0 = k_1(I_4-1)\mathrm{exp}[k_2(I_4-1)^2], \quad \psi_6 = \partial_{I_6}\Psi_0 = k_1(I_6-1)\mathrm{exp}[k_2(I_6-1)^2]. \tag{3.24}$$

The sensitivity of the effective Kirchhoff stress tensor is established by the spatial elasticity tensor $\mathbb{c}_0$. Thus,

$$\mathbb{c}_0 = 4\partial^2_{\boldsymbol{g}\boldsymbol{g}}\Psi_0 = 2\partial_{\boldsymbol{g}}\boldsymbol{\tau}_0 = \mathbb{c}_0^{\mathrm{iso}} + \mathbb{c}_0^{\mathrm{ani}}, \tag{3.25}$$

in which the effective elasticity tensor $\mathbb{c}_0^{\mathrm{iso}}$ due to the isotropic part reads

$$\mathbb{c}_0^{\mathrm{iso}} = (\hat{p}+\kappa)\boldsymbol{g}^{-1}\otimes\boldsymbol{g}^{-1} - 2(\hat{p}-\mu)\mathbb{I}_{\boldsymbol{g}^{-1}}. \tag{3.26}$$

Therein, the symmetric fourth-order identity tensor $\mathbb{I}_{\boldsymbol{g}^{-1}}$ has the following index form $(\mathbb{I}_{\boldsymbol{g}^{-1}})^{ijkl} = (\delta^{ik}\delta^{jl} + \delta^{il}\delta^{jk})/2$. In (3.25) $\mathbb{c}_0^{\mathrm{ani}}$ describes the anisotropic part of the effective elasticity tensor, which can be expressed as

$$\mathbb{c}_0^{\mathrm{ani}} = 4\psi_{44}\mathbb{M} + 4\psi_{66}\mathbb{M}', \tag{3.27}$$

with the scalar coefficients ψ_{44} and ψ_{66} defined as

$$\begin{aligned}\psi_{44} &= \partial_{I_4}\Psi_4 = k_1[1+2k_2(I_4-1)^2]\mathrm{exp}[k_2(I_4-1)^2],\\ \psi_{66} &= \partial_{I_6}\Psi_6 = k_1[1+2k_2(I_6-1)^2]\mathrm{exp}[k_2(I_6-1)^2].\end{aligned} \tag{3.28}$$

Finally, the fourth-order structure tensors in (3.27) take on the following forms

$$\mathbb{M} = \boldsymbol{m}\otimes\boldsymbol{m}\otimes\boldsymbol{m}\otimes\boldsymbol{m}, \qquad \mathbb{M}' = \boldsymbol{m}'\otimes\boldsymbol{m}'\otimes\boldsymbol{m}'\otimes\boldsymbol{m}'. \tag{3.29}$$

3.2.5 Continuous variational formulation based on power balance

This part is concerned with the saddle point principle of the global power balance which yields the coupled Euler-Lagrange equations governing the evolution of the crack phase-field in (i) a rate-independent and (ii) a rate-dependent setting, the balance of linear momentum. We first consider the Helmholtz free-energy function Ψ for a degrading continuum according to

$$\Psi(\boldsymbol{g}, \boldsymbol{F}, \boldsymbol{A}_{\boldsymbol{m}}, \boldsymbol{A}_{\boldsymbol{m}'}; d) = g(d)\Psi_0(\boldsymbol{g}, \boldsymbol{F}, \boldsymbol{A}_{\boldsymbol{m}}, \boldsymbol{A}_{\boldsymbol{m}'}), \tag{3.30}$$

where Ψ_0 is the effective Helmholtz free-energy function of the hypothetically intact solid according to (3.18). In (3.30) the monotonically decreasing quadratic degradation function g has the form

$$g(d) = (1-d)^2. \tag{3.31}$$

It describes the degradation of the solid/tissue with the evolving crack phase-field parameter d subject to the growth conditions

$$g'(d) \leq 0 \qquad \text{with} \qquad g(0) = 1, \qquad g(1) = 0, \qquad g'(1) = 0. \tag{3.32}$$

The first condition ensures degradation, while the second and third conditions set the limits for the intact and the ruptured state, and the final condition ensures the saturation of $g(d)$ as $d \to 1$. With this at hand, we can further describe the isotropic and the anisotropic parts of the free-energy function $\Psi = \hat{\Psi}^{\text{iso}} + \hat{\Psi}^{\text{ani}}$ for a degrading material, i.e.

$$\hat{\Psi}^{\text{iso}}(J, I_1; d) = g(d)\hat{\Psi}_0^{\text{iso}}(J, I_1), \quad \hat{\Psi}^{\text{ani}}(I_4, I_6; d) = g(d)\hat{\Psi}_0^{\text{ani}}(I_4, I_6), \tag{3.33}$$

respectively. Nevertheless, $g(d)$ may assume an entirely generic form and may be divided into an isotropic and an anisotropic part, as pointed out in Remark 2.

Remark 2. We hereby present two possible generic forms for the degradation function $g(d)$ in (3.31) such that

$$g(d) = b[\,(1-d)^a - (1-d)^{a-1}\,] + a(1-d)^{a-1} - (a-1)(1-d)^a, \tag{R2.1}$$

as an extension of the cubic degradation function suggested by Borden et al. [14], and

$$g(d) = (1-d)^a, \tag{R2.2}$$

expanding the quadratic form (3.31). The exponent a and the coefficient b in (R2.1) appear as model and control parameters regulating the softening behavior of the material and the slope of $g(d)$, respectively, see Fig. 3.5(a)–(c). They are bounded such that $a \geq 2$ and $0 \leq b \leq 2$ to guarantee a monotonic decrease of $g(d)$. The exponent a in (R2.2), however, accepts values $a > 0$ to ensure the monotonic reduction of the bulk response, see Fig. 3.5(d). The values $a = 3$ and $b = 2$ in (R2.1) retrieves the $g(d)$ used in various crack phase-field models, see, e.g., Bourdin et al. [18] and Miehe et al. [143], whereas $a = 2$ reproduces the same for (R2.2). The classical continuum damage model (Kachanov [109])

is also a special case of (R2.2) for $a = 1$. Figure 3.5 reveals the qualitative behavior of the generic form of $g(d)$ due to (R2.1) and (R2.2).

In view of the above-mentioned formalism, distinct degradation functions as to the isotropic and the anisotropic free-energy contributions may become particularly meaningful in soft biological tissues. To this end, we conjecture on (R2.1), i.e.

$$g_{\text{iso}}(d) = b_{\text{iso}}[\,(1-d)^{a_{\text{iso}}} - (1-d)^{a_{\text{iso}}-1}\,] + a_{\text{iso}}(1-d)^{a_{\text{iso}}-1} - (a_{\text{iso}}-1)(1-d)^{a_{\text{iso}}}, \quad \text{(R2.3)}$$

and

$$g_{\text{ani}}(d) = b_{\text{ani}}[\,(1-d)^{a_{\text{ani}}} - (1-d)^{a_{\text{ani}}-1}\,] + a_{\text{ani}}(1-d)^{a_{\text{ani}}-1} - (a_{\text{ani}}-1)(1-d)^{a_{\text{ani}}}, \quad \text{(R2.4)}$$

which account for the distinct stress softening behavior of the continuum according to the isotropic and anisotropic parameters $a_{\text{iso}}, b_{\text{iso}}, a_{\text{ani}}, b_{\text{ani}}$, respectively. Hence, (R2.2) can be split as follows

$$g_{\text{iso}}(d) = (1-d)^{a_{\text{iso}}} \qquad \text{and} \qquad g_{\text{ani}}(d) = (1-d)^{a_{\text{ani}}}. \quad \text{(R2.5)}$$

The parameters may be adjusted in accordance with experimental observations which are rather scarce. Since the focus of this manuscript is largely confined to the analysis of anisotropic failure criteria, further insight into the generic degradation functions is spared as a major subject matter for another article.

3.2.5.1 Rate of energy storage functional in an anisotropic solid and the external power functional

As a point of departure, we define the energy storage functional E of an anisotropic hyperelastic solid as

$$E(\boldsymbol{\varphi}, d) = \int_{\mathcal{B}} \Psi(\boldsymbol{g}, \boldsymbol{F}, \boldsymbol{A}_{\boldsymbol{m}}, \boldsymbol{A}_{\boldsymbol{m}'}; d)\mathrm{d}V, \quad (3.34)$$

by considering the contributions of the free-energy function in (3.33). The time derivative of (3.34) gives the rate of energy storage functional $\mathcal{E}$, i.e.

$$\mathcal{E} = \int_{\mathcal{B}} (\boldsymbol{\tau} : \boldsymbol{g}\nabla_x\dot{\boldsymbol{\varphi}} - f\dot{d})\mathrm{d}V, \quad (3.35)$$

with the Kirchhoff stress tensor $\boldsymbol{\tau}$ and the energetic force f defined as

$$\boldsymbol{\tau} = g(d)\boldsymbol{\tau}_0, \qquad f = -\partial_d\Psi(\boldsymbol{g}, \boldsymbol{F}, \boldsymbol{A}_{\boldsymbol{m}}, \boldsymbol{A}_{\boldsymbol{m}'}; d), \quad (3.36)$$

where $\boldsymbol{\tau}_0$ is expressed in (3.22). We emphasize that the energetic force f is the work conjugate to d. Subsequently, the external power functional $\mathcal{P}$ can be described as

$$\mathcal{P}(\dot{\boldsymbol{\varphi}}) = \int_{\mathcal{B}} \rho_0\tilde{\boldsymbol{\gamma}} \cdot \dot{\boldsymbol{\varphi}}\mathrm{d}V + \int_{\partial\mathcal{B}_t} \tilde{\boldsymbol{t}} \cdot \dot{\boldsymbol{\varphi}}\mathrm{d}a, \quad (3.37)$$

where ρ_0, $\tilde{\boldsymbol{\gamma}}$ and $\tilde{\boldsymbol{t}}$ represent the material density, the prescribed body force and the spatial surface traction, respectively.

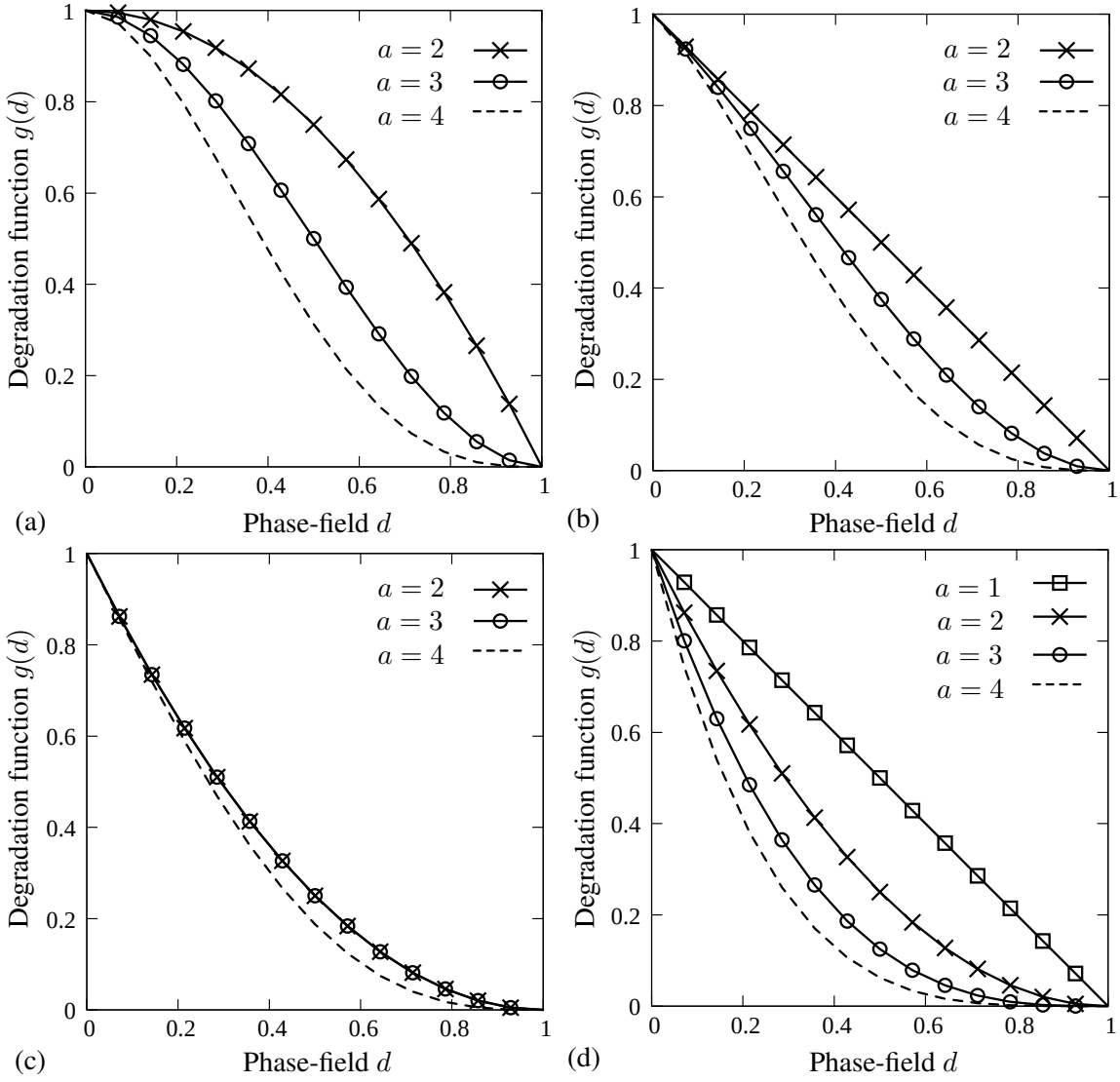

Figure 3.5 Qualitative behavior of the degradation function $g(d)$ vs d: (a) $b = 0$; (b) $b = 1$; (c) $b = 2$, according to (R2.1), while for (R2.2) $g(d)$ is stated in (d).

3.2.5.2 Rate-independent crack dissipation functional with threshold function

To account for the energy dissipated in the continuum, the dissipation functional $\mathcal{D}$ is introduced as

$$\mathcal{D}(\dot{d}) = \int_{\mathcal{B}} g_{\mathrm{c}}[\delta_d \gamma(d, \nabla d; \boldsymbol{\mathcal{L}})]\, \dot{d}\, \mathrm{d}V, \tag{3.38}$$

where $\delta_d \gamma$ denotes the variational derivative of the anisotropic volume-specific crack surface γ, whereas g_{c} is referred as the critical fracture energy (Griffith-type critical energy release rate), see Miehe et al. [143] and Gültekin et al. [66]. The second law of ther-

modynamics strictly demands that the dissipation functional has to be non-negative for all admissible deformation processes ($\mathcal{D} \geq 0$). This thermodynamic inequality is *a priori* fulfilled by a constitutive dissipation function Φ featuring a positive and convex propensity (Miehe [136] and Miehe and Schänzel [141]). This function can readily be stated by the principle of maximum dissipation via the following constrained optimization problem

$$\Phi(\dot{d}; d, \nabla d) = \sup_{\beta \in \mathbb{E}} \beta \dot{d}, \tag{3.39}$$

which can be solved by a Lagrange method that leads to

$$\Phi(\dot{d}; d, \nabla d) = \sup_{\beta, \lambda \geq 0} [\beta \dot{d} - \lambda t_{\mathrm{c}}(\beta; d, \nabla d)], \tag{3.40}$$

in terms of the local driving force β, dual to $\dot{d}$, and λ is the Lagrange multiplier that enforces the constraint. Additionally, we have defined the threshold function t_{c} delineating a reversible domain $\mathbb{E}$ such that

$$\mathbb{E}(\beta) = \{\beta \in \mathbb{R} \mid t_{\mathrm{c}}(\beta; d, \nabla d) = \beta - g_{\mathrm{c}}[\delta_d \gamma(d, \nabla d; \boldsymbol{\mathcal{L}})] \leq 0\}. \tag{3.41}$$

Based on (3.40) the extended dissipation functional $\mathcal{D}_\lambda$ reads

$$\mathcal{D}_\lambda(\dot{d}, \beta, \lambda; d) = \int_{\mathcal{B}} [\beta \dot{d} - \lambda t_{\mathrm{c}}(\beta; d, \nabla d)] \mathrm{d}V. \tag{3.42}$$

3.2.5.3 Rate-independent variational formulation based on power balance

A summation of the aforestated functionals (3.35), (3.37), and (3.42) for the description of a rate-type potential Π_λ provides the power balance, i.e.

$$\Pi_\lambda = \mathcal{E} + \mathcal{D}_\lambda - \mathcal{P}. \tag{3.43}$$

On the basis of the rate-type potential (3.43), we introduce the saddle point principle for the quasi-static process, i.e.

$$\{\dot{\boldsymbol{\varphi}}, \dot{d}, \beta, \lambda\} = \mathrm{Arg} \left\{ \inf_{\dot{\boldsymbol{\varphi}} \in \mathcal{W}_{\dot{\varphi}}} \inf_{\dot{d} \in \mathcal{W}_{\dot{d}}} \sup_{\beta, \lambda \geq 0} \Pi_\lambda \right\}, \tag{3.44}$$

with the admissible domains for the primary variables

$$\mathcal{W}_{\dot{\varphi}} = \{\dot{\boldsymbol{\varphi}} \mid \dot{\boldsymbol{\varphi}} = \boldsymbol{0} \quad \text{on} \quad \partial\mathcal{B}_\varphi\}, \qquad \mathcal{W}_{\dot{d}} = \{\dot{d} \mid \dot{d} = 0 \quad \text{on} \quad \partial\mathcal{B}_d\}. \tag{3.45}$$

The variation of the functional Π_λ leads to the Euler-Lagrange equations describing the multi-field problem for the rate-independent fracture of an anisotropic hyperelastic solid, i.e.

$$\boxed{\begin{aligned} &1\text{:}\ J \operatorname{div}(J^{-1}\boldsymbol{\tau}) + \rho_0 \tilde{\boldsymbol{\gamma}} = \boldsymbol{0}, \\ &2\text{:}\ \beta - f = 0, \\ &3\text{:}\ \dot{d} - \lambda = 0, \end{aligned}} \tag{3.46}$$

along with the Karush-Kuhn-Tucker-type loading-unloading conditions ensuring the principal of maximum dissipation for the case of an evolution of the crack phase-field parameter d, i.e.

$$\lambda \geq 0, \qquad t_{\mathrm{c}} \leq 0, \qquad \lambda t_{\mathrm{c}} = 0. \tag{3.47}$$

In addition, Neumann-type boundary conditions can be defined as follows

$$J^{-1}\boldsymbol{\tau} \cdot \boldsymbol{n} = \tilde{\boldsymbol{t}}, \qquad \boldsymbol{\mathcal{L}} \nabla d \cdot \boldsymbol{N} = 0, \tag{3.48}$$

where $\boldsymbol{n}$ and $\boldsymbol{N}$ represent the unit surface normal oriented outwards in the spatial and the reference configuration, respectively. The elimination of β and λ through $(3.46)_{2,3}$ and the explicit form of the threshold function t_{c} result in

$$\dot{d} \geq 0, \qquad f - g_{\mathrm{c}} \delta_d \gamma(d, \nabla d; \boldsymbol{\mathcal{L}}) \leq 0, \qquad [f - g_{\mathrm{c}} \delta_d \gamma(d, \nabla d; \boldsymbol{\mathcal{L}})] \dot{d} = 0. \tag{3.49}$$

The first condition ensures the irreversibility of the evolution of the crack phase-field parameter. The second condition is an equality for an evolving crack, and is negative for a stable crack. The third condition is the balance law for the evolution of the crack phase-field subjected to the former conditions.

3.2.5.4 Rate-dependent variational formulation based on power balance

The viscous regularization of the rate-independent modality essentially confers stability on the algorithmic setting, a benefit which is purely related to numerics. To this end, we introduce a Perzyna-type (Perzyna [163]) viscous extension of the dissipation functional, i.e.

$$\mathcal{D}_\eta(\dot{d}, \beta; d) = \int_{\mathcal{B}} [\beta \dot{d} - \frac{1}{2\eta} \langle t_{\mathrm{c}}(\beta; d, \nabla d) \rangle^2] \mathrm{d}V, \tag{3.50}$$

where the viscosity η determines the viscous over-force governing the evolution of $\dot{d}$. In (3.50) the positive values for the threshold function t_{c} are always filtered out owing to the ramp function $\langle x \rangle = (x + |x|)/2$. Accordingly, the corresponding viscous rate-type potential reads

$$\Pi_\eta = \mathcal{E} + \mathcal{D}_\eta - \mathcal{P}. \tag{3.51}$$

On the basis of the rate-type potential (3.51), we propose a viscous extended saddle point principle for the quasi-static process, i.e.

$$\{\dot{\boldsymbol{\varphi}}, \dot{d}, \beta\} = \mathrm{Arg} \left\{ \inf_{\dot{\boldsymbol{\varphi}} \in \mathcal{W}_{\dot{\varphi}}} \inf_{\dot{d} \in \mathcal{W}_{\dot{d}}} \sup_{\beta \geq 0} \Pi_\eta \right\}, \tag{3.52}$$

with the admissible domains for the primary state variables as given in (3.45). Evaluating the variation of the potential Π_η we obtain the coupled set of Euler-Lagrange equations for

the rate-dependent fracture of an anisotropic hyperelastic solid as

$$\boxed{\begin{aligned} &1:\ J\,\mathrm{div}(J^{-1}\boldsymbol{\tau}) + \rho_0\tilde{\boldsymbol{\gamma}} = \boldsymbol{0},\\ &2:\ \beta - f = 0,\\ &3:\ \dot{d} - \frac{1}{\eta}\langle t_{\mathrm{c}}(\beta; d, \nabla d)\rangle = 0. \end{aligned}} \tag{3.53}$$

Substituting f into β, the explicit form of the threshold function t_{c} recasts the equality $(3.53)_3$ in such a form

$$f = \eta\dot{d} + g_{\mathrm{c}}\delta_d\gamma(d, \nabla d; \boldsymbol{\mathcal{L}}). \tag{3.54}$$

The rate-independent case is recovered for $\eta \to 0$. Note that the Perzyna-type viscous extension transforms the local driving force β such that it becomes unbounded, which enables β to take values outside the domain $\mathbb{E}$ in (3.41). This domain is originally described in elasto-visco-plasticity and continuum damage models, see Miehe [134] and Simo and Hughes [197] among others, and later in the crack phase-field models of Miehe et al. [143] and Miehe and Schänzel [141].

3.3 Theoretical Aspects of Anisotropic Failure Criteria

Focusing on the rate-independent case (3.54), for $\eta \to 0$, we engage ourselves in building a general framework for the crack phase-field model into which distinct failure criteria can easily be incorporated. We start by elaborating on the energetic force $(3.36)_2$. Accordingly, we substitute the equations (3.31) and (3.33) into $(3.36)_2$ to arrive at

$$f = 2(1-d)\Psi_0. \tag{3.55}$$

Inserting (3.55) into (3.54) for the rate-independent case and adopting $(3.15)_1$, the following relation holds

$$2(1-d)\frac{\Psi_0}{g_{\mathrm{c}}/l} = d - \nabla\cdot(\boldsymbol{\mathcal{L}}\nabla d), \tag{3.56}$$

whereby one can define the dimensionless crack driving force

$$\boxed{\overline{\mathcal{H}} = \frac{\Psi_0}{g_{\mathrm{c}}/l},} \tag{3.57}$$

which already characterizes a criterion for general isotropic materials. Another important feature of (3.57) is that the dimensionless characteristics of $\overline{\mathcal{H}}$, as discussed by Miehe et al. [142], allows to incorporate different types of failure criteria which we will address in the forthcoming sections. Following this, we stipulate two significant conditions, i.e. the irreversibility of the crack preventing healing effects, and the positiveness of the crack driving force ensuring that the crack growth solely takes place upon loading. Thus,

$$\boxed{\mathcal{H}(t) = \max_{s\in[0,t]}\left[\langle\overline{\mathcal{H}}(s) - 1\rangle\right].} \tag{3.58}$$

The above ramp-type function is described by the Macaulay brackets which filter out the positive values for $\overline{\mathcal{H}}(s) - 1$ and keeps the solid intact below a threshold value, i.e. until the failure surface is reached; therefore, the crack phase-field does not evolve for $\overline{\mathcal{H}}(s) < 1$. We also note that (3.58) always takes into account the maximum value of $\bar{\mathcal{H}}(s) - 1$ in the deformation history thereby ensuring the irreversibility of cracking. With these adjustments, (3.56) now takes on the form

$$\boxed{2(1-d)\mathcal{H} = d - \nabla \cdot (\boldsymbol{\mathcal{L}} \nabla d),} \tag{3.59}$$

where the right-hand side of (3.59) is the geometric resistance to crack whereas the left-hand side is the local source term for the crack growth (Miehe et al. [142]). Bearing this in mind, we recall the rate-dependent case for $\eta \neq 0$, i.e.

$$\boxed{\dot{d} = \frac{1}{\eta}[2(1-d)\mathcal{H} - d + \nabla \cdot (\boldsymbol{\mathcal{L}} \nabla d)],} \tag{3.60}$$

which compares to (3.54) with the replacement of the dimensional energetic force by the dimensionless failure Ansatz, the cornerstone of the crack phase-field model. We emphasize that the variational formulation in Sec. 3.2 does not apply to cases where stress-based failure criteria are incorporated into the crack phase-field evolution (3.60). In other words, stress-based criteria, as described in the Sec. 3.3.2–3.3.4, can only be added on a rather *ad hoc* basis.

3.3.1 Energy-based anisotropic failure criterion

The phase-field approach outlined in (3.53) induces anisotropic failure because of (i) an anisotropic constitutive response and (ii) an anisotropic crack surface energy function. However, the crack driving force $\mathcal{H}$ has a single threshold energy g_{c}/l for all directions. This is a strong restriction and does not comply with the physically observed phenomenon. In order to characterize anisotropic failure in arterial walls, we have recently proposed a novel energy-based anisotropic failure criterion (Gültekin et al. [66]). This proposed approach is now further elaborated in the present paper.

We start with the assumption that two distinct failure processes governing the cracking of the ground matrix and the fibers, whereby the anisotropic structure tensor $\boldsymbol{\mathcal{L}}$, as introduced in (3.12), also assumes a distinct form such that

$$\boldsymbol{\mathcal{L}}^{\mathrm{iso}} = l^2 \boldsymbol{I}, \qquad \boldsymbol{\mathcal{L}}^{\mathrm{ani}} = l^2[\omega_{\mathrm{M}}(\boldsymbol{M} \otimes \boldsymbol{M}) + \omega_{\mathrm{M}'}(\boldsymbol{M}' \otimes \boldsymbol{M}')], \tag{3.61}$$

which modifies (3.56) to account for the distinct failure assumption. Thus,

$$f^{\mathrm{iso}} - \frac{g_{\mathrm{c}}^{\mathrm{iso}}}{l}[d - \nabla \cdot (\boldsymbol{\mathcal{L}}_{\mathrm{iso}} \nabla d)] = 0, \qquad f^{\mathrm{ani}} - \frac{g_{\mathrm{c}}^{\mathrm{ani}}}{l}[d - \nabla \cdot (\boldsymbol{\mathcal{L}}_{\mathrm{ani}} \nabla d)] = 0. \tag{3.62}$$

Note that the energetic force f in (3.55) is additively decomposed into an isotropic part f^{iso} and an anisotropic part f^{ani} such that

$$f^{\mathrm{iso}} = 2(1-d)\hat{\Psi}_0^{\mathrm{iso}}, \qquad f^{\mathrm{ani}} = 2(1-d)\hat{\Psi}_0^{\mathrm{ani}}. \tag{3.63}$$

In (3.62) we have introduced the critical fracture energies over the length scale, namely $g_{\mathrm{c}}^{\mathrm{iso}}/l$ for the ground matrix and $g_{\mathrm{c}}^{\mathrm{ani}}/l$ for the fibers, which are dual to the effective free-energy functions delineating the isotropic and the anisotropic response, respectively. Insertion of (3.63) into (3.62) leads to

$$2(1-d)\frac{\hat{\Psi}_0^{\mathrm{iso}}}{g_{\mathrm{c}}^{\mathrm{iso}}/l} = d - \nabla\cdot(\boldsymbol{\mathcal{L}}_{\mathrm{iso}}\nabla d), \qquad 2(1-d)\frac{\hat{\Psi}_0^{\mathrm{ani}}}{g_{\mathrm{c}}^{\mathrm{ani}}/l} = d - \nabla\cdot(\boldsymbol{\mathcal{L}}_{\mathrm{ani}}\nabla d). \tag{3.64}$$

According to the structure of (3.62) we need to define dimensionless crack driving forces for the isotropic part $\overline{\mathcal{H}}^{\mathrm{iso}}$ and the anisotropic part $\overline{\mathcal{H}}^{\mathrm{ani}}$ such that $\overline{\mathcal{H}} = \overline{\mathcal{H}}^{\mathrm{iso}} + \overline{\mathcal{H}}^{\mathrm{ani}}$. Thus,

$$\overline{\mathcal{H}}^{\mathrm{iso}} = \frac{\hat{\Psi}_0^{\mathrm{iso}}}{g_{\mathrm{c}}^{\mathrm{iso}}/l}, \qquad \overline{\mathcal{H}}^{\mathrm{ani}} = \frac{\hat{\Psi}_0^{\mathrm{ani}}}{g_{\mathrm{c}}^{\mathrm{ani}}/l}. \tag{3.65}$$

Superposing the isotropic and anisotropic failure processes (3.64) with the use of (3.65), we obtain $(1-d)\overline{\mathcal{H}} = d - \nabla\cdot(\boldsymbol{\mathcal{L}}\nabla d)/2$. Since $\overline{\mathcal{H}} = \overline{\mathcal{H}}^{\mathrm{iso}} + \overline{\mathcal{H}}^{\mathrm{ani}}$ enters in (3.58) we can rewrite it as

$$(1-d)\mathcal{H} = d - \frac{1}{2}\nabla\cdot(\boldsymbol{\mathcal{L}}\nabla d), \tag{3.66}$$

for the rate-independent case, where the irreversibility of the crack growth is enforced by (3.58). Without loss of generality, the rate-dependent case can be shown, i.e.

$$\dot{d} = \frac{1}{\eta}[(1-d)\mathcal{H} - d + \frac{1}{2}\nabla\cdot(\boldsymbol{\mathcal{L}}\nabla d)]. \tag{3.67}$$

The crack phase-field parameter d in (3.66) and (3.67) can be considered as a homogenized damage parameter for the anisotropic continuum consisting of matrix and two families of fibers. Nevertheless, one can also envisage n distinct failure processes for the anisotropic part, with n distinct fiber families, i.e. each fiber family may undergo a separate failure process. In that case, the evolution equation for the crack phase-field parameter then reads

$$\dot{d} = \frac{1}{\eta}\left[\frac{2}{n+1}(1-d)\mathcal{H} - d + \frac{1}{n+1}\nabla\cdot(\boldsymbol{\mathcal{L}}\nabla d)\right], \quad \text{with} \quad \boldsymbol{\mathcal{L}} = \boldsymbol{\mathcal{L}}^{\mathrm{iso}} + \sum_{i}^{n}\boldsymbol{\mathcal{L}}_i^{\mathrm{ani}}. \tag{3.68}$$

3.3.2 Stress-based anisotropic Tsai-Wu failure criterion

The Tsai-Wu criterion is based on the strength of the material at which the stress space intercepts the assumed failure surface (Tsai and Wu [222]). Accordingly, the dimensionless crack driving force (3.57) with respect to the effective Cauchy stress tensor $\boldsymbol{\sigma}_0$ assumes the following composition of two scalar functions, i.e.

$$\overline{\mathcal{H}} = \boldsymbol{T} : \boldsymbol{\sigma}_0 + \boldsymbol{\sigma}_0 : \mathbb{T} : \boldsymbol{\sigma}_0, \tag{3.69}$$

where $\boldsymbol{T}$ denotes a second-order strength tensor while $\mathbb{T}$ is a fourth-order strength tensor. In the crack phase-field model of fracture the crack driving force (3.69) can easily be

incorporated into (3.58). Note that the principal axes of anisotropy lie on the reference axes – an appropriate transformation can be obtained by rotating the stress components. Through the exploitation of the major and minor symmetries of the strength tensors $\boldsymbol{T}$ and $\mathbb{T}$ they can be expressed in matrix notation as

$$[\boldsymbol{T}] = \begin{bmatrix} T_1 \\ T_2 \\ T_3 \\ T_4 \\ T_5 \\ T_6 \end{bmatrix}, \qquad [\mathbb{T}] = \begin{bmatrix} T_{11} & T_{12} & T_{13} & T_{14} & T_{15} & T_{16} \\ & T_{22} & T_{23} & T_{24} & T_{25} & T_{26} \\ & & T_{33} & T_{34} & T_{35} & T_{36} \\ & \text{sym} & & T_{44} & T_{45} & T_{46} \\ & & & & T_{55} & T_{56} \\ & & & & & T_{66} \end{bmatrix}, \tag{3.70}$$

which fall into the triclinic class of material symmetry for a fully anisotropic material. The numbers of independent strength components render 6 and 21, for $(\boldsymbol{T})_i$ and $(\mathbb{T})_{ij}$, respectively, where $i, j \in \{1, \ldots, 6\}$ (Tsai and Wu [222]). Other classes of symmetry relations, e.g., monoclinic, orthotropic, transversely isotropic, cubic and isotropic materials can also be characterized with the help of the strength tensors. In fact, the transformation relations are carried out in accordance with the classical approach to anisotropy, i.e. making use of invariant restrictions to the free-energy function, stress and elasticity tensors.

A particular stability condition is imposed on the strength components of the Tsai-Wu criterion to enforce an ellipsoidal failure surface which necessitates the positive-definiteness of the fourth-order strength tensor such that

$$T_{ii}T_{jj} - T_{ij}^2 \geq 0, \tag{3.71}$$

where repeated indices are not summations. In addition, the diagonal terms of the fourth-order strength matrix must be positive so that they become physically meaningful. The symmetry relations endow the model with a feature that causes a number of interaction terms in the fourth-order strength matrix to vanish. As a matter of fact, no interaction exists between the normal/shear components and between the shear/shear components in the off-diagonal terms of the fourth-order strength matrix for an orthotropic material. In particular, the following components would then vanish:

$$T_{14} = T_{24} = T_{34} = T_{15} = T_{25} = T_{35} = T_{45} = T_{16} = T_{26} = T_{36} = T_{46} = T_{56} \equiv 0. \tag{3.72}$$

Having identified the simplifications due to symmetry relations, we now proceed to other assumptions which involve further simplifications on the strength matrices $[\boldsymbol{T}]$ and $[\mathbb{T}]$. First, it is assumed that the failure strength remains the same due to a change in the sign of the normal or the shear stress which yields

$$T_1 = T_2 = T_3 = T_4 = T_5 = T_6 \equiv 0, \tag{3.73}$$

thereby rendering the second-order strength matrix $[\boldsymbol{T}]$ obsolete. For a detailed derivation, we refer to Tsai and Wu [222]. This assumption also brings forth the following definition

$$T_{ii} = \frac{1}{(\sigma_i^{\mathrm{u}})^2}, \tag{3.74}$$

for the diagonal terms of the fourth-order strength matrix which are related to the ultimate normal and shear stresses σ_i^{u}, with $i \in \{1, \dots, 6\}$. The off-diagonal terms emanating from the interaction of normal stresses, namely T_{12}, T_{13} and T_{23}, can be ignored, as they are equal to zero, as suggested by Pipes and Cole [165]. On the other hand, Tsai and Hahn [221] proposed an alternative way to identify these terms, i.e.

$$T_{12} = -\sqrt{\frac{T_{11}T_{22}}{4}}, \qquad T_{13} = -\sqrt{\frac{T_{11}T_{33}}{4}}, \qquad T_{23} = -\sqrt{\frac{T_{22}T_{33}}{4}}. \tag{3.75}$$

3.3.3 Stress-based anisotropic Hill failure criterion

Postulated on the basis of the well-known von Mises-Huber criterion, the anisotropic Hill criterion (Hill [77]) uses the following quadratic form of the dimensionless crack driving force (defined in (3.57))

$$\overline{\mathcal{H}} = \boldsymbol{\sigma}_0^{\mathrm{vm}} : \mathbb{T} : \boldsymbol{\sigma}_0^{\mathrm{vm}}, \tag{3.76}$$

where $\boldsymbol{\sigma}_0^{\mathrm{vm}}$ represents the effective von Mises stress tensor. The components of $\boldsymbol{\sigma}_0^{\mathrm{vm}}$ can be defined in terms of general stress components, i.e.

$$\sigma_{0_1}^{\mathrm{vm}} = \sigma_{0_1} - \sigma_{0_2}, \qquad \sigma_{0_2}^{\mathrm{vm}} = \sigma_{0_2} - \sigma_{0_3}, \qquad \sigma_{0_3}^{\mathrm{vm}} = \sigma_{0_3} - \sigma_{0_1}, \tag{3.77}$$

for the effective normal stresses. The effective shear stress components of $\boldsymbol{\sigma}_0^{\mathrm{vm}}$ are given as

$$\sigma_{0_4}^{\mathrm{vm}} = \sigma_{0_4}, \qquad \sigma_{0_5}^{\mathrm{vm}} = \sigma_{0_5}, \qquad \sigma_{0_6}^{\mathrm{vm}} = \sigma_{0_6}. \tag{3.78}$$

Note that in (3.76) the principal axes of anisotropy are chosen to be the reference axes. However, transformations can also be carried out by rotating the stress components. To characterize the current state of anisotropy, the matrix form of the fourth-order strength tensor $\mathbb{T}$ has only non-zero terms in the diagonal, i.e.

$$\begin{aligned}
T_{11} &= \frac{1}{2}\left[\frac{1}{(\sigma_1^{\mathrm{u}})^2} + \frac{1}{(\sigma_2^{\mathrm{u}})^2} - \frac{1}{(\sigma_3^{\mathrm{u}})^2}\right], \\
T_{22} &= \frac{1}{2}\left[\frac{1}{(\sigma_2^{\mathrm{u}})^2} + \frac{1}{(\sigma_3^{\mathrm{u}})^2} - \frac{1}{(\sigma_1^{\mathrm{u}})^2}\right], \\
T_{33} &= \frac{1}{2}\left[\frac{1}{(\sigma_3^{\mathrm{u}})^2} + \frac{1}{(\sigma_1^{\mathrm{u}})^2} - \frac{1}{(\sigma_2^{\mathrm{u}})^2}\right],
\end{aligned} \tag{3.79}$$

which relate to the effective normal stresses. In addition, (3.79) accounts for the interactions between the effective normal stresses. The terms connected to the effective shear stresses are given by

$$T_{44} = \frac{1}{4(\sigma_4^{\mathrm{u}})^2}, \qquad T_{55} = \frac{1}{4(\sigma_5^{\mathrm{u}})^2}, \qquad T_{66} = \frac{1}{4(\sigma_6^{\mathrm{u}})^2}. \tag{3.80}$$

Significant features of the Hill criterion are that the failure surface is not necessarily ellipsoidal as no constraint on $\mathbb{T}$ exists, and the failure essentially admits a surface of the von Mises-Huber-type along the isotropic directions.

Remark 3. It is important to note that in the crack driving forces (3.69) and (3.76) the principal axes of anisotropy for the material, say $\{\hat{\boldsymbol{e}}_1, \hat{\boldsymbol{e}}_2, \hat{\boldsymbol{e}}_3\}$, are aligned with the reference basis system, say $\{\boldsymbol{e}_1, \boldsymbol{e}_2, \boldsymbol{e}_2\}$, with the properties

$$\hat{\boldsymbol{e}}_i \cdot \hat{\boldsymbol{e}}_j = \delta_{ij} \qquad \text{and} \qquad \boldsymbol{e}_i \cdot \boldsymbol{e}_j = \delta_{ij}, \tag{R3.1}$$

where δ_{ij} denotes the Kronecker delta. In order to apply the mentioned crack driving forces, which are based on the fourth-order strength tensor $\mathbb{T}$, the effective stress tensor $\boldsymbol{\sigma}_0$, obtained according to the reference basis system, needs to be transformed to the material axis, i.e.

$$\hat{\boldsymbol{\sigma}}_0 = \boldsymbol{Q}\boldsymbol{\sigma}_0\boldsymbol{Q}^{\mathrm{T}}. \tag{R3.2}$$

Therein $\boldsymbol{Q}$ is an orthogonal tensor with the form

$$\boldsymbol{Q} = Q_{ij}\boldsymbol{e}_i \otimes \boldsymbol{e}_j, \qquad Q_{ij} = \boldsymbol{e}_i \cdot \hat{\boldsymbol{e}}_j, \tag{R3.3}$$

which transforms the basis system (of analysis) onto the material axis according to

$$\hat{\boldsymbol{e}}_i = \boldsymbol{Q}\boldsymbol{e}_i. \tag{R3.4}$$

3.3.4 Principal stress criterion

Developed on the basis of the Rankine theory of failure, the criterion of Raina and Miehe [168] reports on the spectral decomposition of the effective Cauchy stress tensor $\boldsymbol{\sigma}_0$. The authors merely consider the positive principal stresses. Thus,

$$\boldsymbol{\sigma}_0^+ = \sum_{i=1}^{3} \langle \sigma_{0_i} \rangle \boldsymbol{n}_i \otimes \boldsymbol{n}_i, \tag{3.81}$$

where σ_{0_i} denotes the effective principal stresses, and $\boldsymbol{n}_i$ are the corresponding eigenvectors for $i \in \{1, 2, 3\}$. Accordingly, the dimensionless crack driving force $\overline{\mathcal{H}}$ in (3.57) is rewritten as

$$\overline{\mathcal{H}} = \boldsymbol{\sigma}_0^+ : \mathbb{T} : \boldsymbol{\sigma}_0^+, \tag{3.82}$$

for which the fourth-order strength tensor $\mathbb{T}$ reads in the index notation

$$(\mathbb{T})_{ijkl} = \frac{1}{4\sigma_{\mathrm{crit}}^2}(A_{ik}A_{jl} + A_{il}A_{jk}), \tag{3.83}$$

where σ_{crit} denotes the reference critical stress associated with uniaxial loading in a certain axis that can be conceptually replaced by an ultimate stress. The second-order anisotropy tensor $(\boldsymbol{A})_{ij}$ in (3.83), expressed in index notation for $i, j, k, l \in \{1, 2, 3\}$, deals with the

mechanical response of orthotropic, transversely isotropic and isotropic materials. Details concerning how to construct the tensor $\boldsymbol{A}$ can be found in Raina and Miehe [168]. For a simplified case, when the principal axes coincide with the axes of reference, the crack driving force in (3.82) turns into

$$\overline{\mathcal{H}} = \sum_{i=1}^{3} \left(\frac{\langle \sigma_{0_i} \rangle}{\sigma_{\text{crit}} / \mathfrak{a}_i} \right)^2 . \tag{3.84}$$

It needs to be emphasized that $\mathfrak{a}_i$ are scaling factors to impose a certain class of material, e.g., transversely isotropic material, which also enters in $(\boldsymbol{A})_{ij}$.

3.4 Decoupled Weak Formulation

This section is devoted to a Galerkin-type weak formulation of the strong forms presented in Sec. 3.2. In particular, a staggered solution procedure is implemented, where the coupled Euler-Lagrange equations are successively solved on the basis of a one-pass operator-splitting algorithm on the temporal side, whereas a Galerkin-type weak formulation on the spatial side furnishes the rate-dependent formulation of the phase-field. Such a solution algorithm sequentially updates the crack phase-field and the deformation map in a typical time step by means of a Newton-Raphson scheme.

3.4.1 One-pass operator-splitting algorithm

We first perform a decoupling of the mechanical and crack phase-field sub-problems by the virtue of a one-pass operator-splitting algorithm composed of two sub-algorithms, i.e.

$$\texttt{ALGO}_{\text{CM}} = \texttt{ALGO}_{\text{C}} \circ \texttt{ALGO}_{\text{M}}, \tag{3.85}$$

for a typical time increment $\tau = t_{n+1} - t_n$, where t_{n+1} and t_n stand for the current and previous time steps, respectively. For the sake of keeping the notation compact, all field variables without subscript are hereinafter evaluated at time t_{n+1}. The operator-splitting algorithm basically converts the non-convex coupled problem into two convex and symmetric sub-problems which are computationally more feasible than the monolithic scheme. The algorithm of each sub-problem reads

$$(\text{M}): \begin{cases} J \operatorname{div}(J^{-1}\boldsymbol{\tau}) + \rho_0 \tilde{\boldsymbol{\gamma}} = \boldsymbol{0}, \\ \dot{d} = 0, \end{cases} \qquad (\text{C}): \begin{cases} \dot{\boldsymbol{\varphi}} = \boldsymbol{0}, \\ d - \nabla \cdot (\boldsymbol{\mathcal{L}} \nabla d) - 2(1-d)\mathcal{H} + \eta \dot{d} = 0. \end{cases} \tag{3.86}$$

The algorithm (M) is the mechanical predictor step which is solved for the frozen crack phase-field parameter $d = d_n$, while the algorithm (C) is the crack evolution step for the frozen deformation map $\boldsymbol{\varphi} = \boldsymbol{\varphi}_n$.

3.4.2 Time-discrete weak formulation

We construct the weak forms of the balance of linear momentum $(3.53)_1$ and the rate-dependent evolution equation of the crack phase-field (3.60). For the quasi-static problem under consideration, we introduce two test function fields $\delta\boldsymbol{\varphi}$ and δd, regarded as the virtual deformation and the crack phase-field, respectively. Thereby, $\delta\boldsymbol{\varphi}$ and δd satisfy the homogeneous form of the Dirichlet boundary conditions on their corresponding reference surfaces $\partial\mathcal{B}_\varphi$ and $\partial\mathcal{B}_d$ according to

$$\delta\boldsymbol{\varphi} \in \mathcal{W}_{\delta\varphi} = \{\delta\boldsymbol{\varphi} \mid \delta\boldsymbol{\varphi} = \boldsymbol{0} \quad \text{on} \quad \partial\mathcal{B}_\varphi\}, \quad \delta d \in \mathcal{W}_{\delta d} = \{\delta d \mid \delta d = 0 \quad \text{on} \quad \partial\mathcal{B}_d\}. \tag{3.87}$$

A conventional Galerkin procedure leads to the weighted residual expressions of the field variables for the mechanical problem, i.e.

$$G^\varphi = G^\varphi_{\text{int}}(\delta\boldsymbol{\varphi}, \boldsymbol{\varphi}, d) - G^\varphi_{\text{ext}}(\delta\boldsymbol{\varphi}) = 0, \tag{3.88}$$

and the phase-field problem

$$G^d = G^d_{\text{int}}(\delta d, \boldsymbol{\varphi}, d) - G^d_{\text{ext}}(\delta d) = 0. \tag{3.89}$$

The term G^φ_{ext} in (3.88) represents the external weighted-residual due to the action of $\tilde{\boldsymbol{\gamma}}$ and $\tilde{\boldsymbol{t}}$, whereas the term for the phase-field in (3.89) vanishes ($G^d_{\text{ext}} = 0$), see Gültekin et al. [66]. The explicit expressions for G^φ_{int} and G^d_{int} with respect to (3.86) read

$$\begin{aligned} G^\varphi_{\text{int}} &= \int_{\mathcal{B}} \boldsymbol{g}\nabla_x(\delta\boldsymbol{\varphi}) : \boldsymbol{\tau}\,\mathrm{d}V, \\ G^d_{\text{int}} &= \int_{\mathcal{B}} \left\{ \delta d \left[d - 2(1-d)\mathcal{H} + \eta\frac{d-d_n}{\tau} \right] + \nabla(\delta d)\cdot\boldsymbol{\mathcal{L}}\nabla d \right\} \mathrm{d}V. \end{aligned} \tag{3.90}$$

A reliable and efficient solution of the above-mentioned equations entails a consistent linearization with respect to all quantities, i.e. $\boldsymbol{\varphi}$ and d, associated with the nonlinear problem about $\boldsymbol{\varphi} = \tilde{\boldsymbol{\varphi}}$ and $d = \tilde{d}$. Thus,

$$\begin{aligned} \mathrm{Lin} G^\varphi|_{\tilde{\boldsymbol{\varphi}}} &= G^\varphi(\delta\boldsymbol{\varphi}, \tilde{\boldsymbol{\varphi}}, d) + \Delta G^\varphi(\delta\boldsymbol{\varphi}, \tilde{\boldsymbol{\varphi}}, d; \Delta\boldsymbol{\varphi}) = 0, \\ \mathrm{Lin} G^d\Big|_{\tilde{d}} &= G^d(\delta d, \boldsymbol{\varphi}, \tilde{d}) + \Delta G^d(\delta d, \boldsymbol{\varphi}, \tilde{d}; \Delta d) = 0. \end{aligned} \tag{3.91}$$

The expressions in (3.91) are given by the Taylor's expansion through the Gâteaux derivative yielding the linear incremental terms ΔG^φ and ΔG^d, which are decomposed in the following way

$$\Delta G^\varphi = \Delta G^\varphi_{\text{int}} - \Delta G^\varphi_{\text{ext}}, \qquad \Delta G^d = \Delta G^d_{\text{int}} - \Delta G^d_{\text{ext}}. \tag{3.92}$$

Table 3.1 Algorithm for the multi-field problem in $[t_n, t_{n+1}]$.

1. *Initialization*	–	At time t_n given: deformation map, phase-field, history field $\boldsymbol{\varphi}_n$, d_n, $\mathcal{H}_n$
2. *Update*	–	Update the prescribed loads $\tilde{\boldsymbol{\gamma}}$, $\overline{\boldsymbol{\varphi}}$ and $\tilde{\boldsymbol{t}}$ at current time t_{n+1}
3. *Compute* $\boldsymbol{\varphi}_{n+1}$	–	Determine $\boldsymbol{\varphi}_{n+1}$ from the minimization problem of elasticity
$\texttt{ALGO}_{\mathrm{M}}$	•	$G^{\varphi} = \int_{\mathcal{B}} [\boldsymbol{g}\nabla_x(\delta\boldsymbol{\varphi}) : \boldsymbol{\tau}]\mathrm{d}V - \int_{\mathcal{B}} \delta\boldsymbol{\varphi}\cdot\rho_0\tilde{\boldsymbol{\gamma}}\mathrm{d}V - \int_{\partial\mathcal{B}} \delta\boldsymbol{\varphi}\cdot\tilde{\boldsymbol{t}}\mathrm{d}a = 0$
4. *Compute history*	–	Check crack initiation/propagation condition, update history
	•	$\mathcal{H}(t_{n+1}) \leftarrow \begin{cases} \mathcal{H}(t_n) & \text{if} \quad \mathcal{H}(t_{n+1}) < \mathcal{H}(t_n) \\ \mathcal{H}(t_{n+1}) & \text{else} \end{cases}$
5. *Compute* d_{n+1}	–	Determine d_{n+1} from the minimization problem of crack topology
$\texttt{ALGO}_{\mathrm{C}}$	•	$G^{d} = \int_{\mathcal{B}} \delta d \left[d - 2(1-d)\mathcal{H} + \eta\frac{d-d_n}{\tau}\right]\mathrm{d}V + \int_{\mathcal{B}} \nabla(\delta d)\cdot\boldsymbol{\mathcal{L}}\nabla d\mathrm{d}V = 0$

While the external terms vanish (Gültekin et al. [66]), the explicit forms of the internal terms are given as

$$\begin{aligned} \Delta G^{\varphi}_{\mathrm{int}} &= \int_{\mathcal{B}} \boldsymbol{g}\nabla_x(\delta\boldsymbol{\varphi}) : \mathbb{C} : \boldsymbol{g}\nabla_x(\Delta\boldsymbol{\varphi})\mathrm{d}V + \int_{\mathcal{B}} \nabla_x(\delta\boldsymbol{\varphi}) : \nabla_x(\Delta\boldsymbol{\varphi})\boldsymbol{\tau}\mathrm{d}V \\ \Delta G^{d}_{\mathrm{int}} &= \int_{\mathcal{B}} \delta d\left(1 + 2\mathcal{H} + \frac{\eta}{\tau}\right)\Delta d\mathrm{d}V + \int_{\mathcal{B}} \nabla(\delta d)\cdot\boldsymbol{\mathcal{L}}\nabla(\Delta d)\mathrm{d}V, \end{aligned} \tag{3.93}$$

where the Eulerian elasticity tensor $\mathbb{C}$ takes on the form $\mathbb{C} = g(d)(\mathbb{C}_0^{\mathrm{iso}} + \mathbb{C}_0^{\mathrm{ani}})$. The spatial discretization of the time-discrete decoupled weak forms in (3.90) and their corresponding linearizations documented in (3.93), provide their algebraic counterparts, namely the discrete residual vectors and the stiffness matrices. For an elaborate treatment of discretization methods and a staggered solution procedure based on a one-pass operator-splitting algorithm we refer to, e.g., Miehe et al. [143] and Gültekin et al. [66]. A general outlook of the staggered solution scheme is provided in Table 1.

3.5 Representative Numerical Examples

We start by demonstrating the effect of the anisotropic crack phase-field model on the propagation of the crack, in particular a sensitivity analysis is provided. Subsequently, the anisotropic failure criteria imparted in Sec. 3.3 are scrutinized from a numerical point of

view, i.e. the failure surface and the crack propagation associated with the distinct failure criteria are compared with each other on the basis of simple numerical examples.

3.5.1 Sensitivity analysis of the anisotropic phase-field model

In order to show the purely geometric effect that the anisotropy tensor $\boldsymbol{\mathcal{L}}$ grants to the phase-field formulation, a 2-D square benchmark problem, as described in the Fig. 3.6(a) and (b), is considered. This problem, unlike the majority of the examples in the crack phase-field literature, is performed in the absence of the mechanical field. The benchmark displays an anisotropic propensity via a single family of fibers $\boldsymbol{M}$, oriented by an angle of $\alpha = 30^{\circ}$ with respect to the x-axis. The (unstructured) finite element mesh consists of $10\,362$ four-noded quadrilateral elements. The phase-field parameter d is assigned a unit value within a disc with $1\,\text{mm}$ in diameter at the center of the domain thereby creating a difference between the surfaces energies ($g_c \Gamma_l(d)$) of the disc and the rest of the domain. The computations performed for the evolution of the crack phase-field ($\texttt{ALGO}_{\mathrm{C}}$) in a typical Newton iteration yield the diffusion of the phase-field for different values of the anisotropy parameter $\omega_{\mathrm{M}} = \{0, 1, 5, 10\}$, see the Fig. 3.6(c)–(f), respectively. In fact, the evolution of the phase-field parameter d starts to diverge from being isotropic (Fig. 3.6(c)), and becomes oriented along the direction of the fibers as the anisotropy parameter ω_{M} increases (Fig. 3.6(d)–(f)). This palpably suggests that the proposed model can handle transitions from isotropic to weak and strong anisotropy.

3.5.2 Numerical investigation of the failure surfaces

This investigation deals with a homogeneous problem of a unit cube discretized by one hexahedral element (Fig. 3.7(a)) that resolves the analytical solution for the deformation and the stress fields as all non-local effects due to the gradient of the crack phase-field ∇d are discarded. The effect of the length-scale parameter vanishes since l approaches to unity. As a loading protocol, we first consider separate uniaxial extension tests along the x-, y- and z-directions with a stretch ratio $\lambda_x = \lambda_y = \lambda_z \equiv 2$ which is followed by a series of planar biaxial deformations in the xy-plane with stretch ratios $\lambda_x : \lambda_y = 2 : 1.1$, $2 : 1.25$, $2 : 1.5$, $2 : 1.75$, $2 : 2$, $1.75 : 2$, $1.5 : 2$, $1.25 : 2$, $1.1 : 2$. Stretch ratios in the xz- and yz-planes $\lambda_x : \lambda_z$ and $\lambda_y : \lambda_z$ are applied in an analogous manner as for $\lambda_x : \lambda_y$, see the Fig. 3.7(b)–(d). The tissue is regarded as transversely isotropic consisting of one family of fibers with orientation $\boldsymbol{M}$ along the x-direction, and it is embedded in the ground matrix. The elastic material parameters and the crack phase-field parameters are listed for each failure criterion in Table 3.2.

Figure 3.8(a)–(c) illustrate the resulting failure surfaces at the instance when $d \neq 0$ for the energy-based criterion, the Tsai-Wu criterion and the principal stress criterion, respectively. The results of simulations conspicuously manifest the transverse isotropy of the three failure criteria as the failure surfaces are elliptical in shape (only one eight of an ellipsoid is shown due to the tensile characteristic of the deformation). The onset of crack occurs when the normal stress $\sigma_{xx} \approx 140\,\text{kPa}$, whilst the value of the other normal stresses

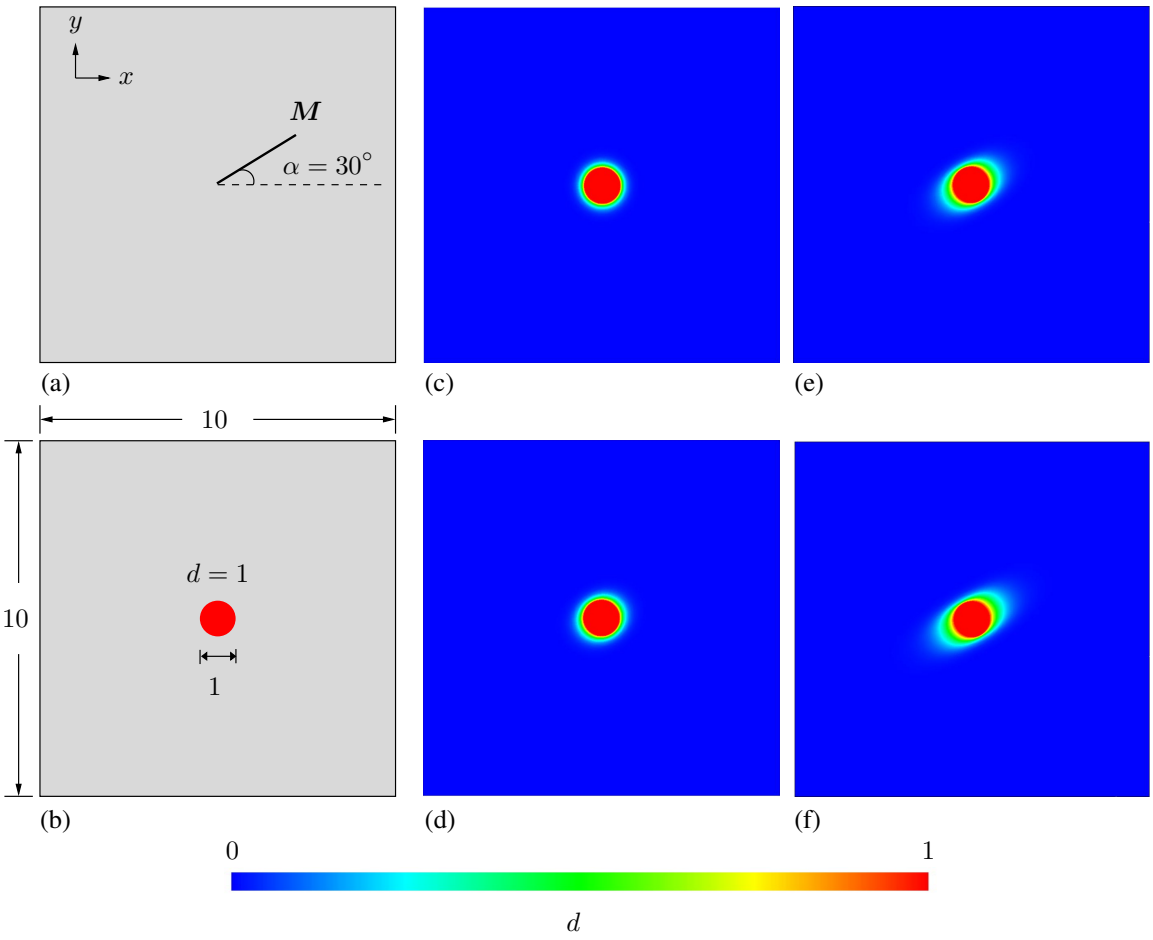

Figure 3.6 (a) 2-D square domain with one family of fibers oriented with an angle of $\alpha = 30^\circ$ with respect to the x-axis; (b) geometry of the domain and boundary condition delineating a disc, where $d = 1$. Evolution of the phase-field parameter d for a varying anisotropy parameter ω_{M}: (c) 0; (d) 1; (e) 5, (f) 10. Dimensions are provided in millimeters.

σ_{yy} and σ_{zz} are around 20 kPa. It needs to be emphasized that one can envisage a zone between the macroscopic onset ($d \neq 0$) and the completion ($d = 1$) of the crack in the context of diffusive crack modeling such as the crack phase-field. This example points out the associated macroscopic onset of the crack.

Figure 3.8(d) demonstrates the failure surfaces obtained at $d \neq 0$ for the Hill criterion. We note that the Hill criterion becomes in line with the von Mises-Huber criterion for the isotropic situation, namely the yz-plane. With the specified deformations the criterion cannot be satisfied when $\sigma_x^{\mathrm{u}} = 140$ kPa and $\sigma_y^{\mathrm{u}} = \sigma_z^{\mathrm{u}} = 20$ kPa. In fact, the failure envelope on the isotropic yz-plane becomes open-ended. Therefore, a different set of phase-field parameters are used, as listed in Table 3.2 in order to retrieve a closed-ended failure surface. The distinct shape of the failure envelope on the yz-plane eventually becomes discernable,

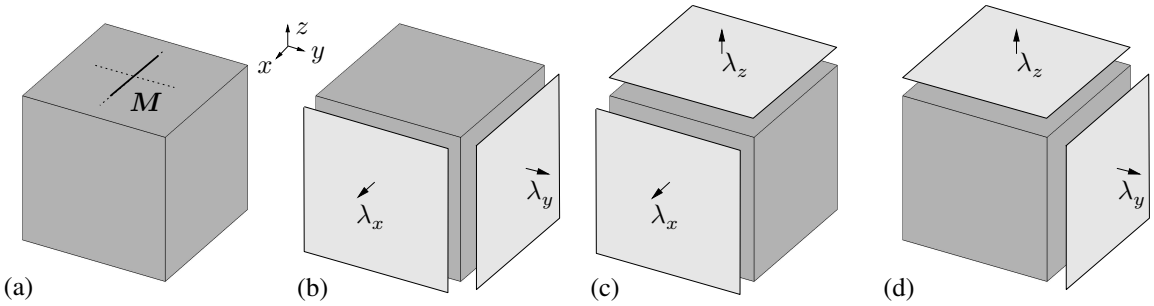

Figure 3.7 (a) Unit cube of a transversely isotropic tissue consisting of one family of fibers with the orientation $\boldsymbol{M}$ parallel to the x-direction, initially subjected to uniaxial deformations in the x-, y- and z-directions followed by a series of planar biaxial deformations (b) in the xy-plane; (c) in the xz-plane; (d) in the yz-plane.

Table 3.2 Elastic material parameters and crack phase-field parameters for a transversely isotropic material, as studied in Sec. 3.5.2.

Elastic		$\mu = 10\,\text{kPa}$	
		$k_1 = 20\,\text{kPa}$	
		$k_2 = 1$	
Crack phase-field	Energy-based criterion	$g_\text{c}^\text{iso} = 5\,\text{kPa mm}$	$g_\text{c}^\text{ani} = 15\,\text{kPa mm}$
	Tsai-Wu criterion	$\sigma_x^\text{u} = 140\,\text{kPa}$	$\sigma_y^\text{u} = \sigma_z^\text{u} = 20\,\text{kPa}$
	Principal stress criterion	$\sigma_\text{crit} = 140\,\text{kPa}$	$\mathfrak{a}_1 = 1,\ \mathfrak{a}_2 = \mathfrak{a}_3 = 7$
	Hill criterion	$\sigma_x^\text{u} = 30\,\text{kPa}$	$\sigma_y^\text{u} = \sigma_z^\text{u} = 20\,\text{kPa}$

see Fig. 3.8(d), which retrieves the von Mises-Huber criterion, as expected.

3.5.3 Uniaxial extension test investigated with different failure criteria

This benchmark represents a notched strip of a hypothetical arterial tissue with two families of fibers oriented in the directions $\boldsymbol{M}$ and $\boldsymbol{M}'$ and symmetrically arranged with respect to the x-axis by an angle α. The fibers correspond to the collagenous component of the tissue. The geometric setup and the loading condition are indicated in Fig. 3.9(a). The finite element mesh consists of $35\,163$ four-node tetrahedral elements connected by $7\,553$ nodes, and it comprises a refined zone beyond the notch where the crack is expected to propagate, see Fig. 3.9(b). As stated by Miehe et al. [143], in order to resolve the crack zone properly, the length-scale parameter l needs to be chosen at least twice as large as the minimum mesh size realized in the refined region. Accordingly, the length-scale parameter is selected as $l = 0.06\,\text{mm}$, and the viscosity η is set to zero. The weak anisotropy as corroborated by experimental results (see, e.g., Fig. 1 in [66]) is accommodated by the

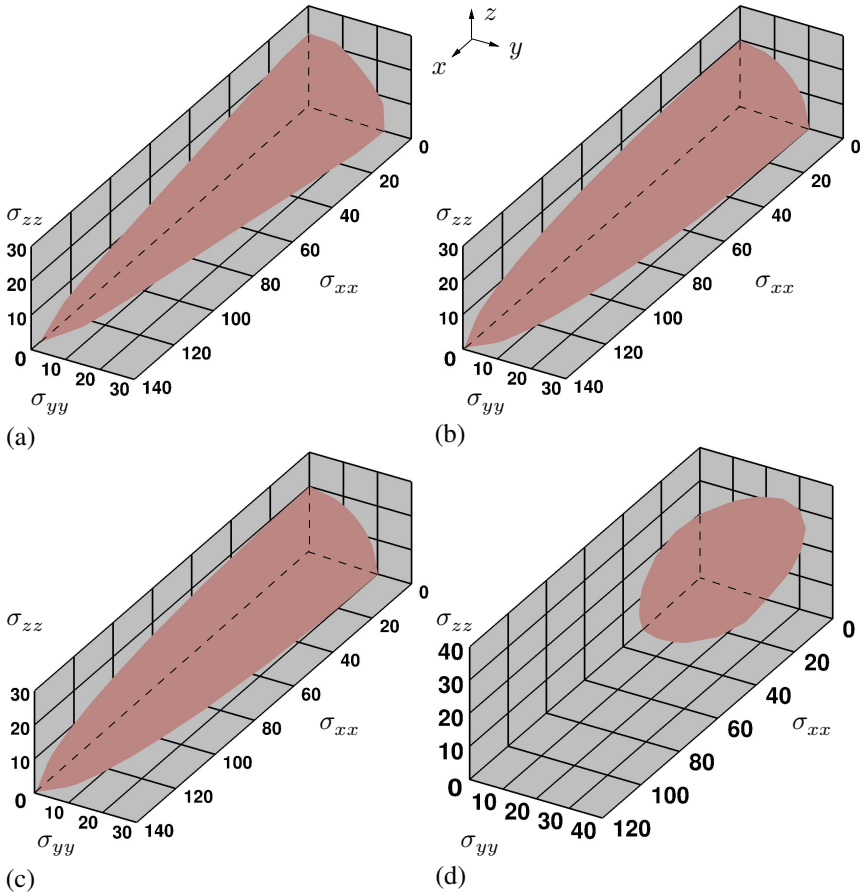

Figure 3.8 Failure surfaces in regard to Cauchy stresses σ_{xx}, σ_{yy} and σ_{zz} in kPa at which the failure conditions are satisfied, leading to $d > 0$ for (a) the energy-based; (b) the Tsai-Wu; (c) the maximum principal stress and (d) the Hill criterion.

anisotropy parameters $\omega_{\mathrm{M}} = \omega_{\mathrm{M}'} = 1.0$. The displacements are constrained in the planes $x = 0$, $y = 0$, and $z = 0$ along the x-, y-, and z- directions, respectively. The used elastic material parameters and the crack phase-field parameters are summarized in Table 3.3. The crack growth with respect to each failure criterion is analyzed for a monotonic load pattern driven by the displacement u throughout the numerical simulation, whereby the performance of the failure criteria is assessed in terms of their ability to mimic the crack propagation resulting in a complete rupture of the strip. Table 3.4 summarizes the number of simulation steps times step sizes considered for each criterion.

Figure 3.10 depicts the evolution of the crack phase-field d with respect to the four failure criteria at instants t_1, t_2, t_3 and t_4. The crack in the first and last case, namely the energy-based and the Hill criterion (Fig. 3.10(a) and (d)), grows by following a nearly straight pattern in the refined zone upon its initiation at the tip of the notch. However, both the Tsai-Wu and the principal stress criteria (Fig. 3.10(b) and (c)) show a spurious crack branching, not observed experimentally, see, e.g., Fig. 1 in [66]. The damaged zone also spreads

Table 3.3 Elastic material parameters and crack phase-field parameters for a strip extended uniaxially, as studied in Sec. 3.5.3.

Elastic		$\kappa = 10^4\,\text{kPa}$	
		$\mu = 16.95\,\text{kPa}$	
		$k_1 = 243.57\,\text{kPa}$	
		$k_2 = 2.57$	
		$\alpha = 44.5^\circ$	
Crack phase-field	Energy-based criterion	$g_\text{c}^\text{iso} = 1\,\text{kPa mm}$	$g_\text{c}^\text{ani} = 1.5\,\text{kPa mm}$
	Tsai-Wu criterion	$\sigma_x^\text{u} = \sigma_y^\text{u} = 1000\,\text{kPa}$	$\sigma_z^\text{u} = 333\,\text{kPa}$
	Principal stress criterion	$\sigma_\text{crit} = 1000\,\text{kPa}$	$\mathfrak{a}_1 = \mathfrak{a}_2 = 1, \quad \mathfrak{a}_3 = 3$
	Hill criterion	$\sigma_x^\text{u} = \sigma_y^\text{u} = 1000\,\text{kPa}$	$\sigma_z^\text{u} = 333\,\text{kPa}$

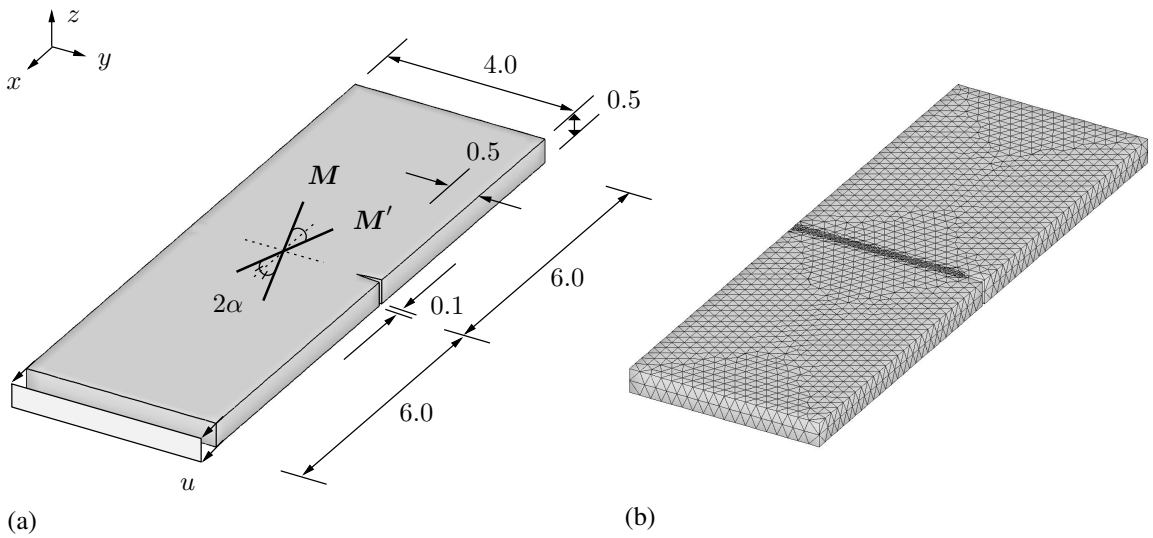

(a) (b)

Figure 3.9 (a) Geometry of the strip with two families of fibers oriented in the directions $\boldsymbol{M}$ and $\boldsymbol{M}'$ and symmetrically arranged with respect to the x-axis by an angle α. The strip is uniaxially loaded by means of a displacement u; (b) finite element mesh of the corresponding geometry with refinement beyond the notch. Dimensions are provided in millimeters.

out of the refined region. In this respect, the Hill criterion provides a more physically admissible picture than the other stress-based criteria albeit the crack front still remains spurious compared with that of the energy-based one. In fact, the energy-based criterion predicts a smoother crack-front than all stress-based criteria. Figure 3.11 illustrates curves that correspond to force F vs displacement u and to crack driving force $\overline{\mathcal{H}}$ vs time t, where the particular instants t_1, t_2, t_3 and t_4 are indicated for each failure criterion. As can be seen, a typical nonlinear response is followed by a sudden decrease in the load-bearing capacity,

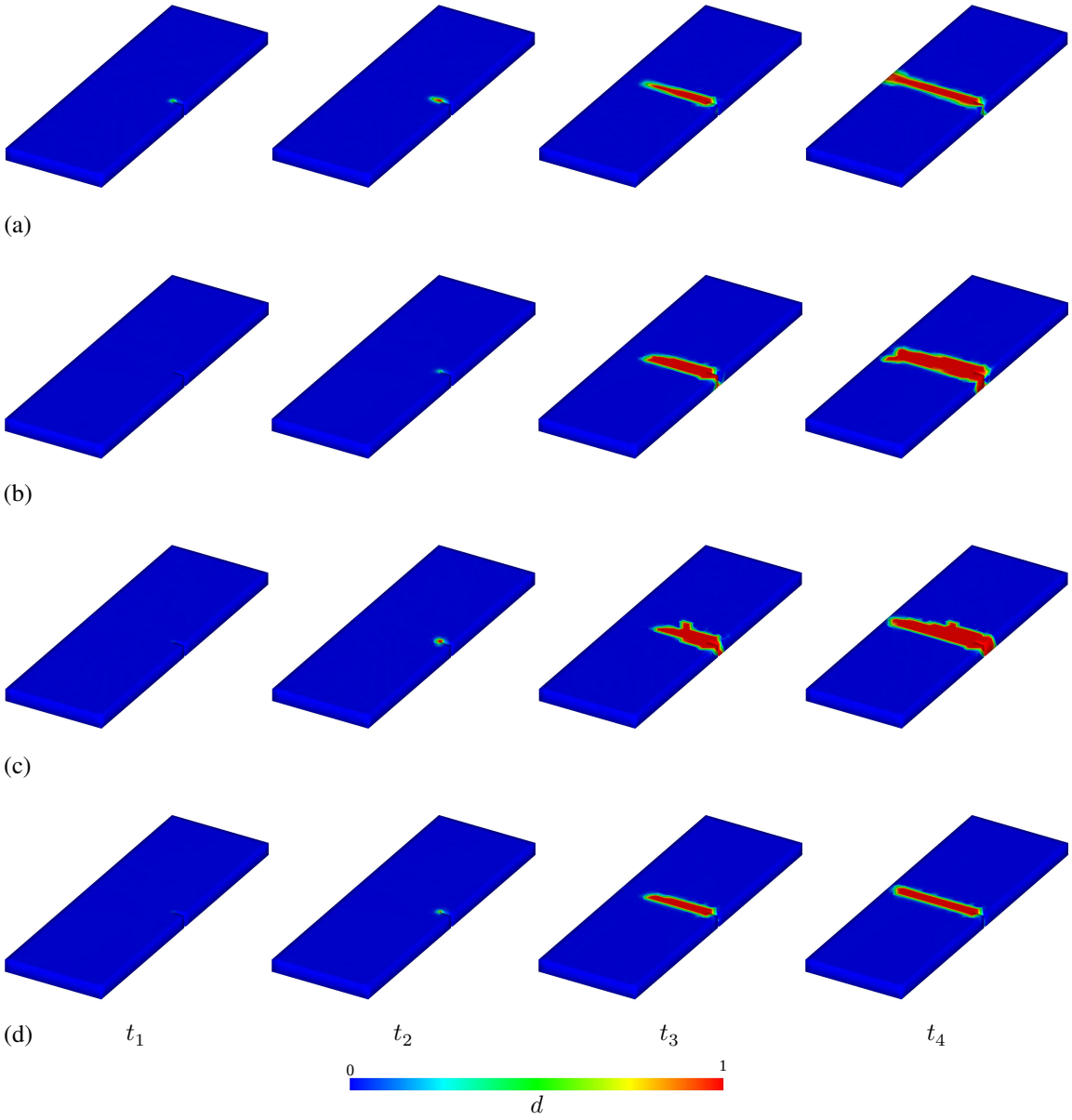

Figure 3.10 Evolution of the crack phase-field d in a notched strip of a hypothetical tissue uniaxially elongated: (a) energy-based criterion; (b) Tsai-Wu criterion; (c) principal stress criterion; (d) Hill criterion. The particular instants t_1, t_2, t_3 and t_4 manifest snapshots, compare with Fig. 3.11.

while a dramatic increase in the value of the crack driving force becomes evident upon the onset of macro-cracks at the tip of the notched region. Note that the force-displacement curves are obtained at the plane $x = 12\,\text{mm}$, whereas the crack driving force-time curves are depicted for a node just beyond the tip of the notch. The isotropic and anisotropic contributions due to $\overline{\mathcal{H}}^{\text{iso}}$ and $\overline{\mathcal{H}}^{\text{ani}}$ are discernable for the energy-based failure criterion. What is also intriguing is that there exists at least two orders of magnitude difference between the energy-based and the stress-based criteria in terms of the values of the crack

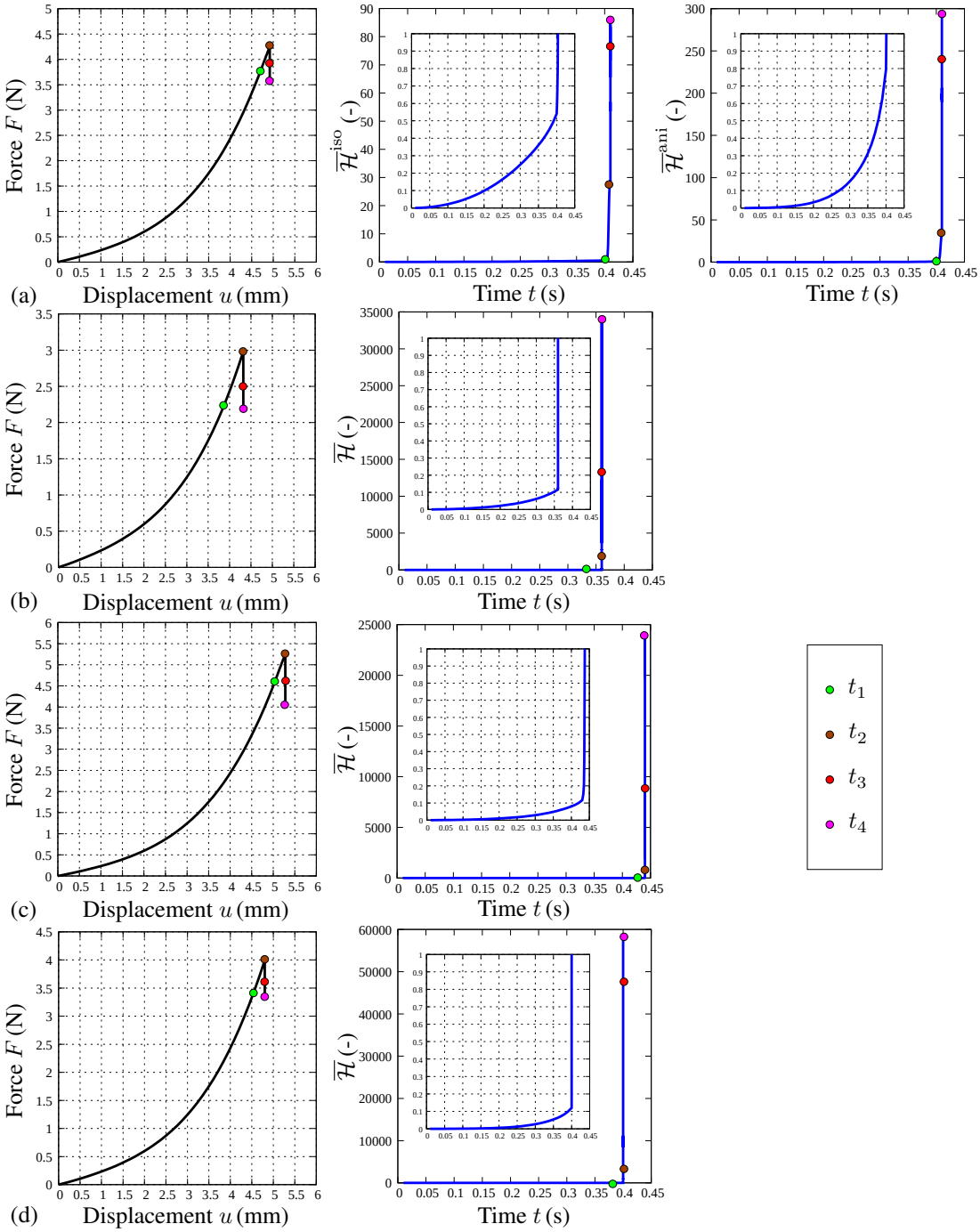

Figure 3.11 Plots corresponding to force F vs displacement u and to crack driving force $\overline{\mathcal{H}}$ vs time t, with regard to (a) energy-based criterion; (b) Tsai-Wu criterion; (c) principal stress criterion; (d) Hill criterion. The particular instants t_1, t_2, t_3 and t_4 manifest the snapshots in the previous figure (Fig. 3.10), and are also indicated here on curves. Zoom-in views for the $\overline{\mathcal{H}}$-t curves are also shown.

driving forces. That entails the use of smaller step sizes for all stress-based criteria after the fully initiated crack (indicated in Table 3.4) to avoid an unstable crack growth which may eventually lead to the loss of global convergence, and a sudden crush of the simulation.

Table 3.4 Number of steps times step sizes considered to simulate the uniaxial extension test for four different failure criteria.

Energy-based criterion	40×10^{-2}	10×10^{-3}	55×10^{-6}	
Tsai-Wu criterion	36×10^{-2}	10×10^{-5}	129×10^{-8}	
Principal stress criterion	43×10^{-2}	10×10^{-3}	10×10^{-6}	172×10^{-10}
Hill criterion	40×10^{-2}	5×10^{-5}	157×10^{-8}	

3.5.4 Peel test investigated with different failure criteria

Peel tests bear an immense resemblance to the physical phenomena of, e.g., aortic dissections and allow a computational analysis of the dissection propagation in terms of various failure criteria mentioned in Sec. 3.3. The benchmark involves an initial tear at the middle, and idealizes an arterial wall with a morphology rendered by a single family of fibers $\boldsymbol{M}$ oriented in the y-direction, see Fig. 3.12(a). We imitate the tailored geometry provided by Gasser and Holzapfel [57] and discretize the strip with $2\,640$ eight-node hexahedral elements connected by $5\,536$ nodes, see Fig. 3.12(b). Appropriate Dirichlet and Neumann-type boundary conditions are considered in order to avoid rigid body motions. A horizontal displacement $u_x = 4\,\text{mm}$ is incrementally applied at the arms on the top plane in the x-direction, while all nodes on the plane at $y = 0$ are fixed in all directions, see Fig. 3.12(a). In addition, the displacements in the z-direction are prevented to reflect the plain strain condition.

As to the elastic material parameters, we adopt $\mu = 16.2\,\text{kPa}$, $k_1 = 98.1\,\text{kPa}$ and $k_2 = 10$ according to Gasser and Holzapfel [57]. The penalty parameter and the length-scale parameter are chosen as $\kappa = 1\,000\,\text{kPa}$ and $l = 0.05\,\text{mm}$, respectively. The viscosity parameter is adjusted to be $\eta = 1\,\text{kPa s}$ for the energy-based criterion and $\eta = 10\,\text{kPa s}$ for the stress-based criteria, while the anisotropy parameters are selected as $\omega_{\text{M}} = 1.0$ and $\omega_{\text{M}'} = 0$. The other phase-field parameters are taken from Table 3.5.

Table 3.5 Crack phase-field parameters for a transversely isotropic strip peeled off as studied in Sec. 3.5.4.

Crack phase-field	Energy-based criterion	$g_{\text{c}}^{\text{iso}} = 4.17\,\text{kPa mm}$	$g_{\text{c}}^{\text{ani}} = 12.5\,\text{kPa mm}$
	Tsai-Wu criterion	$\sigma_y^{\text{u}} = 2500\,\text{kPa}$	$\sigma_x^{\text{u}} = \sigma_z^{\text{u}} = 500\,\text{kPa}$
	Principal stress criterion	$\sigma_{\text{crit}} = 2500\,\text{kPa}$	$\mathfrak{a}_2 = 1,\ \ \mathfrak{a}_1 = \mathfrak{a}_3 = 5$
	Hill criterion	$\sigma_y^{\text{u}} = 2500\,\text{kPa}$	$\sigma_x^{\text{u}} = \sigma_z^{\text{u}} = 500\,\text{kPa}$

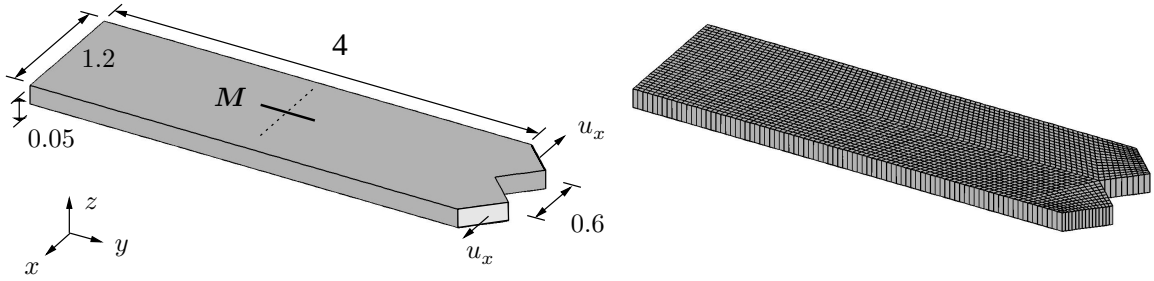

(a) (b)

Figure 3.12 (a) Geometry of the strip with a single family of fibers with orientation $\boldsymbol{M}$ in the y-direction, corresponding to the collagenous component of the material. The strip is torn apart by means of a displacement u_x applied at the two arms in the positive and negative x-direction; (b) finite element mesh of the corresponding geometry. Dimensions are provided in millimeters.

Figure 3.13 depicts the spatial distribution and the evolution of the crack phase-field for the energy-based, Tsai-Wu, principal stress and the Hill criterion, as the two arms of the strip separated by an initial tear are being pulled in opposite directions. The problems associated with all stress-based criteria in the previous example, see Sec. 3.5.3, seem to resume and they can only be circumvented via the use of smaller step sizes, see Table 3.6. Besides, the phase-field also evolves at locations where two arms bend which is also demonstrated by Ferrara and Pandolfi [51] as regions of higher stress concentrations compared with the dissecting zone at the middle. This undesired behavior is not present in the case of the energy-based criterion.

In Fig. 3.14 the force per unit width is plotted against the displacement applied (the separation of one arm) in regard to the energy-based, Tsai-Wu, principal stress and the Hill criterion. A weakly nonlinear response is observed until the ultimate load bearing capacity is reached, which is realized by a kind of plateau region. The load bearing capacity significantly diminishes afterwards for all failure criteria. It needs to be highlighted that the computation suffers due to incomplete convergence discernable from the jags in the loading path for the stress-based criteria, see Fig. 3.14(b)–(d).

Table 3.6 Number of steps times step sizes considered to simulate the peel test with four different failure criteria.

Energy-based criterion	1000×10^{-3}	
Tsai-Wu criterion	490×10^{-3}	5100×10^{-4}
Principal stress criterion	490×10^{-3}	5100×10^{-4}
Hill criterion	180×10^{-3}	8200×10^{-4}

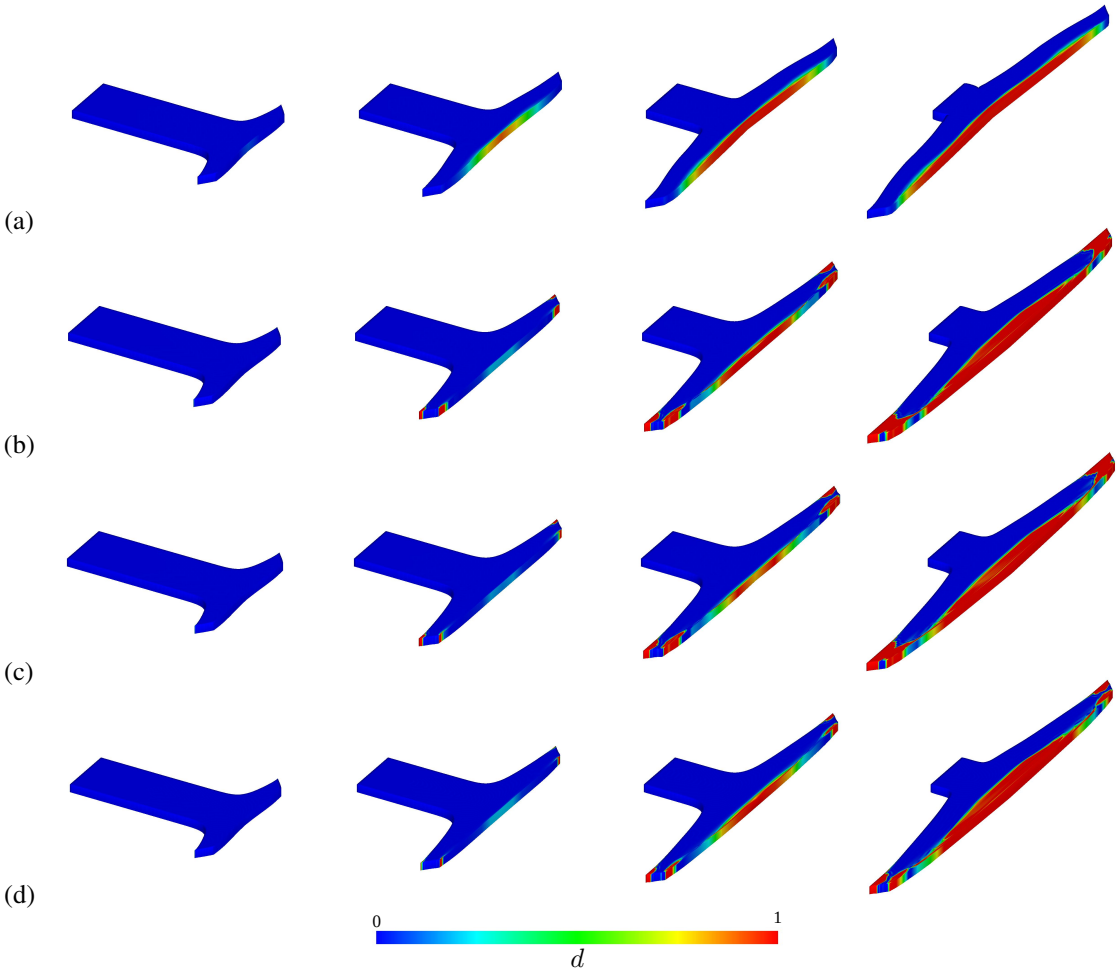

Figure 3.13 Evolution of the crack phase-field d for (a) the energy-based; (b) the Tsai-Wu; (c) the principal stress criterion; (d) the Hill criterion, as the arterial tissue with an initial tear is being pulled in two opposite directions.

3.6 Discussion

The most likely cause of numerical instability related with stress-based criteria may be that these criteria are essentially driven by the effective complementary energy $\Psi_{0_{\text{com}}}$ through the fourth-order strength tensor which is the analogue of the elastic compliance tensor. However, energy-based criteria are governed by the effective strain energy $\Psi_{0_{\text{str}}}$ *per se*. As a result, the changes $\Delta\Psi_{0_{\text{com}}}$ and $\Delta\Psi_{0_{\text{str}}}$ are not equivalent in a typical time increment $\Delta t = t_{n+1} - t_n$ provided that the mechanical response of the material is non-linear – typically the stress in a tissue grow faster at finite strains. Note that the two terms are interchangeable for the case of linear elasticity or in the context of small strains. In conclusion, the typical exponential nature of the stress-stretch relationship in soft biological tissues renders stress-based criteria non-functional. Figure 3.15 illustrates a qualitative sketch elucidating how the equivalence between $\Delta\Psi_{0_{\text{com}}}$ and $\Delta\Psi_{0_{\text{str}}}$ changes in the favor of $\Delta\Psi_{0_{\text{com}}}$ as the response of the material becomes highly nonlinear which utterly leads to

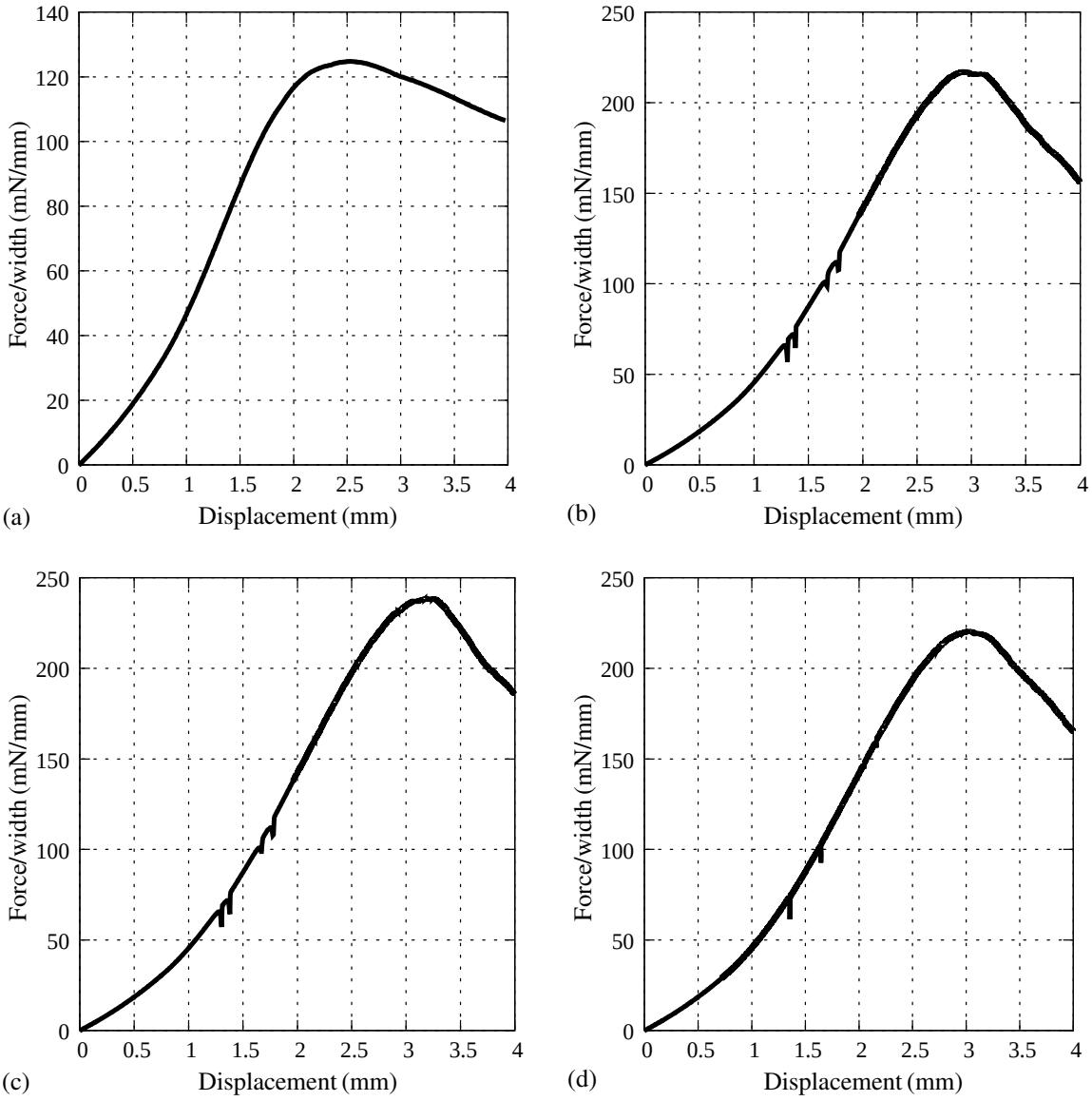

Figure 3.14 Plots of force per unit width for one arm against the applied displacement for (a) the energy-based; (b) the Tsai-Wu; (c) the principal stress criterion; (d) the Hill criterion.

an unstable crack growth. This phenomenon presents itself conspicuously in magnitudes of the dimensionless crack driving forces in Fig. 3.11 of Sec. 3.5.3.

The multi-field variational formulation leads to Euler-Lagrange equations governing the crack phase-field evolution and the static equilibrium in the absence of inertial effects. Hence, the derived formulation inherently leads to the crack path which minimizes the energy and maximizes the dissipation through the crack propagation process. However, the stress-based failure criteria merely describe the elastic domain of a brittle anisotropic material corresponding to the onset of the macro-cracks. The magnitudes of stress-based

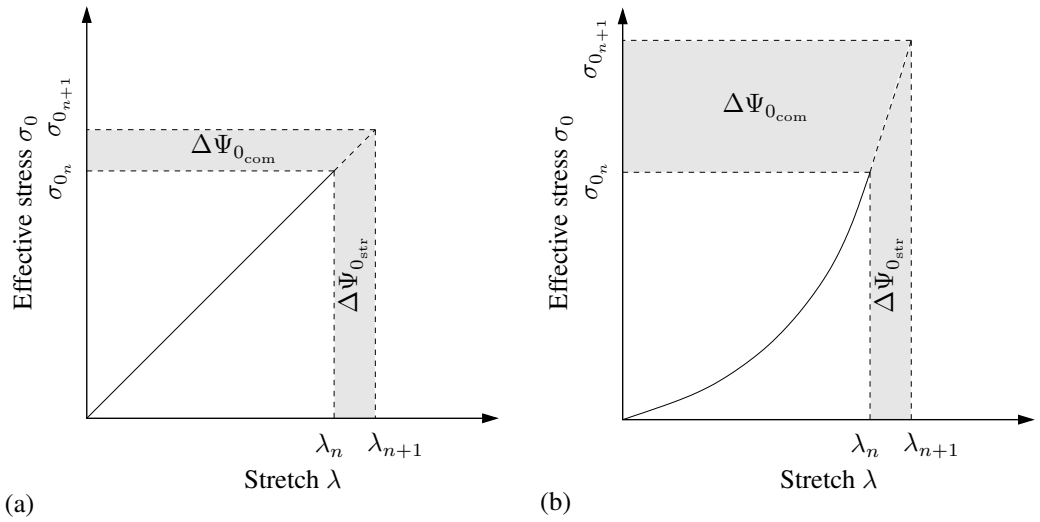

Figure 3.15 Qualitative sketch showing the relationship between the effective stress σ_0 and stretch λ, and the incremental change from σ_{0_n}–λ_n to $\sigma_{0_{n+1}}$–λ_{n+1} at a typical time step $\Delta t = t_{n+1} - t_n$: (a) linear; (b) nonlinear material behavior with the corresponding changes in the effective complementary energy $\Delta\Psi_{0_{\text{com}}}$ and the effective strain energy $\Delta\Psi_{0_{\text{str}}}$.

criteria beyond the failure surface do not necessarily lead to maximum dissipation or a minimum energy state since they can only be incorporated into the crack phase-field evolution equation on a rather *ad hoc* basis by taking the advantage of the crack driving force being dimensionless. As a matter of fact, the variational formulation does not hold for stress-based criteria producing a cracked zone in certain directions which may not correspond to a maximum dissipation or a minimum energy state of the effective material. Therefore, as evidently noticed in the Sec. 3.5.3, and 3.5.4, stress-based criteria are not able to portray physically relevant post-cracking states. However, in biomechanical applications, e.g., rupture of thoracic aortas, where not only the crack initiation but also the crack propagation is of fundamental concern, an energy criterion prevails.

The plots in Fig. 3.14 showing the force per unit width against the applied displacement seem to fall short of reproducing an asymptotic jagged plateau unlike those of Gasser and Holzapfel [57] and Ferrara and Pandolfi [51]. Nevertheless, the sensitivity analyses of [51] in the sense of mesh size and strength values suggest similar post-cracking states as in Fig. 3.14 when the analysis is performed by using a relatively coarse mesh along with high strength values. However, our study primarily spotlights the comparison of numerical performances obtained for various failure criteria. At this stage we do not look for model parameters that are fitted to experimental data.

3.7 Conclusion

In the present study we have compared a number of anisotropic failure criteria, essentially based on the free energy or the stress, with respect to their ability to capture admissible anisotropic failure surfaces and crack propagations for simple boundary-value

problems. On the theoretical side, the crack phase-field model, established according to a continuous variational setup due to a power balance, provided the backbone of our modeling endeavors. In the sequel, this framework was extended to the local rate-dependency of the phase-field evolution. The resulting Euler-Lagrange equations were recast by simple algebraic manipulations, and then solved by a one-pass operator-splitting algorithm on the temporal side which was ensued by a Galerkin-type weak formulation on the spatial side. On the constitutive part, a short summary of the energy-based criterion was given from our previous contribution. Subsequently, we introduced stress-based criteria (Tsai-Wu and Hill) together with the principal stress criterion.

On the numerical side, we focused on the anisotropic evolution of the crack phase-field. This was followed by the comparison of failure surfaces associated with the aforementioned criteria dealing with a homogeneous problem. The second investigation was performed on a notched strip of a hypothetical arterial tissue undergoing uniaxial extension, whereby the corresponding crack growth for each failure criterion was demonstrated. Finally, peel tests of a hypothetical arterial strip subjected to the aforementioned failure criteria were performed, and the respective dissections were systematically examined. The results of the simulations in Sec. 3.5.2 suggest that the energy-based criterion and the stress-based criteria, namely the Tsai-Wu and the principal stress criterion, can reflect the onset of the crack where the expected failure surfaces attributed to the transverse isotropy were acquired; however, the tests on the propagation of the crack in the Sec. 3.5.3 and 3.5.4 evidently favor the energetic-based criterion to accomplish a stable crack growth for the analyzed three-dimensional boundary-value problems blended with anisotropy at finite strains.

Acknowledgments

H.D. gratefully acknowledges financial support from TUBITAK (BIDEB 2232, Project # 114C073), while O.G. acknowledges financial support from the National Institutes of Health (research grant no. NIH 7R01HL117063-03).

4 COMPUTATIONAL MODELING OF PROGRESSIVE DAMAGE AND RUPTURE IN FIBROUS BIOLOGICAL TISSUES. APPLICATION TO AORTIC DISSECTION

Abstract This study analyzes the highly lethal clinical condition of aortic dissections from a numerical perspective. On the basis of previous contributions by Gültekin et al. (Comput. Methods Appl. Mech. Engrg. 312:542–566, 2016 and 331:23–52, 2018), we apply a holistic geometrical approach to fracture, namely the crack phase-field which inherits the intrinsic features of gradient damage and variational fracture mechanics. The continuum framework captures anisotropy, is thermodynamically consistent and based on finite strains. The balance of linear momentum and the crack evolution equation govern the coupled mechanical and phase-field problem. The solution scheme features the robust one–pass operator–splitting algorithm upon temporal and spatial discretizations. Subsequently, based on experimental data of diseased human thoracic aortic samples, the elastic material parameters are identified followed by a sensitivity analysis of the anisotropic phase-field model. Finally, we simulate an incipient propagation of an aortic dissection within a multi–layered segment of a thoracic aorta that involves a prescribed initial tear. The finite element results demonstrate a severe damage zone around the initial tear, exhibit a helical crack pattern, also observed in clinics, that aligns with the orientation of fibers. There is hope that the current contribution can provide some avenues for further investigations of this disease.

4.1 Introduction

Aortic dissection is a highly lethal condition revealed by a delamination and a separation of the adjacent lamellae within the media of the aorta. The annual incidences of aortic dissection ranges from 2 to 9 per $100\,000$ patients according to Clouse et al. [29] and Howard et al. [94]. It is of utmost importance to better understand the underlying mechanisms contributing to the development of the disease. Meanwhile, mathematically robust and physically relevant computational models can communicate certain aspects of this intricate phenomena.

4.1.1 Histology of the aortic wall

The aortic wall, the main conduction tube for the blood delivery, is an elastic artery which consists of three distinct layers: the *tunica intima*, the *tunica media* and the *tunica adventitia*. Being the main layer for metabolic processes, the intima is comprised of mono-layered endothelial cells supported by a fairly loose connective tissue, therefore imparts a negligible mechanical contribution to the wall resistance in young and healthy

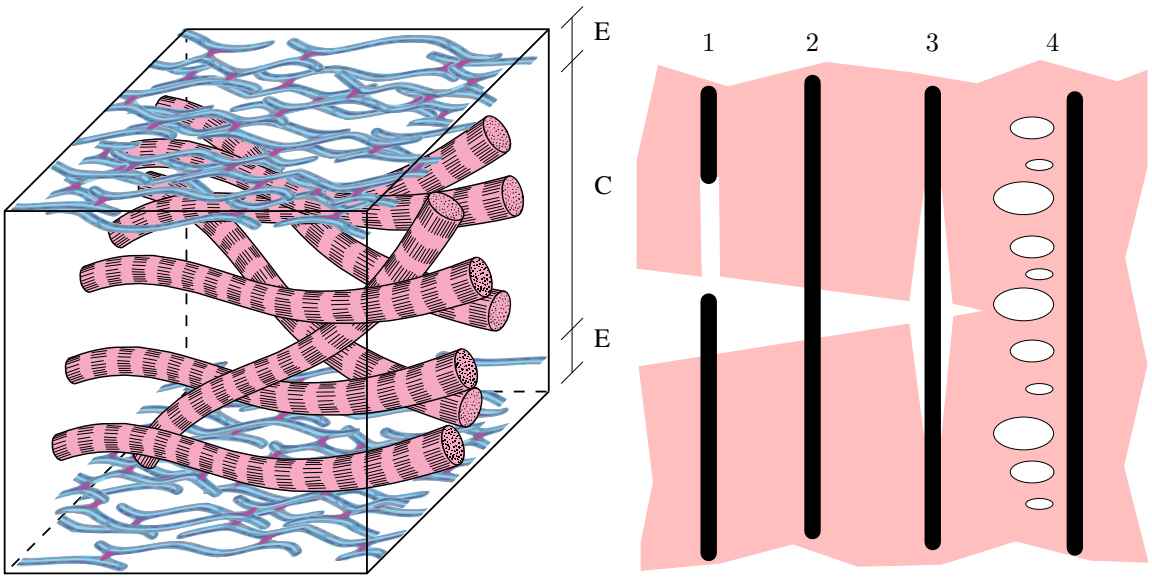

(a) (b)

Figure 4.1 (a) Schematic view of an aortic medial lamellar unit composed of two adjacent elastic lamellae (at the top and bottom represented by the letter E) including elastin and fibrillin microfibrils. In between the elastic lamellae is the embedded collagenous lamella (denoted by the letter C) that involves smooth muscle cells, adhesion molecules as well as GAGs and PGs not shown here due to illustrative reasons. This unit corresponds to the micro–scale outlook of the aortic wall with the typical thickness of the elastic lamella E around $1.5\,\mu$m and the collagenous lamella C around $12\,\mu$m, reconstructed from Ross & Pawlina [177]; (b) Possible damage and fracture mechanisms that are likely to occur in the aorta during *mode I*, *mode II* and *mixed–mode* fracture, 1: collagen fiber pull–out, 2: collagen fiber bridging, 3: collagen fiber/matrix debonding, 4: matrix cracking; reconstructed from Anderson [5].

individuals. Separated from the intima by the internal elastic lamina is the the mid–layer media supporting the aortic wall against the physiological blood pressure. The media is composed of as many as 70 fenestrated medial lamellar units, hosting two adjacent elastic lamellae (involving elastin) which are interposed by collagen fibers, smooth muscle cells and glycosaminoglycans (GAGs), proteogylcans (PGs) etc., see Fig. 4.1(a). As reported by Schriefl et al. [188] the media mainly involves two families of collagen fibers organized successively in the laminar unit each of which contains a single fiber family. The outermost layer of the artery is referred to as the adventitia, which prevents the excessive expansion of the wall during systole in a cardiac cycle. In contrast to the media, the adventitia forms a network of collagen fibers arranged in a helical structure and is in general stiffer than the media (Gasser et al. [58], Ross & Pawlina [177], Humphrey [98]).

A closer look into the structural features of the media and the adventitia unequivocally renders the elastin and the collagen fibers the most significant extra–cellular matrix pro-

teins, as illustrated in Fig. 4.1(a). Out of several damage and fracture mechanisms that exist in the variety of materials, collagen fiber pull–out, collagen fiber bridging, collagen fiber/matrix debonding and matrix cracking seem likely to occur in the aortic wall in *mode I*, *mode II* and *mixed–mode* fracture, see Fig. 4.1(b). Such an hypothesis is justified by studies summarized in Secs. 4.1.3 and 4.1.4. That the ultimate rupture stress values for single human collagen fibrils generally reach hundreds of MPa s, see, e.g., Svensson et al. [210], is a further evidence substantiating our theory that during the rupture of an aortic wall, the fiber–matrix and/or matrix–matrix interactions that keep the wall in register are broken, not the fibers *per se*.

4.1.2 General aspects of aortic dissection

An aortic dissection may present as an acute or a chronic type, depending on the duration clinical symptoms have lasted, Criado [35]. Of all factors that can be associated with the aortic dissection, hypertension appears to be the most common predisposing factor, diagnosed in 77% of patients according to an extensive review study conducted by Mussa et al. [150]. Among other factors are the cystic medial necrosis, connective tissue disorders, e.g., Marfan syndrome and Ehlers–Danlos syndrome, aneuryms, trauma, e.g., car accidents, cardiac catherization, male sex, and old individuals aged 60 to 70 years, see Dunning et al. [43], Criado [35] and Tsamis et al. [223].

The initial phase of an aortic dissection, in most cases, manifests itself with an initial tear in the intima due to some structural weakening in a localized part of the endothelium, see Fig. 4.2(a), the cause of which is an elusive phenomenon. An aortic dissection, however, may also commence within the wall due to an intramural haemorrhage or a hematoma formation in the media (Thubrikar et al. [217] and Khan & Nair [114]). Two third of all initial tears happen within the ascending aorta at $2\,\mathrm{cm}$ above the aortic root near the sinotubular junction (Pasta et al. [162]). The second common location is the isthmus of the descending thoracic aorta beyond the origin of the left subclavian artery, as depicted in Fig. 4.2(a) (Cherry & Dake [27]). From the hemodynamics point of view, the most likely reason that makes these areas prone to aortic dissection is the turbulent pulsatile blood flow imposed by the geometry, i.e. the blood pumped out of the left ventricle has to navigate the turn of the aortic arch, see Rajagopal et al. [169] and Cherry & Dake [27]. Upon the initial tear formation characterizing a radial propagation across the sub–layers of the media, the dissection changes its course and follows (mostly) a helical path, tracking the orientation of the single fiber family that exists in a single medial lamellar unit, creating a false lumen next to the true one, see Fig. 4.2(a). In any case, a crack propagation across the entire lamellae is not energetically favored (Ottani et al. [161]). A significant amount of the blood now enters in the dissected part of the wall, causing even more tearing as blood jets through the tear in each cardiac cycle. The dissection henceforth may continue to propagate down towards the abdominal aorta or create an exit (reentry) tear so that the blood can flow back into the true lumen (Cherry & Dake [27]). In the absence of an exit tear, more and more blood enters the false lumen which decreases the blood volume through the true lumen leaving the remaining wall susceptible to a dilatation. Over time

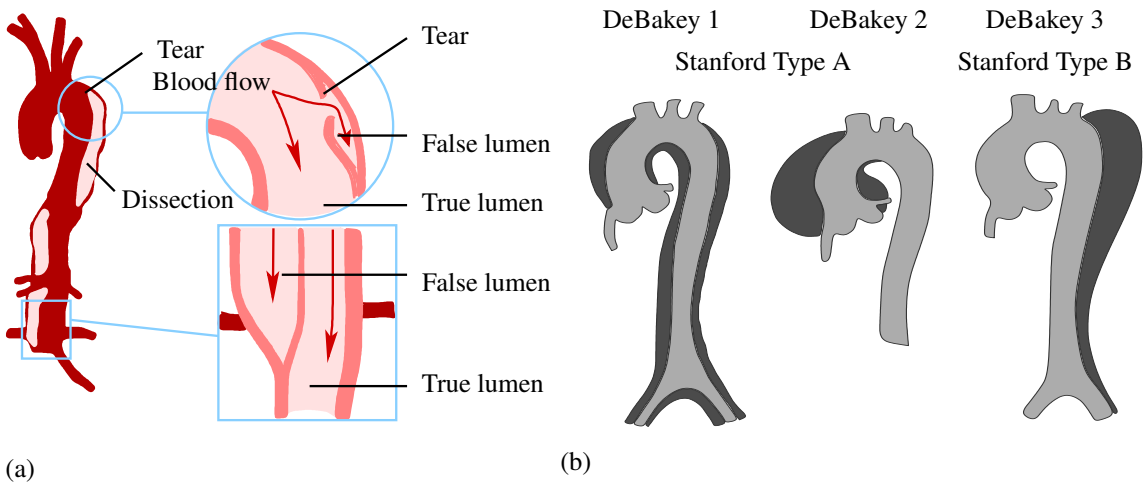

Figure 4.2 (a) Schematic view of aortic dissection which starts with an initial tear near the left subclavian artery and propagates downwards, while following a spiral path that results in the formation of a false lumen next to the true one through which the blood flow jet; (b) Classifications of the aortic dissection; while Stanford Type A always involves the ascending aorta, Stanford Type B excludes the ascending part. In the DeBakey system, type 1 includes the entire aorta, type 2 contains only the ascending aorta, and type 3 excludes the ascending aorta, reconstructed from Tsamis et al. [223].

this may cause other severe pathologies such as the rupture of the remaining aortic wall.

Classification of the aortic dissection is realized by the Stanford system and the DeBakey system, depicted in Fig. 4.2(b). In the Stanford classification, type A involves the ascending segment of the aorta, whereas in type B the ascending aorta is not affected. The DeBakey system, on the other hand, characterizes three different types of aortic dissection; type 1 involves the ascending and descending part of the aorta, and commonly extends beyond the arch distally. In type 2 the only part affected is the ascending aorta, while type 3 describes an aortic dissection excluding the ascending part (Tsamis et al. [223]).

4.1.3 Experimental studies on aortic dissection

Early experimental investigations on aortic dissections mostly followed methods such as pressurization, direct tension and peel tests. Carson & Roach [24], Roach & Song [174] infused fluid via a needle through the media extracted from porcine aortas, causing a bleb formation starting at a non–physiological pressure value of $579\,\mathrm{mmHg}$. Notably, the dissection later continued to propagate at physiological pressure values. In another study by Tam et al. [214], the pressure was found to be inversely correlated with the initial tear depth under static conditions. All studies stated above reported on the energy release rates ($\mathrm{mJ/cm^2}$), i.e. the energy expended to create a unit area of ruptured material, a significant concept in fracture mechanics. Later the experimental studies focused more on the direct tension and peel tests which were among others presented by Sommer et al. [203], Tong et

al. [219], Pasta et al. [162] and Wang et al. [230]. All investigations provided energy release rates which are spatially varying for different layers, i.e. intima, media and adventitia, and along different orientations the tests conducted, e.g., circumferential and longitudinal directions, suggesting an anisotropic rupture process.

Microscopical images of the dissected surfaces in the study of Sommer et al. [203] provided visual evidences for fiber pull–out and fiber/matrix debonding mechanisms. Nonetheless, direct tension, peel and trouser tests led to a delamination of the adjacent medial lamellae, which is undoubtedly driven by normal stress components, i.e. σ_{rr}, $\sigma_{\theta\theta}$, σ_{zz}, referring to *mode I* fracture. Later, Sommer et al. [205] found that ultimate in–plane shear stresses ($\sigma^u_{r\theta}$ and σ^u_{rz}) are consistently around one–order lower than ultimate out–of–plane shear stresses ($\sigma^u_{\theta z}$) based on simple shear tests performed on medial specimens which are cut off from the aneurysmatic human thoracic aorta. Such a result can be attributed to the collagen fibers embedded in the ground–matrix which are barely deformed in their mean orientation in the case of in–plane shear tests. Hence, the aortic dissection is less likely to propagate in the radial direction running across several collagenous lamellae, a conclusion which was also proposed by Haslach et al. [131], where a circumferential–longitudinal rupture plane was observed upon the inflation of bovine aortic ring segments regardless of the alterations made in the initial tear configuration. Haslach et al. [131] concluded that the dissection propagation, which can be explained by the relative slip between the adjacent medial lamellae on the circumferential–longitudinal plane, is an in–plane shear driven process evoking *mode II* fracture.

4.1.4 Numerical studies on aortic dissection

To date aortic dissection has been the subject matter of several numerical models in solid mechanics. Ferrara & Pandolfi [51] applied a cohesive zone model (CZM) together with an anisotropic traction–separation law and investigated a peel test that hinged on the experimental work by Sommer et al. [203]. In an experimental and computational study, Leng et al. [119] employed the CZM to fit the model parameters to load–displacement curves obtained from a shear dominated *mixed–mode* and a *mode I* peel test along both circumferential and longitudinal directions. Apart from that, Noble et al. [154] carried out experimental and computational analyses of a catheter–induced delamination. Gasser & Holzapfel [57] implemented an extended finite element method (XFEM) combined with the partition of unity finite element method and studied the peel test. Other studies resorting to XFEM were by Wang et al. [228, 229] where peel tests similar to the afore–mentioned contributions were numerically examined. Moreover, the authors therein presented an inflation test of a residually stressed plane strain solid model of a hollow circle representing the aortic wall cross–section, with varying opening angles. An identical blood pressure was applied on both the inner layer and the tear edge. The tear edge describes a prescribed circumferentially dissected zone where the nodal enrichments are introduced. As a result, the critical pressure value for aortic dissection to propagate was found to increase with the opening angle; therefore, residual stresses seem to prevent the artery against tear propagation. Even though several simplified solid domains (mostly in 2–D) hinged on CZM and

XFEM exist, which are relatively easy to handle in terms of tracking the discontinuities by means of remeshing and nodal/element enrichment functions, more complex and histologically representative 3–D geometries render CZM and XFEM arduous tasks to deal with.

In contrasts, a recently developed crack phase-field approach (CPFA) by Francfort & Marigo [54], i.e. a continuum model determined by a specific evolution equation next to the momentum balance, ultimately circumvents the modeling of discontinuities (Miehe et al. [138, 139], Ambati et al. [3], Borden et al. [14]). Resembling the gradient damage models, CPFA contains the critical fracture energy g_{c} (critical energy release rate), an essential ingredient of fracture mechanics. Within CPFA, Gültekin et al. [66, 67] studied rupture in human aortic tissues induced by uniaxial extension, simple shear and peeling. Therein, the authors assumed a distinct fracture mechanism involved in the overall macroscopic fracture process and introduced distinct critical fracture energies to the ground–matrix $g_{\mathrm{c}}^{\mathrm{iso}}$, and the fibrous content $g_{\mathrm{c}}^{\mathrm{ani}}$. They represent the up-scaled, homogenized, macro–resistance of the interactions within the ground–matrix and between the matrix and collagen fibers against damage and rupture. A more elaborate account on the extant computational solid models can be found in Gültekin & Holzapfel [69].

Aside from the benchmark solid models presented in the literature, there are a few patient–specific studies dealing with computational fluid dynamics (CFD) for exploring the underlying hemodynamics of the aorta. Tse et al. [225] found a blood pressure difference as high as 0.21 kPa between the true and the false lumen and pinpointed the proximal ascending aorta and the distal aortic arch as the areas subject to vortex flow, which coincides with the prevalent initial tear locations, see Sec. 4.1.2. Besides, on the basis of a helical blood pattern observed solely in the ascending aorta, the authors inferred that the clinically observed helical dissection propagation is the result of the vortex flow. Cheng et al. [26] showed that aortic morphology, initial tear size and position influence the flow and other hemodynamic parameters. Although most of the CFD studies consider the wall shear stress as a direct contributor in the development of the aortic dissection, such a hypothesis does not seem probable as the wall shear stresses range between 3 and 10 Pa, negligibly small compared with the stresses experienced within the wall. It is also worth emphasizing some fluid–solid interaction models within the context of aortic dissection, e.g., Qiao et al.[167] and Malvindi et al. [126].

4.1.5 Aims of the present study

In view of our previous findings and contributions in Gültekin et al. [66, 67], the present study delivers a computational protocol with novel features in order to investigate the nascent propagation of aortic dissection, addresses certain mechanical aspects of the phenomena which ultimately relies on the phase-field modeling of progressive damage and rupture.

The article is organized as follows. Section 4.2 offers a whirlwind tour of the continuum mechanical and algorithmic framework in terms of geometry, kinematics, governing balance equations and the solution strategy. Section 4.3 outlines a parameter identification

against the experimental data from a diseased human aorta and lays bare the anisotropic features of the model in relation to uniaxial extension of a single-notched edge solid domain. In addition, certain physical aspects of the nascent aortic dissection in an idealized cylindrical tube with a prescribed initial tear are touched upon. Secs. 4.4 and 4.5 provide a critical discussion and overview of some open problems and possible improvements regarding the discussed modeling concepts.

4.2 Multi-field Framework for Rupture

This section is devoted to anisotropic phase-field modeling of fracture. To this end, the primary field variables, namely the crack phase-field d and the deformation map $\boldsymbol{\varphi}$, are introduced along with their governing equations, i.e. the evolution of the crack phase-field and the balance of linear momentum. Subsequently, an account on the numerical edifice is given which features the operator-splitting algorithm. For the related continuum mechanics see, e.g., the books by Ogden [156] and Holzapfel [80].

4.2.1 Primary field variables of the multi-field problem

Let $\mathcal{B} \subset \mathbb{R}^3$ be a continuum body at time $t_0 \in \mathcal{T} \subset \mathbb{R}^+$ and $\mathcal{S} \subset \mathbb{R}^3$ at current time $t \in \mathcal{T} \subset \mathbb{R}^+$ in the Euclidean space. The coupled problem of rupture is expressed by the bijective deformation map $\boldsymbol{\varphi}_t$ and the auxiliary crack phase-field d, i.e.

$$\boldsymbol{\varphi}_t(\boldsymbol{X}) : \begin{cases} \mathcal{B} \times \mathcal{T} & \to & \mathcal{S}, \\ (\boldsymbol{X}, t) & \mapsto & \boldsymbol{x} = \boldsymbol{\varphi}(\boldsymbol{X}, t), \end{cases} \qquad d : \begin{cases} \mathcal{B} \times \mathcal{T} & \to & [0, 1], \\ (\boldsymbol{X}, t) & \mapsto & d(\boldsymbol{X}, t), \end{cases} \tag{4.1}$$

where $\boldsymbol{\varphi}_t$ maps a material point $\boldsymbol{X} \in \mathcal{B}$ onto a spatial point $\boldsymbol{x} \in \mathcal{S}$, see Fig. 4.3, while d, a thermodynamic measure of damage in the solid, interpolates between the intact ($d = 0$) and the ruptured ($d = 1$) state of the material corresponding to a domain regulated by the length–scale parameter l, as illustrated in Fig. 4.4. Note that the crack phase-field d is formulated in the reference configuration $\mathcal{B}$.

4.2.2 Kinematics of the mechanical problem

Let the gradient operators $\nabla(\bullet)$ and $\nabla_x(\bullet)$ denote the gradients with respect to the reference and the spatial coordinates $\boldsymbol{X}$ and $\boldsymbol{x}$. The continuous manifolds, i.e. $\mathcal{B}$ and $\mathcal{S}$, are locally equipped with the covariant reference and spatial metric tensors $\boldsymbol{G} = \delta_{IJ}\boldsymbol{E}^I \otimes \boldsymbol{E}^J$ and $\boldsymbol{g} = \delta_{ij}\boldsymbol{e}^i \otimes \boldsymbol{e}^j$, respectively, where δ_{IJ} and δ_{ij} simply denote the Kronecker deltas. Next, the bodies $\mathcal{B}$ and $\mathcal{S}$ are considered to admit the deformation gradient $\boldsymbol{F}$ and the left Cauchy-Green tensor $\boldsymbol{b}$ such that

$$\boldsymbol{F} = \nabla\boldsymbol{\varphi} \qquad \text{and} \qquad \boldsymbol{b} = \boldsymbol{F}\boldsymbol{G}^{-1}\boldsymbol{F}^{\mathrm{T}}, \tag{4.2}$$

for non–penetrable deformations, i.e. $J > 0$ where $J = \det\boldsymbol{F}$, see Fig. 4.3. The energy

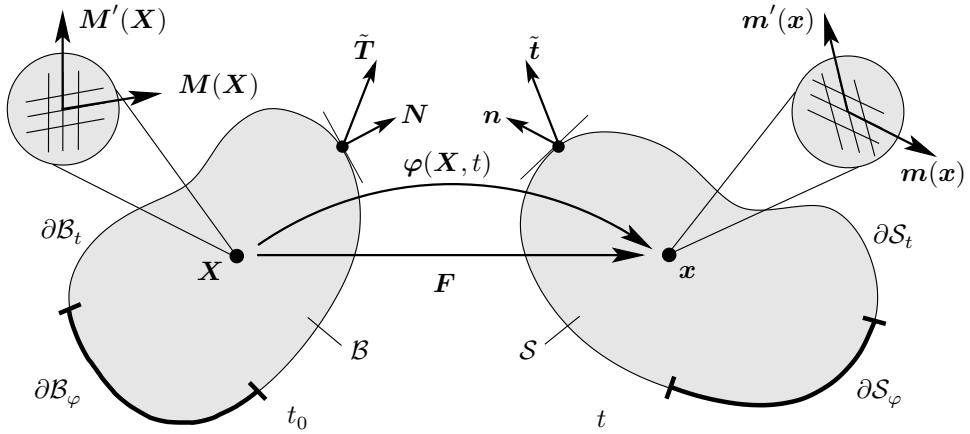

Figure 4.3 Nonlinear deformation of an anisotropic solid with the reference configuration $\mathcal{B} \subset \mathbb{R}^3$ and the spatial configuration $\mathcal{S} \subset \mathbb{R}^3$. The surface boundary associated with $\mathcal{B}$ is defined by $\partial\mathcal{B} \subset \mathbb{R}^2 = \partial\mathcal{B}_\varphi \cup \partial\mathcal{B}_t$ and $\partial\mathcal{B}_\varphi \cap \partial\mathcal{B}_t = \emptyset$, and the respective surface boundary in $\mathcal{S}$ is given by $\partial\mathcal{S} \subset \mathbb{R}^2 = \partial\mathcal{S}_\varphi \cup \partial\mathcal{S}_t$ and $\partial\mathcal{S}_\varphi \cap \partial\mathcal{S}_t = \emptyset$. The surface tractions $\tilde{\boldsymbol{T}}$ and $\tilde{\boldsymbol{t}}$ are applied on $\partial\mathcal{B}_t$ and $\partial\mathcal{S}_t$ with unit normals $\boldsymbol{N}$ and $\boldsymbol{n}$ pointing outward, respectively. The bijective deformation map is $\boldsymbol{\varphi} : \mathcal{B} \times \mathcal{T} \to \mathcal{S}$, which transforms a material point $\boldsymbol{X} \in \mathcal{B}$ onto a spatial point $\boldsymbol{x} = \boldsymbol{\varphi}(\boldsymbol{X}, t) \in \mathcal{S}$ at time t. The anisotropic micro-structure of the material point $\boldsymbol{X}$ is rendered by two families of fibers with unit vectors $\boldsymbol{M}$ and $\boldsymbol{M}'$. Likewise, the anisotropic micro-structure of the spatial point $\boldsymbol{x}$ is described by $\boldsymbol{m}$ and $\boldsymbol{m}'$ as the spatial counterparts of $\boldsymbol{M}$ and $\boldsymbol{M}'$, respectively.

stored in a hyperelastic isotropic continuum can be characterized by the three irreducible invariants

$$I_1 = \mathrm{tr}\boldsymbol{b}, \qquad I_2 = \frac{1}{2}\left[I_1^2 - \mathrm{tr}(\boldsymbol{b}^2)\right], \qquad I_3 = \det \boldsymbol{b}. \tag{4.3}$$

The anisotropic structure of the aortic wall that consists of a collagenous structure is registered by two reference unit vectors $\boldsymbol{M}$ and $\boldsymbol{M}'$ representing the mean fiber orientations, see Fig. 4.3, with their spatial counterparts, i.e. $\boldsymbol{m} = \boldsymbol{F}\boldsymbol{M}$ and $\boldsymbol{m}' = \boldsymbol{F}\boldsymbol{M}'$. This idealization of the micro-structure of the tissue leads to the respective Eulerian form of the structure tensors, i.e.

$$\boldsymbol{A}_{\boldsymbol{m}} = \boldsymbol{m} \otimes \boldsymbol{m}, \qquad \boldsymbol{A}_{\boldsymbol{m}'} = \boldsymbol{m}' \otimes \boldsymbol{m}', \tag{4.4}$$

compare with their Lagrangean counterparts, i.e. $\boldsymbol{A}_{\boldsymbol{M}} = \boldsymbol{M} \otimes \boldsymbol{M}$ and $\boldsymbol{A}_{\boldsymbol{M}'} = \boldsymbol{M}' \otimes \boldsymbol{M}'$. In what follows, we introduce the (physically meaningful) additional invariants

$$I_4 = \boldsymbol{m} \cdot \boldsymbol{g}\boldsymbol{m}, \qquad I_6 = \boldsymbol{m}' \cdot \boldsymbol{g}\boldsymbol{m}', \tag{4.5}$$

which measure the squares of stretches along each mean fiber direction.

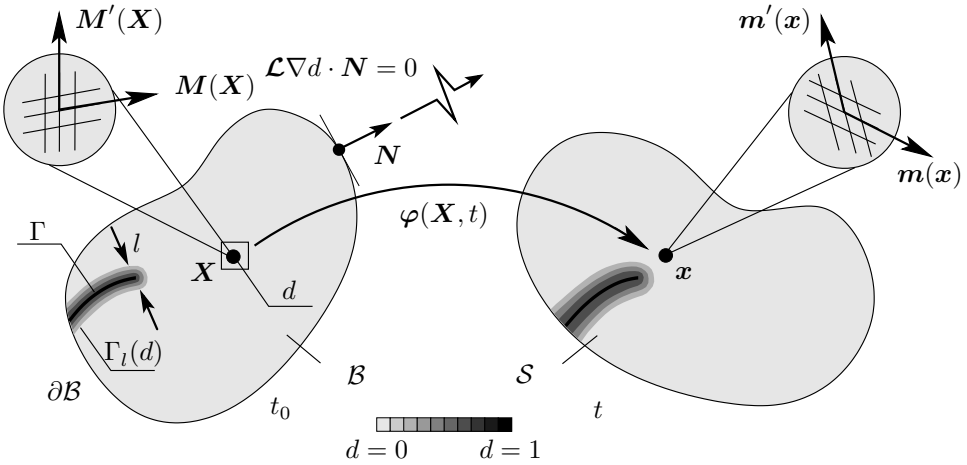

Figure 4.4 Schematic view of the diffusive crack topology in $\mathcal{B}$ and $\mathcal{S}$ with the crack phase-field $d : \mathcal{B} \times \mathcal{T} \rightarrow [0, 1]$, while the sharp crack surface Γ smears out in the respective solid domain, denoted by $\Gamma_l(d)$, which is regularized by the length–scale parameter l. The material anisotropy is imparted by the two families of fibers with material unit vectors $\boldsymbol{M}$ and $\boldsymbol{M}'$ along with their spatial counterparts $\boldsymbol{m}$ and $\boldsymbol{m}'$. The anisotropic crack phase-field problem is further characterized by a traction–free Neumann-type boundary condition $\boldsymbol{\mathcal{L}}\nabla d \cdot \boldsymbol{N} = 0$ on $\partial\mathcal{B}$.

4.2.3 Kinematics of the phase-field problem

Let Γ designate a discontinuous boundary such that $\Gamma \in \partial\mathcal{B}_\varphi \subset \mathbb{R}^2$ at time t_0, which characterizes a sharp crack surface, i.e. $\Gamma = \int_\Gamma \mathrm{d}A$, as indicated by a thick solid curve in Fig. 4.4. Instead of tracking such an interface, the phase-field approach approximates the surface integral by a volume integral engendering a regularized crack surface $\Gamma_l(d)$, i.e.

$$\Gamma_l(d) = \int_{\mathcal{B}} \gamma(d, \nabla d)\mathrm{d}V, \quad \text{where} \quad \gamma(d, \nabla d) = \frac{1}{2l}(d^2 + l^2 \nabla d \cdot \nabla d) \tag{4.6}$$

describes the *isotropic crack surface density* function that satisfies the condition $\gamma(d, \boldsymbol{Q} \star \nabla d) = \gamma(d, \nabla d)$, $\forall \boldsymbol{Q} \in \mathcal{O}(3)$. The tensor variable $\boldsymbol{Q}$ denotes the rotations in the orthogonal group $\mathcal{O}(3)$, which contains rotations and reflections, while $\star$ stands for the Rayleigh product. This approximation can be extended to a class of anisotropic materials such that

$$\Gamma_l(d) = \int_{\mathcal{B}} \gamma(d, \nabla d; \boldsymbol{\mathcal{L}})\mathrm{d}V, \quad \text{where} \quad \gamma(d, \nabla d; \boldsymbol{\mathcal{L}}) = \frac{1}{2l}(d^2 + \nabla d \cdot \boldsymbol{\mathcal{L}} \nabla d) \tag{4.7}$$

describes the *anisotropic crack surface density* function subject to the condition $\gamma(d, \boldsymbol{Q} \star \nabla d) = \gamma(d, \nabla d)$, $\forall \boldsymbol{Q} \in \mathcal{G} \subset \mathcal{O}(3)$, in which $\mathcal{G}$ designates a symmetry group as a subset of $\mathcal{O}(3)$. In (4.7), the second–order anisotropic structure tensor $\boldsymbol{\mathcal{L}}$ reads

$$\boldsymbol{\mathcal{L}} = l^2(\boldsymbol{I} + \omega_{\mathrm{M}} \boldsymbol{M} \otimes \boldsymbol{M} + \omega_{\mathrm{M}'} \boldsymbol{M}' \otimes \boldsymbol{M}'), \tag{4.8}$$

which aligns the crack in accordance with the orientation of fibers in the continuum as the phase-field evolves. Therein, the anisotropy parameters ω_{M} and $\omega_{\mathrm{M}'}$ regulate the transition from weak to strong anisotropy for two families of fibers. In other words, they weight the crack growth along the directions $\boldsymbol{M}$ and $\boldsymbol{M}'$ of the fibers. Hence, in the limit case, i.e. $\omega_i \to \infty$, $i \in \{\mathrm{M}, \mathrm{M}'\}$, the crack path perfectly lies parallel to the fiber directions. For isotropic solids, the parameters $\omega_{\mathrm{M}} = \omega_{\mathrm{M}'}$ are zero, whereas for a general anisotropic continuum with several family of fibers, each of them lie in an open range, i.e. $-1 < \omega_i < \infty$, $i \in \{\mathrm{M}, \mathrm{M}', \ldots\}$, dictated by the ellipticity condition for $\Gamma_l(d)$, see Teichtmeister et al. [216] and Gültekin et al. [67].

4.2.4 Euler–Lagrange equations of the phase-field problem

In view of (4.7) we can state the minimization principle for the regularized crack surface $\Gamma_l(d)$ as

$$d(\boldsymbol{X}, t) = \mathrm{Arg}\left\{\inf_{d \in \mathcal{W}_{\Gamma(t)}} \Gamma_l(d)\right\}, \tag{4.9}$$

subject to the Dirichlet-type boundary constraint

$$\mathcal{W}_{\Gamma(t)} = \{d | d(\boldsymbol{X}, t) = 1 \quad \text{at} \quad \boldsymbol{X} \in \Gamma(t)\}. \tag{4.10}$$

Upon the minimization of the regularized crack surface functional we derive the Euler–Lagrange equations, i.e.

$$\frac{1}{l}[d - \mathrm{Div}(\boldsymbol{\mathcal{L}} \nabla d)] = 0 \quad \text{in } \mathcal{B}, \qquad \text{and} \qquad \boldsymbol{\mathcal{L}} \nabla d \cdot \boldsymbol{N} = 0 \quad \text{on } \partial\mathcal{B}, \tag{4.11}$$

where the divergence term interpolates d between the intact and the ruptured state of the material, while $\boldsymbol{N}$ denotes the unit surface normal oriented outward in the reference configuration.

4.2.5 A particular form of the degradation function

The macroscopic damage accumulated in the anisotropic solid manifests itself in the mechanical response in the sense of a degradation, which may assume generic distinct functional forms in accordance with the additively split isotropic and anisotropic mechanical contributions, i.e.

$$g_{\mathrm{iso}}(d) = (1-d)^{a_{\mathrm{iso}}}, \qquad g_{\mathrm{ani}}(d) = (1-d)^{a_{\mathrm{ani}}}, \tag{4.12}$$

satisfying the following growth conditions

$$g_i'(d) \leq 0 \qquad \text{with} \qquad g_i(0) = 1, \qquad g_i(1) = 0, \qquad g_i'(1) = 0, \tag{4.13}$$

where $i \in \{\mathrm{iso}, \mathrm{ani}\}$. The first condition ensures monotonic degradation, while the second and third conditions set the limits for the intact and the ruptured states, and the final condition ensures the saturation of $g_i(d)$ as $d \to 1$ provided that a_{iso} and a_{ani}, which controls the

rate of the mechanical degradation with respect to the evolution of d, lie in the open range $(a_{\rm iso}, a_{\rm ani}) \in (1, \infty)$. We further emphasize that $a_{\rm iso}$ and $a_{\rm ani}$ can also be a function of stretch or stress depending on the concept of modeling, and can be identified, albeit rather scarce as of yet, via *ex vivo* biomechanical experiments, see the Secs. 4.4 for a discussion. Hence, for the sake of simplicity we restrict ourselves to the quadratic degradation, i.e. $a_{\rm iso} = 2$ and $a_{\rm ani} = 2$, as given in Miehe et al. [143], which also retrieves the multi–field formulation of the fracture problem presented in Gültekin et al. [66, 67].

4.2.6 A particular form of the anisotropic constitutive model

We now briefly touch upon the specific form of the effective Helmholtz free-energy function for the purely hyperelastic anisotropic mechanical response of the aortic wall which can be split into an isotropic and anisotropic part, i.e.

$$\Psi_0(\boldsymbol{g}, \boldsymbol{F}, J, \boldsymbol{A}_{\boldsymbol{m}}, \boldsymbol{A}_{\boldsymbol{m}'}) = \Psi_0^{\rm iso}(\boldsymbol{g}, \boldsymbol{F}, J) + \Psi_0^{\rm ani}(\boldsymbol{g}, \boldsymbol{F}, \boldsymbol{A}_{\boldsymbol{m}}, \boldsymbol{A}_{\boldsymbol{m}'}), \tag{4.14}$$

for which the effective isotropic and the anisotropic parts can be expressed as functions of invariants, i.e.

$$\Psi_0^{\rm iso}(\boldsymbol{g}, \boldsymbol{F}, J) = \hat{\Psi}_0^{\rm iso}(J, I_1), \qquad \Psi_0^{\rm ani}(\boldsymbol{g}, \boldsymbol{F}, \boldsymbol{A}_{\boldsymbol{m}}, \boldsymbol{A}_{\boldsymbol{m}'}) = \hat{\Psi}_0^{\rm ani}(I_4, I_6). \tag{4.15}$$

The effective isotropic part follows from neo-Hookean hyperelasticity accounting for the mechanical response of the ground matrix, whereas the effective anisotropic response features the hyperelasticity of the two distinct families of collagen fibers. The explicit forms of $\Psi_0^{\rm iso}$ and $\Psi_0^{\rm ani}$ are proposed in Holzapfel et al. [83] (it is straightforward to adopt here any anisotropic model, see, e.g., Holzapfel & Ogden [89, 90]). In what follows, the mechanical response of the degrading wall due to macroscopic damage in the isotropic and the anisotropic parts is stated via the degradation function in (4.12) such that

$$\Psi(\boldsymbol{g}, \boldsymbol{F}, J, \boldsymbol{A}_{\boldsymbol{m}}, \boldsymbol{A}_{\boldsymbol{m}'}; d) = g_{\rm iso}(d)\Psi_0^{\rm iso}(\boldsymbol{g}, \boldsymbol{F}, J) + g_{\rm ani}(d)\Psi_0^{\rm ani}(\boldsymbol{g}, \boldsymbol{F}, \boldsymbol{A}_{\boldsymbol{m}}, \boldsymbol{A}_{\boldsymbol{m}'}), \tag{4.16}$$

which modifies the undamaged energy storage functional given in (4.14). The respective expressions for the Kirchhoff stress and the elasticity tensors are presented in Gültekin et al. [67].

4.2.7 Governing equations of the anisotropic fracture

This section is devoted to the governing equations of the coupled multi–field problem of fracture where the classical balance of linear momentum is accompanied by the evolution equation for the crack phase-field, strong forms of the boundary–value problem. Details can be found in Gültekin et al. [67]. For the canonically compact gradient–damage formulations of the boundary–value problems in regard to the standard dissipative solids, the interested reader is referred to Mielke & Roubíček [144] and Miehe [136].

4.2.7.1 Rate–dependent variational formulation based on power balance

As a point of departure, we introduce the viscous rate–type potential Π_η as

$$\Pi_\eta = \mathcal{E} + \mathcal{D}_\eta - \mathcal{P}. \tag{4.17}$$

The first term $\mathcal{E}$ on the right–hand–side of (4.17) represents the rate of energy storage functional, i.e.

$$\mathcal{E}(\dot{\boldsymbol{\varphi}}; \dot{d}) = \int_{\mathcal{B}} (\,\boldsymbol{\tau} : \boldsymbol{g}\nabla_x \dot{\boldsymbol{\varphi}} - f\dot{d}\,)\mathrm{d}V, \tag{4.18}$$

where the work conjugate variables to $\boldsymbol{\varphi}$ and d are the Kirchhoff stress tensor $\boldsymbol{\tau}$ and the scalar energetic force f, respectively, i.e.

$$\boldsymbol{\tau} = 2\partial_{\boldsymbol{g}}\Psi(\boldsymbol{g}, \boldsymbol{F}, \boldsymbol{A}_{\boldsymbol{m}}, \boldsymbol{A}_{\boldsymbol{m}'}; d), \qquad f = -\partial_d \Psi(\boldsymbol{g}, \boldsymbol{F}, \boldsymbol{A}_{\boldsymbol{m}}, \boldsymbol{A}_{\boldsymbol{m}'}; d). \tag{4.19}$$

The second term $\mathcal{D}_\eta$ on the right–hand–side of (4.17) is a viscous regularized dissipation functional due to fracture, i.e.

$$\mathcal{D}_\eta(\dot{d}, \beta; d) = \int_{\mathcal{B}} [\beta\dot{d} - \frac{1}{2\eta}\langle\chi(\beta; d, \nabla d)\rangle^2]\mathrm{d}V, \tag{4.20}$$

where the artificial viscosity $\eta \geq 0$ regulates the scalar viscous over–stress χ, which reads

$$\chi(\beta; d, \nabla d) = \beta - g_{\mathrm{c}}[\delta_d \gamma(d, \nabla d; \boldsymbol{\mathcal{L}})], \tag{4.21}$$

for which the Macaulay brackets in (4.20) filter out the positive values, i.e. $\chi > 0$. Note that in (4.21), g_{c} stands for the critical fracture energy. Finally, the last term $\mathcal{P}$ on the right–hand–side of (4.17) denotes the (classical) external power functional acting on the body according to

$$\mathcal{P}(\dot{\boldsymbol{\varphi}}) = \int_{\mathcal{B}} \rho_0 \tilde{\boldsymbol{\gamma}} \cdot \dot{\boldsymbol{\varphi}}\mathrm{d}V + \int_{\partial\mathcal{B}_t} \tilde{\boldsymbol{t}} \cdot \dot{\boldsymbol{\varphi}}\mathrm{d}a, \tag{4.22}$$

where ρ_0, $\tilde{\boldsymbol{\gamma}}$ and $\tilde{\boldsymbol{t}}$ represent the material density, the prescribed spatial body force and the spatial surface traction, respectively. Now, with the rate–type potential Π_η at hand, we propose a mixed variational principle of the evolution problem as

$$\{\dot{\boldsymbol{\varphi}}, \dot{d}, \beta\} = \mathrm{Arg}\left\{\inf_{\dot{\boldsymbol{\varphi}}\in\mathcal{W}_{\dot{\varphi}}} \inf_{\dot{d}\in\mathcal{W}_{\dot{d}}} \sup_{\beta\geq 0} \Pi_\eta\right\}, \tag{4.23}$$

with the admissible domains for the primary variables

$$\mathcal{W}_{\dot{\varphi}} = \{\dot{\boldsymbol{\varphi}} \mid \dot{\boldsymbol{\varphi}} = \boldsymbol{0} \quad \text{on} \quad \partial\mathcal{B}_\varphi\}, \qquad \mathcal{W}_{\dot{d}} = \{\dot{d} \mid \dot{d} = 0 \quad \text{on} \quad \partial\mathcal{B}_d\}. \tag{4.24}$$

Afterwards, the variation of the potential Π_η with respect to the fields $\{\, \dot{\boldsymbol{\varphi}}, \dot{d}, \beta \,\}$ along with simple algebraic manipulations via elimination and substitution of the respective terms (see Gültekin et al. [67] for more details) yields the strong form of the field equations, i.e.

$$\boxed{\begin{aligned} &1\text{:}\;\; J\,\mathrm{div}(J^{-1}\boldsymbol{\tau}) + \rho_0\tilde{\boldsymbol{\gamma}} = \boldsymbol{0}, \\ &2\text{:}\;\; \eta\dot{d} = 2(1-d)\overline{\mathcal{H}} - d + \mathrm{Div}(\boldsymbol{\mathcal{L}}\nabla d). \end{aligned}} \tag{4.25}$$

The first equation in (4.25) simply describes the balance of linear momentum, whereas the latter states the evolution equation for the crack phase-field in which $\overline{\mathcal{H}}$ indicates the crack driving source term such that

$$\overline{\mathcal{H}} = \frac{\Psi_0}{g_{\mathrm{c}}/l}. \tag{4.26}$$

4.2.7.2 Energy–based anisotropic failure criterion

Following Gültekin et al. [66, 67], the anisotropic failure criterion is elaborated. We begin with the assumption that two distinct failure processes govern the cracking of the ground matrix and the fibers whereby the anisotropic structure tensor $\boldsymbol{\mathcal{L}}$ in (4.8) is additively split into distinct forms as

$$\boldsymbol{\mathcal{L}}^{\mathrm{iso}} = l^2\boldsymbol{I}, \qquad \boldsymbol{\mathcal{L}}^{\mathrm{ani}} = l^2(\omega_{\mathrm{M}}\boldsymbol{M}\otimes\boldsymbol{M} + \omega_{\mathrm{M}'}\boldsymbol{M}'\otimes\boldsymbol{M}'). \tag{4.27}$$

In what follows, we introduce $g_{\mathrm{c}}^{\mathrm{iso}}$ and $g_{\mathrm{c}}^{\mathrm{ani}}$ corresponding to the critical fracture energies attributed to the ground–matrix (isotropic) and the fibrous content (anisotropic) of the aortic wall, respectively, which homogenizes the distinct mechanical resistance of the respective interactions against rupture. Such a model consideration lends itself suitable for the distinct mechanical response of fibrous biological tissues. The crack driving source term in (4.26) can therefore be decomposed as follows

$$\overline{\mathcal{H}}^{\mathrm{iso}} = \frac{\Psi_0^{\mathrm{iso}}}{g_{\mathrm{c}}^{\mathrm{iso}}/l}, \qquad \overline{\mathcal{H}}^{\mathrm{ani}} = \frac{\Psi_0^{\mathrm{ani}}}{g_{\mathrm{c}}^{\mathrm{ani}}/l}. \tag{4.28}$$

For a rate–independent case where $\eta \to 0$, the above expressions (4.27) and (4.28) lead to distinct evolution equations of the crack phase-field in relation to the ground–matrix and the fibrous content, i.e.

$$\begin{aligned} 2(1-d)\overline{\mathcal{H}}^{\mathrm{iso}} &= d - \mathrm{Div}(\boldsymbol{\mathcal{L}}^{\mathrm{iso}}\nabla d), \\ 2(1-d)\overline{\mathcal{H}}^{\mathrm{ani}} &= d - \mathrm{Div}(\boldsymbol{\mathcal{L}}^{\mathrm{ani}}\nabla d). \end{aligned} \tag{4.29}$$

What remains now is to superpose the two distinct failure processes emanating from (4.29), which leads to the rate–independent evolution equation of the phase-field, i.e.

$$\boxed{(1-d)\mathcal{H} = d - \frac{1}{2}\mathrm{Div}(\boldsymbol{\mathcal{L}}\nabla d),} \tag{4.30}$$

along with the specific form of the dimensionless crack driving source term

$$\boxed{\mathcal{H}(t) = \max_{s\in[0,t]} \left[\langle \overline{\mathcal{H}}(s) - 1\rangle\right] \qquad \text{where} \qquad \overline{\mathcal{H}} = \overline{\mathcal{H}}^{\text{iso}} + \overline{\mathcal{H}}^{\text{ani}}.} \tag{4.31}$$

Relation (4.31) brings on an irreversible and positive crack driving source term such that the maximum positive value of $\overline{\mathcal{H}}(s) - 1$ is tracked down in the entire deformation history $s \in [0, t]$, and the Macaulay brackets filter out the positive values for $\overline{\mathcal{H}}(s) - 1$, keeps the solid intact until the failure surface is reached, which hallmarks the energetic criterion proposed by Gültekin et al. [66, 67]. Next, we specify the rate–dependent case in view of (4.30), i.e.

$$\boxed{\underbrace{\eta \dot{d}}_{\text{crack evolution}} = \underbrace{(1-d)\mathcal{H}}_{\text{driving force}} - \underbrace{[d - \frac{1}{2}\,\text{Div}(\boldsymbol{\mathcal{L}}\nabla d)]}_{\text{geometric resistance}},} \tag{4.32}$$

where the evolution of the crack is characterized by the balance between the crack driving force and the geometric resistance to the crack, see Miehe et al. [142].

4.2.8 A note on the weak formulation and numerical implementation

We now give a brief account to the staggered solution procedure of the multi-field problem associated with the primary field variables $\boldsymbol{\varphi}(\boldsymbol{X}, t)$ and $d(\boldsymbol{X}, t)$. An identical temporal as well as spatial discretization scheme is employed for the mechanical and the phase-field problem so as to transform the continuous integral equations into sets of discrete algebraic equations. This set of algebraic equations are solved by a one-pass operator-splitting algorithm in a Newton-type iterative solver for the nodal degrees of freedom.

4.2.8.1 Temporal discretization

The field variables are considered at discrete times $0, t_1, t_2, \ldots, t_n, t_{n+1}, \ldots, T$ in the process interval $[0, T]$. Focusing on a typical time increment $\tau = t_{n+1} - t_n$ in a solution process where t_{n+1} and t_n stand for the current and previous time steps, respectively, all field variables at time t_n are assumed to be known, e.g., $\boldsymbol{\varphi}_n$ and d_n, together with the crack driving source term $\mathcal{H}_n$, which is stored as a history variable. In the sequel, the unknown field variables at time t_{n+1} are aimed at. Note that for the sake of simplicity, all field variables without a subscript such as $\boldsymbol{\varphi}$ and d are hereinafter evaluated at time t_{n+1}.

4.2.8.2 One-pass operator-splitting algorithm

The mechanical and crack phase-field sub–problems can be decoupled by means of one–pass operator–splitting algorithm, i.e.

$$\texttt{ALGO}_{\text{CM}} = \texttt{ALGO}_{\text{C}} \circ \texttt{ALGO}_{\text{M}}, \tag{4.33}$$

for the time increment τ. Such an algorithm is extremely robust, although it slightly underestimates the speed of the crack evolution, see Miehe et al. [140] and Gültekin et al. [67] for details.

4.2.8.3 Spatial discretization of the mechanical problem

The genesis of the following compact notation is according to Miehe et al. [140, 143] in which a finite element discretization $\mathfrak{T}^h$ of the solid $\mathcal{B}$ is considered, where h denotes the mesh size composed of E^h finite element domains $\mathcal{B}_e^h \in \mathfrak{T}^h$ and N^h global nodal points. In accordance with the discretization $\mathfrak{T}^h$, the finite element interpolations of the deformation map and the deformation gradient can be expressed by a state vector

$$\mathfrak{c}_\varphi^h := \{\boldsymbol{\varphi}, \nabla\boldsymbol{\varphi}\}^h = \boldsymbol{B}_\varphi(\boldsymbol{X})\boldsymbol{d}_\varphi(t) \tag{4.34}$$

in relation to the nodal position vector $\boldsymbol{d}_\varphi \in \mathbb{R}^\delta$ where $\delta \in \{1, 2, 3\}$ indicates the space dimension, while $\boldsymbol{B}_\varphi$ serves as a symbolic representation of the global interpolation matrix comprising the shape functions and its derivatives[1]. For a known phase-field d at t_{n+1}, the algorithmic potential energy functional related to $(4.25)_1$ is

$$\pi_\varphi^\tau(\mathfrak{c}_\varphi^h) = \int_{\mathcal{B}} [\Psi(\nabla\boldsymbol{\varphi}; d) - \rho_0\tilde{\boldsymbol{\gamma}}\cdot\boldsymbol{\varphi}]\,\mathrm{dV} - \int_{\partial\mathcal{S}_\mathrm{t}} \tilde{\boldsymbol{t}}\cdot\boldsymbol{\varphi}\mathrm{da}, \tag{4.35}$$

for which the algorithmic form of the variational principle is described as

$$\boldsymbol{d}_\varphi = \mathrm{Arg}\left\{\inf_{\boldsymbol{d}_\varphi}\int_{\mathcal{B}^h} \pi_\varphi^\tau(\mathfrak{c}_\varphi^h)\,\mathrm{d}V\right\}. \tag{4.36}$$

The respective Euler equation features nonlinear elasticity at finite strains, which is solved by a Newton–type iteration based on a sequence of updates

$$\boldsymbol{d}_\varphi \Leftarrow \boldsymbol{d}_\varphi - \left(\int_{\mathcal{B}^h} \boldsymbol{B}_\varphi^\mathrm{T}[\partial^2_{\mathfrak{c}_\varphi^h\,\mathfrak{c}_\varphi^h}\pi_\varphi^\tau(\mathfrak{c}_\varphi^h)]\boldsymbol{B}_\varphi\,\mathrm{d}V\right)^{-1}\int_{\mathcal{B}^h} \boldsymbol{B}_\varphi^\mathrm{T}[\partial_{\mathfrak{c}_\varphi^h}\pi_\varphi^\tau(\mathfrak{c}_\varphi^h)]\,\mathrm{d}V. \tag{4.37}$$

[1] **FE discretization:** For a plane strain problem ($\delta = 2$) the state vector of the deformation field reads $[\mathfrak{c}_\varphi^h] = [\varphi_1, \varphi_2, \varphi_{1,1}, \varphi_{2,2}, \varphi_{1,2}, \varphi_{2,1}]$ for which the finite element interpolation matrix takes on the following form

$$[\boldsymbol{B}_\varphi]_I^e = \begin{bmatrix} N & 0 & N_{,1} & 0 & N_{,2} & 0 \\ 0 & N & 0 & N_{,2} & 0 & N_{,1} \end{bmatrix}_I^\mathrm{T}$$

in terms of the shape function N_I at node I and its derivatives. Analogously, the state vector of the phase-field reads $[\mathfrak{c}_d^h] = [d, d_{,1}, d_{,2}]$ for which the finite element interpolation matrix gives

$$[\boldsymbol{B}_d]_I^e = \begin{bmatrix} N & N_{,1} & N_{,2} \end{bmatrix}_I^\mathrm{T}.$$

4.2.8.4 Spatial discretization of the phase-field problem

In a precisely analogous way to that given in Sec. 4.2.8.3, we write the finite element interpolations of the phase-field and its gradient by

$$\mathfrak{c}_d^h := \{d, \nabla d\}^h = \boldsymbol{B}_d(\boldsymbol{X})\boldsymbol{d}_d(t), \tag{4.38}$$

in relation to the nodal phase-field vector $\boldsymbol{d}_d \in \mathbb{R}^\delta$ where $\delta \in \{1, 2, 3\}$ indicates again the space dimension, while $\boldsymbol{B}_d$ serves as a symbolic representation of the global interpolation matrix comprising the shape functions and its derivatives[1]. For a known $\boldsymbol{\varphi}$ at time t_{n+1}, the algorithmic potential energy density functional in view of $(4.25)_2$ states

$$\pi_d^\tau(\mathfrak{c}_d^h) = \int_{\mathcal{B}} \left[\eta\frac{(d-d_n)^2}{2\tau} + g_c\gamma(d, \nabla d; \boldsymbol{\mathcal{L}}) - g(d)\Psi_0(\nabla\boldsymbol{\varphi})\right] \mathrm{d}V. \tag{4.39}$$

Then, the discretized form of the variational principle is written as

$$\boldsymbol{d}_d = \mathrm{Arg}\left\{\inf_{\boldsymbol{d}_d}\int_{\mathcal{B}^h} \pi_d^\tau(\mathfrak{c}_d^h)\,\mathrm{d}V\right\}. \tag{4.40}$$

The respective Euler equation is linear, therefore, can be solved in a closed form

$$\boldsymbol{d}_d = \left(\int_{\mathcal{B}^h} \boldsymbol{B}_d^{\mathrm{T}}[\partial^2_{\mathfrak{c}_d^h\,\mathfrak{c}_d^h}\pi_d^\tau(\mathfrak{c}_d^h)]\boldsymbol{B}_d\,\mathrm{d}V\right)^{-1}\int_{\mathcal{B}^h} \boldsymbol{B}_d^{\mathrm{T}}[\partial_{\mathfrak{c}_d^h}\pi_d^\tau(\mathfrak{c}_d^h)]\,\mathrm{d}V. \tag{4.41}$$

4.3 Representative Numerical Examples

Beginning with the material parameter identification of the elastic response fitted against the experimental data, anisotropic attributes of the phase-field model are examined by means of sensitivity analyses, which is followed by the analyses of a nascent aortic dissection propagation within a multi–layered thoracic aortic wall tailored for an optimum geometry involving prescribed initial tear with two different sizes.

4.3.1 Identification of material parameters

We first fit the elastic constitutive response to the experimental data obtained by means of uniaxial and in–plane simple shear tests performed on medial strips, which are cut out from the aneurysmatic human thoracic aorta in accordance with the testing protocol documented in Sommer et al. [205]. In particular, specimens subjected to uniaxial extension are tested in the circumferential θ– and longitudinal z–directions, referred to as $(\theta\theta)$ and (zz) modes, while in–plane simple shear tests are carried out on the radial r plane along the θ– and z–directions, indicated by $(r\theta)$ and (rz) modes, respectively.

Table 4.1 Parameters (μ, k_1, k_2, α) fitted through a nonlinear least–squares analysis in regard to the combined in–plane shear and uniaxial extension tests along with the correlation coefficient $R^2_{(ij)}$ and the corresponding root-mean-square error ϵ.

	μ (kPa)	k_1 (kPa)	k_2 (–)	$\alpha\,(^\circ)$
Parameter	83.509	101.651	4.173	44.705
Correlation coefficient	$R^2_{(r\theta)} = 0.991$	$R^2_{(rz)} = 0.978$	$R^2_{(\theta\theta)} = 0.979$	$R^2_{(rz)} = 0.990$
Root-mean-square error	$\epsilon = 0.104$			

The elastic parameters are estimated through a nonlinear least–squares analysis based on a single objective function $\chi^2(\mathfrak{p})$ characterizing the sum of squares of the analytical model predictions to the Cauchy stresses $\sigma^n_{(ij)}$ subtracted by $\bar{\sigma}^n_{(ij)}$, values obtained experimentally, i.e.

$$\min_{\mathfrak{p}} \chi^2(\mathfrak{p}) = \sum_{(ij)\in\mathfrak{m}} \sum_{n=1}^{N^{(ij)}_{\text{exp}}} (\sigma^n_{(ij)} - \bar{\sigma}^n_{(ij)})^2. \tag{4.42}$$

The objective function $\chi^2(\mathfrak{p})$ is minimized with respect to the set of the fitting parameters $\mathfrak{p} = \{\mu, k_1, k_2, \alpha\}$ of the constitutive model stated in Holzapfel et al. [83]. Note that α represents the angle between the mean fiber direction and the circumferential θ-direction. Since a direct visualization of α is lacking, it is used as a fitting parameter in addition to the material parameters. Furthermore, $\mathfrak{m} = \{(\theta\theta), (zz), (r\theta), (rz)\}$ denote the set of aforementioned modes describing the test (ij) along with the associated number of data points $N^{(ij)}_{\text{exp}}$. A MATLAB® [130] built–in function referred to as *lsqnonlin* is implemented in order to compute the minimization problem. The set of elastic parameters identified are summarized in Table 4.1 together with the correlation coefficients $R^2_{(ij)}$ and the root-mean-square error ϵ according to

$$\epsilon = \frac{\sqrt{\dfrac{\chi^2(\mathfrak{p})}{\displaystyle\sum_{(ij)\in\mathfrak{m}} N^{(ij)}_{\text{exp}} - q}}}{\displaystyle\sum_{(ij)\in\mathfrak{m}} \bar{\sigma}^{\text{mean}}_{(ij)}}, \tag{4.43}$$

used as a measure for the 'goodness of fit', see Holzapfel et al. [91]. Therein, q specifies the number of fitting parameters $\mathfrak{p}$, whereas $\bar{\sigma}^{\text{mean}}_{(ij)}$ is the arithmetic mean of the corresponding Cauchy stresses for each mode. The associated hyperelastic constitutive responses are depicted with a reference to experimental data in Fig. 4.5, where the results agree favorably with each other.

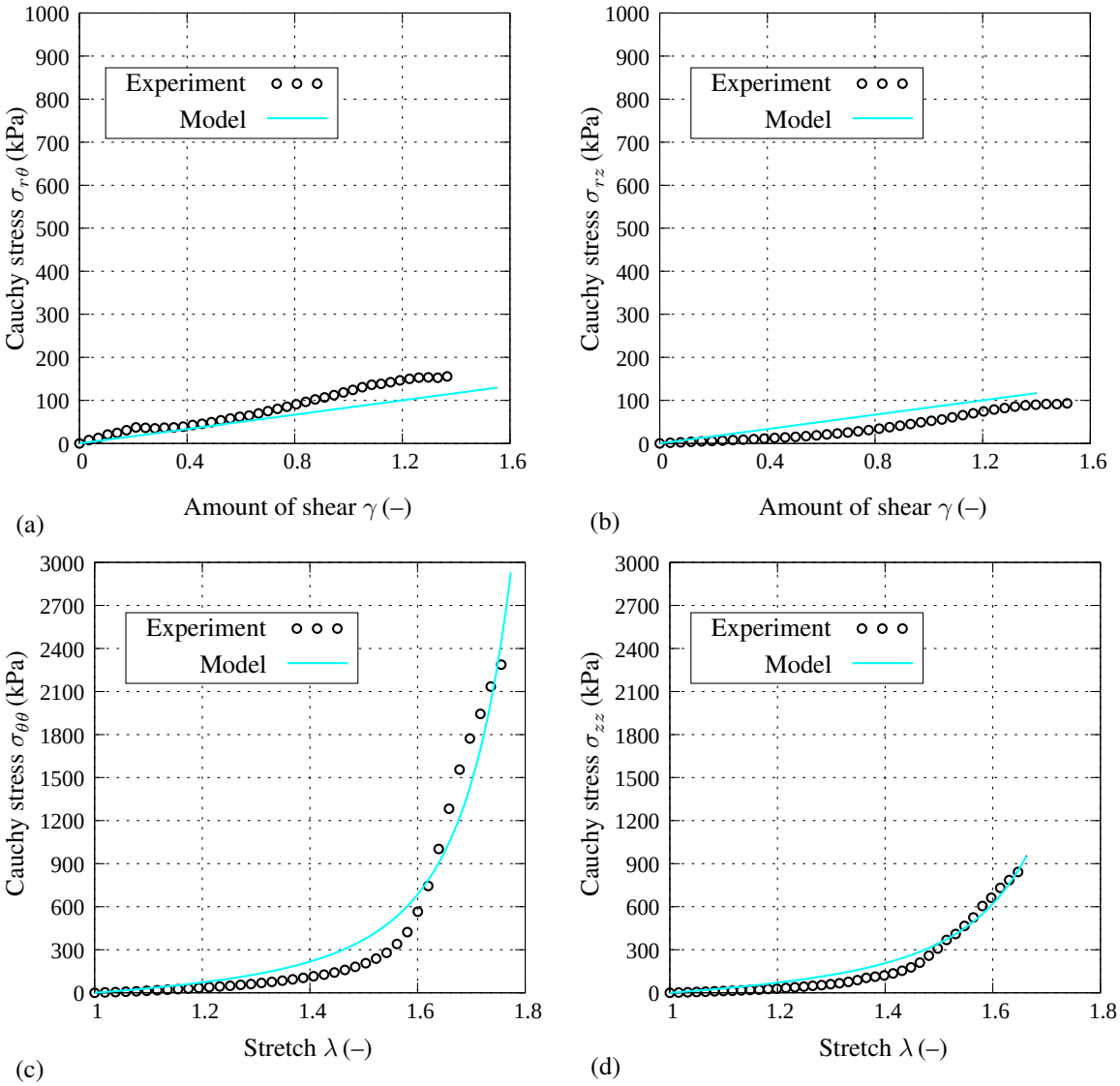

Figure 4.5 In–plane simple shear and uniaxial extension test data (empty circles) and corresponding model fits (solid curves): Cauchy stress σ vs amount of shear γ and stretch λ for (a) $(r\theta)$; (b) (rz); (c) $(\theta\theta)$; (d) (zz) modes.

4.3.2 Sensitivity analysis of the anisotropy parameter ω_{M}

To demonstrate how sensitive the crack path is with respect to the anisotropy parameter ω_{M}, a plane strain boundary–value problem involving a square single edge–notched solid domain is considered with $38\,800$ quadrilateral elements connected by $39\,295$ nodes upon discretization. The material exhibits anisotropy characterized by a single family of fibers $\boldsymbol{M}$, orientated with an angle $\alpha = 45^{\circ}$ with respect to the x-axis, see Fig. 4.6(a). While the bottom edge of the domain is fixed in the y–direction, i.e. $u_y = 0$, the top edge is subjected to a monotonically increasing vertical displacement, i.e. $u_y = \bar{u}$.

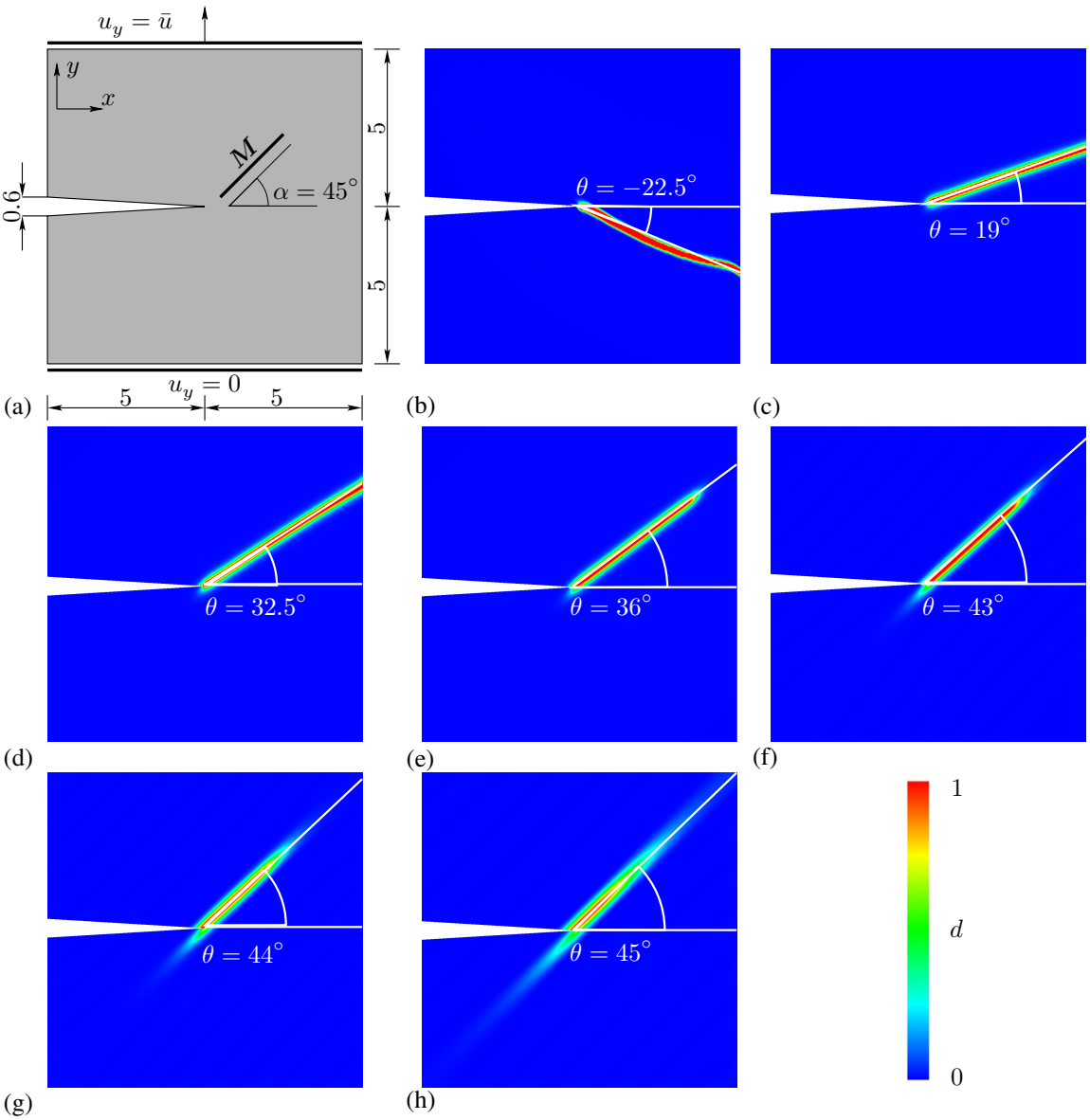

Figure 4.6 (a) Geometry of the single edge–notched domain assumed in plain strain conditions is extended in the y–direction. Diffusive crack patterns with distinct crack angles θ in relation to different ω_{M} are visualized such as (b) $\omega_{\mathrm{M}} \approx -1$; (c) $\omega_{\mathrm{M}} = 1$; (d) $\omega_{\mathrm{M}} = 5$; (e) $\omega_{\mathrm{M}} = 10$; (f) $\omega_{\mathrm{M}} = 50$; (g) $\omega_{\mathrm{M}} = 100$; (h) $\omega_{\mathrm{M}} = 500$. All dimensions are in millimeters unless otherwise noted.

The material parameters used in the simulations are $\mu = 1.0\,\mathrm{kPa}$, $k_1 = 1.0\,\mathrm{kPa}$, $k_2 = 1.0$ together with the bulk modulus $\kappa = 3.0\,\mathrm{kPa}$. The phase-field parameters are chosen as $g_{\mathrm{c}}^{\mathrm{iso}}/l = 10^{-2}\,\mathrm{kPa}$ and $g_{\mathrm{c}}^{\mathrm{ani}}/l = 10^{-2}\,\mathrm{kPa}$ with the length–scale $l = 0.1\,\mathrm{mm}$ satisfying $l > 2h$ to resolve the diffusive crack surface, where h refers to the minimum mesh size.

Figs. 4.6(b)–(h) depict the influence of the anisotropy parameter ω_{M} on the crack pattern

starting with $\omega_{\mathrm{M}} \approx -1$ up to $\omega_{\mathrm{M}} = 500$; the crack starts to trail the orientation of fibers, i.e. $\alpha = 45^{\circ}$, as ω_{M} increases, which complies with the findings of Teichtmeister et al. [216] within the small strain context. In fact, the crack path becomes almost parallel to the fibers for $\omega_{\mathrm{M}} = 500$. To elucidate more on the results obtained, let us substitute (4.8) for $\boldsymbol{\mathcal{L}}$ into $(4.7)_2$ that reshapes the anisotropic crack surface density to

$$\gamma(d, \nabla d; \boldsymbol{\mathcal{L}}) = \frac{d^2}{2l} + \frac{l}{2}\nabla d \cdot \nabla d + \frac{l}{2}\omega_{\mathrm{M}}(\nabla d \cdot \boldsymbol{M})(\boldsymbol{M} \cdot \nabla d) \tag{4.44}$$

for the specific problem considered. From (4.44) it is easily discernible that ω_{M} serves as a penalty parameter, which enforces $\nabla d \cdot \boldsymbol{M} = 1$ as $\omega_{\mathrm{M}} \to \infty$ in the limit case; namely, the crack path is aligned parallel to the orientation of the fiber family $\boldsymbol{M}$. It is worth emphasizing that for $\omega_{\mathrm{M}} \approx -1$, a slight crack kinking is observed which may be the result of the limit imposed by the ellipticity condition and possible multiple minima of the energy encountered on the path. The anisotropy parameter ω_{M}, in the physical sense, is responsible from the transition of the fracture mechanism depicted in Fig. 4.1(b), in particular from fiber bridging to matrix cracking as its value increases.

Stability becomes an apparent issue for cases where $\omega_{\mathrm{M}} \geq 10$, causing computations to abort prematurely for the standard displacement-based *Q1* finite element formulation. Given the fact that such a predicament is not observed within the small strain context, see Li et al. [121] and Teichtmeister et al. [216], the reason may lie in both the finite strain framework employed here, and the exponential stiffening attributed to the fibrous content that might have hampered the stability of the model upon $d \to 1$.

A theoretical prediction for the crack angle θ is suggested by Takei et al. [212] where the authors translate the maximum energy release rate concept, see Erdoğan & Sih [46], into a graphical representation by analogy with the so–called Wulff's plot for crystal growth, see, e.g., Herring [76]. The graphical construction consists of a polar plot of the inverse anisotropic critical energy release rate $G_{\mathrm{c}}^{-1}(\alpha, \theta)$ and a line plot of the anisotropic energy release rate $G(\theta)$ imposed by loading, which is tangent to the polar plot. This tangency marks the angle with which the crack propagates in the anisotropic continuum. Although this method is applicable within the small strain context, its use for finite deformations is largely debatable, as the experimental analysis in Takei et al. [212] neglects elastic stretching. Figures 4.7(a) and (b) show the corresponding force–displacement curves along with the sensitivity of the crack angle θ with respect to the anisotropy parameter ω_{M}, respectively. The force required for fracture is remarkably elevated by the increase of ω_{M}, which can be ascribed to the increased effective length–scale parameter due to ω_{M}, see Gültekin et al. [66], thereby resulting in a greater geometric resistance against fracture. Aside from that, a notably sensitive character of the crack angle θ associated with relatively low values of ω_{M} is followed by a saturation–type behavior for larger values of ω_{M}, e.g., $\omega_{\mathrm{M}} > 100$. Note that in order to have the traceable curve in Fig. 4.7(b), additional computations with varying ω_{M} were performed.

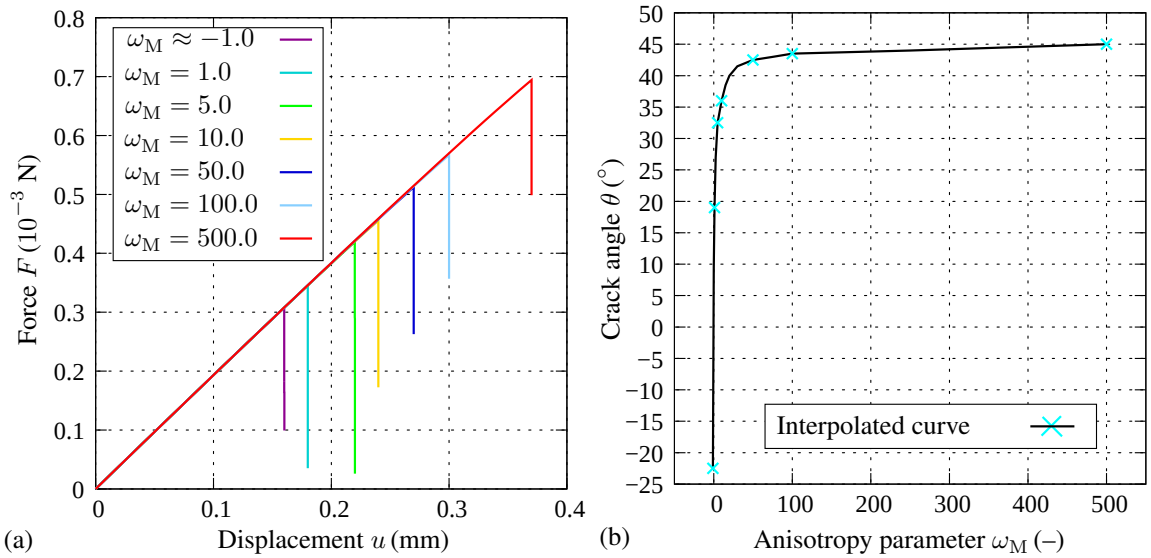

Figure 4.7 (a) Force-displacement curve with respect to different anisotropy parameters ω_M; (b) sensitivity of the crack angle θ in relation to the anisotropy parameter ω_M.

4.3.3 Aortic dissection propagation

This example marks a concept of proof in regard to the 3–D modeling of the aortic dissection propagation upon its initiation, which delineates a helical pattern within the multi–layered wall structure, specifically inside a medial sub–layer in the neighborhood of the prescribed initial tear due to stress concentrations.

4.3.3.1 Geometry and material

A segment with $H = 40$ mm length is isolated from the human ascending aorta possessing typical values for the inner and outer aortic radii, i.e. $R_i = 15$ and $R_o = 17.5$ mm, respectively, as measured at the end–diastolic phase, as reported by Mao et al. [127]. The geometrical setup is tailored for an idealized geometry, which features a cylindrical tube consisting of 6 layers. Starting from the endothelium, the first four layers (with color codes pink, blue, cyan, green) belong to the combination of intima and media, whilst the outermost two layers represent the adventitia (with color code yellow and orange), as illustrated in Fig. 4.8(a). Each medial and adventitial sub–layer holds reference thicknesses of $T_{med} = 0.375$ and $T_{adv} = 0.5$ mm, respectively.

The initial tear–size and tear–shape are assumed to be *a priori* known spanning three medial sub–layers across the thickness of the wall, i.e. from the endothelium up to *media 4* sub–layer. Notches with varying length $\pi R_i \beta / 180°$, where $\beta \in \{30°, 60°\}$, with a width of $w = 2$ mm, are incorporated into the solid model to examine the influence of the initial tear–size on the progression of the dissection, as depicted in Fig. 4.8(b).

The parameters identified in Sec. 4.3.1 stand for a degenerated media whose constitutive

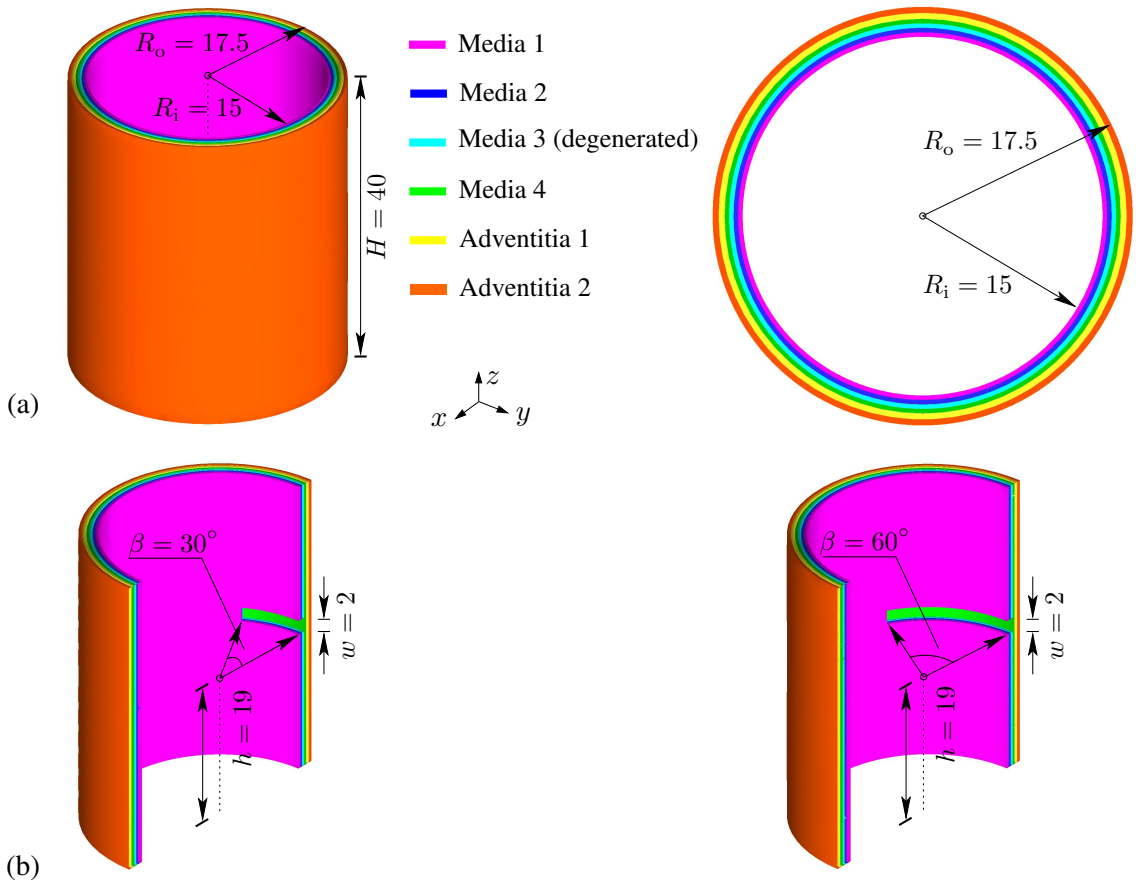

Figure 4.8 (a) Idealized geometry of an extracted 3–D segment obtained from an ascending aorta composed of four medial sub–layers associated with the color codes pink, blue, cyan and green, and two adventitial sub–layers represented by yellow and orange colors. Note that *media 3* refers to a degenerated layer (with lower strength); (b) the sliced view of the entire geometry depicting the prescribed initial tear–size depends on the varying parameter β that regulates the length of the tear. All dimensions are in millimeters unless otherwise noted.

Table 4.2 Elastic and anisotropic crack phase-field parameters related with the individual layers, used for the extension–inflation–torsion analysis.

Layer	μ (kPa)	k_1 (kPa)	k_2 (–)	α ($^\circ$)	g_c^{iso}/l (kPa)	g_c^{ani}/l (kPa)	ω_M (–)
Healthy media	100.21	121.98	5.01	44.71	100.0	300.0	10^3
Degenerated media	83.51	101.65	4.17	44.71	6.0	18.0	10^3
Adventitia	200.0	400.0	4.0	44.71	100.0	300.0	10^3

Table 4.3 Total number of nodes and elements pertaining to each geometry given in Fig. 4.8(b) designed according to the parameters controlling the length and width of the initial tear, i.e. β and w.

Geometry	# of nodes	# of elements
$\beta = 30^{\circ}$, $w = 2$	20 109	101 400
$\beta = 60^{\circ}$, $w = 2$	20 943	105 571

response exhibits a mechanical degradation, which expresses itself in the material parameters. Particularly, the degenerated media corresponds to the sub–layer *media 3*. Since the respective tests on the healthy medial specimens from the same sample are lacking, we have increased the values of the constitutive parameters μ, k_1, k_2 by 20% and attributed the intima/media, namely *media 1*, *media 2* and *media 4* with values summarized in Table 4.2. Because of lack of experimental data of the adventitial layer, we assume a relatively stiffer response for the healthy adventitial layer than the healthy medial layer, and use (rather) arbitrary constitutive parameters.

As for the phase-field parameters, a direct measurement is generally obstructed by the size effect during a rupture test. Most of the extant studies report solely the ultimate stress and stretch values that evoke a rather rudimentary strength of materials approach falling short of describing a progressive fracture. Therefore, arbitrary values for g_{c}^{i}/l are considered for the sake of proving the concept elucidated in the present study. Nonetheless, the anisotropy parameters are specified in the light of the sensitivity analysis, as described in Sec. 4.3.2.

4.3.3.2 Mesh and fiber orientation

The corresponding finite element meshes consist of four–node tetrahedral elements, see Table 4.3, with a constant length–scale parameter $l = 0.1875\,\mathrm{mm}$. Figure 4.9(a) depicts a typical meshed geometry for the problem considered. In addition, for the sake of simplicity the fitted angle $\alpha = 44.71$ (see Table 4.1) between the direction of the fiber families $\{\boldsymbol{M}, \boldsymbol{M}'\}$ and the circumferential direction of *media 3* is applied to each of the sub-layers of media and adventitia in a discrete sense, as visualized in Figs. 4.9(b) and (c), respectively.

4.3.3.3 Boundary and loading conditions

The solid domain is subjected to an extension–inflation–torsion test with appropriate boundary conditions, see Fig. 4.10(a), which is performed in two loading cycles. The first loading cycle refers to a physiological state, while the second cycle refers to a supra–physiological loading state. In particular, in the physiological state the aortic pressure $\hat{p}$ ranges between 80 and $120\,\mathrm{mmHg}$, while the supra–physiological state reaches a peak

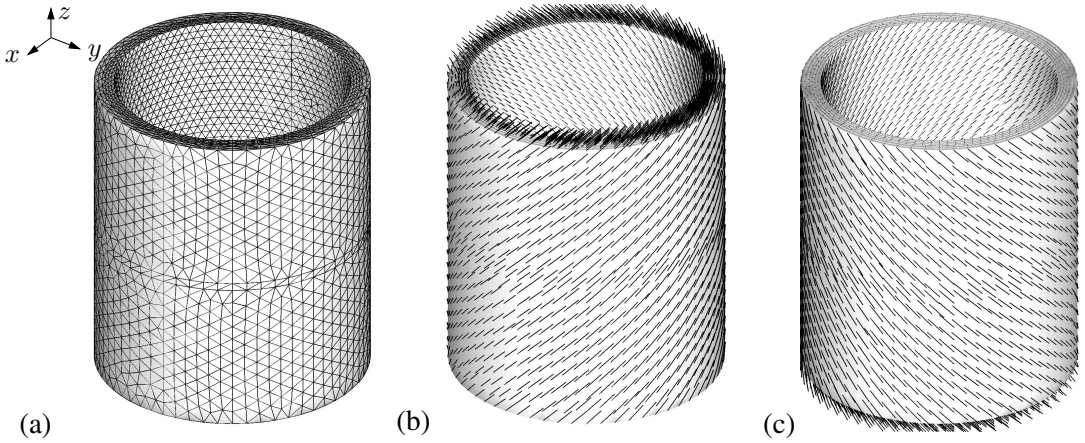

Figure 4.9 (a) Finite element mesh of the idealized cylindrical tube with an initial tear; (b) orientation of first the family of fibers (denoted by $\boldsymbol{M}$); (c) second family of fibers (denoted by $\boldsymbol{M}'$).

pressure value of 600 mmHg, applied on the inner surface of the wall in a saw-tooth loading manner, as depicted in Fig. 4.10(b). We emphasize that such a supra–physiological state is relevant to an aortic dissection, and can be experienced during extreme sport activities such as weight–lifting, as reported by Kenney et al. [113]. Arteries are significantly pre–stretched, and the axial deformations are close to zero during pressure cycles (Schulze-Bauer et al. [191]). Following the study by Horný et al. [93] on the age–dependence of the axial pre–stretch values of human abdominal aortas, a representative axial displacement of $\hat{u}_z = 8$ mm, which is the equivalent of an axial stretch of $\lambda_z = 1.2$, is applied during the physiological state and maintained during the supra–physiological loading cycle, see Fig. 4.10(c). Experimental measurements suggest an end–systolic twisting angle $\hat{\phi}$ for a healthy left–ventricle which ranges between 8 and 12° in the physiological state, as reported by Carreras et al. [23], which is also predicted for the ascending part of the aorta. Nonetheless, a higher value of the twisting angle may occur. We assume here a peak twist angle of 10° and 30° with regard to the physiological and supra–physiological scenarios, as illustrated in Fig. 4.10(d).

4.3.3.4 Simulations and numerical results

In view of the loading scenario described in Sec. 4.3.3.3, all simulations start with a time increment of $\tau = 10^{-2}$, which is decreased up to $\tau = 10^{-4}$ when a stability issue is faced upon a fully initiated crack. The 3–D evolution of the crack phase-field d in the degenerated medial sub–layer (*media 3*) at instants A, B, and C is depicted in Fig. 4.11. In particular, the damage zone of the thoracic aortic segment is shown for $d \geq 0.8$ and for varying initial tear–sizes, as specified in Fig. 4.8(b). As a matter of fact, none of the geometric descriptions result in an acute/excessive damage zone around the tear at instant A referring to the peak physiological loading state indicated in Fig. 4.10. A cross-sectional

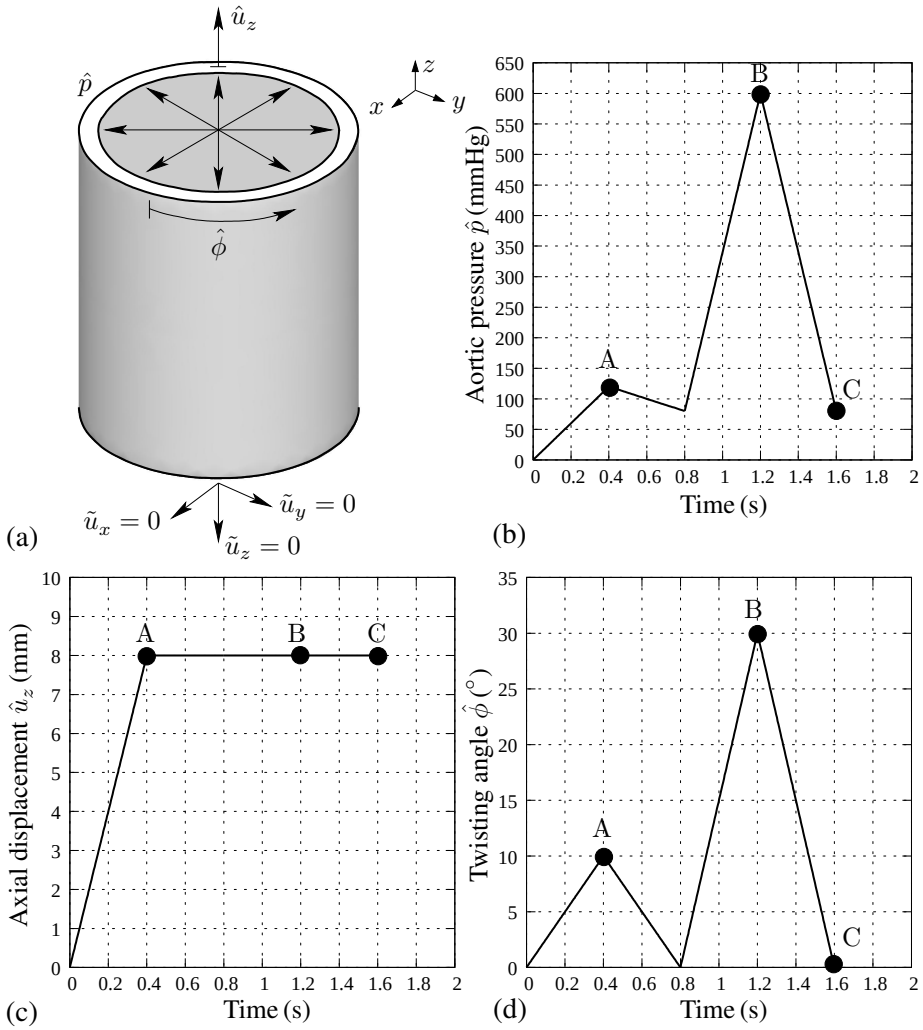

Figure 4.10 (a) Displacements are constrained at the bottom plane where $z = 0\,\text{mm}$, along the x-, y-, and z-directions, required to twist the specimen at the top plane at $z = 40\,\text{mm}$; loading conditions for the extension–inflation–torsion test realized by one physiological and one supra–physiological cycle in a saw-tooth manner with regard to (b) aortic pressure $\hat{p}$; (c) axial displacement $\hat{u}_z$ (remains constant after the peak in the physiological cycle is reached); (d) twisting angle $\hat{\phi}$. Snapshots of the results are shown at instants A, B, and C at time $t \in \{0.4, 1.2, 1.6\}$ corresponding to the peak physiological, supra–physiological loading states, and to the end of the simulation.

view obtained from the top plane at $z = 40\,\text{mm}$ in Fig. 4.12 also affirms an intact solid domain at instant A.

The analysis shows a crack initiation around the initial tear due to stress concentration, which propagates in a specific manner by aligning with the direction of the first fiber family, as seen in Fig. 4.11 for the phase-field $d \geq 0.8$. In fact, the crack follows a helical path in the 3–D domain manifesting not only a longitudinal but also a circumferential growth. A

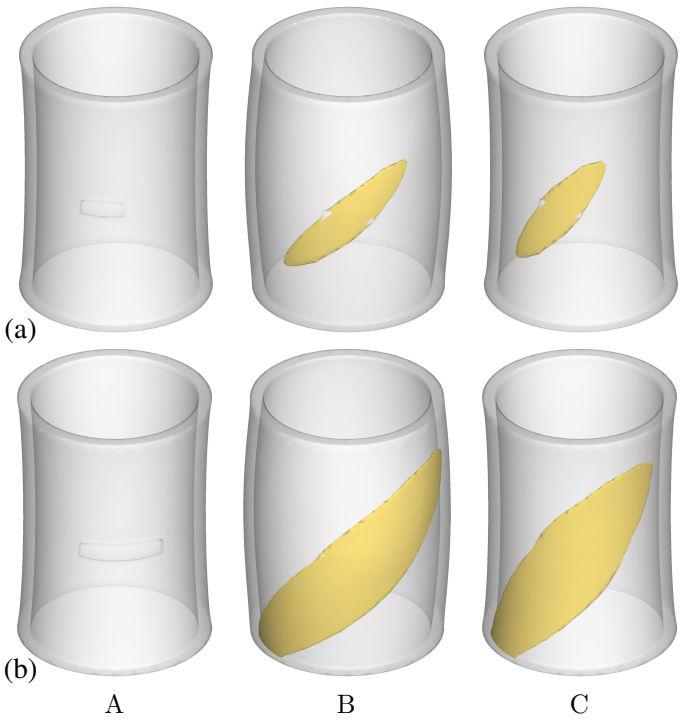

Figure 4.11 3–D evolution of the crack phase-field in the degenerated media, i.e. *media 3*, at instants A, B and C, according to Fig. 4.10, in regard to varying tear–sizes: (a) $\beta = 30^{\circ}$, $w = 2$; (b) $\beta = 60^{\circ}$, $w = 2$ (see Fig. 4.8(b)). Isosurface effect is used to visualize the damage zone corresponding to $d \geq 0.8$.

special focus is now given to the related stress distributions in Figs. 4.13(a)-(c) (for the case of Fig. 4.11(b)). These figures indicate a significant loss of the load–bearing capacity of the degenerated medial sub–layer (*media 3*) at instant B within the damage zone, compare with Fig. 4.11(b). Such a mechanical degradation is undoubtedly accompanied with a loss of intactness in the respective sub–layer. It causes the blood in the supra–physiological cardiac cycle to enter the wall through the initial tear which will peel off *media 1* and *media 2* from *media 4*, *adventitia 1* and *adventitia 2*. A cascade of supra–physiological cycles would trigger even more tearing as the blood jets through the medial sub–layer yielding a false lumen next to the true one. It is also worth highlighting that larger initial tears provide larger damage zones associated with higher stress concentrations, as demonstrated in Figs. 4.11(a) and (b). For the sake of completeness, the end–simulation snapshots for the phase-field $d \geq 0.8$ are shown at instant C in Figs. 4.11–4.13. The results are in conformity with the model consideration that features a thermodynamically irreversible character.

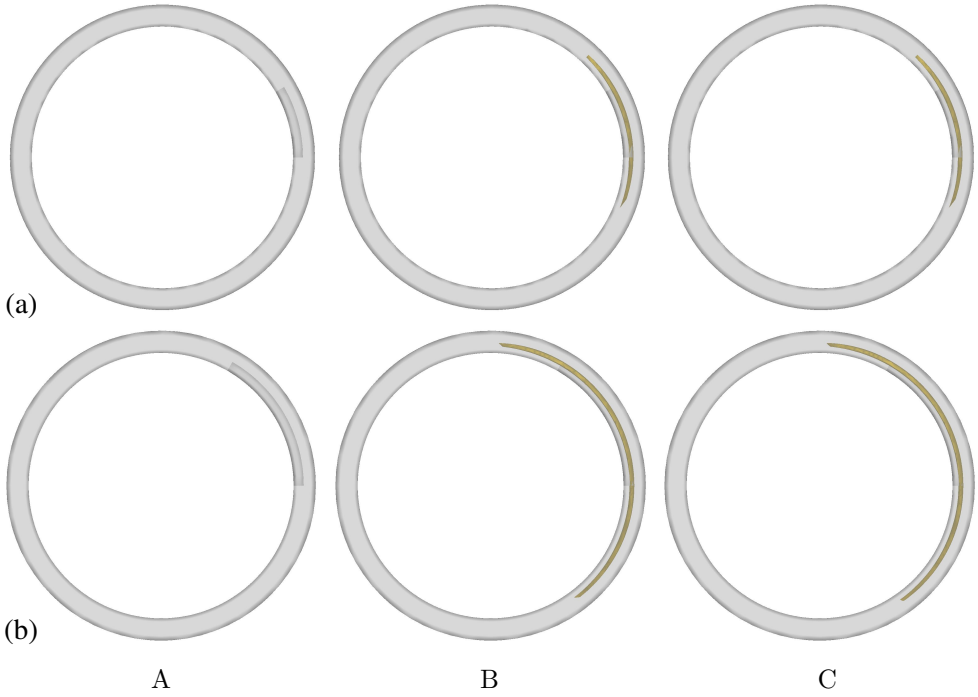

Figure 4.12 Circumferential evolution of the crack phase-field in the degenerated media, i.e. *media 3*, at instants A, B and C, according to Fig. 4.10, when viewed from the top plane at $z = 40$ mm in regard to varying tear–sizes: (a) $\beta = 30^{\circ}$, $w = 2$; (b) $\beta = 60^{\circ}$, $w = 2$ (see Fig. 4.8(b)). Isosurface effect is used to visualize the damage zone corresponding to $d \geq 0.8$.

4.4 Discussion

In the light of the mechanical tests documented by Sommer et al. [205] and Haslach et al. [131], the focus is placed on the ubiquitous (elastic) mechanical factors involved in the aortic dissection, particularly on the normal and in–plane shear stresses. The elastic material properties are identified from experimental data, as depicted in Fig. 4.5. However, it is most likely the case that a certain amount of damage, e.g., stress softening, is induced prior to the ultimate stresses, which motivates further studies on the parameter quantification. Another important observation we identified by conducting the analyses is the fact that displacement driven tests such as uniaxial extension, shear and peel tests seem to overestimate the rupture properties. In particular, for a dissecting aortic tissue, basically no severely damaged zone is achieved when the energy release rates are used from the literature (Sommer et al. [203, 205], Tong et al. [218], Leng et al. [119]).

Separation of the medial lamellae seems to follow a twofold mechanism. Inhomogeneity in the respective mechanical properties results in in–plane circumferential and longitudinal shear components ($\sigma_{r\theta}$ and σ_{rz}) during inflation of the aortic segment. They are likely responsible for the rupture of interfacial bonds between two adjacent lamellae which goes

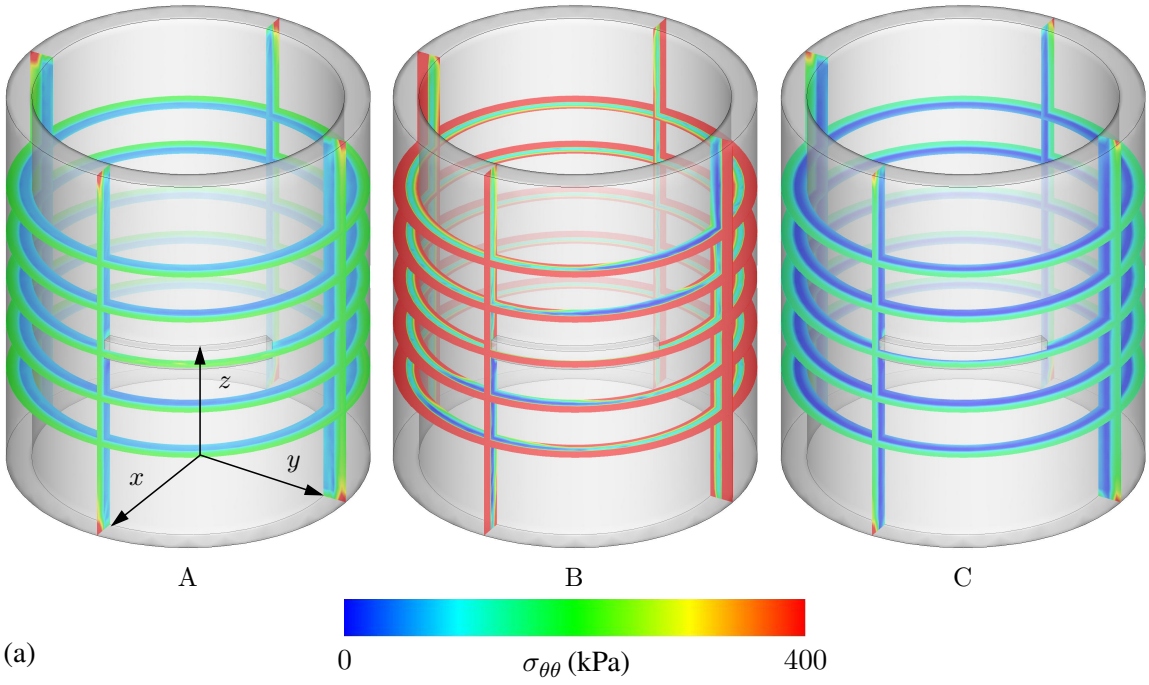

(a)

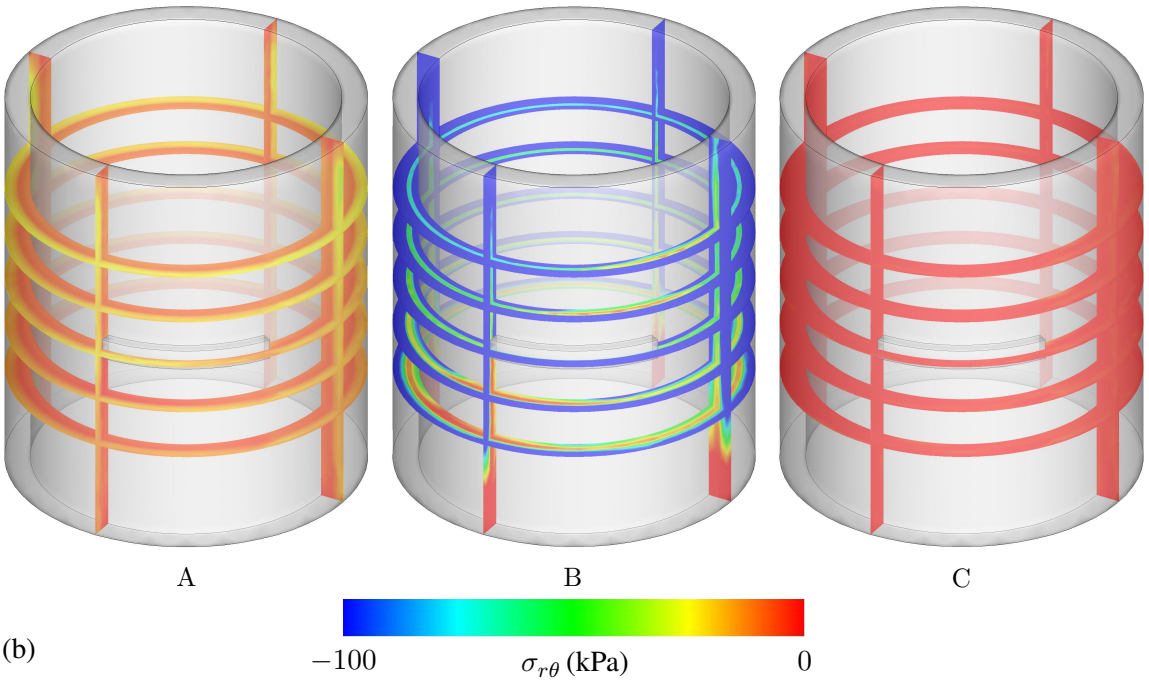

(b)

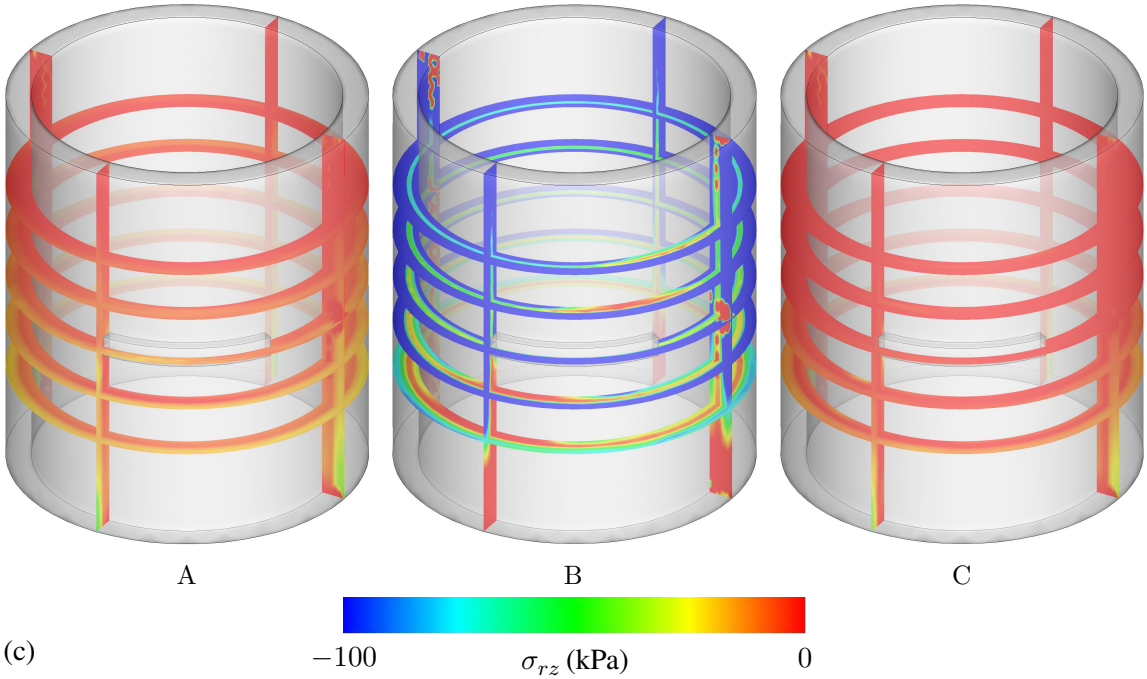

Figure 4.13 Distributions of (a) the circumferential Cauchy stress $\sigma_{\theta\theta}$, (b) the in–plane shear stress $\sigma_{r\theta}$ and (c) the in–plane shear stress σ_{rz} with the initial tear-size $\beta = 60^{\circ}$, $w = 2$ (see Fig. 4.8(b)) obtained at the instants A, B and C. Transparency is used with slices extracted on planes at $z = 10$, 15, 20, 25, 30, then at $x = 0$, and $y = 0$ (for the related coordinate system see (a)).

along the fracture mechanisms described in Sec. 4.1.1 (fiber pull–out, fiber bridging, fiber debonding, matrix failure). This rupture enables the blood to enter the interface through the initial tear, while the lamellae have mostly lost their mechanical resistance as $d \geq 0.8$. In a sense, the crack propagation seems to follow a *mode II* type of fracture rather than *mode I*. In a nutshell, inhomogeneous in–plane shear deformations catalyzed by the heterogeneous material properties evoke *mode II* fracture in the form of failure mechanisms elucidated in Fig. 4.1(b). That forms a breeding ground for the separation of the medial lamellae that manifest as aortic dissection at the macro-scale.

A systematic characterization of the elastic and rupture properties of the aorta is of particular importance to fracture models in order to cope with the elusive phenomena of aortic rupture. In fact, constituent–specific mechanical tests (uniaxial extension, shear, peel tests etc.) on adjacent tissue strips extracted from the ascending and descending parts of the aorta should be performed after elastease (breaks down elastin) and collagenase (break peptide bonds in collagen). Such enzymatic removals (enzymolyses) of elastin and collagen have been studied by, e.g., Roach & Burton [173] and more recently by Schriefl et al. [187]. To a certain extent this enables a better understanding of the mechanical role of elastin/collagen and would allow a refined quantitative assessment of the individual rupture

behavior via the identification of degradation parameters a_{iso}, a_{ani} (see Sec. 4.2.5) and critical fracture energies $g_{\mathrm{c}}^{\mathrm{iso}}$, $g_{\mathrm{c}}^{\mathrm{ani}}$ (see Sec. 4.2.7.2). By the same token, the determination of refined layer–specific elastic and rupture properties of the ascending and descending parts of the aorta would definitely enhance our understanding of the role of altered mechanical wall properties, and better inform computational models.

It has been speculated that PGs contribute to the mechanics of arterial walls by linking the individual collagen fibers together. In this respect, matrilysins (Ross & Pawlina [177]) can be used before mechanical tests to better decipher the role of PGs on the mechanical wall response. In this regard, the reader is also referred to the study by Roccabianca et al. [175], which presents finite element simulations that support a hypothesis for the initiation of aortic dissections. In particular, the authors show that the pooling of GAGs/PGs within the medial layer of the thoracic aorta can lead to significant stress concentrations and intra–lamellar Donnan swelling pressures responsible for a localized increase in intramural stress that disrupt the normal cell-matrix interactions and delaminate the layered microstructure of the aortic wall.

It should also be underlined that the simulations we documented in Sec. 4.3.3 provide limited validity from a quantitative perspective. Nevertheless, to show the capability of the algorithm as a concept of proof to determine the nascent progression of a dissection is the ultimate goal of this example. The phase-field approach lends itself very well to a combination with XFEM in order to visually capture the delamination phenomena. Thereby, the global problem would probably render a dynamical character which might be computationally a troublesome task to undertake via implicit solvers; therefore, an explicit analysis is recommended.

4.5 Conclusion

The present contribution addresses the incipient anisotropic propagation of an aortic dissection that takes place in a degenerated medial sub–layer within the vicinity of a prescribed initial tear. The aortic wall segment comprises several layers of intima/media and adventitia with various mechanical properties. The proposed crack phase-field model blended with the hyperelastic constitutive relations communicates the anisotropic rupture behavior of the aortic wall subject to progressive damage and rupture. Together with improved imaging techniques and computational means, high–end mechanistic models can further be calibrated and optimized to touch upon the emergent aspects of aortic dissections.

Acknowledgments

O.G. acknowledges partly financial support from the National Institutes of Health (research grant no. NIH 7R01HL117063-03).

5 AN ORTHOTROPIC VISCOELASTIC MODEL FOR THE PASSIVE MYOCARDIUM: CONTINUUM BASIS AND NUMERICAL TREATMENT

Abstract. This study deals with the viscoelastic constitutive modeling and the respective computational analysis of the human passive myocardium. We start by recapitulating the locally orthotropic inner structure of the human myocardial tissue and model the mechanical response through invariants and structure tensors associated with three orthonormal basis vectors. In accordance with recent experimental findings the ventricular myocardial tissue is assumed to be incompressible, thick-walled, orthotropic and viscoelastic. In particular, one spring element coupled with Maxwell elements in parallel endows the model with viscoelastic features such that four dashpots describe the viscous response due to matrix, fiber, sheet and fiber-sheet fragments. In order to alleviate the numerical obstacles, the strictly incompressible model is altered by decomposing the free-energy function into volumetric-isochoric elastic and isochoric-viscoelastic parts along with the multiplicative split of the deformation gradient which enables the three-field mixed finite element method. The crucial aspect of the viscoelastic formulation is linked to the rate equations of the viscous overstresses resulting from a 3-D analogy of a generalized 1-D Maxwell model. We provide algorithmic updates for second Piola-Kirchhoff stress and elasticity tensors. In the sequel, we address some numerical aspects of the constitutive model by applying it to elastic, cyclic and relaxation test data obtained from biaxial extension and triaxial shear tests whereby we assess the fitting capacity of the model. With the tissue parameters identified, we conduct (elastic and viscoelastic) finite element simulations for an ellipsoidal geometry retrieved from a human specimen.

5.1 Introduction

Being the major component in the cardiovascular system, the heart has emerged as a prominent research topic in medical science over the last century. This leaves no room for doubt on the priority of the state-of-the-art treatment techniques with regard to cardiovascular diseases (CVDs). According to a recent report on noncommunicable diseases (NCDs) prepared by the World Health Organization, 38 million of 56 million total deaths in 2012 were due to NCDs and CVDs are responsible for the largest proportion of these, i.e. 46.2% [158]. The recent extensive efforts to understand the fundamental mechanisms governing cardiac mechanics necessitate the development of structure-based continuum models together with their computational aspects which need to replace the empirical approaches common in clinics.

5.1.1 Basics of histology, architecture and mechanics of human passive myocardium

Composed of four chambers, the left and right *atria* and *ventricles*, the human heart is considered to be a helical network of the muscle fibers structured in laminar sheets. The left ventricle, spanning the largest volume among others, pumps the arterial blood to the rest of the body through the aortic valve and the aorta with a high pressure resisted by its relatively thicker wall compared to the right ventricle. The ventricular wall is comprised of three layers: the innermost *endocardium*, the middle *myocardium* and the outermost *epicardium* [97]. While the epicardium and the endocardium consist largely of elastin and epimysial collagen, the myocardium is mainly composed of laminae of parallel myocytes collocating with endomysial and perimysial collagen which defines an orthotropic local structure characterized by three distinct material axes [86]. Throughout this article we place an emphasis on the structure and function of the myocardium in the left ventricle.

Morphological studies on animals have shown that muscle fibers made up of myocytes are oriented in an organized pattern across the wall in such a manner that they track a coiled right-handed helix from the endocardium towards the mid-wall. In contrast, the pathway is altered to be left-handed between the mid-wall and the epicardium [132, 180, 181]. Furthermore, the laminae of the fiber bundles enclosing 3–4 cells thickness exhibit a transmural variation in their arrangement [118, 181]. However, a recent study on excised human heart samples visualizes how fiber and sheet orientations vary not only across the wall but also in each section defined from the apex to the base within the regions of the anterior, posterior, lateral and septal wall [176]. There are a number of studies available that focus on animal samples manifesting deviations of both fiber arrangements [111, 112, 209, 226] and sheet arrangements [31, 34] from their mean direction for intact and diseased specimens, albeit none of them elucidates the phenomena in the case of the human heart nor do they resolve their findings into a measurable concept that can fit into a computational model. Nevertheless, a new study [204] quantitatively measures the in-plane and out-of plane dispersion from mean fiber orientation for samples taken from human hearts.

From the modeling point of view, myocardial tissue like several other soft biological tissues, is regarded as an incompressible material. Considering the directional dependence of the mechanical behavior of the tissue, the model considerations have followed a trend from *isotropic* [39] to *transversely isotropic* models based on invariants [100] and on the Green-Lagrangian strain tensor [64]. Later, *orthotropic* models have been proposed [32, 184] in terms of a modified Fung-type model [55] because the myocardium shows distinct mechanical responses along the six simple shear modes associated with its three mutually orthogonal planes [41, 204]. The fact that the aforementioned models lack either the micro-mechanical motivation or the property to be polyconvex, which is closely related to material stability, emerged as a desirable feature from the numerical point of view. This leads to the need for an incompressible, thick-walled, orthotropic, convex and microstructurally motivated constitutive model, as suggested in [86]. This approach renders an entirely invariant-based framework that can characterize the nonlinear elastic behavior of the tissue. For more elaborate discussions on the convexity, the reader is referred to [86, 157] and references therein. In an attempt to consider the disarray in the collagen

orientation, this model is slightly modified to take account of the dispersion along the fiber and sheet directions [48]. In the present study we adopt the approach documented in [48] to account for the elastic response of the passive myocardium. The numerical performance of that model has already been addressed in some papers within the context of the finite element method see, e.g., [48, 62]. Apart from that, a notable variational approach satisfying *a priori* the Legendre-Hadamard condition for materially stable anisotropic hyperelasticity can be found in [189]. It should also be mentioned that we entirely neglect the contractile behavior of the myocardium to the extent that we essentially restrict ourselves to the passive mechanical response.

5.1.2 Orthotropic viscoelastic behavior of the human passive myocardium

The myocardial tissue has hitherto generally been treated as a hyperelastic material due to the lack of experimental evidence for a viscoelastic behavior. However, according to an experimental study on explanted pig hearts [41], the hystereses response observed in all shear modes for homogeneous cyclic triaxial shear tests along with the stress relaxation during step tests have portrayed its viscoelastic features under shear deformation. A more affirmative investigation has been conducted on the human myocardium recently [204] in which the viscoelastic mechanical response was recovered in both biaxial and shear experiments with various stretch amplitudes; thereby specimens underwent cyclic biaxial extension and shear loading. Furthermore, stress relaxation for biaxial extension and triaxial shear tests were examined in the aforementioned study. In line with the structural architecture, the directional dependence of the stiffness for different tests and modes was addressed.

Some studies available in the literature suggest that the extracellular fluid filtrating through the elastic body is one of the possible reasons for the viscoelastic response of the passive myocardium under mechanical loading, see [224, 238]. In addition, it is argued that the myocardial contractile behavior has inconsequential effects on the stress relaxation referring to a purely passive process. The fact that proteoglycans, located in the extracellular matrix, regulate the fluid flow in and out of the articular cartilage might also be true in the case of the myocardium, although this needs to be investigated for the myocardium [53]. As a consequence, the authors believe that the viscoelastic response of myocardial tissues is governed by a combined action of constituents of the extracellular matrix and the cardiac muscle fibers.

To the best of our knowledge, the earliest endeavor to model viscoelasticity of myocardial tissue was elucidated in the work of [124] in which a one-dimensional viscoelastic model accounts for both passive and active responses of the tissue. It was developed by considering Maxwell elements for the passive branch, whereas either the Maxwell or the Voigt element indicates the active branch of the model. A biphasic (fluid and solid) viscoelastic material law, along with its numerical implementation, is established for the passive heart [103, 104] and it is based on the quasi-linear approach represented in the form of a convolution integral [55]. This model regards the elastic response as transversely isotropic, while the relaxation function reflects isotropy.

More descriptive approaches on modeling anisotropic viscoelastic materials at finite strains are elaborated in [82, 84] where the stress update algorithm is derived through a convolution integral representation. The evolution equations are ultimately motivated by a rheological analogue, see [79, 194]. Nonetheless, they provide inadequate validity from the perspective of the fitting. The recent orthotropic viscoelastic model on the passive myocardium, as documented in [22], shows a robust finite element analysis of the biventricular heart. The authors have used shear data obtained from the passive ventricular myocardium of pig hearts [41], and the employed constitutive model uses the logarithmic strain space. However, that orthotropic viscoelastic model was used for experimental data, which are not capturing the time-dependent behavior of the human myocardium such as the stress relaxation which occurs during biaxial extension and triaxial shear tests.

5.1.3 Scope of the work

We propose a finite strain constitutive model in the following in order to delineate the orthotropic viscoelastic response of the human passive myocardium as experimentally shown in [204]. To this end, we adopt a common approach in finite strain viscoelasticity that expresses additively a Helmholtz free-energy function in terms of an *equilibrium* part and a *non-equilibrium* part [125, 194] with the assumption that the time-dependent changes are solely due to the volume-preserving deformations. This is also motivated for nearly incompressible materials where the bulk response has a relatively small effect on the stresses. Considering the elastic equilibrium part, we follow a volumetric and isochoric formulation of finite elasticity for which the deformation gradient is multiplicatively decomposed into its dilatational and distortional parts [62]. The non-equilibrium response is governed by stress evolution equations derived from the three-dimensional analogy of the generalized Maxwell model formed by connecting Maxwell elements and one spring element in parallel [79, 80]. Therein, each Maxwell element corresponds to a distinct response reflected by a specific invariant in the free-energy function, namely matrix, fiber, sheet and relative shear between fiber and sheet [86]. Establishing the framework we quantitatively investigate the numerical performance of the model via a finite element analysis.

The present paper is organized as follows. In Sec. 5.2, we outline the viscoelastic constitutive model designed to capture the mechanical response of the orthotropic human passive myocardium at finite strain with an emphasis given to the reference configuration. Section 5.3 is concerned with the parameter estimation according to the experimental data. In the sequel, we present finite element simulations of a monoventricular human heart model which is based on realistic orientations of fibers and sheets. Finally, in Sec. 5.4, we discuss the finite element results, in particular we compare the results for both equilibrium and non-equilibrium cases.

5.2 Continuum Model for the Viscoelastic Passive Myocardium

In this section we introduce the required kinematics of finite deformation and propose a general framework for orthotropic viscoelasticity formulated in the Lagrangian description. We then provide the related equations for the evolution of the internal variables that determine the viscous response. Accordingly, for a particular form of a decoupled free-energy function we derive the algorithmic stress and elasticity tensors for each integration point.

5.2.1 Kinematics of finite deformation

Let us assume a solid body at time $t_0 \subset \mathbb{R}^1$, which we refer to as the reference configuration designated as $\mathcal{B} \subset \mathbb{R}^3$ with the material points $\boldsymbol{X} \in \mathcal{B}$. In the same manner the placement of the deformed body at current time $t \subset \mathbb{R}^1$ we refer to as the spatial configuration denoted by $\mathcal{S} \subset \mathbb{R}^3$ with the spatial points $\boldsymbol{x} \in \mathcal{S}$ mapped through the motion $\boldsymbol{\chi}_t(\boldsymbol{X}) : \mathcal{B} \to \mathcal{S}$ such that $\boldsymbol{x} = \boldsymbol{\chi}_t(\boldsymbol{X})$. Next, we define the most fundamental deformation measure, the deformation gradient $\boldsymbol{F} = \nabla_{\boldsymbol{X}} \boldsymbol{\chi}_t(\boldsymbol{X})$, which is regarded as a linear map of tangents of material curves onto those of spatial curves. Due to the numerical complications documented in [239], we follow Flory [52] and use a multiplicative decomposition of the deformation gradient $\boldsymbol{F} = \boldsymbol{F}_{\text{vol}}\overline{\boldsymbol{F}}$ into volume-changing (dilatational) $\boldsymbol{F}_{\text{vol}}$ and volume-preserving (distortional) $\overline{\boldsymbol{F}}$ parts, i.e.

$$\boldsymbol{F}_{\text{vol}} = J^{1/3}\boldsymbol{I}, \qquad \overline{\boldsymbol{F}} = J^{-1/3}\boldsymbol{F}, \tag{5.1}$$

where $J = \det \boldsymbol{F} > 0$ is the volume ratio. Myocardium, like most soft biological tissues, is considered to be incompressible under deformation with the constraint on the volume ratio $J = \det \boldsymbol{F}_{\text{vol}} = 1$ to be satisfied. The right Cauchy-Green tensor $\boldsymbol{C}$, together with its unimodular analogue $\overline{\boldsymbol{C}}$ signifying the deformation process for an isotropic material, are defined to be

$$\boldsymbol{C} = \boldsymbol{F}^{\mathrm{T}}\boldsymbol{F}, \qquad \overline{\boldsymbol{C}} = \overline{\boldsymbol{F}^{\mathrm{T}}}\overline{\boldsymbol{F}}. \tag{5.2}$$

Subsequently, we introduce a specific elastic anisotropic material response, i.e. an orthotropic material behavior by means of structure tensors and invariants. Given the idealized laminar organization of the myocardial tissue, the endomysial and perimysial collagen arise as the primary structural elements of the extracellular matrix rendering the passive behavior. While the perimysial collagen network, essentially made up of type I collagen (high strength), sits on the cleavage planes and connects the contiguous lamina, the endomysial fibers, mainly consisting of Type III collagen (highly deformable), are woven around the long axes of the myocytes, see [176] and references therein. As a consequence of the material symmetry the isotropic material response depends only on the principal stretches that can be expressed via the three isotropic unimodular invariants $\bar{I}_1$, $\bar{I}_2$ and $\bar{I}_3$ [80]. The orthotropic material behavior is characterized by three orthonormal basis vectors: *fiber* $\boldsymbol{f}_0$, *sheet* $\boldsymbol{s}_0$, and *normal* $\boldsymbol{n}_0$, as indicated in Fig. 5.1. Upon simplifications elucidated through

incompressibility and particular mechanical responses provided by experiments, the following unimodular form of invariants are sufficient to reflect the orthotropic feature of the myocardium [48, 86], i.e.

$$\bar{I}_1 = \overline{\boldsymbol{C}} : \boldsymbol{I}, \qquad \bar{I}_{4\mathrm{f}} = \overline{\boldsymbol{C}} : (\boldsymbol{f}_0 \otimes \boldsymbol{f}_0), \tag{5.3}$$

$$\bar{I}_{4\mathrm{s}} = \overline{\boldsymbol{C}} : (\boldsymbol{s}_0 \otimes \boldsymbol{s}_0), \qquad \bar{I}_{8\mathrm{fs}} = \overline{\boldsymbol{C}} : \mathrm{sym}(\boldsymbol{f}_0 \otimes \boldsymbol{s}_0). \tag{5.4}$$

Thereafter, the unimodular invariants $\bar{I}_{4\mathrm{f}}$ and $\bar{I}_{4\mathrm{s}}$ are modified to take account of the dispersion of collagen orientation along the $\boldsymbol{f}_0$ and $\boldsymbol{s}_0$ direction that can be prevalent for diseased myocardium. According to [48] we set κ_{f} and κ_{s} to be the observed scalar parameters representing fiber and sheet distributions, respectively. As a result, the modified unimodular fourth-invariants have the following form

$$\bar{I}^*_{4\mathrm{f}} = \kappa_{\mathrm{f}}\bar{I}_1 + (1-3\kappa_{\mathrm{f}})\bar{I}_{4\mathrm{f}}, \qquad \bar{I}^*_{4\mathrm{s}} = \kappa_{\mathrm{s}}\bar{I}_1 + (1-3\kappa_{\mathrm{s}})\bar{I}_{4\mathrm{s}}, \tag{5.5}$$

where $\kappa_i \in [0, 1/3]$, $i \in \{\mathrm{f}, \mathrm{s}\}$. If $\kappa_i = 0$ then we have an alignment of fibers while isotropy is recovered for the case that $\kappa_i = 1/3$. As such, we can express the related structure tensors $\boldsymbol{H}_l$, $l = \{4\mathrm{f}, 4\mathrm{s}, 8\mathrm{fs}\}$, and the ensuing invariants as

$$\boldsymbol{H}_{4\mathrm{f}} = \kappa_{\mathrm{f}}\boldsymbol{I} + (1-3\kappa_{\mathrm{f}})\boldsymbol{f}_0 \otimes \boldsymbol{f}_0, \qquad \bar{I}^*_{4\mathrm{f}} = \overline{\boldsymbol{C}} : \boldsymbol{H}_{4\mathrm{f}}, \tag{5.6}$$

$$\boldsymbol{H}_{4\mathrm{s}} = \kappa_{\mathrm{s}}\boldsymbol{I} + (1-3\kappa_{\mathrm{s}})\boldsymbol{s}_0 \otimes \boldsymbol{s}_0, \qquad \bar{I}^*_{4\mathrm{s}} = \overline{\boldsymbol{C}} : \boldsymbol{H}_{4\mathrm{s}}, \tag{5.7}$$

$$\boldsymbol{H}_{8\mathrm{fs}} = \mathrm{sym}(\boldsymbol{f}_0 \otimes \boldsymbol{s}_0), \qquad \bar{I}_{8\mathrm{fs}} = \overline{\boldsymbol{C}} : \boldsymbol{H}_{8\mathrm{fs}}. \tag{5.8}$$

Viscoelasticity is a dissipative (irreversible) material response described by time-dependent *internal variables* which are not suitable for a direct phenomenological observation. In fact, these variables define the state of the material in addition to strain measures discernable from experiments, see [79, 80, 84]. A collective description of the internal variables can be designated by second-order tensors, $\boldsymbol{\mathcal{I}}_\alpha$, akin to $\overline{\boldsymbol{C}}$, with $\alpha = \{\mathrm{m}, \mathrm{f}, \mathrm{s}, \mathrm{fs}\}$ characterizing the viscoelastic processes associated with the matrix, the fiber, the sheet and the fiber-sheet, respectively. Each relaxation/creeping process is accompanied by the *relaxation/retardation time* $\tau_\alpha \in (0, \infty)$ determining the rate of decay of the stress/strain in a viscoelastic process.

5.2.2 General framework for orthotropic viscoelasticity

We provide here a general framework for orthotropic viscoelasticity in the Lagrangian description. The local balance of the linear and angular momentum serve as a basic set of equations in continuum mechanics to set up quasi-static equilibrium

$$\mathrm{Div}(\boldsymbol{F}\boldsymbol{S}) + \boldsymbol{B} = \boldsymbol{0}, \qquad \boldsymbol{S} = \boldsymbol{S}^{\mathrm{T}}, \tag{5.9}$$

where $\boldsymbol{S}$ is the second Piola-Kirchhoff stress tensor and $\boldsymbol{B}$ is the reference body force per unit volume in material coordinates. Next, we define the *Clausius-Planck* inequality for an isothermal process, i.e.

$$\mathcal{D}_{\mathrm{loc}} := \frac{1}{2}\boldsymbol{S} : \dot{\boldsymbol{C}} - \dot{\Psi} \geq 0, \tag{5.10}$$

from which the stress response can readily be derived, see [80]. Herein, $\mathcal{D}_{\text{loc}}$ and $\dot{\Psi}$ designate the local part of the dissipation and the time evolution of the free-energy function Ψ that portrays the energy storage for the orthotropic viscoelastic material. Motivated by a standard linear theory defined in [194] through a Legendre transformation between strain deviator and the non-equilibrium stress, we now additively decompose the free-energy function into its *volumetric-equilibrium* $\Psi^{\infty}_{\text{vol}}$, *isochoric-equilibrium* $\Psi^{\infty}_{\text{iso}}$, and *isochoric-non-equilibrium* (*configurational*) Υ_{iso} parts with their corresponding arguments, i.e.

$$\Psi\left(\boldsymbol{C},\boldsymbol{H},\boldsymbol{\mathcal{I}}\right)=\Psi^{\infty}_{\text{vol}}\left(J\right)+\Psi^{\infty}_{\text{iso}}\left(\overline{\boldsymbol{C}},\boldsymbol{H}\right)+\Upsilon_{\text{iso}}\left(\overline{\boldsymbol{C}},\boldsymbol{H},\boldsymbol{\mathcal{I}}\right), \tag{5.11}$$

where the structure tensor $\boldsymbol{H}=\{\boldsymbol{H}_{4\text{f}},\boldsymbol{H}_{4\text{s}},\boldsymbol{H}_{8\text{fs}}\}$ and the internal argument $\boldsymbol{\mathcal{I}}=\{\boldsymbol{\mathcal{I}}_{\text{m}},\boldsymbol{\mathcal{I}}_{\text{f}},\boldsymbol{\mathcal{I}}_{\text{s}},\boldsymbol{\mathcal{I}}_{\text{fs}}\}$ are henceforth given in their respective sets. Here $\Psi^{\infty}_{\text{vol}}$ and $\Psi^{\infty}_{\text{iso}}$ recover the thermodynamic equilibrium state, i.e. the elastic response, as $t\rightarrow\infty$, whereas Υ_{iso}, also known as the *dissipative potential*, governs the thermodynamic non-equilibrium state, i.e. the relaxation and creep response. Thereafter we obtain the local dissipation inequality with regard to the material time derivative of (5.11) and use (5.10) such that

$$\mathcal{D}_{\text{loc}}:=\left(\boldsymbol{S}-2\frac{\partial\Psi}{\partial\boldsymbol{C}}\right):\frac{\dot{\boldsymbol{C}}}{2}-2\frac{\partial\Psi}{\partial\boldsymbol{\mathcal{I}}}:\frac{\dot{\boldsymbol{\mathcal{I}}}}{2}\geq 0. \tag{5.12}$$

For thermoelastic solids, in general, eq. (5.12) needs to be satisfied for an arbitrary rate of $\dot{\boldsymbol{C}}$ [30]. This gives rise to the Coleman-Noll exploitation that implies the particular form of the constitutive equation, i.e. $\boldsymbol{S}-2\partial\Psi/\partial\boldsymbol{C}=\boldsymbol{0}$, from which the physical expression for stresses can be additively obtained as follows

$$\boldsymbol{S}=\boldsymbol{S}^{\infty}_{\text{vol}}+\boldsymbol{S}^{\infty}_{\text{iso}}+\boldsymbol{Q}, \tag{5.13}$$

where $\boldsymbol{Q}$ represents the total viscous overstress. It can be also interpreted as a thermodynamic work conjugate variable to $\boldsymbol{\mathcal{I}}$ as a result of the reduced dissipation inequality, i.e.

$$\mathcal{D}_{\text{loc}}:=-2\frac{\partial\Psi}{\partial\boldsymbol{\mathcal{I}}}:\frac{\dot{\boldsymbol{\mathcal{I}}}}{2}\geq 0,\qquad\boldsymbol{Q}=-2\frac{\partial\Psi}{\partial\boldsymbol{\mathcal{I}}}. \tag{5.14}$$

In eq. (5.13) the second Piola-Kirchhoff stress tensor $\boldsymbol{S}$ consists of volumetric, isochoric and viscous contributions according to

$$\boldsymbol{S}^{\infty}_{\text{vol}}=2\frac{\partial\Psi^{\infty}_{\text{vol}}(J)}{\partial\boldsymbol{C}},\qquad\boldsymbol{S}^{\infty}_{\text{iso}}=2\frac{\partial\Psi^{\infty}_{\text{iso}}(\overline{\boldsymbol{C}},\boldsymbol{H})}{\partial\boldsymbol{C}},\qquad\boldsymbol{Q}=2\frac{\partial\Upsilon_{\text{iso}}(\overline{\boldsymbol{C}},\boldsymbol{H},\boldsymbol{\mathcal{I}})}{\partial\boldsymbol{C}}. \tag{5.15}$$

Accordingly, the explicit forms of the stresses $\boldsymbol{S}^{\infty}_{\text{vol}}$ and $\boldsymbol{S}^{\infty}_{\text{iso}}$ are furnished by

$$\boldsymbol{S}^{\infty}_{\text{vol}}=Jp\boldsymbol{C}^{-1},\qquad\boldsymbol{S}^{\infty}_{\text{iso}}=\overline{\boldsymbol{S}}^{\infty}:\mathbb{P}, \tag{5.16}$$

with the hydrostatic pressure $p=\mathrm{d}\Psi_{\text{vol}}(J)/\mathrm{d}J$, and the projection tensor $\mathbb{P}=J^{-2/3}(\mathbb{I}-\boldsymbol{C}^{-1}\otimes\boldsymbol{C}/3)$ in the reference configuration, where $\mathbb{I}$ denotes the fourth-order identity tensor. We elaborate more on the unimodular (fictitious) part of the isochoric-equilibrium stress tensor $\overline{\boldsymbol{S}}^{\infty}$ in Sec. 5.2.4.

An essential part of the solution of nonlinear problems is the incremental form of the material equation differentiated with respect to time which yields the material elasticity tensor $\mathbb{C}$ [80, 235],

$$\dot{\boldsymbol{S}} = \mathbb{C} : \frac{\dot{\boldsymbol{C}}}{2}, \qquad \mathbb{C} = 4\frac{\partial^2 \Psi}{\partial \boldsymbol{C} \partial \boldsymbol{C}}. \tag{5.17}$$

The incremental form of the constitutive equation in (5.17) involves algorithmic treatment resulting from the viscous part. However, without losing generality we can furnish the continuous formulation of the equilibrium volumetric elasticity tensor [80]

$$\mathbb{C}^{\infty}_{\text{vol}} = J\tilde{p}\boldsymbol{C}^{-1} \otimes \boldsymbol{C}^{-1} - 2Jp\mathbb{I}_{\boldsymbol{C}^{-1}}, \tag{5.18}$$

along with the equilibrium isochoric elasticity tensor

$$\mathbb{C}^{\infty}_{\text{iso}} = \mathbb{P} : \overline{\mathbb{C}}^{\infty} : \mathbb{P}^{\text{T}} + \frac{2}{3}(\overline{\boldsymbol{S}}^{\infty} : \boldsymbol{C})\mathbb{P}_{\boldsymbol{C}^{-1}} - \frac{2}{3}(\boldsymbol{S}^{\infty}_{\text{iso}} \otimes \boldsymbol{C}^{-1} + \boldsymbol{C}^{-1} \otimes \boldsymbol{S}^{\infty}_{\text{iso}}). \tag{5.19}$$

In (5.18) and (5.19), we have introduced a scalar function $\tilde{p} = p + Jp'$ where $p' = \mathrm{d}p/\mathrm{d}J$. The geometric transformation tensors read

$$\mathbb{I}_{\boldsymbol{C}^{-1}} = (\boldsymbol{C}^{-1} \odot \boldsymbol{C}^{-1})_{ABCD} = \frac{1}{2}(C^{-1}_{AC}C^{-1}_{BD} + C^{-1}_{AD}C^{-1}_{BC}), \tag{5.20}$$

$$\mathbb{P}_{\boldsymbol{C}^{-1}} = \mathbb{I}_{\boldsymbol{C}^{-1}} - \frac{1}{3}\boldsymbol{C}^{-1} \otimes \boldsymbol{C}^{-1}. \tag{5.21}$$

As an important task of our work we engage in the derivation of the viscous stress $\boldsymbol{Q}$ and the third (viscoelastic) contribution to $\mathbb{C}$ via a time integration algorithm in the forthcoming section.

5.2.3 Evolution equations

In this section we aim at retrieving the mechanical response to be identified in a time discrete sense that takes account of the history. Once again we declare that the viscous response is determined by taking notice of the local structure of the tissue, i.e orthotropy, portrayed via invariants in the free-energy function. Due to this orthotropic set-up we particularly require an update algorithm for the isochoric non-equilibrium stresses, namely $\boldsymbol{Q}_{\text{m}}$, $\boldsymbol{Q}_{\text{f}}$, $\boldsymbol{Q}_{\text{s}}$, $\boldsymbol{Q}_{\text{fs}}$ at each integration point [80, 82] which leads to the total viscous overstress $\boldsymbol{Q}$ such that

$$\boldsymbol{Q} = \boldsymbol{Q}_{\text{m}} + \boldsymbol{Q}_{\text{f}} + \boldsymbol{Q}_{\text{s}} + \boldsymbol{Q}_{\text{fs}}, \tag{5.22}$$

which is related to the isochoric equilibrium stresses, i.e.

$$\boldsymbol{S}^{\infty}_{\text{iso}} = \boldsymbol{S}^{\infty}_{\text{iso,m}} + \boldsymbol{S}^{\infty}_{\text{iso,f}} + \boldsymbol{S}^{\infty}_{\text{iso,s}} + \boldsymbol{S}^{\infty}_{\text{iso,fs}}, \tag{5.23}$$

where $\boldsymbol{S}^{\infty}_{\text{iso,m}}$, $\boldsymbol{S}^{\infty}_{\text{iso,f}}$, $\boldsymbol{S}^{\infty}_{\text{iso,s}}$, and $\boldsymbol{S}^{\infty}_{\text{iso,fs}}$ are the matrix, fiber, sheet and fiber-sheet contributions of the isochoric equilibrium stresses, respectively.

Analogous to the 1-D generalized Maxwell model, see [80] for detailed analysis, the following first-order linear differential equation (rate equation) together with the initial values govern the evolution of the viscous overstresses within a semi-closed time interval $t \in (0, T]$, i.e.

$$\dot{\boldsymbol{Q}}_\alpha + \frac{\boldsymbol{Q}_\alpha}{\tau_\alpha} = \beta_\alpha \dot{\boldsymbol{S}}^\infty_{\mathrm{iso},\alpha}, \qquad \boldsymbol{Q}_\alpha\big|_{t=0} = \boldsymbol{0}, \tag{5.24}$$

where all the viscous effects a priori vanish at the stress-free reference configuration for $\alpha = \{\mathrm{m}, \mathrm{f}, \mathrm{s}, \mathrm{fs}\}$. The parameter constants specify the non-dimensional *free-energy factors* $\beta_\alpha \in [0, \infty)$ and *relaxation times* $\tau_\alpha \in (0, \infty)$. A closed-form solution of (5.24) is the convolution integral expression

$$\boldsymbol{Q}_\alpha = \int_0^t \exp\left(-\frac{t-s}{\tau_\alpha}\right) \beta_\alpha \dot{\boldsymbol{S}}^\infty_{\mathrm{iso},\alpha} \mathrm{d}s. \tag{5.25}$$

Now let us consider a time sub-interval $[t_n, t_{n+1}]$ for which the time increment $\Delta t = t_{n+1} - t_n$ describes the algorithmic formulation. Following the derivation in [80, 194] circumventing the necessity of incremental objectivity, see [96], we split up the integral (5.25) into two parts for the current viscous overstress at $t = t_{n+1}$, i.e.

$$\boldsymbol{Q}^{n+1}_\alpha = \int_0^{t_n} \exp\left(-\frac{t_{n+1}-s}{\tau_\alpha}\right) \beta_\alpha \dot{\boldsymbol{S}}^\infty_{\mathrm{iso},\alpha} \mathrm{d}s + \int_{t_n}^{t_{n+1}} \exp\left(-\frac{t_{n+1}-s}{\tau_\alpha}\right) \beta_\alpha \dot{\boldsymbol{S}}^\infty_{\mathrm{iso},\alpha} \mathrm{d}s, \tag{5.26}$$

with a standard property utilized for the first integral expression as

$$\exp\left(-\frac{t_{n+1}-s}{\tau_\alpha}\right) = \exp\left(-\frac{t_n-s}{\tau_\alpha}\right) \exp\left(-\frac{\Delta t}{\tau_\alpha}\right). \tag{5.27}$$

As a consequence we may define the viscous overstress $\boldsymbol{Q}^n_\alpha$ at $t = t_n$ by substituting (5.27) into (5.26) that reshapes (5.26) as

$$\boldsymbol{Q}^n_\alpha = \int_0^{t_n} \exp\left(-\frac{t_n-s}{\tau_\alpha}\right) \beta_\alpha \dot{\boldsymbol{S}}^\infty_{\mathrm{iso},\alpha} \mathrm{d}s, \tag{5.28}$$

$$\boldsymbol{Q}^{n+1}_\alpha = \exp\left(-\frac{\Delta t}{\tau_\alpha}\right) \boldsymbol{Q}^n_\alpha + \int_{t_n}^{t_{n+1}} \exp\left(-\frac{t_{n+1}-s}{\tau_\alpha}\right) \beta_\alpha \dot{\boldsymbol{S}}^\infty_{\mathrm{iso},\alpha} \mathrm{d}s. \tag{5.29}$$

It should be highlighted that the result is still exact. Hence, it is compulsory to approximate the integral term of (5.29) in the sense of numerical integration associated with $[t_n, t_{n+1}]$. To this end, we exploit the *mid-point rule* leading to a truncation error of the second order with respect to the time step Δt, i.e. t is approximated by $(t_{n+1} + t_n)/2$. Thus,

$$\boldsymbol{Q}^{n+1}_\alpha = \exp\left(-\frac{\Delta t}{2\tau_\alpha}\right) \left[\exp\left(-\frac{\Delta t}{2\tau_\alpha}\right) \boldsymbol{Q}^n_\alpha - \beta_\alpha \boldsymbol{S}^{\infty^n}_{\mathrm{iso},\alpha}\right] + \exp\left(-\frac{\Delta t}{2\tau_\alpha}\right) \beta_\alpha \boldsymbol{S}^{\infty^{n+1}}_{\mathrm{iso},\alpha}. \tag{5.30}$$

Here, (5.30) can be reformulated to form a recursive update algorithm to obtain the viscous overstress as

$$\begin{aligned} \boldsymbol{\mathcal{H}}_{\alpha}^{n} &= \exp\left(-\frac{\Delta t}{2\tau_{\alpha}}\right)\left[\exp\left(-\frac{\Delta t}{2\tau_{\alpha}}\right)\boldsymbol{Q}_{\alpha}^{n} - \beta_{\alpha}\boldsymbol{S}_{\mathrm{iso},\alpha}^{\infty^{n}}\right], \\ \boldsymbol{\mathcal{H}}_{\alpha}^{n+1} &= \exp\left(-\frac{\Delta t}{2\tau_{\alpha}}\right)\beta_{\alpha}\boldsymbol{S}_{\mathrm{iso},\alpha}^{\infty^{n+1}}, \end{aligned} \tag{5.31}$$

where $\boldsymbol{\mathcal{H}}_{\alpha}^{n}$ and $\boldsymbol{\mathcal{H}}_{\alpha}^{n+1}$ are the history terms stored in the previous and the current time step, respectively. As such, the algorithmic expression for the continuous stress terms as in (5.13) take on the following form

$$\boldsymbol{S}^{n+1} = \boldsymbol{S}_{\mathrm{vol}}^{\infty^{n+1}} + \boldsymbol{S}_{\mathrm{iso}}^{\infty^{n+1}} + \boldsymbol{Q}^{n+1}. \tag{5.32}$$

An indispensable part of the solution of nonlinear problems is the consistent linearization of the underlying decoupled stress expressions which can algorithmically be expressed as

$$\mathbb{C}^{n+1} = \mathbb{C}_{\mathrm{vol}}^{\infty^{n+1}} + \mathbb{C}_{\mathrm{iso}}^{\infty^{n+1}} + \mathbb{C}_{\mathrm{vis}}^{n+1}, \tag{5.33}$$

where the material description of the continuum provides a relatively easy realization of the third (viscoelastic) contribution to $\mathbb{C}$. Thus, the viscous contribution is [80]

$$\mathbb{C}_{\mathrm{vis}}^{n+1} = \mathbb{C}_{\mathrm{vis,m}}^{n+1} + \mathbb{C}_{\mathrm{vis,f}}^{n+1} + \mathbb{C}_{\mathrm{vis,s}}^{n+1} + \mathbb{C}_{\mathrm{vis,fs}}^{n+1}, \qquad \mathbb{C}_{\mathrm{vis},\alpha}^{n+1} = \exp\left(-\frac{\Delta t}{2\tau_{\alpha}}\right)\beta_{\alpha}\mathbb{C}_{\mathrm{iso},\alpha}^{n+1}. \tag{5.34}$$

5.2.4 Decoupled free-energy function

We adopt a convex, invariant-based constitutive model by Holzapfel and Ogden [86] that is able to reflect the local orthotropic micro-structure of the passive myocardium, and its modification carried out to represent the dispersion of the fiber and sheet orientation [48]. The constitutive model has the following decoupled volumetric-isochoric form

$$\Psi^{\infty} = \Psi_{\mathrm{vol}}^{\infty}(J) + \Psi_{\mathrm{iso}}^{\infty}(\bar{I}_1, \bar{I}_{4\mathrm{f}}^{*}, \bar{I}_{4\mathrm{s}}^{*}, \bar{I}_{8\mathrm{fs}}), \tag{5.35}$$

where the volumetric part is specified as

$$\Psi_{\mathrm{vol}}^{\infty}(J) = \frac{\kappa}{2}(\ln J)^2, \tag{5.36}$$

along with the isochoric contribution according to

$$\begin{aligned} \Psi_{\mathrm{iso}}^{\infty} = {} & \frac{a}{2b}\left\{\exp[b(\bar{I}_1 - 3)] - 1\right\} \\ & + \sum_{i=\mathrm{f,s}} \frac{a_i}{2b_i}\left\{\exp[b_i(\bar{I}_{4i}^{*} - 1)^2] - 1\right\} + \frac{a_{\mathrm{fs}}}{2b_{\mathrm{fs}}}\left\{\exp[b_{\mathrm{fs}}\bar{I}_{8\mathrm{fs}}^{2}] - 1\right\}, \end{aligned} \tag{5.37}$$

where in (5.36) κ denotes the bulk modulus (numerically used as a penalty parameter), while in (5.37) a, a_{f}, a_{s}, a_{fs} stand for the stress-like material constants and b, b_{f}, b_{s}, b_{fs} are

dimensionless constants. Since the stress and elasticity tensors have already been provided in Sec. 5.2.2, we hereinafter focus on the determination of the unimodular correspondences for the volume preserving part. Explicitly, the unimodular part $\overline{\boldsymbol{S}}^{\infty}$ of the second Piola-Kirchhoff stress tensor may be expressed by

$$\overline{\boldsymbol{S}}^{\infty} = 2\left[\Psi_{\mathrm{iso}}^{\infty'}(\bar{I}_1)\boldsymbol{I} + \Psi_{\mathrm{iso}}^{\infty'}(\bar{I}_{4\mathrm{f}}^{*})\boldsymbol{H}_{4\mathrm{f}} + \Psi_{\mathrm{iso}}^{\infty'}(\bar{I}_{4\mathrm{s}}^{*})\boldsymbol{H}_{4\mathrm{s}} + \Psi_{\mathrm{iso}}^{\infty'}(\bar{I}_{8\mathrm{fs}})\boldsymbol{H}_{8\mathrm{fs}}\right], \tag{5.38}$$

with the derivatives having the definition $\Psi_{\mathrm{iso}}^{\infty'}(\bar{I}_i) = \partial\Psi_{\mathrm{iso}}^{\infty}(\bar{I}_i)/\partial\bar{I}_i$, $i \in \{1, 8\mathrm{fs}\}$, and $\Psi_{\mathrm{iso}}^{\infty'}(\bar{I}_j^{*}) = \partial\Psi_{\mathrm{iso}}^{\infty}(\bar{I}_j^{*})/\partial\bar{I}_j^{*}$, $j \in \{4\mathrm{f}, 4\mathrm{s}\}$. A closer look into these terms yields

$$\Psi_{\mathrm{iso}}^{\infty'}(\bar{I}_1) = \frac{a}{2}\exp[b(\bar{I}_1 - 3)], \qquad \Psi_{\mathrm{iso}}^{\infty'}(\bar{I}_{4\mathrm{f}}^{*}) = a_{\mathrm{f}}\exp[b_{\mathrm{f}}(\bar{I}_{4\mathrm{f}}^{*} - 1)^2](\bar{I}_{4\mathrm{f}}^{*} - 1), \tag{5.39}$$

$$\Psi_{\mathrm{iso}}^{\infty'}(\bar{I}_{4\mathrm{s}}^{*}) = a_{\mathrm{s}}\exp[b_{\mathrm{s}}(\bar{I}_{4\mathrm{s}}^{*} - 1)^2](\bar{I}_{4\mathrm{s}}^{*} - 1), \qquad \Psi_{\mathrm{iso}}^{\infty'}(\bar{I}_{8\mathrm{fs}}) = a_{\mathrm{fs}}\exp(b_{\mathrm{fs}}\bar{I}_{8\mathrm{fs}}^2)\bar{I}_{8\mathrm{fs}}. \tag{5.40}$$

In the subsequent treatment, we identify the unimodular part $\overline{\mathbb{C}}^{\infty}$ of the material elasticity tensor, i.e.

$$\overline{\mathbb{C}}^{\infty} = 4\left[\Psi_{\mathrm{iso}}^{\infty''}(\bar{I}_1)\boldsymbol{I}\otimes\boldsymbol{I} + \Psi_{\mathrm{iso}}^{\infty''}(\bar{I}_{4\mathrm{f}}^{*})\mathbb{H}_{4\mathrm{f}} + \Psi_{\mathrm{iso}}^{\infty''}(\bar{I}_{4\mathrm{s}}^{*})\mathbb{H}_{4\mathrm{s}} + \Psi_{\mathrm{iso}}^{\infty''}(\bar{I}_{8\mathrm{fs}})\mathbb{H}_{8\mathrm{fs}}\right], \tag{5.41}$$

where the second-order derivatives are given as $\Psi_{\mathrm{iso}}^{\infty''}(\bar{I}_i) = \partial^2\Psi_{\mathrm{iso}}^{\infty}(\bar{I}_i)/\partial\bar{I}_i^2$, $i \in \{1, 8\mathrm{fs}\}$, and $\Psi_{\mathrm{iso}}^{\infty''}(\bar{I}_j^{*}) = \partial^2\Psi_{\mathrm{iso}}^{\infty}(\bar{I}_j^{*})/\partial\bar{I}_j^{*^2}$; $j \in \{4\mathrm{f}, 4\mathrm{s}\}$. They are particularly characterized through

$$\Psi_{\mathrm{iso}}^{\infty''}(\bar{I}_1) = \frac{ab}{2}\exp\left[b(\bar{I}_1 - 3)\right], \tag{5.42}$$

$$\Psi_{\mathrm{iso}}^{\infty''}(\bar{I}_{4\mathrm{f}}^{*}) = a_{\mathrm{f}}[1 + 2b_{\mathrm{f}}(\bar{I}_{4\mathrm{f}}^{*} - 1)^2]\exp[b_{\mathrm{f}}(\bar{I}_{4\mathrm{f}}^{*} - 1)^2], \tag{5.43}$$

$$\Psi_{\mathrm{iso}}^{\infty''}(\bar{I}_{4\mathrm{s}}^{*}) = a_{\mathrm{s}}[1 + 2b_{\mathrm{s}}(\bar{I}_{4\mathrm{s}}^{*} - 1)^2]\exp[b_{\mathrm{s}}(\bar{I}_{4\mathrm{s}}^{*} - 1)^2], \tag{5.44}$$

$$\Psi_{\mathrm{iso}}^{\infty''}(\bar{I}_{8\mathrm{fs}}) = a_{\mathrm{fs}}(1 + 2b_{\mathrm{fs}}\bar{I}_{8\mathrm{fs}}^2)\exp(b_{\mathrm{fs}}\bar{I}_{8\mathrm{fs}}^2). \tag{5.45}$$

We close this section with the elaboration of the first-order derivatives of the structure tensors with the definitions $\mathbb{H}_i = \partial^2\bar{I}_i^{*}/\partial\overline{\boldsymbol{C}}^2$, $i \in \{4\mathrm{f}, 4\mathrm{s}\}$, and $\mathbb{H}_j = \partial^2\bar{I}_j/\partial\overline{\boldsymbol{C}}^2$, $j \in \{8\mathrm{fs}\}$, such that

$$\mathbb{H}_{4\mathrm{f}} = \kappa_{\mathrm{f}}\boldsymbol{I}\otimes\boldsymbol{I} + (1 - 3\kappa_{\mathrm{s}})\boldsymbol{f}_0\otimes\boldsymbol{f}_0\otimes\boldsymbol{f}_0\otimes\boldsymbol{f}_0, \tag{5.46}$$

$$\mathbb{H}_{4\mathrm{s}} = \kappa_{\mathrm{s}}\boldsymbol{I}\otimes\boldsymbol{I} + (1 - 3\kappa_{\mathrm{s}})\boldsymbol{s}_0\otimes\boldsymbol{s}_0\otimes\boldsymbol{s}_0\otimes\boldsymbol{s}_0, \tag{5.47}$$

$$\mathbb{H}_{8\mathrm{fs}} = \frac{1}{4}[(\boldsymbol{f}_0\otimes\boldsymbol{s}_0 + \boldsymbol{s}_0\otimes\boldsymbol{f}_0)\otimes(\boldsymbol{f}_0\otimes\boldsymbol{s}_0 + \boldsymbol{s}_0\otimes\boldsymbol{f}_0)]. \tag{5.48}$$

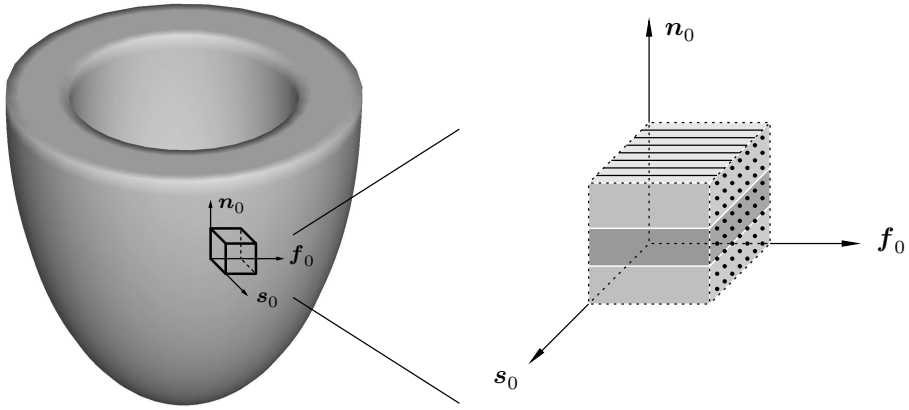

Figure 5.1 Schematic diagram of a human left ventricle and the idealized orthotropic architecture with its orthonormal basis vectors $\boldsymbol{f}_0$, $\boldsymbol{s}_0$ and $\boldsymbol{n}_0 = \boldsymbol{s}_0 \times \boldsymbol{f}_0$, denoted by endomysial, perimysial and normal to cleavage planes, respectively.

5.3 Representative Numerical Examples

Having outlined the constitutive update algorithm for the constitutive model documented in the previous section, we now validate our approach, retrieve the material parameters by fitting them to experimental data, and show its capability to serve under various types of loading. In particular, we perform a finite element analysis of a representative boundary-value problem together with the heterogeneity of fiber-sheet arrangement. To that end the finite element analysis program FEAP is utilized as a simulation tool [215].

5.3.1 Identification of material parameters

Excised myocardial tissue from the passive human left ventricular wall underwent biaxial extension and triaxial shear tests to characterize the elastic and viscoelastic properties of the tissue concerned. Within a given type of loading the following tests were performed: elastic, cyclic and relaxation tests [204]. Concerning biaxial deformation, the homogeneous true stresses along the mean fiber direction (MFD) and the cross-fiber direction (CFD) versus the corresponding stretches (in case of hysteresis) or time (in case of relaxation) were attained from the average of 26 and 5 tissue samples, respectively, dissected from the mid-wall of the left ventricle. Likewise, the average of 18 (in case of hysteresis) and 5 (in case of relaxation) cubic samples cutout from the mid-layer were tested on a triaxial shear testing machine. The results yield uniform true stresses with regard to the amount of shear or time (in case of relaxation) [204]. Figure 5.2 illustrates the reference and spatial configuration of a specimen undergoing biaxial extension tests with two distinctive modes, (ff) and (nn) occurring simultaneously, while Fig. 5.3 shows the respective configurations of a specimen undergoing triaxial shear associated with six different modes, i.e. (fs), (fn), (sf), (sn), (nf), and (ns) – hereby the first symbol relates to the plane while the second symbol indicates the loading direction. The deformation gradient $\boldsymbol{F}$ expresses

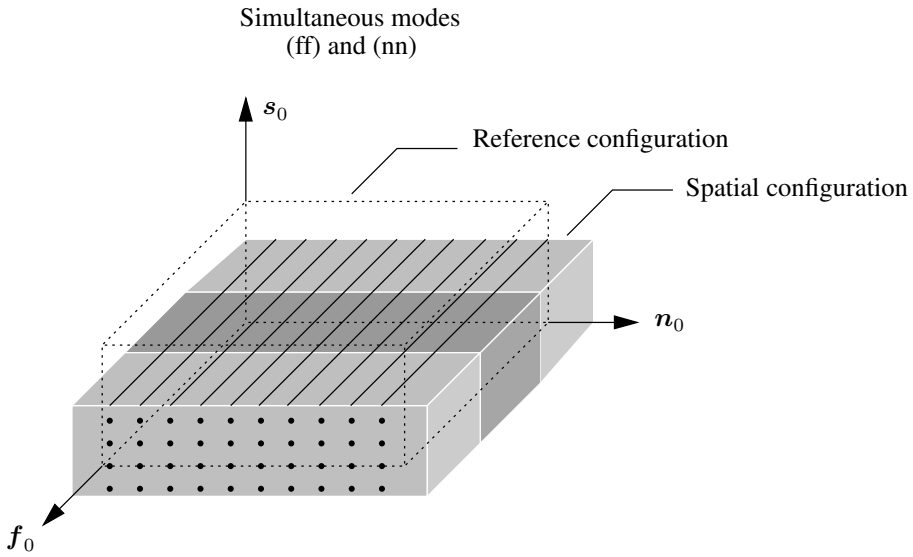

Figure 5.2 Specimen subjected to biaxial extension with (ff) and (nn) modes occurring simultaneously corresponding to the mean fiber direction (MFD) and the cross-fiber direction (CFD), respectively.

itself in the following form for triaxial shear and biaxial extension tests

$$\boldsymbol{F}^{\alpha\beta} = \boldsymbol{I} + \gamma \boldsymbol{e}_\beta \otimes \boldsymbol{e}_\alpha, \qquad [\boldsymbol{F}] = \mathrm{diag}[\lambda_\mathrm{f} \lambda_\mathrm{s} \lambda_\mathrm{n}], \tag{5.49}$$

respectively. In particular, the shear mode $\alpha\beta$ reads $\alpha, \beta = \{\mathrm{f}, \mathrm{s}, \mathrm{n}\}$, $\alpha \neq \beta$, where $\boldsymbol{e}_\mathrm{f} = \boldsymbol{f}_0$, $\boldsymbol{e}_\mathrm{s} = \boldsymbol{s}_0$ and $\boldsymbol{e}_\mathrm{n} = \boldsymbol{n}_0$ with γ being the amount of shear. The stretches along the fiber, sheet and normal direction are characterized by λ_f, λ_s and λ_n, respectively. Additionally, regarding the cyclic tests possessing 2 preconditioning and 1 main loading cycle, we consider a sinusoidal displacement load pattern in order to replicate the experiments. Thus,

$$\gamma(t) = \gamma_{\max} \sin\left(\frac{2\pi}{\tau} t\right), \tag{5.50}$$

where $\gamma_{\max} = 0.5$ and the period τ is equal to 130 and 56 s for biaxial extension and triaxial shear tests, respectively. However, we apply constant deformations in conformity with the loading throughout the simulation time in the case of relaxation tests, i.e. $\lambda_\mathrm{f}(t) = \lambda_\mathrm{f}(t_0) = 1.1$, and $\lambda_\mathrm{n}(t) = \lambda_\mathrm{n}(t_0) = 1.1$ for biaxial extension tests. By the same token, we retain the same amount of shear, i.e. $\gamma(t) = \gamma(t_0) = 0.5$ for triaxial shear tests.

As a first step, we identify the elastic parameters corresponding to the biaxial extension and triaxial shear tests by considering a hyperelastic incompressible material response of the tissue. To this end, the parameters are estimated through nonlinear least-squares analysis based on the separate objective functions $\phi(\boldsymbol{p}_\mathrm{biax})$ and $\phi(\boldsymbol{p}_\mathrm{shear})$ formed as the sum of squares of the analytical model predictions to the true stresses $\sigma_n^{(ij)}$, the outcome of the

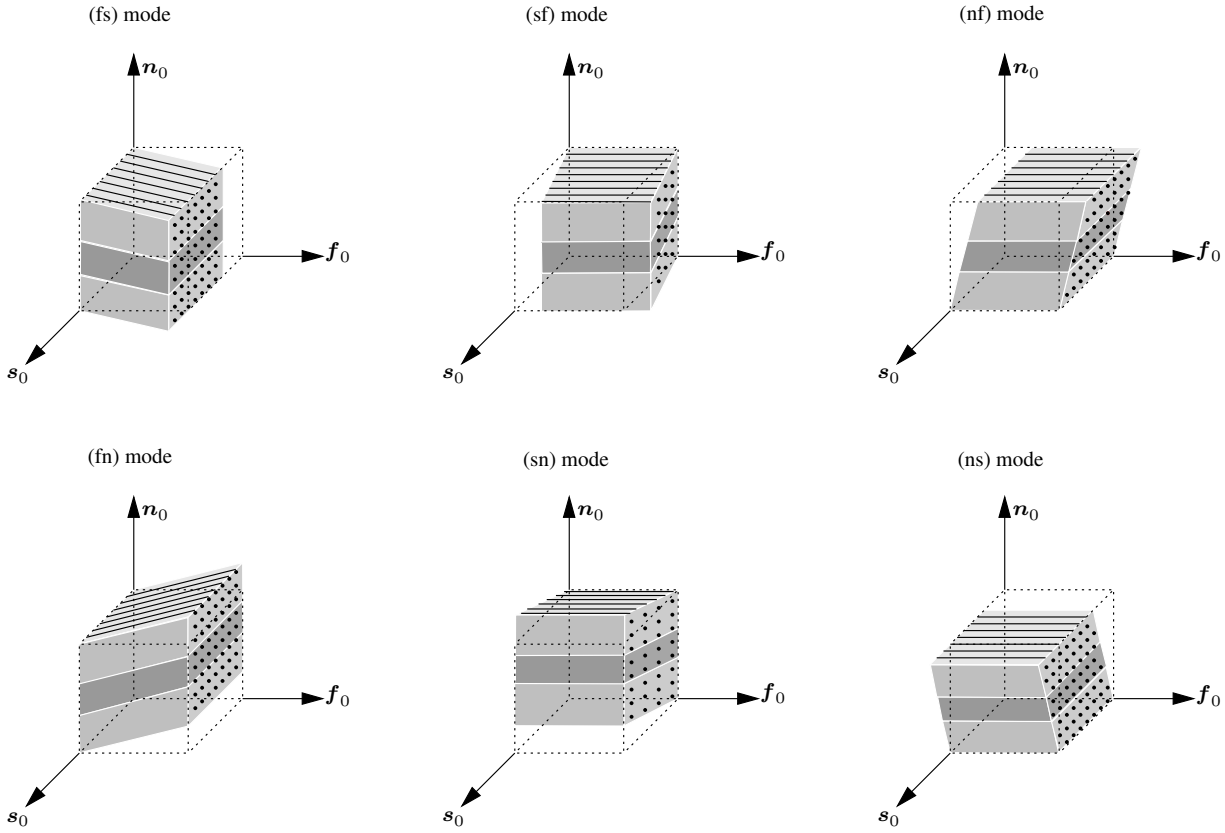

Figure 5.3 Specimens subjected to triaxial shear loading with six different shear modes identified, i.e. (fs), (fn), (sf), (sn), (nf), (ns).

incompressible formulation, subtracted by the experimental data $\bar{\sigma}_n^{(ij)}$, i.e.

$$\min_{\boldsymbol{p}_{\text{biax}}} \phi(\boldsymbol{p}_{\text{biax}}) = \sum_{(ij)\in \boldsymbol{m}_{\text{biax}}} \sum_{n=1}^{N_{\text{exp}}^{(ij)}} (\sigma_n^{(ij)} - \bar{\sigma}_n^{(ij)})^2, \tag{5.51}$$

$$\min_{\boldsymbol{p}_{\text{shear}}} \phi(\boldsymbol{p}_{\text{shear}}) = \sum_{(ij)\in \boldsymbol{m}_{\text{shear}}} \sum_{n=1}^{N_{\text{exp}}^{(ij)}} (\sigma_n^{(ij)} - \bar{\sigma}_n^{(ij)})^2, \tag{5.52}$$

which are minimized with respect to the material parameters $\boldsymbol{p}_{\text{biax}} = \{a, a_{\text{f}}, b, b_{\text{f}}\}$ and $\boldsymbol{p}_{\text{shear}} = \{a, a_{\text{f}}, a_{\text{s}}, a_{\text{fs}}, b, b_{\text{f}}, b_{\text{s}}, b_{\text{fs}}\}$ entering in the experiment of interest. Here, $\boldsymbol{m}_{\text{biax}} = \{(\text{ff}), (\text{nn})\}$ and $\boldsymbol{m}_{\text{shear}} = \{(\text{fs}), (\text{fn}), (\text{sf}), (\text{sn}), (\text{nf}), (\text{ns})\}$ denote the set of modes portrayed in the tests characterizing (ij) along with the number of data points, $N_{\text{exp}}^{(ij)}$ associated with it. To compute these minimization problems, a MATLAB® built in function referred to as *lsqnonlin* is implemented with a *trust-region-reflective* algorithm based on the update of a trust region in the neighborhood of a point where the solution is approximated for the function to be minimized [129, 147]. The set of elastic parameters identified are summarized in Tables 5.1 and 5.2 for which the hyperelastic model response comply with

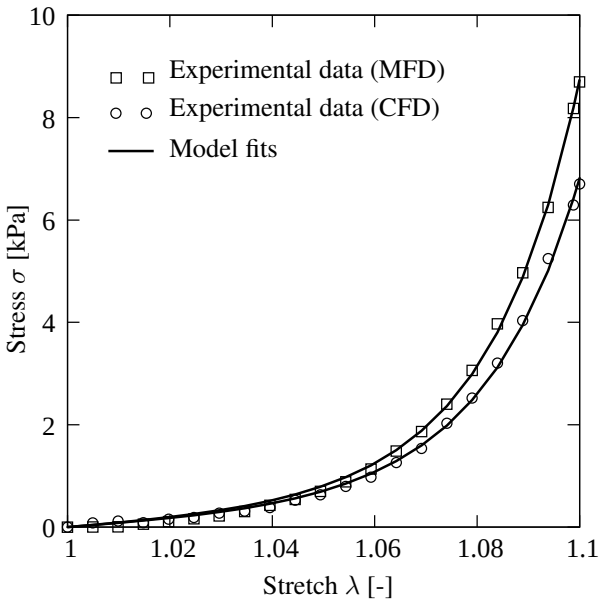

Figure 5.4 Elastic biaxial extension test data and corresponding model fits along the mean fiber direction (MFD) and the cross-fiber direction (CFD). Cauchy stress σ vs stretch λ.

the experimental data, see Fig. 5.4 and 5.5. Note that unlike stated in [48] the dispersion parameters κ_{f} and κ_{s} no longer appear as a fitting parameter, since their values have already been identified via an experimental process [204]. For the sake of compliance the parameters obtained are implemented into a finite element code and the numerical results exhibit a perfect overlap with the experimental data.

Subsequently, the viscoelastic parameters are identified by means of a cyclic and relaxation type of loading in regard to the tests conducted, i.e. biaxial extension and triaxial shear. Here, it needs to be stated that apart from the elastic response where a least-squares analysis makes it possible to obtain the elastic material parameters, a trial-and-error method furnishes the numerical aspects of the cyclic and relaxation tests via finite element analyses where we consider 8 structured and 1 unstructured hexahedral elements with necessary boundary conditions for biaxial extension and triaxial shear tests, respectively. The parameter sets obtained are listed in the Tables 5.1 and 5.2.The corresponding plots are provided in Fig. 5.6–5.9.

5.3.2 Simulation of a monoventricular heart model

In this section we engage in the numerical treatment of a monoventricular heart model via nonlinear finite element analysis. To this end, we idealize the intricate geometry of the left ventricle and adopt a common representation in terms of prolate spheroidal coordinates (λ, μ, θ) that are mapped onto Cartesian coordinates via

$$x = d \cosh\lambda \cos\mu, \qquad y = d \sinh\lambda \sin\mu \cos\theta, \qquad z = d \sinh\lambda \sin\mu \sin\theta, \tag{5.53}$$

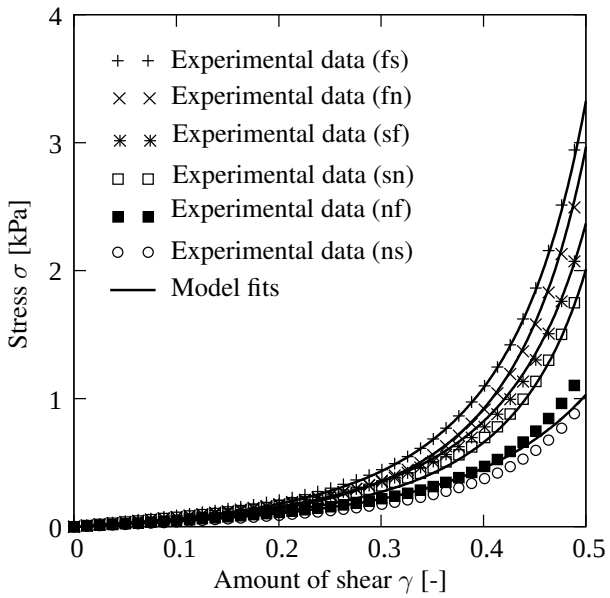

Figure 5.5 Elastic triaxial shear test data and corresponding model fits of modes (fs), (fn), (sf), (sn), (nf), (ns). The model fits for (nf) and (ns) modes overlap each other. Cauchy stress σ vs amount of shear γ.

Table 5.1 Material parameters obtained from biaxial extension tests

Elastic	$a = 1.36\,\text{kPa}$	$b = 21.75$	$a_\text{f} = 0.49\,\text{kPa}$	$b_\text{f} = 90.10$
	$\kappa_\text{f} = 0.08$	$\kappa_\text{s} = 0.09$		
Hysteresis (Cyclic)	$\beta_\text{m} = 0.70$	$\tau_\text{m} = 250\,\text{s}$	$\beta_\text{f} = 2.50$	$\tau_\text{f} = 3.50\,\text{s}$
Relaxation	$\beta_\text{m} = 0.90$	$\tau_\text{m} = 10\,\text{s}$	$\beta_\text{f} = 0.40$	$\tau_\text{f} = 80\,\text{s}$

where d ($= 60\,\text{mm}$) designates the focal length [33, 97, 153]. The dimensions of the truncated ellipsoidal geometry is retrieved from [204], and depicted in Fig. 5.10(a). In order to reflect regional variations in the fiber and sheet arrangements the wall is considered to be made up of four sub-walls, i.e. septal, anterior, lateral and posterior which is in accordance with [176], as illustrated in Fig. 5.10(b). The quantitative distribution of the fiber and sheet angles through the thickness (see Fig. 4(b) and 8(a) in [176]), is discretized with respect to the number of elements spanning the thickness of the mesh, and the mean values of angles are assigned to elements. In the sequel, a mesh composed of 4960 hexahedral elements with 6144 nodes is generated through discretization of the eq. (5.53), see Fig. 5.10(c). Accordingly, the orientation of the fibers and sheets throughout the wall are obtained in a discrete sense by using data provided in [176]. Figure 5.11(a) and 5.11(b) reveal the re-

Table 5.2 Material parameters obtained from triaxial shear tests

Elastic	$a = 0.40\,\text{kPa}$	$b = 6.55$	$a_\text{f} = 3.05\,\text{kPa}$	$b_\text{f} = 29.05$
	$a_\text{s} = 1.25\,\text{kPa}$	$b_\text{s} = 36.65$	$a_\text{fs} = 0.15\,\text{kPa}$	$b_\text{fs} = 6.28$
	$\kappa_\text{f} = 0.08$	$\kappa_\text{s} = 0.09$		
Hysteresis (Cyclic)	$\beta_\text{m} = 20$	$\tau_\text{m} = 20\,\text{s}$	$\beta_\text{f} = 475$	$\tau_\text{f} = 45\,\text{s}$
	$\beta_\text{s} = 1000$	$\tau_\text{s} = 30\,\text{s}$	$\beta_\text{fs} = 40$	$\tau_\text{fs} = 60\,\text{s}$
Relaxation	$\beta_\text{m} = 3.30$	$\tau_\text{m} = 12\,\text{s}$	$\beta_\text{f} = 2.30$	$\tau_\text{f} = 24\,\text{s}$
	$\beta_\text{s} = 1.75$	$\tau_\text{s} = 14\,\text{s}$	$\beta_\text{fs} = 6$	$\tau_\text{fs} = 45\,\text{s}$

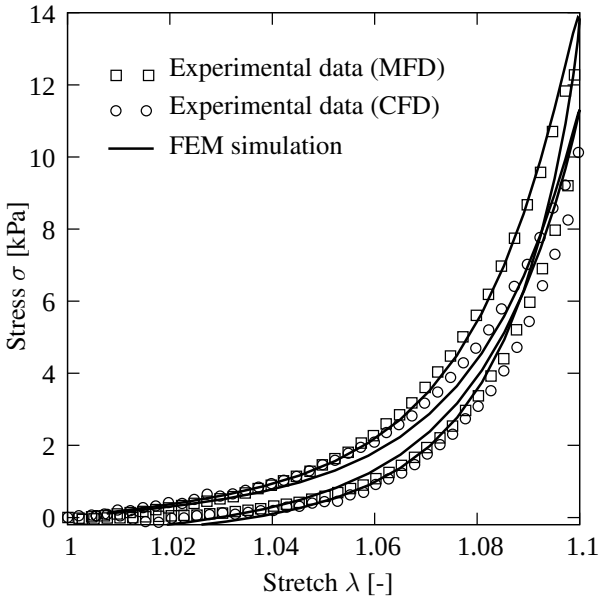

Figure 5.6 Cyclic biaxial extension test data and corresponding finite element results along the mean fiber direction (MFD) and the cross-fiber direction (CFD) for the hystereses response. Cauchy stress σ vs stretch λ.

spective fiber and sheet orientations for the mesh-size considered. The ventricular pressure as a function of time, as shown in Fig. 5.11(c), is applied by means of a follower load with two cycles exerting on the inner surface nodes following a fashion that is described in, e.g., [62]. Algorithmic approaches in the treatment of incompressible material behavior require further effort to avert volumetric locking phenomena which, in our case, is carried by the use of the mixed Jacobian-pressure element Q1P0. For details of the mixed finite element procedure based on a three-field Hu-Washizu-type formulation the reader is referred to [81, 133, 200, 201]. The penalty parameter κ is taken in general as $\kappa \approx 10^3 a$, where a is the material constant as given in (5.37). However, a well-known problem that the tangent arrays in the FE solution procedure become undesirably ill-conditioned as κ gets

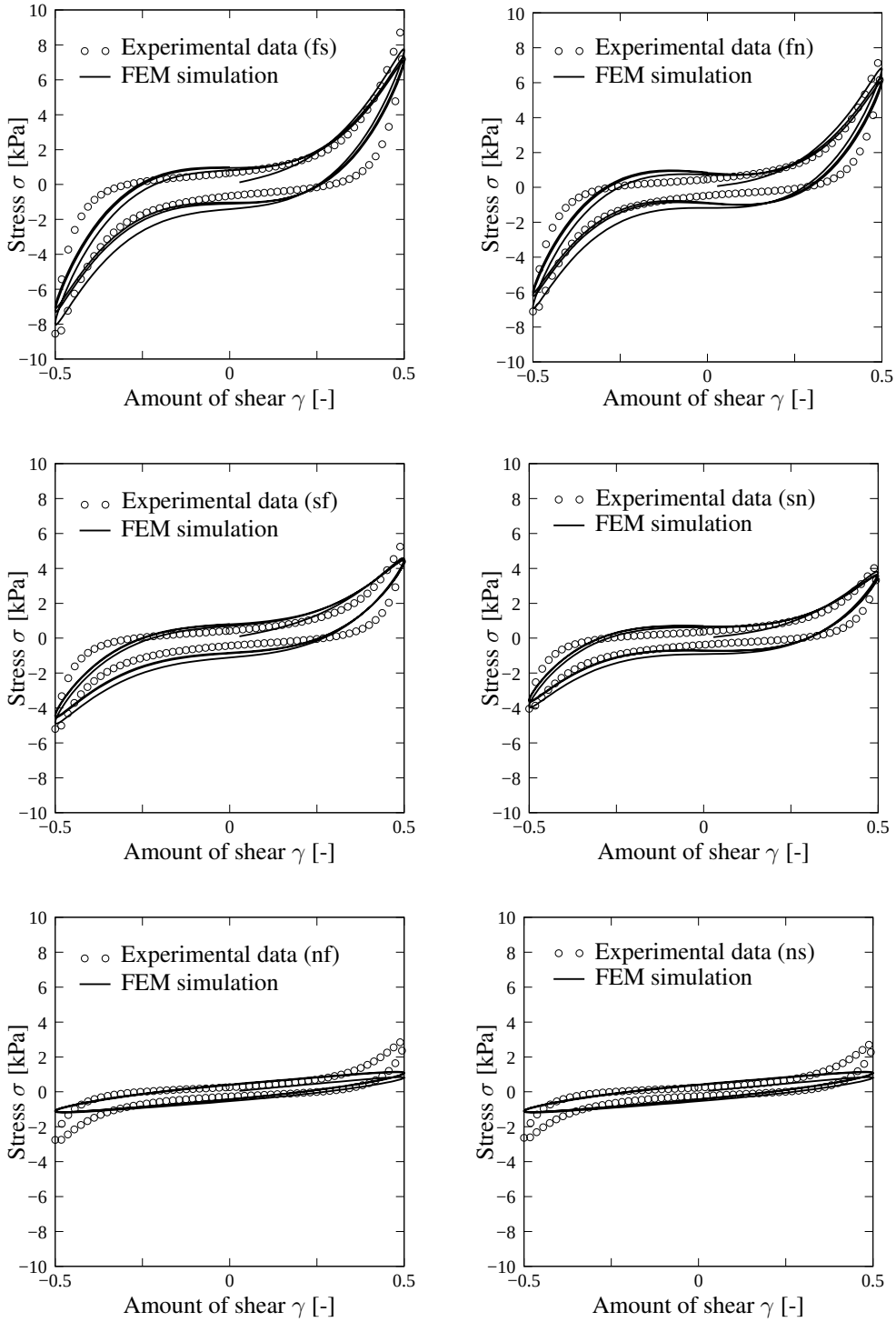

Figure 5.7 Cyclic triaxial shear test data and corresponding finite element results of modes (fs), (fn), (sf), (sn), (nf), (ns) for the hystereses response. Cauchy stress σ vs amount of shear γ.

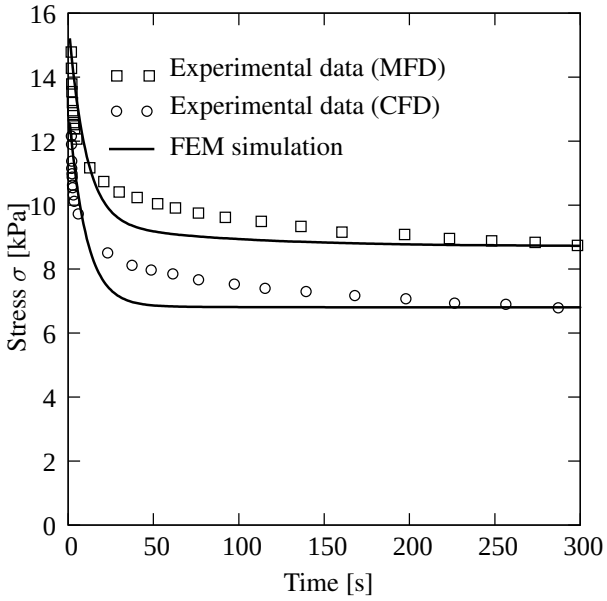

Figure 5.8 Relaxation test data of the biaxially loaded specimen with corresponding finite element results along the mean fiber direction (MFD) and the cross-fiber direction (CFD). Cauchy stress σ vs time.

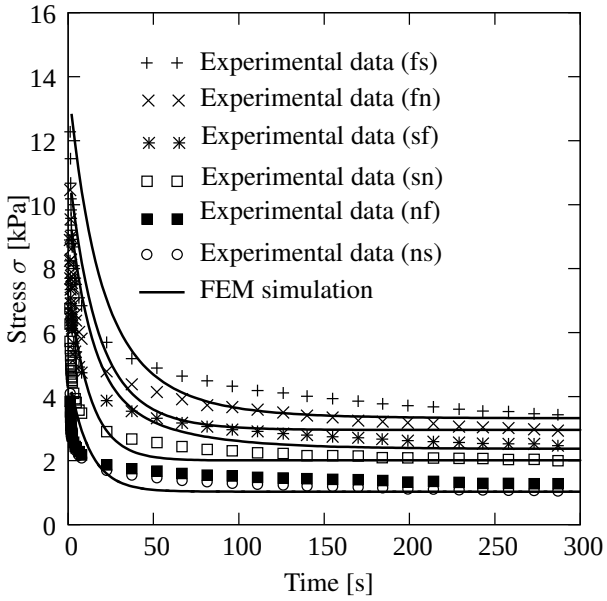

Figure 5.9 Relaxation test data of the triaxially loaded specimens with the corresponding finite element results of modes (fs), (fn), (sf), (sn), (nf), (ns). The curves for (nf) and (ns) modes overlap each other. Cauchy stress σ vs time.

larger values leads us to implement the augmented-Lagrangian method so that the incompressibility constraint is enforced in a robust manner. Concerning the Dirichlet-boundary

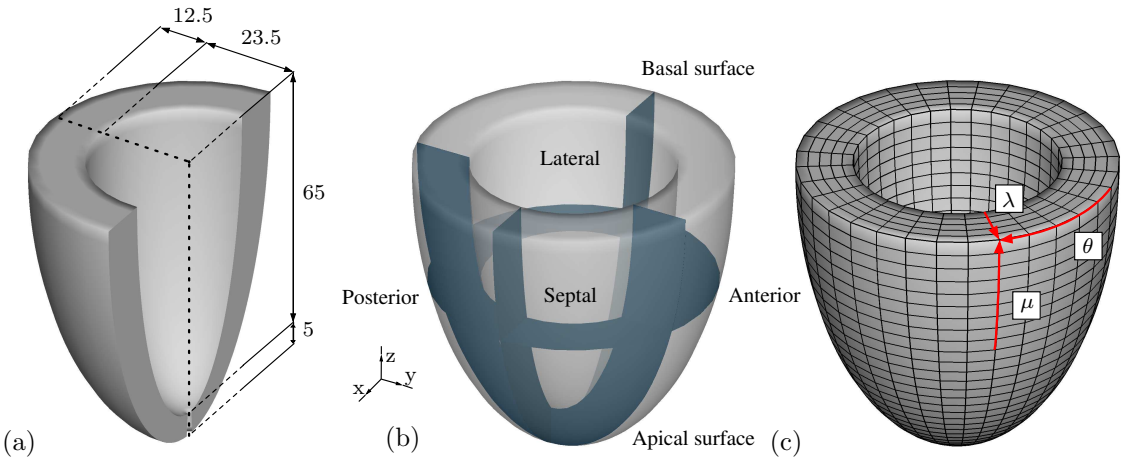

Figure 5.10 (a) Truncated thick-walled ellipsoidal geometry of the human left ventricle with its major and minor radii of the outer and inner surfaces. Dimensions provided in millimeters; (b) regions of the left ventricular wall; (c) mesh generated with the discrete setting of the prolate spheroidal coordinates (λ, μ, θ).

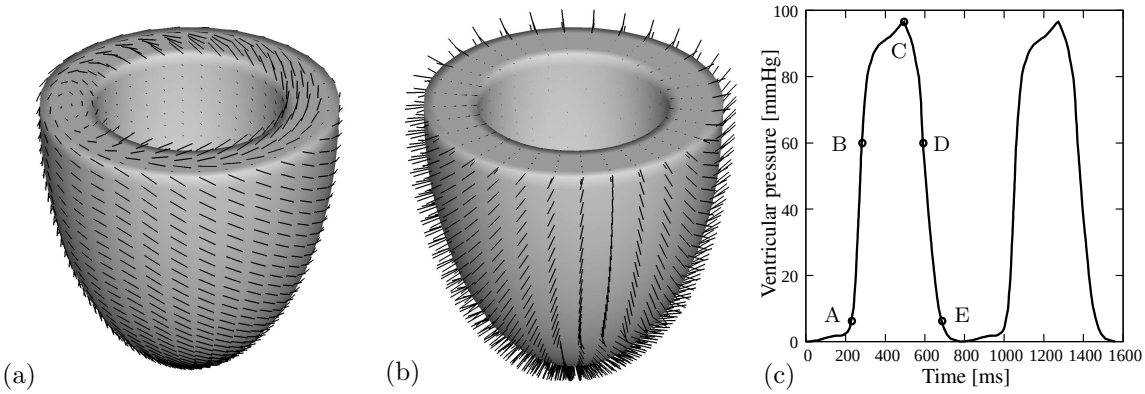

Figure 5.11 (a) Inhomogeneous fiber orientation field $\boldsymbol{f}_0$; (b) inhomogeneous sheet orientation field $\boldsymbol{s}_0$; (c) left ventricular cyclic pressure applied on the inner surface plotted against time.

condition, all nodes on the basal surface are restrained along the z-direction while those located on the outermost circle also have zero displacement in x- and y-directions. The encompassing tissue response is adjusted to be characterized by linear springs in the x and y directions, exercised on all nodes on the epicardial surface with a directional stiffness $k_x = k_y = 10^{-3}$ N/mm as considered in [22].

We employ essentially the computer analysis of both the elastic and viscoelastic model with the elastic parameters obtained from triaxial shear tests (Table 5.2). Regarding the viscoelastic parameters, they are used from the triaxial relaxation tests (Table 5.2). The snapshots extracted from the particular load-time pairs A, B, C, D, and E, on the curve in

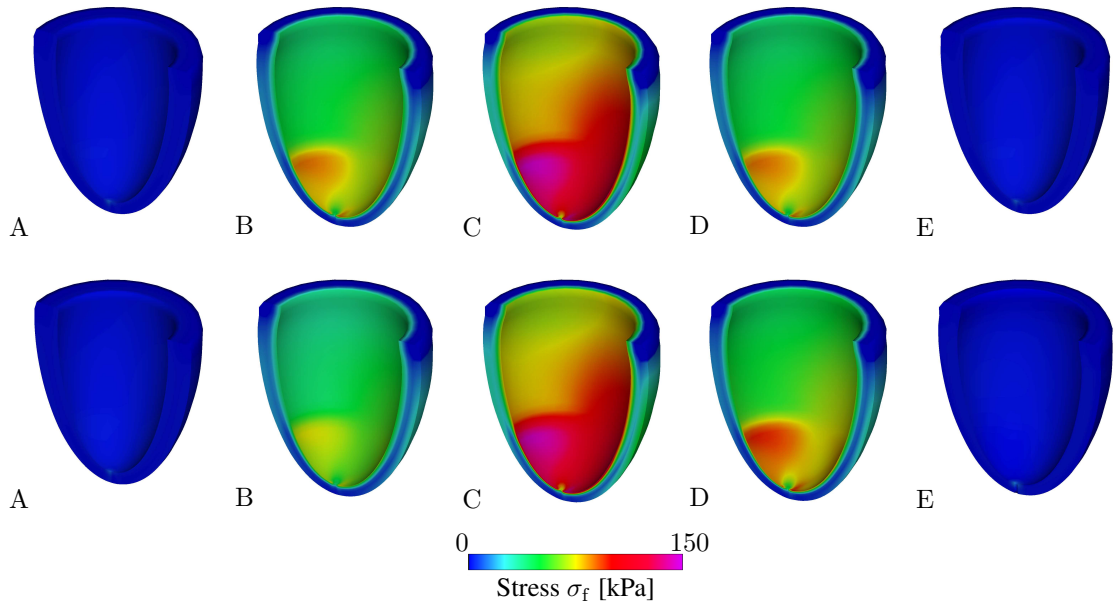

Figure 5.12 True stress distribution σ_f along the fiber direction for the elastic (first row) and the viscoelastic case (second row) on snapshots A, B, C, D, E taken the from pressure-time curve of Fig. 5.11(c).

Fig. 5.11(c) portray the true stress σ_f and the stretch λ_f along the fiber direction denoted in Fig. 5.12 and 5.13. In addition, the analyses of the stress-stretch response of particular nodes taken from the mesh provide a closer scrutiny, as depicted in Fig. 5.14.

5.4 Discussion

In this paper we have incorporated an orthotropic viscoelastic model into the constitutive model outlined in [86], as recent experimental data of the passive response of myocardial tissues strongly predicate their viscoelastic features by means of hystereses and stress relaxation, as articulated in [204]. We base the construction of the model on an additive split of the free-energy function, composed of an equilibrium part and a non-equilibrium part distinctively portraying the viscous response of the matrix, fiber, sheet and fiber-sheet fragments in line with what is contributing to the hyperelastic response. The viscous overstress obtained from the non-equilibrium part is dictated by rate equations corresponding to each fragment. With this framework at hand, we also focus on the numerical implementation of the model and touch upon its fitting capability. In addition, we closely examine a boundary-value problem of a tailored geometry of the representative continuum.

The criticism of the constitutive model imparted in the present paper may be the choice of the material parameters that render four different parameter sets, see Tables 5.1 and 5.2. We hereby point out that a fusion of biaxial extension and triaxial shear data, at least for the experimental data set we use, was not satisfactory with the present constitutive framework,

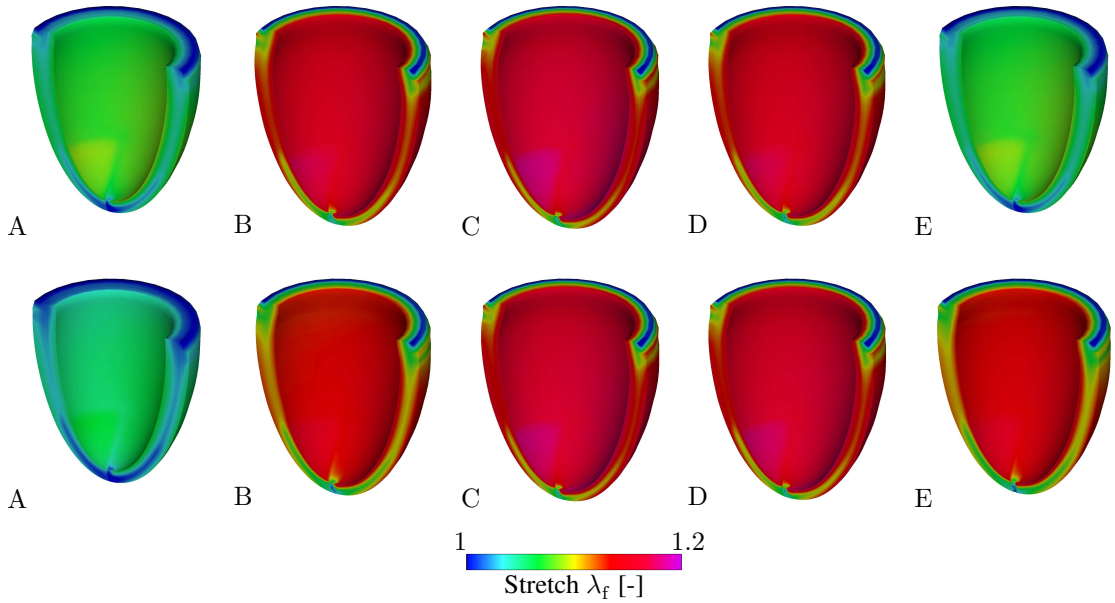

Figure 5.13 Fiber stretch distribution λ_f throughout the body for the elastic (first row) and the viscoelastic case (second row) on snapshots A, B, C, D, E, taken from the pressure-time curve of Fig. 5.11(c).

albeit we tried to minimize one objective function involving the sum of squares of both biaxial and shear responses. Hence, the single set of material parameters obtained from both biaxial extension and triaxial shear data was not used herein.

The fits against the cyclic experimental data, where we observe salient hystereses distinct for each mode, suitably mimic the data for biaxial loading while the simulations display notable deviations in all shear modes. Particularly, the proposed constitutive model cannot fully recover the flexure-like path on the loading-unloading curve as the amount of shear approaches to higher values, i.e. 0.5, depicted in Fig. 5.7. Apart from the (nf) and (ns) modes, where a relatively low level of time dependent behavior occurs, the hystereses lack the exponential stiffening due to the mere isotropic response inherited from the constitutive model. Nevertheless, the proposed model is able to capture the overall dissipated energy realized by the hystereses response which occurs because of the inner structure of the myocardial tissue

As far as the fits to the relaxation behavior is concerned, some disparity between the finite element results and the experimental data are highlighted in the biaxial extension and triaxial shear tests associated with each mode at the early stages of stress relaxation, albeit they later fully recover the thermodynamic equilibrium stresses, see Fig. 5.8 and 5.9. Nonetheless, the demonstrated capability of the material model to capture experimental data provides sufficient validity from both quantitative and qualitative aspects. It should be mentioned that for more dashpots delineating the viscous response of the separated contributions in the model (matrix, fiber, sheet and fiber-sheet) we obtain a more coherent hysteresis and stress relaxation behavior. However, for characterization and implementa-

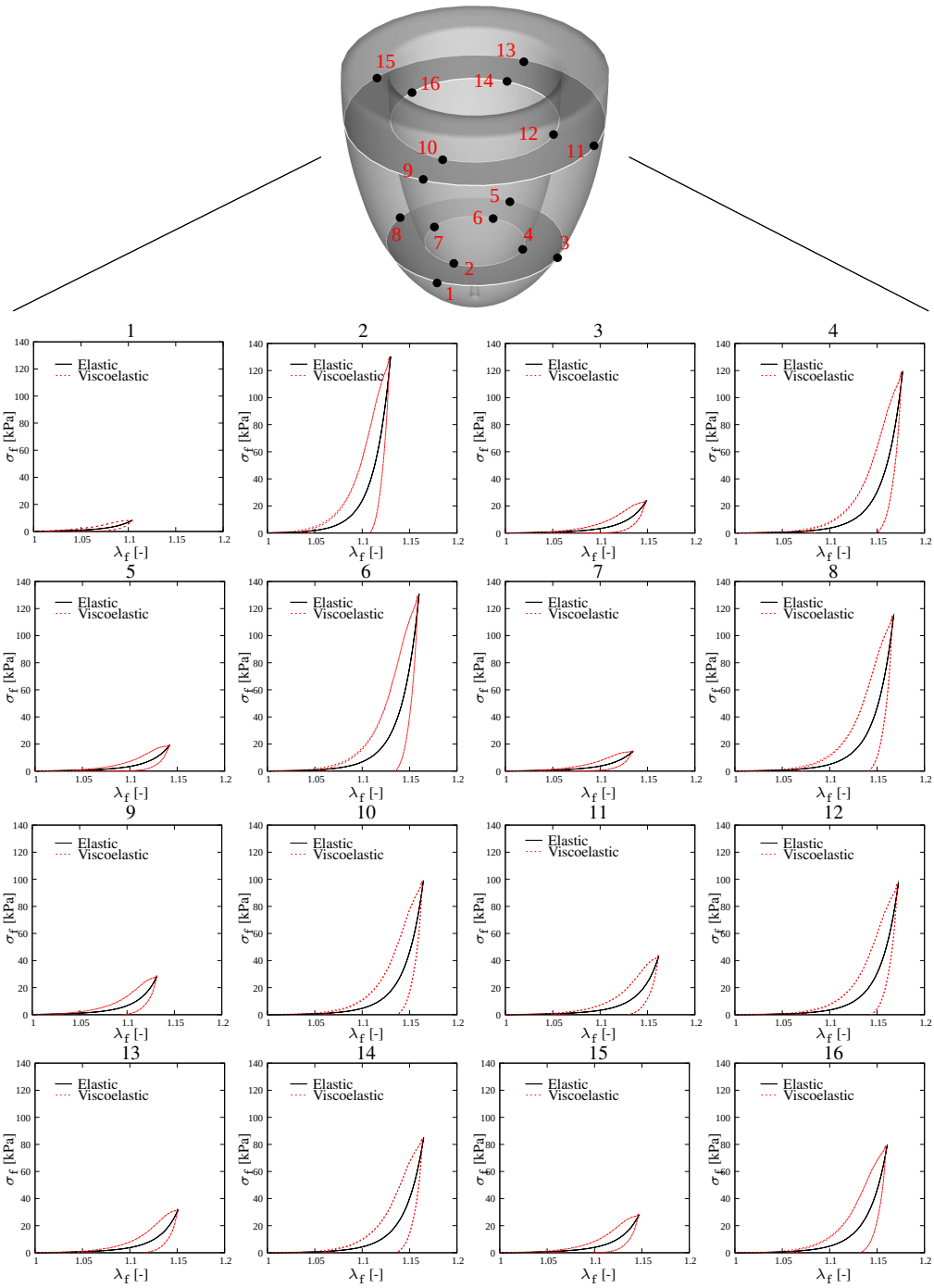

Figure 5.14 True stress σ_f as a function of fiber stretch λ_f at nodal points taken from an apical and a basal sub-layer for the elastic and the viscoelastic case.

tion problems, this makes an analysis less favorable (too many material parameters), and the plots are not included here.

With respect to the monoventricular simulation results, we conclude that the mechanical response of the tissue under loading is highly dependent on the inner structural arrangement and the loading condition. As the pressure increases to its maximum value at A (depicted in Fig. 5.11(c)) the inhomogeneity of the stress response becomes more evident (see Fig. 5.12). Moreover, due to the viscoelastic tissue behavior the loading-unloading path is quite different from the elastic path (see Fig. 5.12), which is conspicuously expressed in Fig. 5.14 with a clear transmural variation of the constitutive response accompanied with significant hystereses on the endocardial surface. It must be mentioned that the viscoelastic simulation reveals some remaining fiber stretches as the pressure vanishes at time $t = 780$ and $t = 1560$ ms. It is the set of material parameters identified from the triaxial relaxation tests that leads to this specific response. Moreover, the results show a twist in the left ventricle in form of a clockwise rotation when viewed from the apex to the base which is related to the helical network of the muscle fibers. This is in agreement with the numerical analysis of, e.g., [47], and with clinical observations [23, 179]. The simulation results show displacements not only along the long axis of the monoventricular model, but there is also a horizontal displacement of the apex in the direction represented in between the lateral and the posterior wall. This displacement, also observed clinically, is due to the heterogeneity of the fiber orientation. In contrast, for a generic transmural variation of the fiber arrangement between the epicardium and the endocardium we have not obtained that horizontal displacement.

When examined, the discrepancies between the data and the fits are probably due to the nature of the viscoelastic model, imparted here, which is originally set up for small perturbations away from the thermodynamic equilibrium as it overestimates the stresses at higher values of strain, as discussed in [171]. For the viscous response of the simulated ellipsoidal left ventricle we performed two separate analyses; one with material parameters obtained from cyclic tests and the second one with parameters from relaxation tests. With the parameters from the cyclic tests we achieved inappropriate stress-stretch responses in regard to the elastic curve. One possible reason for this simulation results may be that in monoventricular heart simulations the deformation is induced by a peculiar pressure function, as depicted in Fig. 5.11(c), whereas all conducted cyclic tests were displacement driven with sinusoidal load pattern.

It should also be mentioned that the viscoelastic model needs to be investigated through more realistic geometries and boundary conditions that can provide a holistic assessment of the mechanical properties of the human heart. There is a need for more experimental evidence here so that it can be used to orient future computational researches in such a manner that more inclusive and deterministic modeling approaches can be contemplated.

Acknowledgments

The authors are indebted to Faik Barış Can Cansız for his valuable comments and suggestions. Furthermore, we gratefully acknowledge the financial support of the Austrian Science Foundation (FWF), research grant no. P 23830-N13.

6 ON THE QUASI-INCOMPRESSIBLE FINITE ELEMENT ANALYSIS OF ANISOTROPIC HYPERELASTIC MATERIALS

Abstract Quasi-incompressible behavior is a desired feature in several constitutive models within the finite elasticity of solids, such as rubber-like materials and some fiber-reinforced soft biological tissues. The *Q1P0* finite element formulation, derived from the three–field Hu-Washizu variational principle, has hitherto been exploited along with the augmented Lagrangian method to enforce incompressibility. This formulation typically uses the unimodular deformation gradient. However, contributions by Sansour (Eur. J. Mech. A/Solids, 2007, 27:28-39) and Helfenstein et al. (Int. J. Solids Structures, 2010, 47:2056-2061) conspicuously demonstrate an alternative concept for analyzing fiber reinforced solids, namely the use of the (unsplit) deformation gradient for the anisotropic contribution, and these authors elaborate on their proposals with analytical evidence. The present study handles the alternative concept from a purely numerical point of view, and addresses systematic comparisons with respect to the classical treatment of the *Q1P0* element and its coalescence with the augmented Lagrangian method by means of representative numerical examples. The results corroborate the new concept, show its numerical efficiency and reveal a direct physical interpretation of the fiber stretches.

6.1 Introduction

That the constitutive models for finite elasticity of rubber–like materials and some fiber-reinforced soft biological tissues suffer from ill–conditioning of the global stiffness matrix, referred to as the locking phenomenon, is a well–known issue. Locking mainly arises when the standard displacement formulations are used, but is not directly related to a physical response, such as bending and quasi-incompressible elasticity. In fact, for such problems first-order shape functions (bi– or tri–linear interpolations) used to approximate the displacement field over a finite element exhibit convergence issues, see, e.g., Hughes [95], Zienkiewicz & Taylor [239] and Wriggers [235]. One way to avoid this problem is to use a mixed variational formulation that hinges on the Hu–Washizu principle, where the master field appears together with additional subsidiary conditions, as first introduced by Nagtegaal et al. [151] and discussed in Brezzi & Fortin [20] for small strains. It was later extended to finite strain problems by Simo et al. [201] and is also well documented in the literature, by, e.g., Miehe [133] and Wriggers [235]. This approach falls into the category of the three–field Hu-Washizu principle with the constitutive function augmented by a volumetric constraint via the scalar conjugate pairs, i.e. pressure–dilatation. One of the relevant finite element formulations, known as the *Q1P0* element, is robust for most problems in solid mechanics; however, it may cause numerical instabilities for the pressure

for some specific loading and boundary conditions, see Wriggers [235].

Other methods used to circumvent the locking phenomenon include h– and p–refinement strategies (Düster et al., [44]), reduced integration schemes with stabilization techniques (Belytschko et al., [10, 12]; Reese [170]) and enhanced strain formulations based on the Hu–Washizu principle (Simo and coworkers [199], [195], [196]). The above–stated methods, albeit effective in averting the locking issue, are connected with other problems, e.g., increased computational costs, artificial stabilizing parameters and numerical instabilities upon irregular mesh distortion. Therefore, they fall into disfavor among, e.g., the biomechanics community when a mere finite hyperelastic analysis of the material is sought. In addition, the more recent revelations by Schröder et al. [190] and Wriggers et al. [236] highlight the mixed variational principles for the treatment of the inextensibility limit in fiber-reinforced materials and soft biological tissues, which are useful in the presence of extremely stiff fibers, i.e. very high stiffness associated with fibers may lead to low convergence rates in the primary fields, e.g., the displacements.

Since its introduction by Flory [52] the multiplicative decomposition of the deformation gradient has gained popularity in the context of the variational Hu–Washizu principle. This split generates nonphysical results in the case of simple tension and compression problems for isotropic hyperelastic models capturing rubber–like materials, which are known to be quasi–incompressible; for more details see Ehlers & Eipper [45]. By the same token, nonphysical responses may occur in the numerical analysis of anisotropic materials unless the analysis is based on a quasi–incompressible material formulation. In this respect, the multiplicative split of the deformation gradient leads to a twofold issue for fiber–reinforced hyperelastic materials:

(i) Stresses in the fibers are expected to be one–dimensional since fibers are assumed to behave like one–dimensional springs, see Sansour [182]. However, the use of isochoric anisotropic invariants automatically yields a projection tensor that generates the stress components perpendicular to the alignment of the fibers, thereby violating the basic assumption.

(ii) For the anisotropic contribution the use of isochoric anisotropic invariants leads to a 'competition' between the anisotropic part and the volumetric part of the free energies in the process of energy minimization. As a matter of fact, if the solid undergoes volumetric deformations, a much lower strain energy is stored in the system in comparison with that resulting from the fibers undergoing deformation for the same amount of global stretch, say λ, as illustrated in Fig. 6.1. As a consequence, the system favors the volumetric part and tends to generate spurious spherical deformations accompanied by a volume growth at relatively small stretches. Such a disparity is discernable in a typical numerical uniaxial extension test.

Several studies, e.g., Helfenstein et al. [75], Annaidh et al. [6] and Nolan et al. [155], have reported the erroneous analysis results of fiber-reinforced anisotropic material models for soft biological tissues (Weiss et al. [232], Holzapfel et al. [83] and Rubin & Bodner

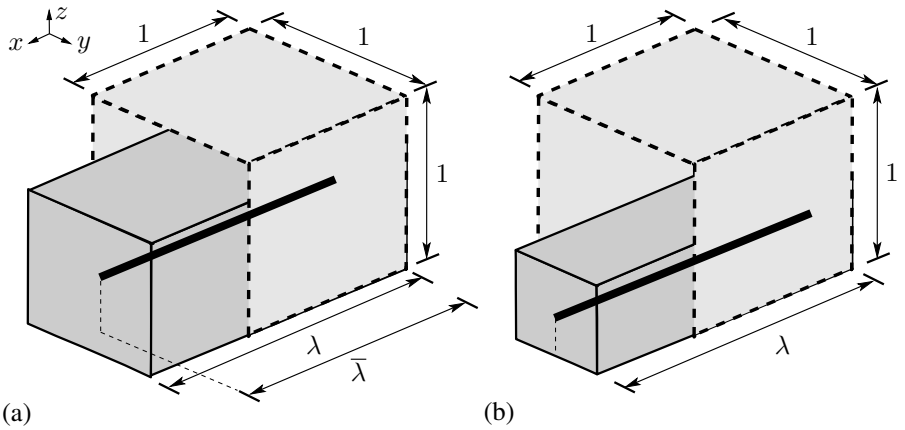

Figure 6.1 Schematic views of a typical uniaxial extension of a transversely isotropic solid with unit dimensions: (a) with the unimodular invariant $\bar{I}_4 = \bar{\lambda}^2$; (b) with the invariant $I_4 = \lambda^2$. Qualitatively (a) reveals erroneous transverse deformations along the y– and z–directions, i.e. isotropic directions upon a uniaxial stretch λ in the x–direction, which is in contrast to (b).

[178]) when they are mistakenly used in the compressible domain; e.g., a sphere reinforced with one family of fibers would be deformed into a sphere with a smaller size upon hydrostatic pressure instead of taking on an ellipsoidal shape. One remedy for (ii) is to implement the computationally (rather) expensive augmented Lagrangian method to bring the analysis towards the incompressibility limit, see Glowinski & Le Tallec [59, 60] and Simo & Taylor [200] among others. Alternatively, the multiplicative decomposition of the deformation gradient can be avoided for the anisotropic part, as suggested by Sansour [182] and Helfenstein et al. [75], which solves the issue on the constitutive level without using any *ad hoc* algorithm.

The emphasis of the present article is placed upon the comparison of two remedies namely the augmented Lagrangian method and the use of an unsplit deformation gradient $\boldsymbol{F}$ for the anisotropic contribution; the consequences thereof are elucidated with simple examples in the context of the *Q1P0* finite element formulation. In the authors' opinion, a systematic comparison of the above-mentioned concepts is particularly relevant for highlighting the issues within the biomechanics community. We further emphasize that for the sake of brevity the classical *Q1P0* element, its coalescence with the augmented Lagrangian method and the *Q1P0* element without the multiplicative split in the anisotropic contribution are hereinafter denoted by *Q1P0*, *Q1P0+AL* (*Q1P0* element along with **A**ugmented **L**agrangian method), and *Q1P0+WAS* (*Q1P0* element **W**ithout **A**nisotropic **S**plit), respectively.

Section 6.2 summarizes in brief the background on the constitutive modeling of fibrous (soft) tissues where the collagen fibers are embedded in an otherwise isotropic matrix material. Subsequently, Sec. 6.4 documents simple yet representative boundary-value problems which demonstrate volume changes, isotropic and anisotropic energy contributions, and the associated Cauchy stresses for the considered material under uniaxial extension and extension–inflation–torsion tests. Finally, Sec. 6.5 concludes the paper with a brief summary and some remarks.

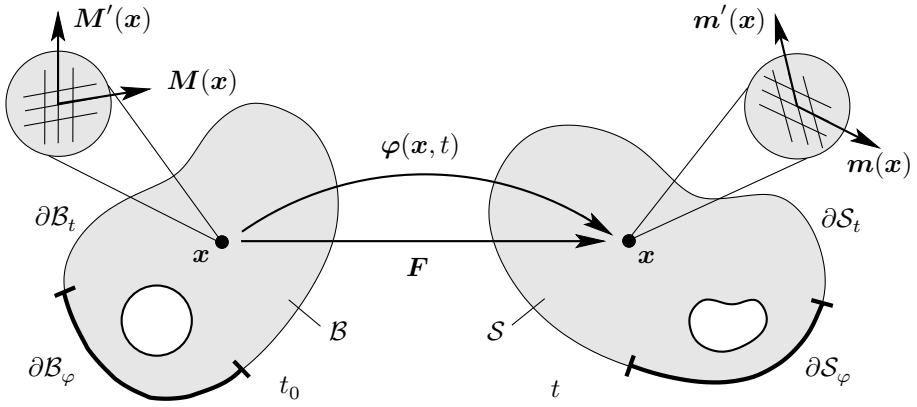

Figure 6.2 Nonlinear deformation of an anisotropic solid with the reference configuration $\mathcal{B} \in \mathbb{R}^3$ and the spatial configuration $\mathcal{S} \in \mathbb{R}^3$. The bijective deformation map is $\boldsymbol{\varphi} : \mathcal{B} \times \mathbb{R}^+ \to \mathcal{S}$, which transforms a material point $\boldsymbol{x} \in \mathcal{B}$ at time t_0 onto a spatial point $\boldsymbol{x} = \boldsymbol{\varphi}(\boldsymbol{x}, t) \in \mathcal{S}$ at time t, with the deformation gradient $\boldsymbol{F}$. The anisotropic micro-structure of the material point $\boldsymbol{x}$ is rendered by two families of fibers with unit vectors $\boldsymbol{M}$ and $\boldsymbol{M}'$. Likewise, the anisotropic micro-structure of the spatial point $\boldsymbol{x}$ is described by $\boldsymbol{m}$ and $\boldsymbol{m}'$, as the spatial counterparts of $\boldsymbol{M}$ and $\boldsymbol{M}'$, respectively.

6.2 Motion and Deformation in an Anisotropic Continuum

Let $\mathcal{B} \subset \mathbb{R}^3$ be a solid body of interest in the reference configuration parametrized by the material point $\boldsymbol{x} \in \mathcal{B}$, while $\partial\mathcal{B} \subset \mathbb{R}^2$ denotes the boundary of the reference configuration $\mathcal{B} \subset \mathbb{R}^3$. The spatial configuration is denoted by $\mathcal{S} \subset \mathbb{R}^3$ with the spatial point $\boldsymbol{x} \in \mathcal{S}$, and its boundary $\partial\mathcal{S} \subset \mathbb{R}^2$. The bijective deformation map $\boldsymbol{\varphi}_t(\boldsymbol{x}) : \mathcal{B} \to \mathcal{S}$, at time $t \in \mathbb{R}^+$, maps a material point $\boldsymbol{x}$ onto a spatial point $\boldsymbol{x}$, i.e. $\boldsymbol{\varphi}_t(\boldsymbol{x}) : \boldsymbol{x} \mapsto \boldsymbol{x}$, see Fig. 6.2. Let $\boldsymbol{E}_I$ and $\boldsymbol{e}_i$ denote rectangular Cartesian base vectors in the reference and spatial configuration, respectively. The fundamental deformation measure, i.e. the deformation gradient, reads

$$\boldsymbol{F} = \nabla_{\mathbf{X}} \boldsymbol{\varphi}_t(\boldsymbol{x}), \tag{6.1}$$

mapping the unit tangent of a reference point onto its counterpart in the spatial configuration. The deformation gradient $\boldsymbol{F}$, its cofactor $\mathrm{cof}\boldsymbol{F} = J\boldsymbol{F}^{-\mathrm{T}}$, and its Jacobian $J = \det\boldsymbol{F}$ relate the deformation of the infinitesimal line ($\mathrm{d}\boldsymbol{x}$ and $\mathrm{d}\boldsymbol{x}$), area ($\mathrm{d}\boldsymbol{A}$ and $\mathrm{d}\boldsymbol{a}$), and volume ($\mathrm{d}V$ and $\mathrm{d}v$) elements, i.e.

$$\mathrm{d}\boldsymbol{x} = \boldsymbol{F}\mathrm{d}\boldsymbol{x}, \qquad \mathrm{d}\boldsymbol{a} = \mathrm{cof}\boldsymbol{F}\mathrm{d}\boldsymbol{A}, \qquad \mathrm{d}v = J\mathrm{d}V. \tag{6.2}$$

The deformations are non-penetrable for $J > 0$. Following Flory [52], one may decouple the deformation gradient $\boldsymbol{F} = \boldsymbol{F}_{\mathrm{vol}}\overline{\boldsymbol{F}}$ into its dilatational $\boldsymbol{F}_{\mathrm{vol}} = J^{1/3}\boldsymbol{I}$ and unimodular $\overline{\boldsymbol{F}} = J^{-1/3}\boldsymbol{F}$ parts. Subsequently, we introduce the right and left Cauchy-Green tensors

$$\boldsymbol{C} = \boldsymbol{F}^{\mathrm{T}}\boldsymbol{F}, \qquad \boldsymbol{b} = \boldsymbol{F}\boldsymbol{F}^{\mathrm{T}}, \tag{6.3}$$

in the reference and spatial configuration, respectively. Their unimodular parts are defined as $\overline{\boldsymbol{C}} = J^{-2/3}\boldsymbol{C}$ and $\overline{\boldsymbol{b}} = J^{-2/3}\boldsymbol{b}$. For an elaborate treatment see, e.g., Truesdell & Noll [220], Holzapfel [80], and Gurtin et al. [70]. Next, we exploit the representation theorem of invariants according to Spencer [208] and Holzapfel [80], and define the three irreducible isotropic invariants

$$I_1 = \mathrm{tr}(\boldsymbol{b}), \qquad I_2 = \frac{1}{2}\left[I_1^2 - \mathrm{tr}(\boldsymbol{b}^2)\right], \qquad I_3 = \det \boldsymbol{b} \tag{6.4}$$

reflecting the isotropic response of the solid and building up an integrity basis of $\boldsymbol{F}$, see Spencer [207]. Accordingly, the physically meaningful fourth and sixth invariants read

$$I_4 = \boldsymbol{m} \cdot \boldsymbol{m}, \qquad I_6 = \boldsymbol{m}' \cdot \boldsymbol{m}', \tag{6.5}$$

which capture the anisotropic response of the solid where $\boldsymbol{m} = \boldsymbol{F}\boldsymbol{M}$ and $\boldsymbol{m}' = \boldsymbol{F}\boldsymbol{M}'$ describe the spatial counterparts of the reference unit vectors $\boldsymbol{M}$ and $\boldsymbol{M}'$, as shown in Fig. 6.2. The corresponding unimodular forms of the aforementioned invariants read $\bar{I}_i = J^{-2/3} I_i$, where $i \in \{1, 2, 4, 6\}$. For the unimodular invariants describing anisotropy, the unimodular spatial vectors $\overline{\boldsymbol{m}} = \overline{\boldsymbol{F}}\boldsymbol{M}$ and $\overline{\boldsymbol{m}}' = \overline{\boldsymbol{F}}\boldsymbol{M}'$ are emphasized.

6.3 A Particular Form of the Model by Holzapfel et al. [83]

In the following we assume the existence of a Helmholtz free-energy function, say $\Psi = \hat{\Psi}(\ldots)$, with function-specific arguments. The *Q1P0* and the *Q1P0+AL* basically rely on the same constitutive equations where the multiplicative decomposition of $\boldsymbol{F} = \boldsymbol{F}_{\mathrm{vol}}\overline{\boldsymbol{F}}$ holds for both isotropic and anisotropic contributions. Hence, we may express the volumetric $U(J)$, the isotropic $\hat{\Psi}_{\mathrm{iso}}$ and the anisotropic $\hat{\Psi}_{\mathrm{ani}}$ parts as

$$\hat{\Psi}(\boldsymbol{F}, \boldsymbol{A}_{\boldsymbol{m}}, \boldsymbol{A}_{\boldsymbol{m}'}) = U(J) + \hat{\Psi}_{\mathrm{iso}}(\overline{\boldsymbol{F}}) + \hat{\Psi}_{\mathrm{ani}}(\overline{\boldsymbol{F}}, \overline{\boldsymbol{A}}_{\boldsymbol{m}}, \overline{\boldsymbol{A}}_{\boldsymbol{m}'}), \tag{6.6}$$

and the formulation for *Q1P0+WAS* reads

$$\hat{\Psi}(\boldsymbol{F}, \boldsymbol{A}_{\boldsymbol{m}}, \boldsymbol{A}_{\boldsymbol{m}'}) = U(J) + \hat{\Psi}_{\mathrm{iso}}(\overline{\boldsymbol{F}}) + \hat{\Psi}_{\mathrm{ani}}(\boldsymbol{F}, \boldsymbol{A}_{\boldsymbol{m}}, \boldsymbol{A}_{\boldsymbol{m}'}), \tag{6.7}$$

where we have introduced the Eulerian form of the structure tensors $\overline{\boldsymbol{A}}_{\boldsymbol{m}}$, $\overline{\boldsymbol{A}}_{\boldsymbol{m}'}$ and $\boldsymbol{A}_{\boldsymbol{m}}$, $\boldsymbol{A}_{\boldsymbol{m}'}$ as $\overline{\boldsymbol{A}}_{\boldsymbol{m}} = \overline{\boldsymbol{m}} \otimes \overline{\boldsymbol{m}}$, $\overline{\boldsymbol{A}}_{\boldsymbol{m}'} = \overline{\boldsymbol{m}}' \otimes \overline{\boldsymbol{m}}'$ and $\boldsymbol{A}_{\boldsymbol{m}} = \boldsymbol{m} \otimes \boldsymbol{m}$, $\boldsymbol{A}_{\boldsymbol{m}'} = \boldsymbol{m}' \otimes \boldsymbol{m}'$, respectively. Note that in (6.7) the multiplicative decomposition is solely used upon the isotropic response, while it is completely excluded from the fiber response.

The volumetric part can simply be chosen as

$$U(J) = \kappa(J - \ln J - 1), \tag{6.8}$$

whereas the isotropic part $\hat{\Psi}_{\mathrm{iso}}$ follows from the neo-Hookean material as (see, e.g., Ogden [156])

$$\hat{\Psi}_{\mathrm{iso}}(\overline{\boldsymbol{F}}) = \hat{\Psi}_{\mathrm{iso}}(\bar{I}_1) = \frac{\mu}{2}(\bar{I}_1 - 3). \tag{6.9}$$

In view of (6.6) the anisotropic part $\hat{\Psi}_{\mathrm{ani}}$ is a function of the unimodular invariants $\bar{I}_4$ and $\bar{I}_6$ such that

$$\hat{\Psi}_{\mathrm{ani}}(\overline{\boldsymbol{F}}, \overline{\boldsymbol{A}}_{\boldsymbol{m}}, \overline{\boldsymbol{A}}_{\boldsymbol{m}'}) = \hat{\Psi}_{\mathrm{ani}}(\bar{I}_4, \bar{I}_6) = \frac{\bar{k}_1}{2\bar{k}_2} \sum_{i=4,6} \{\exp[\bar{k}_2(\bar{I}_i - 1)^2] - 1\}, \tag{6.10}$$

as suggested by Holzapfel et al. [83]. However, for (6.7) $\hat{\Psi}_{\mathrm{ani}}$ becomes a function of the invariants I_4 and I_6, i.e.

$$\hat{\Psi}_{\mathrm{ani}}(\boldsymbol{F}, \boldsymbol{A}_{\boldsymbol{m}}, \boldsymbol{A}_{\boldsymbol{m}'}) = \hat{\Psi}_{\mathrm{ani}}(I_4, I_6) = \frac{k_1}{2k_2} \sum_{i=4,6} \{\exp[k_2(I_i - 1)^2] - 1\}. \tag{6.11}$$

In (6.8) κ denotes the bulk modulus, whereas μ refers to the shear modulus in (6.9). The anisotropic material parameters $\bar{k}_1$, $\bar{k}_2$ in (6.10) and k_1, k_2 in (6.11) represent a stress–like material parameter and a dimensionless parameter, respectively. In general, $\bar{k}_1$, $\bar{k}_2$ and k_1, k_2 are different from one another.

6.3.1 Stress expressions

From the Coleman–Noll procedure we arrive at the definition of the Kirchhoff stress tensor $\boldsymbol{\tau}$ according to

$$\boldsymbol{\tau} = 2\boldsymbol{F}(\partial_{\boldsymbol{C}}\hat{\Psi})\boldsymbol{F}^{\mathrm{T}} = \boldsymbol{\tau}_{\mathrm{vol}} + \boldsymbol{\tau}_{\mathrm{iso}} + \boldsymbol{\tau}_{\mathrm{ani}}, \tag{6.12}$$

where $\boldsymbol{\tau}_{\mathrm{vol}}$, $\boldsymbol{\tau}_{\mathrm{iso}}$, $\boldsymbol{\tau}_{\mathrm{ani}}$ represent the volumetric, isotropic and anisotropic terms associated with the Kirchhoff stress tensor. With the chain rule the volumetric and isotropic parts yield the forms

$$\boldsymbol{\tau}_{\mathrm{vol}} = 2\boldsymbol{F}[\partial_{\boldsymbol{C}}U(J)]\boldsymbol{F}^{\mathrm{T}} = \hat{p}\boldsymbol{I}, \qquad \boldsymbol{\tau}_{\mathrm{iso}} = 2\boldsymbol{F}[\partial_{\boldsymbol{C}}\hat{\Psi}_{\mathrm{iso}}(\overline{\boldsymbol{F}})]\boldsymbol{F}^{\mathrm{T}} = \mu\overline{\boldsymbol{b}} : \mathbb{P}, \tag{6.13}$$

where $\hat{p} = J\mathrm{d}U/\mathrm{d}J = \kappa(J-1)$, and the projection tensor is defined as $\mathbb{P} = \mathbb{I} - \frac{1}{3}(\boldsymbol{I} \otimes \boldsymbol{I})$ in which the symmetric fourth-order identity tensor $\mathbb{I}$ has the index form $(\mathbb{I})^{kl}_{ij} = \frac{1}{2}(\delta^k_i\delta^l_j + \delta^l_i\delta^k_j)$. It needs to be emphasized that a mean dilation approach in the context of the *Q1P0* formulation results in an averaged uniform pressure field, and a dilatation field over a finite element. Therefore, all volumetric responses essentially emerge on an element level instead of a constitutive level. It is also worth mentioning that all three formulations (*Q1P0*, *Q1P0+AL*, *Q1P0+WAS*) assume the same expressions for their volumetric and isotropic stress responses, as stated in (6.13). The mere difference originates from their distinct anisotropic constitutive forms. In fact, in case of *Q1P0* and *Q1P0+AL* the anisotropic Kirchhoff stress tensor $\boldsymbol{\tau}_{\mathrm{ani}}$ reads

$$\boldsymbol{\tau}_{\mathrm{ani}} = 2\boldsymbol{F}[\partial_{\boldsymbol{C}}\hat{\Psi}_{\mathrm{ani}}(\bar{I}_4, \bar{I}_6)]\boldsymbol{F}^{\mathrm{T}} = 2\bar{\psi}_4\overline{\boldsymbol{m}} \otimes \overline{\boldsymbol{m}} : \mathbb{P} + 2\bar{\psi}_6\overline{\boldsymbol{m}}' \otimes \overline{\boldsymbol{m}}' : \mathbb{P}, \tag{6.14}$$

where the deformation-dependent scalar coefficients are defined as $\bar{\psi}_4 = \partial_{\bar{I}_4}\hat{\Psi}_{\mathrm{ani}}(\bar{I}_4, \bar{I}_6)$ and $\bar{\psi}_6 = \partial_{\bar{I}_6}\hat{\Psi}_{\mathrm{ani}}(\bar{I}_4, \bar{I}_6)$. The counterpart of (6.14) for *Q1P0+WAS* is given by

$$\boldsymbol{\tau}_{\mathrm{ani}} = 2\boldsymbol{F}[\partial_{\boldsymbol{C}}\hat{\Psi}_{\mathrm{ani}}(I_4, I_6)]\boldsymbol{F}^{\mathrm{T}} = 2\psi_4\boldsymbol{m} \otimes \boldsymbol{m} + 2\psi_6\boldsymbol{m}' \otimes \boldsymbol{m}', \tag{6.15}$$

where the coefficients in this case read $\psi_4 = \partial_{I_4}\hat{\Psi}_{\rm ani}(I_4, I_6)$ and $\psi_6 = \partial_{I_6}\hat{\Psi}_{\rm ani}(I_4, I_6)$. The solution of nonlinear problems necessitates the consideration of spatial elasticity tensors which can be readily derived, see, e.g., [69, 80].

6.4 Representative Numerical Examples

We hereby touch upon the quasi-incompressible hyperelastic performances of the *Q1P0*, the *Q1P0+AL*, and the *Q1P0+WAS* formulations. Comparisons regarding the uniaxial extension tests are analyzed by considering three different sets of material parameters, as summarized in Table 6.1. The cases b and c provide stiffer constitutive responses than case a in the sense of anisotropy and isotropy, respectively. The final example presents a thick–walled cylindrical tube idealizing a single–layered hypothetical arterial tissue, which is extended, inflated and twisted simultaneously.

Table 6.1 Elastic material parameters used for the analysis of an anisotropic material for Sec. 6.4.1–6.4.3

Case a	$\kappa = 5000\,\text{kPa}$	$\mu = 10\,\text{kPa}$	$\bar{k}_1 = k_1 = 50\,\text{kPa}$	$\bar{k}_2 = k_2 = 2.0$
Case b	$\kappa = 5000\,\text{kPa}$	$\mu = 10\,\text{kPa}$	$\bar{k}_1 = k_1 = 500\,\text{kPa}$	$\bar{k}_2 = k_2 = 2.0$
Case c	$\kappa = 5000\,\text{kPa}$	$\mu = 100\,\text{kPa}$	$\bar{k}_1 = k_1 = 50\,\text{kPa}$	$\bar{k}_2 = k_2 = 2.0$

6.4.1 Numerical investigations of $Q1P0$, $Q1P0 + AL$, and $Q1P0 + WAS$ along a fiber direction

In order to scrutinize the constitutive responses associated with *Q1P0*, *Q1P0+AL*, and *Q1P0+WAS*, a simple unit cube discretized with 8 unstructured hexahedral elements is adopted, see Fig. 6.3. The isotropic ground matrix is reinforced by a single family of fibers with orientation $\boldsymbol{M}$ aligned in the x-direction, which is also the loading direction. Hence, the unit cube undergoes uniaxial extension. In order to better discuss the effect on the volumetric response, comparisons are analyzed by using two different sets of anisotropic material parameters (case a and case b), as provided in Table 6.1. The corresponding results are depicted in Fig. 6.3(a) and (b), respectively.

As far as the *Q1P0* study is concerned, both Fig. 6.3(a) and (b) indicate a tremendous increase of the Jacobian $J^{\rm avg}$ (averaged over the 8 finite elements; subsequently the index $(\bullet)^{\rm avg}$ stands for average) with respect to stretch λ_x for both sets of material parameters – solid curves with empty triangles in Fig. 6.3. It is evident that the anisotropic split creates a kind of 'competition' between the volumetric part and the anisotropic part through the minimization principle, thereby favoring an upsurge in the volumetric free energy, while diminishing the anisotropic contribution, which can be grasped by comparing $U^{\rm avg}$ with

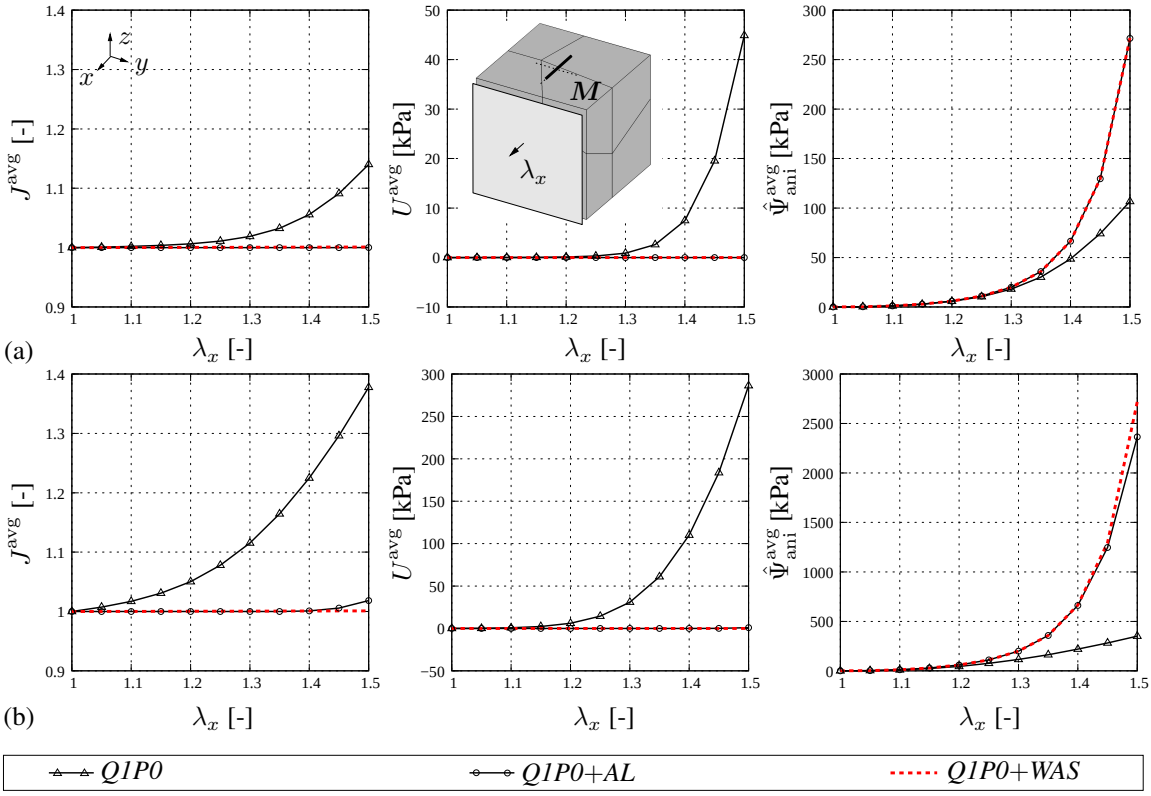

Figure 6.3 Uniaxial extension of a transversely isotropic material with a single family of fibers $\boldsymbol{M}$ aligned in the x-direction, the direction of the displacement-driven loading. The plots show the Jacobian J^{avg} averaged over 8 unstructured hexahedral elements, the average volumetric free energy U^{avg} (in kPa) and the average anisotropic free energy $\hat{\Psi}^{\text{avg}}_{\text{ani}}$ (in kPa) as a function of stretch λ_x. Results are obtained on the basis of: *Q1P0* (solid curve with empty triangles), *Q1P0+AL* (solid curve with empty circles), and the approach avoiding the multiplicative decomposition of $\boldsymbol{F}$ for the anisotropic contribution *Q1P0+WAS* (red dashed curve). The comparison is shown for two different sets of material parameters, namely for case a referring to (a) and for case b referring to (b), compare with Table 6.1.

$\hat{\Psi}^{\text{avg}}_{\text{ani}}$. In fact, high values of U^{avg} are essentially the result of the minimization principle preferring an increase in the volumetric response over the anisotropic one. This predicament can be overcome by applying either *Q1P0+AL* (solid curves with empty circles in Fig. 6.3) or *Q1P0+WAS* (red dashed curves in Fig. 6.3). Note that for *Q1P0+AL* we prescribe a maximum number of 20 augmented Lagrangian iterations for each incremental step which can also be increased in order to achieve a better performance for the case b.

6.4.2 Numerical investigations of $Q1P0$, $Q1P0 + AL$, and $Q1P0 + WAS$ along an isotropic direction

This benchmark is identical to that described in Sec. 6.4.1 in regard to geometry, structure and mesh data, see Fig. 6.4. Yet, the uniaxial extension is in this case applied in the y-direction, hence in an isotropic direction. As the comparison of anisotropic responses become trivial due to the setup of the problem, different isotropic responses are probed in line with two distinct sets of material parameters, cases a and c in Table 6.1. The corresponding results are depicted in Fig. 6.4(a) and (c), respectively.

In all two cases *Q1P0* (solid curves with empty triangles) and *Q1P0+WAS* (red dashed curves) yield identical results in regard to the average values of the Jacobian J^{avg}, the volumetric free energy U^{avg} and the isotropic free energy $\hat{\Psi}_{\text{iso}}^{\text{avg}}$, as expected. The other treatment *Q1P0+AL*, however, does not create any growth in volume, thereby providing the most physical response in a rigorous sense, see Fig. 6.4. Nonetheless, the volume growth associated with *Q1P0* and *Q1P0+WAS* is not pronounced and is minimal when compared with the enormous swelling for *Q1P0* in the previous example, see Fig. 6.3. As a result, the differences in the isotropic response are practically unnoticeable even at relatively large stretches λ_y. All treatments are able to yield, to a large extent, the relevant isotropic response.

6.4.3 Extension–inflation–torsion test for $Q1P0$, $Q1P0 + AL$, and $Q1P0 + WAS$

The aim of this benchmark test is to compare the formulations *Q1P0*, *Q1P0+AL*, and *Q1P0+WAS* in regard to how much the mechanical responses differ from each other under extreme loading conditions. To this end we consider a cylindrical tube as a single–layered hypothetical arterial tissue with the geometry provided in Fig. 6.5(a). The morphology renders anisotropy via two symmetric families of fibers $\boldsymbol{M}$ and $\boldsymbol{M}'$, where 40° is the angle between the fibers and the circumferential axis θ, see Fig. 6.5(c) and (d). The domain is discretized with 960 solid brick elements connected by 1320 nodes, see Fig. 6.5(b). As for loading, monotonically increasing displacements are applied on the top plane in the z–direction up to $\hat{u}_z = 2$ mm; an inner pressure growing up to $\hat{p}_{\text{i}} = 500\,\text{mmHg}$ is monotonically exerted on the inner layer of the tissue, while a monotonically increasing torsion is applied on the top plane reaching an angle of twist $\hat{\gamma} = 60^\circ$, as depicted in Fig. 6.5(a). Figure 6.5(a) also illustrates the boundary conditions, i.e. the displacements on the bottom plane are constrained along all three direction $\tilde{u}_x = \tilde{u}_y = \tilde{u}_z = 0$. For the purpose of comparison we only examine case b, see Table 6.1.

Figure 6.6 reveals dramatic differences in the Cauchy stress responses illustrated along the cylindrical coordinates r, θ and z. The *Q1P0* element formulation generates much lower stress components (σ_{rr}, $\sigma_{\theta\theta}$, σ_{zz}) since the anisotropic contribution, likewise in Fig. 6.3, is disfavored during the energy minimization process, see Fig. 6.6(a), which leads to relatively low stress components. This example ultimately pinpoints how predicted stress values become spurious under a supra-physiological loading scenario an arterial wall might undergo when a classical *Q1P0* finite element formulation is chosen. *Q1P0+WAS*

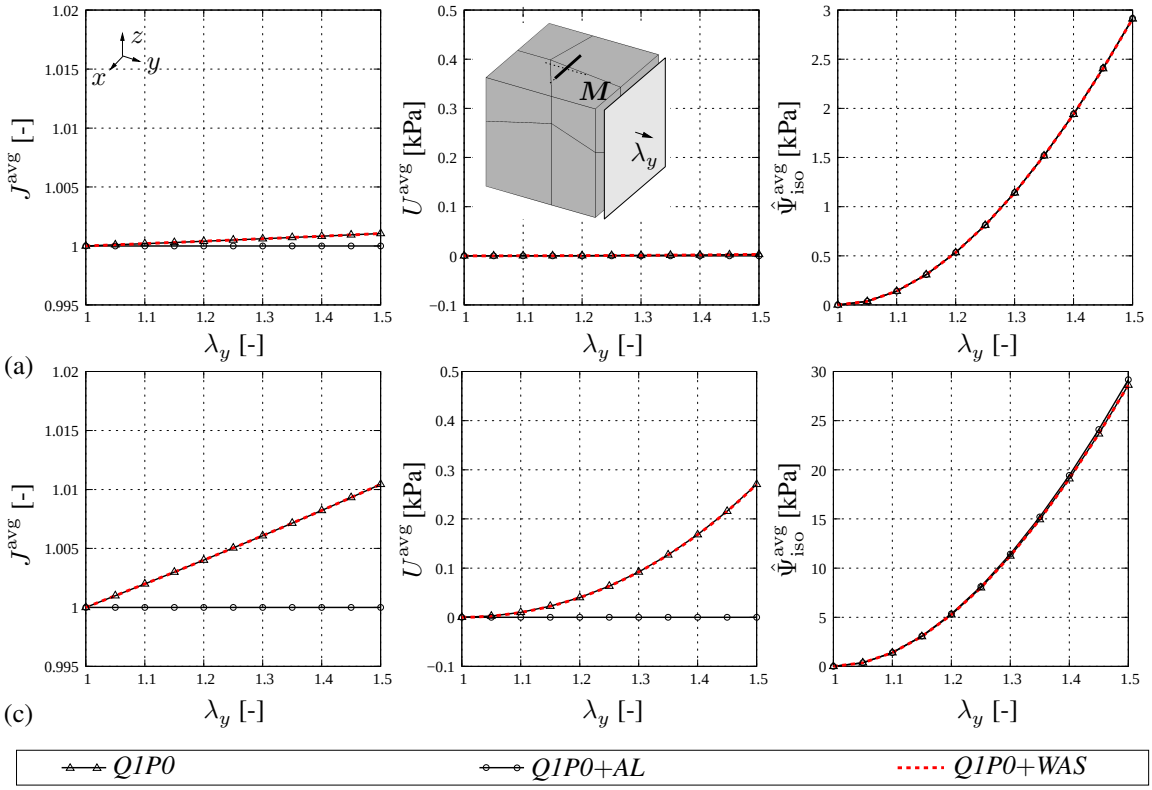

Figure 6.4 Uniaxial extension of a transversely isotropic material with a single family of fibers $\boldsymbol{M}$ aligned in the x-direction, with displacement-driven loading applied in the y-direction. The plots show the Jacobian J^{avg} averaged over 8 unstructured hexahedral elements, the average volumetric free energy U^{avg} (in kPa) and the average isotropic free energy $\hat{\Psi}^{\text{avg}}_{\text{iso}}$ (in kPa) as functions of stretch λ_y. Results are obtained on the basis of: *Q1P0* (solid curve with empty triangles), *Q1P0+AL* (solid curve with empty circles), and the approach avoiding the multiplicative decomposition of $\boldsymbol{F}$ for the anisotropic contribution *Q1P0+WAS* (red dashed curve). The comparison is shown for two different sets of material parameters, namely for case a referring to (a) and for case c referring to (c), compare with Table 6.1.

and *Q1P0+AL* yield very similar responses for this numerical example, with differences less than 5%, compare Fig. 6.6(b) with Fig. 6.6(c). It should also be highlighted that the maximum number of augmented Lagrangian iterations is set to 50 with the augmenting factor `augf` $= 5$ (see in FEAP [215]) in order to enforce incompressibility for *Q1P0+AL* in a strict sense. The augmented Lagrangian method in its turn leads to a major drawback, i.e. the computational time required to simulate the *Q1P0+AL* is around 20 minutes, while only 1 minute is needed for the *Q1P0+WAS*, rendering *Q1P0+WAS* nearly 20 times faster for the problem considered.

In addition, we briefly report on the computational performance of *Q1P0+WAS*; the

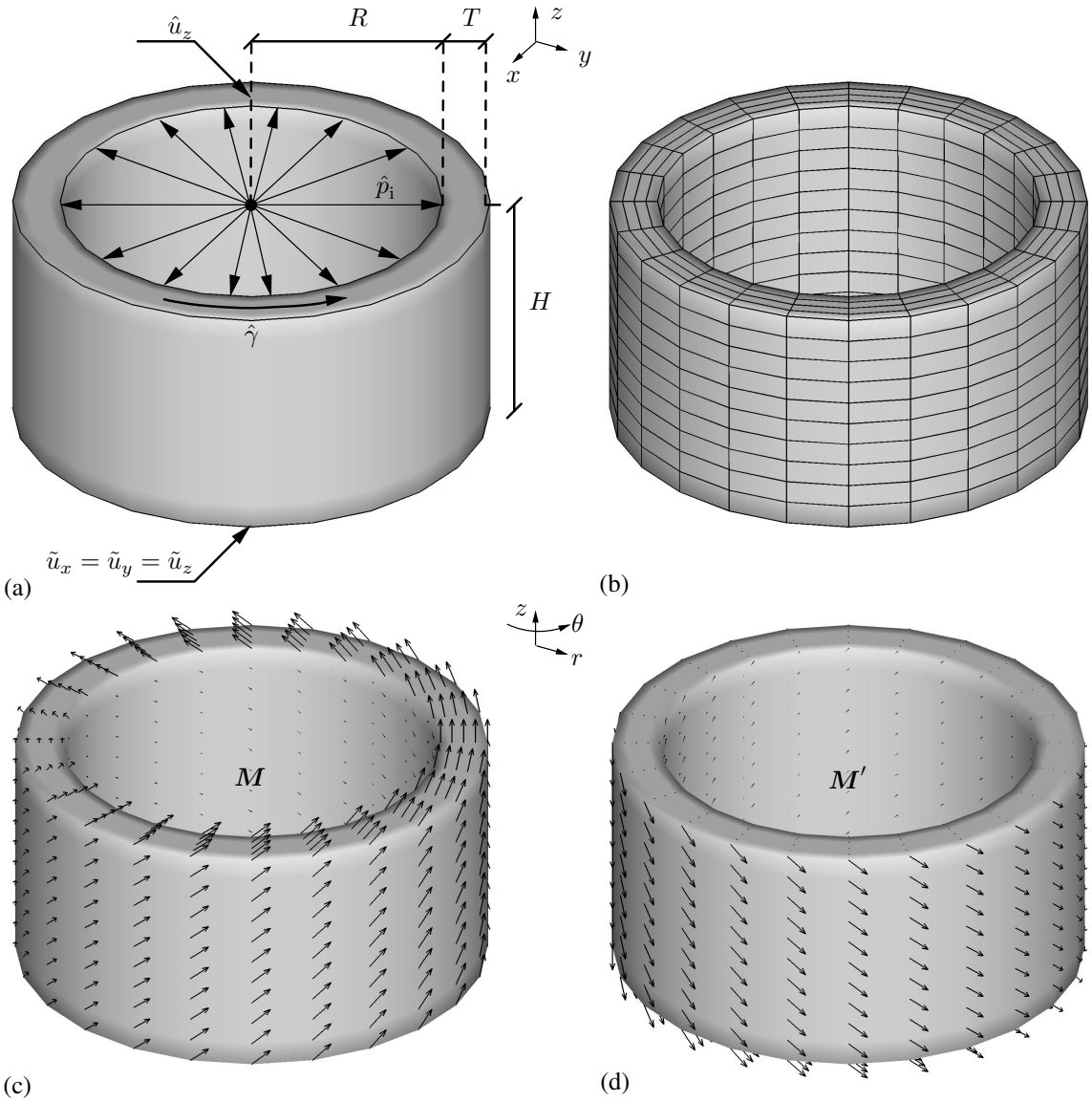

Figure 6.5 (a) Cylindrical tube with a hypothetical tissue and geometry with dimensions $H = 10$, $R = 8$, and $T = 2$ mm with related boundary and loading conditions $\tilde{u}_x = \tilde{u}_y = \tilde{u}_z = 0$ mm, $\hat{u}_z = 2$ mm, $\hat{p}_\mathrm{i} = 500$ mmHg and $\hat{\gamma} = 60^\circ$; (b) finite element mesh of the corresponding geometry; (c) visual representation of the first family of fibers $\boldsymbol{M}$ at each node; (d) visual representation of the second family of fibers $\boldsymbol{M}'$ at each node.

quadratic rate of convergence behavior at $t = 0.25$, 0.5, 0.75, and 1 s is summarized in Table 6.2. All simulations are carried out on a single 3.2 GHz Intel® Core™ i7-3930K CPU on a 64bit Linux operating system with 32GB RAM.

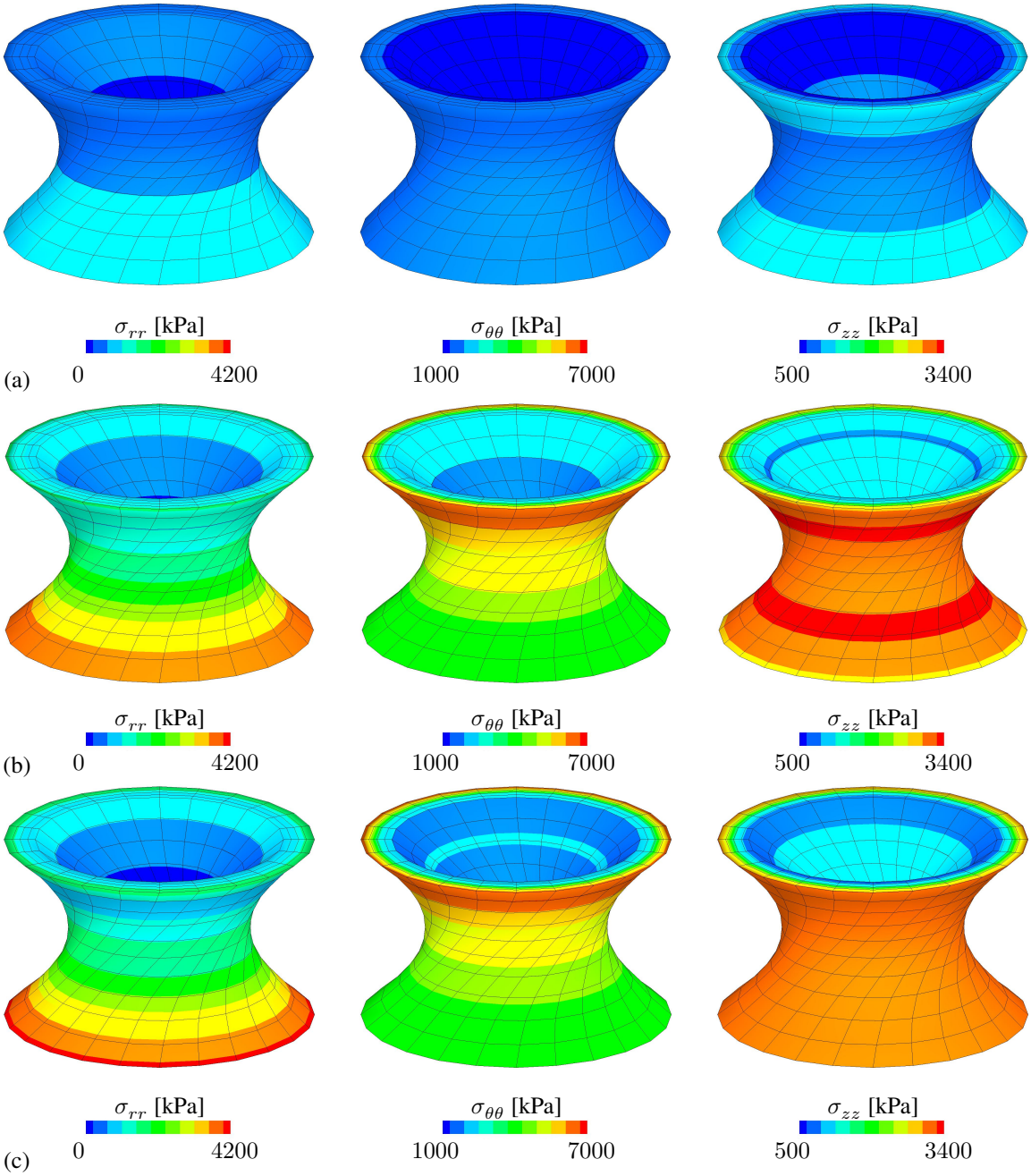

Figure 6.6 Distributions of the radial σ_{rr}, the circumferential $\sigma_{\theta\theta}$ and the axial σ_{zz} Cauchy stress components for (a) *Q1P0*; (b) *Q1P0+WAS*; (c) *Q1P0+AL*.

6.5 Summary and Concluding Remarks

Some important aspects in regard to physically relevant and computationally efficient analyses of fiber-reinforced materials were presented. Following an extensive literature

Table 6.2 Quadratic rate of convergence of the global residual for *Q1P0+WAS*, Sec. 6.4.3.

Time [s]	0.25	0.5	0.75	1.0
Iteration 1	2.004×E+03	2.931×E+03	6.224×E+03	1.638×E+04
Iteration 2	1.276×E+01	1.312×E+01	1.526×E+01	1.894×E+01
Iteration 3	2.223×E−01	1.027×E−03	1.230×E−03	2.146×E−03
Iteration 4	1.255×E−05	4.749×E−10	2.259×E−10	5.249×E−10
Number of iterations	4	4	4	4

overview, a brief theoretical synopsis of anisotropic hyperelasticity was provided. Subsequently, the numerical performance of the classical *Q1P0* element with and without the augmented Lagrangian method was examined together with a rather new concept introduced by Sansour [182] and Helfenstein et al. [75], who proposed the use of the (unsplit) deformation gradient tensor $\boldsymbol{F}$ for the anisotropic part of the constitutive equations. The results corroborate the new concept namely *Q1P0+WAS*.

Several anisotropic constitutive models presume quasi–incompressibility. Hence, there should be no discrepancy between the theoretical structure and the related numerical application. Having scrutinized the results in Fig. 6.3, 6.4, and 6.6 it is palpably shown that the concept *Q1P0+WAS* is able to generate quasi–incompressible responses which are in good conformity with those of *Q1P0+AL* even under extreme loading cases, as in Fig. 6.6. The feature through which *Q1P0+WAS* gains the upper hand over *Q1P0+AL* is the numerical efficiency. In fact, given the size of the mesh domain in Sec. 6.4.3, *Q1P0+WAS* appears to be approximately 20 times as fast as *Q1P0+AL*. It should be underlined that we also performed numerical studies with *Q1P0+WAS* using I_1 instead of $\bar{I}_1$ for the isotropic part. For this case almost the same stress results as in Fig. 6.6 were obtained with the quadratic rate of convergence behavior retained. Another credible aspect of *Q1P0+WAS* is that the formulation leads to a physical interpretation of the fiber stretches through I_4 and I_6. This allows exclusion of compressed fibers, a significant issue which may cause erroneous model considerations, as pointed out by Holzapfel & Ogden [88, 90].

At this point, we highlight that no systematic experimental data are yet available to substantiate or rebut incompressibility/compressibility of rupturing tissues. Moreover, enforcing incompressibility via an expedient method such as the augmented Lagrangian method often generates convergence issues with such highly inelastic constitutive responses. For recent investigations of the rupture behavior of aortic tissues we refer to Gültekin et al. [66, 67, 69] and references therein. For soft biological tissues, it is of utmost importance to carry out fast yet reliable numerical analyses which enable a precise validation of experimental data obtained *in vivo* or *ex vivo*. This will better inform and guide medical monitoring and rupture risk assessment of diseases such as aortic dissection, atherosclerosis and aneurysms.

Bibliography

[1] V. Alastrué, M. A. Martinez, M. Doblaré, and A. Menzel. Anisotropic micro–sphere–based finite elasticity applied to blood vessel modelling. *J. Mech. Phys. Solids*, 57:178–203, 2009.

[2] B. Alberts, A. Johnson, J. Lewis, M. Raff, K. Roberts, and P. Walter. *Molecular Biology of the Cell*. Garland Science, New York, 5th edition, 2008.

[3] M. Ambati, T. Gerasimov, and L. De Lorenzis. Phase-field modeling of ductile fracture. *Comput. Mech.*, 55:1017–1040, 2015.

[4] L. Amborosio and V. M. Tortorelli. Approximation of functionals depending on jumps by elliptic functionals via Γ-convergence. *Commun. Pure Appl. Math.*, 43:999–1036, 1990.

[5] T. L. Anderson. *Fracture Mechanics: Fundamentals and Applications*. CRC Press, Taylor & Francis Group, Boca Raton, FL, 3rd edition, 2005.

[6] A. N. Annaidh, M. Destrade, M. D. Gilchrist, and J. G. Murphy. Deficiencies in numerical models of anisotropic nonlinearly elastic materials. *Biomech. Model. Mechanobiol.*, 12:781–791, 2013.

[7] V. D. Azzi and S. W. Tsai. Anisotropic strength of composites. *Exp. Mech.*, 5:283–288, 1965.

[8] D. Balzani, S. Brinkhues, and G. A. Holzapfel. Constitutive framework for the modeling of damage in collagenous soft tissues with application to arterial walls. *Comput. Meth. Appl. Mech. Eng.*, 213–216:139–151, 2012.

[9] D. Balzani and M. Ortiz. Relaxed incremental variational formulation for damage at large strains with application to fiber-reinforced materials and materials with truss-like microstructures. *Int. J. Numer. Meth. Engng*, 92:551–570, 2012.

[10] T. Belytschko and L. P. Bindeman. Assumed strain stabilization of the eight node hexahedral element. *Comput. Meth. Appl. Mech. Eng.*, 105:225–260, 1993.

[11] T. Belytschko and T. Black. Elastic crack growth in finite elements with minimal remeshing. *Int. J. Numer. Meth. Engng*, 45:601–620, 1999.

[12] T. Belytschko, J. S.-J. Ong, W. K. Liu, and J. M. Kennedy. Hourglass controll in linear and nonlinear problems. *Comput. Meth. Appl. Mech. Eng.*, 43:251–276, 1984.

[13] J. E. Bischoff, E. M. Arruda, and K. Grosh. A microstructurally based orthotropic hyperelastic constitutive law. *J. Appl. Mech.*, 69:570–579, 2002.

[14] M. J. Borden, T. J. R. Hughes, C. M. Landis, A. Anvari, and I. J. Lee. A phase-field formulation for fracture in ductile materials: Finite deformation balance law derivation, plastic degradation, and stress triaxiality effects. *Comput. Meth. Appl. Mech. Eng.*, 312:130–166, 2016.

[15] M. J. Borden, T. J. R. Hughes, C. M. Landis, and C. V. Verhoosel. A higher-order phase-field model for brittle fracture: Formulation and analysis within the isogeometric analysis framework. *Comput. Meth. Appl. Mech. Eng.*, 273:100–118, 2014.

[16] M. J. Borden, C. V. Verhoosel, M. A. Scott, T. J. R. Hughes, and C. M. Landis. A phase-field description of dynamic brittle fracture. *Comput. Meth. Appl. Mech. Eng.*, 217–220:77–95, 2012.

[17] B. Bourdin, G. A. Francfort, and J.-J. Marigo. Numerical experiments in revisited brittle fracture. *J. Mech. Phys. Solids*, 48:797–826, 2000.

[18] B. Bourdin, G. A. Francfort, and J.-J. Marigo. *The Variational Approach to Fracture*. Springer-Verlag, Berlin, 2008.

[19] A. Braides. *Gamma-Convergence for Beginners*. Oxford University Press, New York, 2002.

[20] F. Brezzi and M. Fortin. *Mixed and Hybrid Finite Element Methods*. Springer-Verlag, New York, 1991.

[21] J. W. Cahn and J. E. Hilliard. Free energy of a nonuniform system. i. interfacial free energy. *J. Chem. Phys.*, 28:258–267, 1958.

[22] F. B. C. Cansız, H. Dal, and M. Kaliske. An orthotropic viscoelastic material model for passive myocardium: theory and algorithmic treatment. *Comput. Methods Biomech. Biomed. Engin.*, 18:1160–1172, 2015.

[23] F. Carreras, J. Garcia-Barnes, D. Gil, S. Pujadas, C. H. Li, R. Suarez-Arias, R. Leta, X. Alomar, M. Ballester, and G. Pons-Llado. Left ventricular torsion and longitudinal shortening: two fundamental components of myocardial mechanics assessed by tagged cine-MRI in normal subjects. *Int. J. Cardiovasc. Imaging*, 16:1–12, 2011.

[24] M. W. Carson and M. R. Roach. The strength of the aortic media and its role in the propagation of aortic dissection. *J. Biomech.*, 23:579–588, 1990.

[25] Y. S. Chatzizisis, A. Ü. Coşkun, M. Jonas, E. R. Edelman, C. L. Feldman, and P. H. Stone. Role of endothelial shear stress in the natural history of coronary atherosclerosis and vascular remodeling: molecular, cellular, and vascular behavior. *J. Am. Coll. Cardiol.*, 49:2379–2393, 2007.

[26] Z. Cheng, C. Riga, J. Chan, M. Hamady, N. B. Wood, N. J. W. Cheshire, Y. Xu, and R. G. J. Gibbs. Initial findings and potential applicability of computational simulation of the aorta in acute type B dissection. *J. Vasc. Surg.*, 57:35S–43S, 2013.

[27] K. J. Cherry and M. D. Dake. Chapter 31 - aortic dissection. In J. W. Hallett, J. L. Mills, J. J. Earnshaw, J. A. Reekers, and T. W. Rooke, editors, *Comprehensive Vascular and Endovascular Surgery*, pages 517 – 531. Mosby, Philadelphia, second edition, 2009.

[28] J. D. Clayton and J. Kanp. Phase field modeling of directional fracture in anisotropic polycrystals. *Comput. Mat. Sci.*, 98:158–169, 2015.

[29] W. D. Clouse, Jr J. W. Hallett, H. V. Schaff, P. C. Spittell, C. M. Rowland, D. M. Ilstrup, and L. J. Melton. Acute aortic dissection. *Mayo Clin. Proc.*, 79:176–180, 2004.

[30] B. D. Coleman and M. E. Gurtin. Thermodynamics with internal state variables. *J. Chem. Phys.*, 47:597–613, 1967.

[31] B. A. Coppola and J. H. Omens. Role of tissue structure on ventricular wall mechanics. *Mech. Chem. Biosyst.*, 5:183–196, 2008.

[32] K. D. Costa, J. W. Holmes, and A. D. McCulloch. Modeling cardiac mechanical properties in three dimensions. *Phil. Trans. R. Soc. Lond. A*, 359:1233–1250, 2001.

[33] K. D. Costa, P. J. Hunter, J. S. Wayne, L. K. Waldman, J. M. Guccione, and A. D. McCulloch. A three-dimensional finite element method for large elastic deformations of ventricular mycardium: II–Prolate spheroidal coordinates. *J. Biomech. Eng.*, 118:464–472, 1996.

[34] J. W. Covell. Tissue structure and ventricular wall mechanics. *Circulation*, 118:699–701, 2008.

[35] F. J. Criado. Aortic dissection: a 250-year perspective. *Tex. Heart Inst. J.*, 38:694–700, 2011.

[36] K. S. Cunningham and A. I. Gotlieb. The role of shear stress in the pathogenesis of atherosclerosis. *Lab. Invest.*, 85:9–23, 2005.

[37] H. Dal and M. Kaliske. A micro-continuum-mechanical material model for failure of rubber-like materials: Application to aging-induced fracturing. *J. Mech. Phys. Solids*, 57:1340–1356, 2009.

[38] A. Delfino, N. Stergiopulos, J. E. Moore Jr., and J.-J. Meister. Residual strain effects on the stress field in a thick wall finite element model of the human carotid bifurcation. *J. Biomech.*, 30:777–786, 1997.

[39] H. Demiray. A note on the elasticity of soft biological tissues. *J. Biomech.*, 5:309–311, 1972.

[40] H. Demiray and R. P. Vito. A layered cylindrical shell model for an aorta. *Int. J. Eng. Sci.*, 29:47–54, 1991.

[41] S. Dokos, B. H. Smaill, A. A. Young, and I. J. LeGrice. Shear properties of passive ventricular myocardium. *Am. J. Physiol.*, 283:H2650–H2659, 2002.

[42] T. C. Doyle and J. L. Ericksen. Nonlinear elasticity. In H. L. Dryden and T. von Kármán, editors, *Advances in Applied Mechanics*, volume 4, pages 53–116. Academic Press, New York, 1956.

[43] D. W. Dunning, J. K. Kahn, E. T. Hawkins, and W. W. O'Neill. Iatrogenic coronary artery dissections extending into an involving the aortic root. *Catheter Cardiovasc. Interv.*, 51:387–393, 2000.

[44] A. Düster, S. Hartmann, and E. Rank. p–FEM applied to fininte isotropic hyperelastic bodies. *Comput. Meth. Appl. Mech. Eng.*, 192:5147–5166, 2003.

[45] W. Ehlers and G. Eipper. The simple tension problem at large volumetric strains computed from finite hyperelastic material laws. *Acta Mech.*, 130:17–27, 1998.

[46] F. Erdoğan and G. C. Sih. On the crack extension in plates under plane loading and transverse shear. 85:519–525, 1963.

[47] T. S. E. Eriksson, A. J. Prassl, G. Plank, and G. A. Holzapfel. Influence of myocardial fiber/sheet orientations on left ventricular mechanical contraction. *Math. Mech. Solids*, 18:592–606, 2013.

[48] T. S. E. Eriksson, A. J. Prassl, G. Plank, and G. A. Holzapfel. Modeling the dispersion in electro-mechanically coupled myocardium. *Int. J. Numer. Method Biomed. Eng.*, 29:1267–1284, 2013.

[49] A. C. Eringen. *Nonlinear Theory of Continuous Media*. McGraw-Hill Book Company, Inc., New York, 1962.

[50] A. Ferrara and A. Pandolfi. Numerical modeling of fracture in human arteries. *Comput. Methods Biomech. Biomed. Engin.*, 11:553–567, 2008.

[51] A. Ferrara and A. Pandolfi. A numerical study of arterial media dissection processes. *Int. J. Fracture*, 166:21–33, 2010.

[52] P. J. Flory. Thermodynamic relations for highly elastic materials. *Trans. Faraday Soc.*, 57:829–838, 1961.

[53] G. Fomovsky, S. Thomopoulos, and J. W. Holmes. Contribution of extracellular matrix to the mechanical properties of the heart. *J. Mol. Cell Cardiol.*, 48:490–496, 2010.

[54] G. A. Francfort and J.-J. Marigo. Revisiting brittle fracture as an energy minimization problem. *J. Mech. Phys. Solids*, 46:1319–1342, 1998.

[55] Y. C. Fung. *Biomechanics. Mechanical Properties of Living Tissues*. Springer-Verlag, New York, 2nd edition, 1993.

[56] Y. C. Fung, K. Fronek, and P. Patitucci. Pseudoelasticity of arteries and the choice of its mathematical expression. *Am. J. Physiol.*, 237:H620–H631, 1979.

[57] T. C. Gasser and G. A. Holzapfel. Modeling the propagation of arterial dissection. *Eur. J. Mech. A/Solids*, 25:617–633, 2006.

[58] T. C. Gasser, R. W. Ogden, and G. A. Holzapfel. Hyperelastic modelling of arterial layers with distributed collagen fibre orientations. *J. R. Soc. Interface*, 3:15–35, 2006.

[59] R. Glowinski and P. LeTallec. Finite element analysis in nonlinear incompressible elasticity. In J. T. Oden and G. F. Carey, editors, *Finite elements, Special Problems in Solid Mechanics*, volume V. Prentice-Hall, Englewood Cliffs, New Jersey, 1984.

[60] R. Glowinski and P. LeTallec. *Augmented Lagrangian and Operator Splitting Methods in Nonlinear Mechanicss*. SIAM, Philadelphia, 1989.

[61] S. Göktepe. *Micro–macro approaches to rubbery and glassy polymers: Predictive micromechanically–based models and simulations*. PhD thesis, University of Stuttgart, 2007.

[62] S. Göktepe, S. N. S Acharya, J. Wong, and E. Kuhl. Computational modeling of passive myocardium. *Commun. Numer. Methods Eng.*, 27:1–14, 2011.

[63] A. A. Griffith. The phenomena of rupture and flow in solids. *Phil. Trans. R. Soc. Lond. A*, 221:163–197, 1921.

[64] J. M. Guccione, A. D. McCulloch, and L. K. Waldman. Passive material properties of intact ventricular myocardium determined from a cylindrical model. *J. Biomech. Eng.*, 113:42–55, 1991.

[65] O. Gültekin. A Phase Field Approach to the Fracture of Anisotropic Medium. Master's thesis, University of Stuttgart, Institute of Applied Mechanics (CE), Pfaffenwaldring 7, Stuttgart, 2014.

[66] O. Gültekin, H. Dal, and G. A. Holzapfel. A phase-field approach to model fracture of arterial walls: theory and finite element analysis. *Comput. Meth. Appl. Mech. Eng.*, 312:542–566, 2016.

[67] O. Gültekin, H. Dal, and G. A. Holzapfel. Numerical aspects of anisotropic failure in soft biological tissues favor energy-based criteria: A rate-dependent anisotropic crack phase-field model. *Comput. Meth. Appl. Mech. Eng.*, 331:23–52, 2018.

[68] O. Gültekin, S. P. Hager, H. Dal, and G. A. Holzapfel. Computational modeling of progressive damage and rupture in fibrous biological tissues: Application to aortic dissection. *Biomech. Model. Mechanobiol.* submitted.

[69] O. Gültekin and G. A. Holzapfel. A brief review on computational modeling of rupture in soft biological tissues. In O. Oñate, D. Peric, E. de Souza Neto, and M. Chiumenti, editors, *Advances in Computational Plasticity. A book in Honour of D. R. J. Owen*, volume 46, pages 113–144. Springer, Berlin, 2018.

[70] M. E. Gurtin, E. Fried, and L. Anand. *The Mechanics and Thermodynamics of Continua*. Cambridge University Press, New York, 2010.

[71] M. F. Hadi, E. A. Sander, and V. H. Barocas. Multiscale model predicts tissue-level failure from collagen fiber-level damage. *J. Biomech. Eng.*, 134:1–10, 2012.

[72] V. Hakim and A. Karma. Laws of crack motion and phase-field models of fracture. *J. Mech. Phys. Solids*, 57:342–368, 2009.

[73] Z. Hashin. Failure criteria for unidirectional fiber composites. *J. Appl. Mech.*, 47:329–334, 1980.

[74] U. Heisserer, S. Hartmann, A. Düster, and Z. Yosibash. On volumetric locking–free behaviour of p–version finite ele ments under finite deformations. *Commun. Numer. Methods Eng.*, 24:1019–1032, 2008.

[75] J. Helfenstein, M. Jabareen, E. Mazza, and S. Govindjee. On non-pyhsical response in models for fiber-reinforced hyperelastic materials. *Int. J. Solids Structures*, 47:2056–2061, 2010.

[76] C. Herring. Some theorems on the free energies of crystal surfaces. *Phys. Rev.*, 82:87–93, 1951.

[77] R. Hill. A theory of the yielding and plastic flow of anisotropic metals. *Proc. R. Soc. Lond. A*, 193:281–297, 1948.

[78] M. Hofacker and C. Miehe. A phase-field model of dynamic fracture: robust field updates for the analysis of complex crack patterns. *Int. J. Numer. Meth. Engng*, 93:276–301, 2013.

[79] G. A. Holzapfel. On large strain viscoelasticity: Continuum formulation and finite element applications to elastomeric structures. *Int. J. Numer. Meth. Engng*, 39:3903–3926, 1996.

[80] G. A. Holzapfel. *Nonlinear Solid Mechanics. A Continuum Approach for Engineering*. John Wiley & Sons, Chichester, 2000.

[81] G. A. Holzapfel. Structural and numerical models for the (visco)elastic response of arterial walls with residual stresses. In G. A. Holzapfel and R. W. Ogden, editors, *Biomechanics of Soft Tissue in Cardiovascular Systems*, pages 109–184, Wien, New York, 2003. Springer-Verlag. CISM Courses and Lectures no. 441.

[82] G. A. Holzapfel and T. C. Gasser. A viscoelastic model for fiber-reinforced composites at finite strains: Continuum basis, computational aspects and applications. *Comput. Meth. Appl. Mech. Eng.*, 190:4379–4403, 2001.

[83] G. A. Holzapfel, T. C. Gasser, and R. W. Ogden. A new constitutive framework for arterial wall mechanics and a comparative study of material models. *J. Elasticity*, 61:1–48, 2000.

[84] G. A. Holzapfel, T. C. Gasser, and M. Stadler. A structural model for the viscoelastic behavior of arterial walls: Continuum formulation and finite element analysis. *Eur. J. Mech. A/Solids*, 21:441–463, 2002.

[85] G. A. Holzapfel, J. A. Niestrawska, R. W. Ogden, A. J. Reinisch, and A. J. Schriefl. Modelling non-symmetric collagen fibre dispersion in arterial walls. *J. R. Soc. Interface*, 12:20150188, 2015.

[86] G. A. Holzapfel and R. W. Ogden. Constitutive modelling of passive myocardium: a structurally based framework for material characterization. *Phil. Trans. R. Soc. Lond. A*, 367:3445–3475, 2009.

[87] G. A. Holzapfel and R. W. Ogden. Constitutive modelling of arteries. *Proc. R. Soc. Lond. A*, 466:1551–1597, 2010.

[88] G. A. Holzapfel and R. W. Ogden. On the tension–compression switch in soft fibrous solids. *Eur. J. Mech. A/Solids*, 49:561–569, 2015.

[89] G. A. Holzapfel and R. W. Ogden. Comparison of two model frameworks for fiber dispersion in the elasticity of soft biological tissues. *Eur. J. Mech. A/Solids*, 66:193–200, 2017.

[90] G. A. Holzapfel and R. W. Ogden. On fiber dispersion models: exclusion of compressed fibers and spurious model comparisons. *J. Elasticity*, 129:49–68, 2017.

[91] G. A. Holzapfel, G. Sommer, C. T. Gasser, and P. Regitnig. Determination of layer-specific mechanical properties of human coronary arteries with non-atherosclerotic intimal thickening, and related constitutive modeling. *Am. J. Physiol. Heart Circ. Physiol.*, 289:H2048–2058, 2005.

[92] G. A. Holzapfel, G. Sommer, and P. Regitnig. Anisotropic mechanical properties of tissue components in human atherosclerotic plaques. *J. Biomech. Eng.*, 126:657–665, 2004.

[93] L. Horný, M. Netušil, and T. Voňavková. Axial prestretch and circumferential distensibility in biomechanics of abdominal aorta. *Biomech. Model. Mechanobiol.*, 13:783–799, 2014.

[94] D. P. Howard, A. Banerjee, J. F. Fairhead, J. J. Perkins, L. E. Silver, P. M. Rothwell, and Oxford Vascular Study. Population-based study of incidence and outcome of acute aortic dissection and premorbid risk factor control: 10-year results from the oxford vascular study. *Circulation*, 20:2031–2037, 2013.

[95] T. J. R. Hughes. *The Finite Element Method: Linear Static and Dynamic Finite Element Analysis*. Dover, New York, 2000.

[96] T. J. R. Hughes and J. Winget. Finite rotation effects in numerical integration of rate constitutive equations arising in large-deformation analysis. *Int. J. Numer. Meth. Engng*, 15:1413–1418, 1980.

[97] J. D. Humphrey. *Cardiovascular Solid Mechanics. Cells, Tissues, and Organs*. Springer-Verlag, New York, 2002.

[98] J. D. Humphrey. Possible mechanical roles of glycosaminoglycans in thoracic aortic dissection and associations with dysregulated transforming growth factor-β. *J. Vasc. Res.*, 50:1–10, 2013.

[99] J. D. Humphrey and G. A. Holzapfel. Mechanics, mechanobiology, and modeling of human abdominal aorta and aneurysms. *J. Biomech.*, 45:805–814, 2012.

[100] J. D. Humphrey, R. K. Strumpf, and F. C. P. Yin. Determination of a constitutive relation for passive myocardium: I. A new functional form. *J. Biomech. Eng.*, 112:333–339, 1990.

[101] J. D. Hutcheson, C. Goettsch, S. Bertazzo, N. Maldonado, J. L. Ruiz, W. Goh, K. Yabusaki, T. Faits, C. Bouten, G. Franck, T. Quillard, P. Libby, M. Aikawa, S. Weinbaum, and E. Aikawa. Genesis and growth of extracellular-vesicle-derived microcalcification in atherosclerotic plaques. *Nat. Mater.*, 15:335–343, 2016.

[102] J. W. Hutchinson and Z. Suo. Mixed mode cracking in layered materials. *Adv. in Appl. Math.*, 29:63–191, 1991.

[103] J. M. Huyghe, T. Arts, D. H. van Campen, and R. S. Reneman. Porous medium finite element model of the beating left ventricle. *Am. J. Physiol. Heart Circ. Physiol.*, 262:H1256–H1267, 1992.

[104] J. M. Huyghe, D. H. van Campen, T. Arts, and R. M. Heethaar. The constitutive behaviour of passive heart muscle tissue. A quasi-linear viscoelastic formulation. *J. Biomech.*, 24:841–849, 1991.

[105] C. E. Inglis. Stresses in a plate due to presence of cracks and sharp corners. *Trans. Inst. Naval Archt.*, 55:219–241, 1913.

[106] G. R. Irwin. Fracture dynamics. In *Fracturing of Metals*, pages 147–166, Cleveland, OH, 1948. American Society for Metals.

[107] G. R. Irwin. Onset of fast crack propagation inhigh strength steel and aluminum alloys. *Sagamore Research Conference Proceedings*, 2:289–305, 1956.

[108] G. R. Irwin. Fracture mechanics. In J. N. Goodier and N. J. Hoff, editors, *Structural Mechanics*, pages 557–594, New York, 1960. Pergamon Press.

[109] L. M. Kachanov. Time of the rupture process under creep conditions. *Izvestija Akademii Nauk Sojuza Sovetskich Socialisticeskich Respubliki (SSSR) Otdelenie Techniceskich Nauk (Moskra)*, 8:26–31, 1958.

[110] L. M. Kachanov. *Introduction to Continuum Damage Mechanics*. Martinus Nijhoff Publishers, Dordrecht, The Netherlands, 1986.

[111] W. J. Karlon, J. W. Covell, A. D. McCulloch, J. J. Hunter, and J. H. Omens. Automated measurement of myofiber disarray in transgenic mice with ventricular expression of ras. *Anat. Rec.*, 252:612–625, 1998.

[112] W. J. Karlon, A. D. McCulloch, J. W. Covell, J. J. Hunter, and J. H. Omens. Regional dysfunction correlates with myofiber disarray in transgenic mice with ventricular expression of ras. *Am. J. Physiol. Heart Circ. Physiol.*, 278:H898–906, 2000.

[113] W.L. Kenney, J. H. Wilmore, and D. L. Costill. *Physiology of Sport and Exercise*. Human kinetics, Champaign, IL, 2015.

[114] I. A. Khan and C. K. Nair. Clinical, diagnostic, and management perspectives of aortic dissection. *Chest*, 122:311–328, 2002.

[115] J. H. Kim, S. Avril, A. Duprey, and J. P. Favre. Experimental characterization of rupture in human aortic aneurysms using a full-field measurement technique. *Biomech. Model. Mechanobiol.*, 11:841–853, 2012.

[116] M. Kroon and G. A. Holzapfel. A model for saccular cerebral aneurysm growth by collagen fibre remodelling. *J. Theor. Biol.*, 247:775–787, 2007.

[117] J. K. Lee, L. Yao, C. T. Phelps, C. R. Wirth, J. Czajka, and J. Lozman. Anterior cruciate ligament tears: MR imaging compared with arthroscopy and clinical tests. *Radiology*, 166:861–864, 1988.

[118] I. J. LeGrice, B. H. Smaill, L. Z. Chai, S. G. Edgar, J. B. Gavin, and P. J. Hunter. Laminar structure of the heart: Ventricular myocyte arrangement and connective tissue architecture in the dog. *Am. J. Physiol. Heart Circ. Physiol.*, 269:H571–H582, 1995.

[119] X. Leng, B. Zhou, X. Deng, L. Davis, S. M. Lessner, M. A. Sutton, and T. Shazly. Experimental and numerical studies of two arterial wall delamination modes. *J. Mech. Behav. Biomed. Mater.*, 77:321–330, 2018.

[120] P. N. Lewis, C. Pinali, R. D. Young, K. M. Meek, A. J. Quantock, and C. Knupp. Structural interactions between collagen and proteoglycans are elucidated by three–dimensional electron tomography of bovine cornea. *Structure*, 18:239–245, 2010.

[121] B. Li, C. Peco, D. Millán, I. Arias, and M. Arroyo. Phase-field modeling and simulation of fracture in brittle materials with strongly anisotropic surface energy. *Int. J. Numer. Meth. Engng*, 102:711–727, 2015.

[122] P. Libby, P. M. Ridker, and G. K. Hansson. Progress and challenges in translating the biology of atherosclerosis. *Nature*, 473:317–325, 2011.

[123] C. Linder and F. Armero. Finite elements with embedded branching. *Finite Elem. Anal. Des.*, 45:280–293, 2009.

[124] L. Löffler and K. Sagawa. A one-dimensional viscoelastic model of cat heart muscle studied by small length perturbations during isometric contraction. 36:498–512, 1975.

[125] J. Lubliner. A model of rubber viscoelasticity. *Mech. Res. Commun.*, 12:93–99, 1985.

[126] P. G. Malvindi, S. Pasta, G. M. Raffa, and S. Livesey. Computational fluid dynamics of the ascending aorta before the onset of type A aortic dissection. *Eur. J. Cardiothorac.*, 51:597–599, 2016.

[127] S. S. Mao, N. Ahmadi, B. Shah, D. Beckmann, A. Chen, L. Ngo, F. R. Flores, Y. L. Gao, and M. J. Budoff. Normal thoracic aorta diameter on cardiac computed tomography in helathy asymptomatic adult: Impact of age and gender. *Academic Radiology*, 15:827–834, 2008.

[128] J. E. Marsden and T. J. R. Hughes. *Mathematical Foundations of Elasticity*. Dover, New York, 1994.

[129] MATLAB. R2010a, The Mathworks Inc., Natick, MA, USA, 2010.

[130] MATLAB. R2016a, The Mathworks Inc., Natick, MA, USA, 2016.

[131] H. W. Haslach, Jr., A. Siddiqui, A. Weerasooriya, R. Nguyen, J. Roshgadol, N. Monforte, and E. McMahon. Fracture mechanics of shear crack propagation and dissection in healthy bovine descending aortic media. *Acta Biomater.*, 68:53–66, 2018.

[132] D. D. Streeter, Jr., H. M. Spotnitz, D. P. Patel, J. Ross, Jr., and E. H. Sonnenblick. Fibre orientation in the canine left ventricle during diastole and systole. *Circ. Res.*, 24:339–347, 1969.

[133] C. Miehe. Aspects of the formulation and finite element implementation of large strain isotropic elasticity. *Int. J. Numer. Meth. Engng*, 37:1981–2004, 1994.

[134] C. Miehe. Discontinuous and continuous damage evolution in ogden-type large-strain elastic materials. *Eur. J. Mech. A/Solids*, 14:697–720, 1995.

[135] C. Miehe. Numerical computation of algorithmic (consistent) tangent moduli in large-strain computational inelasticity. *Comput. Meth. Appl. Mech. Eng.*, 134:223–240, 1996.

[136] C. Miehe. A multi-field incremental variational framework for gradient-extended standard dissipative solids. *J. Mech. Phys. Solids*, 59:898–923, 2011.

[137] C. Miehe. Theoretical and computational mechanics at large strains. Lecture Notes, University of Stuttgart, 2012.

[138] C. Miehe, H. Dal, L.-M. Schänzel, and A. Raina. A phase-field model for chemo-mechanical induced fracture in lithium-ion battery electrode particles. *Int. J. Numer. Meth. Engng*, 106:683–711, 2016.

[139] C. Miehe, M. Hofacker, L.-M. Schänzel, and F. Aldakheel. Phase field modeling of fracture in multi-physics problems. Part II. Coupled brittle-to-ductile failure criteria and crack propagation in thermo-elastic-plastic solids. *Comput. Meth. Appl. Mech. Eng.*, 294:486–522, 2015.

[140] C. Miehe, M. Hofacker, and F. Welschinger. A phase field model for rate-independent crack propagation: Robust algorithmic implementation based on operator splits. *Comput. Meth. Appl. Mech. Eng.*, 199:2765–2778, 2010.

[141] C. Miehe and L.-M. Schänzel. Phase field modeling of fracture in rubbery polymers. Part I. Finite elasticity coupled with brittle fracture. *J. Mech. Phys. Solids*, 65:93–113, 2014.

[142] C. Miehe, L.-M. Schänzel, and H. Ulmer. Phase field modeling of fracture in multi-physics problems. Part I. Balance of crack surface and failure criteria for brittle crack propagation in thermo-elastic solids. *Comput. Meth. Appl. Mech. Eng.*, 294:449–485, 2015.

[143] C. Miehe, F. Welschinger, and M. Hofacker. Thermodynamically consistent phase-field models of fracture: Variational principles and multi-field FE implementations. *Int. J. Numer. Meth. Engng*, 83:1273–1311, 2010.

[144] A. Mielke and T. Roubíček. Rate–independent damage process in nonlinear elasticity. *Math. Models Methods Appl. Sci.*, 16:177–209, 2006.

[145] N. Moës and T. Belytschko. Extended finite element method for cohesive crack growth. *Engr. Fracture Mech.*, 69:813–833, 2002.

[146] N. Moës, J. Dolbow, and T. Belytschko. A finite element method for crack growth without remeshing. *Int. J. Numer. Meth. Engng*, 46:131–150, 1999.

[147] J. J. Moré and D. C. Sorensen. Computing a trust region step. *SIAM J. Sci. Statist. Comput.*, 4:553–572, 1983.

[148] L. Mullins. Effect of stretching on the properties of rubber. *J. Rubber Research*, 16:275–289, 1947.

[149] D. Mumford and J. Shah. Optimal approximations by piecewise smooth functions and associated variational problems. *Commun. Pure Appl. Math.*, 42:577–685, 1989.

[150] F. F. Mussa, J. D. Horton, R. Moridzadeh, J. Nicholson, S. Trimarichi, and K. A. Eagle. Acute aortic dissection and intramural hematoma: A systematic review. *J. Am. Med. Assoc.*, 316:754–763, 2016.

[151] J. C. Nagtegaal, D. M. Parks, and J. R. Rice. On numerically accurate finite element solutions in the fully plastic range. *Comput. Meth. Appl. Mech. Eng.*, 4:153–177, 1974.

[152] T.-T. Nguyen, J. Réthéro, J. Yvonnet, and M.C. Baietto. Multi-phase-field modeling of anisotropic crack propagation for polycrystalline materials. *Comput. Mech.*, 60:289–314, 2017.

[153] P. M. F. Nielsen, I. J. LeGrice, B. H. Smaill, and P. J. Hunter. Mathematical model of geometry and fibrous structure of the heart. *Am. J. Physiol. Cell Physiol.*, 260:H1365–H1378, 1991.

[154] C. Noble, O. van der Sluis, R. M. J. Voncken, O. Burke, S. E. Franklin, R. Lewis, and Z. A. Taylor. Simulation of arterial dissection by a penetrating external body using cohesive zone modelling. *J. Mech. Behav. Biomed. Mater.*, 71:95–105, 2017.

[155] D. R. Nolan, A. L. Gower, M. Destrade, R. W. Ogden, and J. P. McGarry. A robust anisotropic hyperelastic formulation for the modelling of soft tissue. *J. Mech. Behav. Biomed. Mater.*, 39:48–60, 2014.

[156] R. W. Ogden. *Non-linear Elastic Deformations*. Dover, New York, 1997.

[157] R. W. Ogden. Anisotropy and nonlinear elasticity in arterial wall mechanics. In G. A. Holzapfel and R. W. Ogden, editors, *Biomechanical Modelling at the Molecular, Cellular and Tissue Levels. CISM Courses and Lectures no. 508*, pages 179–258, Wien, New York, 2009. Springer-Verlag. CISM Courses and Lectures no. 508.

[158] World Health Organization. The world health organization 2014–Global status report on noncommunicable diseases. http://www.who.int/nmh/publications/ncd-status-report-2014/en/, 2014.

[159] World Health Organization. The world health organization 2017–Cardiovascular diseases: Key facts. http://www.who.int/en/news-room/fact-sheets/detail/cardiovascular-diseases-(cvds), 2017.

[160] M. Ortiz and A. Pandolfi. Finite-deformation irreversible cohesive elements for three-dimensional crack-propagation analysis. *Int. J. Numer. Meth. Engng*, 44:1267–1282, 1999.

[161] V. Ottani, M. Raspanti, and A. Ruggeri. Collagen structure and functional implications. *Micron*, 32:251–260, 2001.

[162] S. Pasta, J. A. Phillippi, T. G. Gleason, and D. A. Vorp. Effect of aneurysm on the mechanical dissection properties of the human ascending thoracic aorta. *J. Thorac. Cardiovasc. Surg.*, 143:460–467, 2012.

[163] P. Perzyna. Thermodynamic theory of viscoplasticity. *Adv. Appl. Mech.*, 9:243–377, 1966.

[164] K. Pham, H. Amor, J. J. Marigo, and C. Maurini. Gradient damage models and their use to approximate brittle fracture. 20:618–652, 2011.

[165] R. B. Pipes and B. W. Cole. On the off-axis strength test for anisotropic material 1. *J. Compos. Mater.*, 7:246–256, 1973.

[166] K. R. Popper. *Die Logik der Forschung*. Mohr Siebeck, 1934.

[167] A. Qiao, W. Yin, and B. Chu. Numerical simulation of fluid–structure interaction in bypassed debakey iii aortic dissection. *Comput. Methods Biomech. Biomed. Engin.*, 18:1173–1180, 2015.

[168] A. Raina and C. Miehe. A phase-field model for fracture in biological tissues. *Biomech. Model. Mechanobiol.*, 15:479–496, 2016.

[169] K. Rajagopal, C. Bridges, and K. R. Rajagopal. Towards an understanding of the mechanics underlying aortic dissection. *Biomech. Model. Mechanobiol.*, 6:345–359, 2007.

[170] S. Reese. *Theorie und Numerik des Stabilitätsverhaltens hyperelastischer Festkörper*. Dissertation, Institut für Mechanik IV der Technischen Hochschule Darmstadt, 1994.

[171] S. Reese and S. Govindjee. A theory of finite viscoelasticity and numerical aspects. *Int. J. Solids Structures*, 35:3455–3482, 1998a.

[172] R. S. Rivlin and A. G. Thomas. Rupture of rubber. I. characteristic energy for tearing of elastomers. *Rubber Chem. Technol.*, 18:177–188, 1953.

[173] M. R. Roach and A. C. Burton. The reason for the shape of the distensibility curves of arteries. *Canad. J. Biochem. Physiol.*, 35:681–690, 1957.

[174] M. R. Roach and S. H. Song. Variations in strength of the porcine aorta as a function of location. *Clin. Invest. Med.*, 17:308–318, 1994.

[175] S. Roccabianca, G. A. Ateshian, and J. D. Humphrey. Biomechanical roles of medial pooling of glycosaminoglycans in thoracic aortic dissection. *Biomech. Model. Mechanobiol.*, 13:13–25, 2014.

[176] D. Rohmer, A. Sitek, and G. T. Gullberg. Reconstruction and visualization of fiber and laminar structure in the normal human heart from ex vivo diffusion tensor magnetic resonance imaging (DTMRI) data. *Invest. Radiol.*, 42:777–789, 2007.

[177] M. H. Ross and W. Pawlina. *Histology. A Text and Atlas with Correlated Cell and Molecular Biology*. Lippincott Williams & Wilkins, Baltimore, 2011.

[178] M. B. Rubin and S. R. Bodner. A three-dimensional nonlinear model for dissipative response of soft tissue. *Int. J. Solids Structures*, 39:5081–5099, 2002.

[179] I. K. Rüssel, M. J. Götte, J. G. Bronzwaer, P. Knaapen, W. J. Paulus, and A. C. van Rossum. Left ventricular torsion: an expanding role in the analysis of myocardial dysfunction. *JACC Cardiovasc. Imaging*, 2:648–655, 2009.

[180] G. B. Sands, D. A. Gerneke, D. A. Hooks, C. R. Green, B. H. Smaill, and I. J. LeGrice. Automated imaging of extended tissue volumes using confocal microscopy. *Microsc. Res. Tech.*, 67:227–239, 2005.

[181] G. B. Sands, B. H. Smaill, and I. J. LeGrice. Virtual sectioning of cardiac tissue relative to fiber orientation. In *Proc. 30th Annual Int. Conf. of the IEEE Engineering in Medicine and Biology Society EMBS 2008*, pages 226–229, 2008.

[182] C. Sansour. On the physical assumptions underlying the volumetric isochoric split and the case of anisotropy. *Eur. J. Mech. A/Solids*, 27:28–39, 2007.

[183] F. Schmid, G. Sommer, M. Rappolt, C. A. J. Schulze-Bauer, P. Regitnig, G. A. Holzapfel, P. Laggner, and H. Amenitsch. In situ tensile testing of human aortas by time-resolved small angle X-ray scattering. *Synchro. Rad.*, 12:727–733, 2005.

[184] H. Schmid, M. P. Nash, A. A. Young, and P. J. Hunter. Myocardial material parameter estimation-a comparative study for simple shear. *J. Biomech. Eng.*, 128:742–750, 2006.

[185] T. Schmidt and D. Balzani. Relaxed incremental variational approach for the modeling of damage-induced stress hysteresis in arterial walls. *J. Mech. Behav. Biomed. Mater.*, 58:149–162, 2016.

[186] T. Schmidt, D. Balzani, and G. A. Holzapfel. Statistical approach for a continuum description of damage evolution in soft collagenous tissues. *Comput. Meth. Appl. Mech. Eng.*, 278:41–61, 2014.

[187] A. J. Schriefl, T. Schmidt, D. Balzani, G. Sommer, and G. A. Holzapfel. Selective enzymatic removal of elastin and collagen from human abdominal aortas: uniaxial mechanical response and constitutive modeling. *Acta Biomater.*, 17:125–136, 2015.

[188] A. J. Schriefl, G. Zeindlinger, D. M. Pierce, P. Regitnig, and G. A. Holzapfel. Determination of the layer-specific distributed collagen fiber orientations in human thoracic and abdominal aortas and common iliac arteries. *J. R. Soc. Interface*, 9:1275–1286, 2012.

[189] J. Schröder, P. Neff, and D. Balzani. A variational approach for materially stable anisotropic hyperelasticity. *Int. J. Solids Structures*, 42:4352–4371, 2005.

[190] J. Schröder, N. Viebahn, D. Balzani, and P. Wriggers. A novel mixed finite element for finite anisotropic elasticity: the ska-element simplified kinematics for anisotropy. *Comput. Meth. Appl. Mech. Eng.*, 310:474–494, 2016.

[191] C. A. J. Schulze-Bauer, C. Mörth, and G. A. Holzapfel. Passive biaxial mechanical response of aged human iliac arteries. *J. Biomech. Eng.*, 125:395–406, 2003.

[192] P. Sharma and N. Maffulli. Tendon injury and tendinopathy: healing and repair. *J. Bone Joint Surg.*, 87:187–202, 2005.

[193] V. R. Sherman, W. Yang, and M. A. Meyers. The material science of collagen. *J. Mech. Behav. Biomed. Mater.*, 52:22–50, 2015.

[194] J. C. Simo. On a fully three-dimensional finite-strain viscoelastic damage model: Formulation and computational aspects. *Comput. Meth. Appl. Mech. Eng.*, 60:153–173, 1987.

[195] J. C. Simo and F. Armero. Geometrically non–linear enhanced strain mixed methods and the method of incompatible modes. *Int. J. Numer. Meth. Engng*, 33:1413–1449, 1992.

[196] J. C. Simo, F. Armero, and R. L. Taylor. Improved versions of assumed enhanced strain tri–linear elements for 3D finite deformation problems. *Comput. Meth. Appl. Mech. Eng.*, 110:359–386, 1993.

[197] J. C. Simo and T. J. R. Hughes. *Computational Inelasticity*. Springer-Verlag, New York, 1998.

[198] J. C. Simo, J. Oliver, and F. Amero. An analysis of strong discontinuities induced by strain softening in rate-independent inelastic solids. *Comput. Mech.*, 12:277–296, 1993.

[199] J. C. Simo and M. S. Rifai. A class of mixed assumed strain methods and the method of incompatible modes. *Int. J. Numer. Meth. Engng*, 29:1595–1638, 1990.

[200] J. C. Simo and R. L. Taylor. Quasi-incompressible finite elasticity in principal stretches. Continuum basis and numerical algorithms. *Comput. Meth. Appl. Mech. Eng.*, 85:273–310, 1991.

[201] J. C. Simo, R. L. Taylor, and K. S. Pister. Variational and projection methods for the volume constraint in finite deformation elasto-plasticity. *Comput. Meth. Appl. Mech. Eng.*, 51:177–208, 1985.

[202] J. Skrzypek and A. Ganczarski. *Modeling of Material Damage and Failure of Structures*. Springer Verlag, Berlin, 1999.

[203] G. Sommer, T. C. Gasser, P. Regitnig, M. Auer, and G. A. Holzapfel. Dissection properties of the human aortic media: an experimental study. *J. Biomech. Eng.*, 130:021007–1–12, 2008.

[204] G. Sommer, A. J. Schriefl, M. Andrä, M. Sacherer, Ch. Viertler, H. Wolinski, and G. A. Holzapfel. Biomechanical properties and microstructure of human ventricular myocardium. *Acta Biomater.*, 24:172–192, 2015.

[205] G. Sommer, S. Sherifova, P. J. Oberwalder, O. E. Dapunt, P. A. Ursomanno, A. DeAnda, B. E. Griffith, and G. A. Holzapfel. Mechanical strength of aneurysmatic and dissected human thoracic aortas at different shear loading modes. *J. Biomech.*, 49:2374–2382, 2016.

[206] A. J. M. Spencer. Part III. Theory of invariants. In A. C. Eringen, editor, *Continuum Physics*, volume I – Mathematics, pages 239–353. Academic Press, New York, 1971.

[207] A. J. M. Spencer. *Deformations of Fibre-reinforced Materials*. Clarendon Press, Oxford, 1972.

[208] A. J. M. Spencer. Constitutive theory for strongly anisotropic solids. In A. J. M. Spencer, editor, *Continuum Theory of the Mechanics of Fibre-Reinforced Composites*, pages 1–32. Springer-Verlag, Wien, 1984. CISM Courses and Lectures no. 282.

[209] G. J. Strijkers, A. Bouts, W. M. Blankesteijn, T. H. J. M. Peeters, A. Vilanova, M. C. van Prooijen, H. M. H. F. Sanders, E. Heijman, and K. Nicolay. Diffusion tensor imaging of left ventricular remodeling in response to myocardial infarction in the mouse. *NMR Biomed.*, 22:182–190, 2009.

[210] R. B. Svensson, H. Mulder, V. Kovanen, and S. P. Magnusson. Fracture mechanics of collagen fibrils: Influence of natural cross-links. *Biophys. J.*, 104:2476–2484, 2013.

[211] H. Tada, P. C. Paris, and G. R. Irwin. *The Stress Analysis of Cracks Handbook*. ASME Press, New York, 2000.

[212] A. Takei, B. Roman, J. Bico, E. Hamm, and F. Melo. Forbidden directions for the fracture of thin anisotropic sheets: An analogy with the wulff plot. *Phys. Rev. Lett.*, 110:144301–1–144301–5, 2013.

[213] R. Talreja and C. V. Singh. *Damage and Failure of Composite Materials*. Cambridge University Press, Cambridge, 2012.

[214] A. S. M. Tam, M. C. Sapp, and M. R. Roach. The effect of tear depth on the propagation of aortic dissections in isolated porcine thoracic aorta. *J. Biomech.*, 31:673–676, 1998.

[215] R. L. Taylor. *FEAP – A Finite Element Analysis Program, Version 8.4 User Manual*. University of California at Berkeley, Berkeley, California, 2013.

[216] S. Teichtmeister, D. Kienle, F. Aldakheel, and M.-A. Keip. Phase-field modeling of fracture in anisotropic brittle solids. *Int. J. Non-Linear Mech.*, 97:1–21, 2017.

[217] M. J. Thubrikar, P. Agali, and F. Robicsek. Wall stress as a possible mechanism for the development of transverse intimal tears in aortic dissections. *J. Med. Eng. Technol.*, 23:127–134, 1999.

[218] J. Tong, T. Cohnert, P. Regitnig, J. Kohlbacher, R. Birner-Gruenberger, A. J. Schriefl, G. Sommer, and G. A. Holzapfel. Variations of dissection properties and mass fractions with thrombus age in human abdominal aortic aneurysms. *J. Biomech.*, 47:14–23, 2014.

[219] J. Tong, G. Sommer, P. Regitnig, and G. A. Holzapfel. Dissection properties and mechanical strength of tissue components in human carotid bifurcations. *Ann. Biomed. Eng.*, 39:1703–1719, 2011.

[220] C. Truesdell and W. Noll. *The Non-linear Field Theories of Mechanics*. Springer-Verlag, Berlin, 2nd edition, 1992.

[221] S. W. Tsai and H. T. Hahn. *Introduction to Composite Materials*. Technomic Publishing Company, Lancaster, 1980.

[222] S. W. Tsai and E. M. Wu. A general theory of strength of anisotropic materials. *J. Compos. Mater.*, 5:58–80, 1971.

[223] A. Tsamis, J. T. Krawiec, and D. A. Vorp. Elastin and collagen fibre microstructure of the human aorta in ageing and disease: a review. *J. R. Soc. Interface*, 10:20121004, 2013.

[224] A. K. Tsaturyan, V. J. Izacov, S. V. Zhelamsky, and B. L. Bykov. Extracellular fluid filtration as the reason for the viscoelastic behavior of the passive myocardium. *J. Biomech.*, 17:749–755, 1984.

[225] K. M. Tse, P. Chiu, H. P. Lee, and P. Ho. Investigation of hemodynamics in the development of dissecting aneurysm within patient–specific dissecting aneurismal aortas using computational fluid dynamics (cfd) simulations. *J. Biomech.*, 44:827–836, 2011.

[226] T. P. Usyk, J. H. Omens, and A. D. McCulloch. Regional septal dysfunction in a three-dimensional computational model of focal myofiber disarray. *Am. J. Physiol. Heart Circ. Physiol.*, 281:H506–H514, 2001.

[227] F. Verzár. Aging of the collagen fiber. In D. A. Hall, editor, *International Review of Connective Tissue Research*, volume 2, pages 243–300. Academic Press, New York, 1964.

[228] L. Wang, N. A. Hill, S. M. Roper, and X. Luo. Modelling peeling- and pressure-driven propagation of arterial dissection. *J. Engr. Math.*, 109:227–238, 2018.

[229] L. Wang, S. M. Roper, N. A. Hill, and X. Luo. Propagation of dissection in a residually–stressed artery model. *Biomech. Model. Mechanobiol.*, 16:139–149, 2017.

[230] Y. Wang, J. A. Johnson, F. G. Spinale, M. A. Sutton, and S. M. Lessner. Quantitative measurement of dissection resistance in intimal and medial layers of human coronary arteries. *Exp. Mech.*, 54:677–683, 2014.

[231] J. A. Weiss and J. C. Gardiner. Computational modeling of ligament mechanics. *Crit. Rev. Biomed. Eng.*, 29:303–371, 2001.

[232] J. A. Weiss, B. N. Maker, and S. Govindjee. Finite element implementation of incompressible, transversely isotropic hyperelasticity. *Comput. Meth. Appl. Mech. Eng.*, 135:107–128, 1996.

[233] H. M. Westergaard. Bearing pressures and cracks. *J. Appl. Mech.*, 6:49–53, 1939.

[234] W. E. Wolfe and T. S. Butalia. A strain-energy based failure criterion for non-linear analysis of composite laminates subjected to biaxial loading. *Compos. Sci. Technol.*, 58:1107–1124, 1998.

[235] P. Wriggers. *Nonlinear Finite Element Methods*. Springer-Verlag, Berlin Heidelberg, 2008.

[236] P. Wriggers, J. Schröder, and F. Auricchio. Finite element formulations for large strain anisotropic material with inextensible fibers. *Adv. Model. and Simul. in Eng. Sci.*, pages 3–25, 2016.

[237] L. Yang, K. O. van der Werf, P. J. Dijkstra, J. Feijen, and M. L. Bennink. Micromechanical analysis of native and cross-linked collagen type I fibrils supports the existence of microfibrils. *J. Mech. Behav. Biomed. Mater.*, 6:148–158, 2012.

[238] J. Yao, V. D. Varner, L. L. Brilli, J. M. Young, L. A. Taber, and R. Perucchio. Viscoelastic material properties of the myocardium and cardiac jelly in the looping chick heart. *J. Biomech. Eng.*, 134:1–7, 2012.

[239] O. C. Zienkiewicz and R. L. Taylor. *The Finite Element Method. Solid Mechanics*, volume 2. Butterworth Heinemann, Oxford, 5th edition, 2000.

[240] T. I. Zohdi. A computational framework for network modeling of fibrous biological tissue deformation and rupture. *Comput. Meth. Appl. Mech. Eng.*, 196:2972–2980, 2007.